# Metal-Support Interactions on Fe-based Fischer-Tropsch Catalysts

**Ramoshibidu Patrick Mogorosi**

BSc (Chem. Eng), UCT



Thesis submitted to the University of Cape Town
in fulfilment of the requirements
for the degree of
**Doctor of Philosophy**

Catalysis Research Unit
Department of Chemical Engineering

UNIVERSITY OF CAPE TOWN

Rondebosch
March 2012

# DECLARATION

I, Patrick Mogorosi certify that this submission is my own, unaided work, except for the information obtained from literature sources and my prescribed supervisors. All sources of information have been adequately acknowledged and referenced. I have not received assistance from any other source in completing this submission.

Signature:…… Date:……..

R.P. Mogorosi

# ACKNOWLEDGEMENTS

How does a man begin to give thanks? Does he bow his head in gratitude, soak his words in a sincere tone or lavish the people to whom he is grateful with hugs, kisses, gifts or even song? Unfortunately I lack the charismatic ability to be original and thus I can only offer these words.

First and foremost, I would like to thank my supervisor, Prof Eric van Steen. If there were words that could describe a great man, I would learn them all and use them all to describe what your support means to me. You have been more than a teacher to me; you even took on the tasks of being my support system, advisor, psychologist, critic, motivator, life style coach, lawyer and spiritual guide but most of all you have been a friend. You helped me realised my potential and fulfil a dream. For that I will forever be grateful. I would also like to thank Prof Michael Claeys for his contribution and advice throughout my project.

I would also like to thank my family for their continued and relentless support during my post graduate study. Most of all, a special thank you to my mother, Jacobeth Mogorosi, and my grandmother, Mary Mogorosi, for their encouragement when times were hard; and my two little brothers, Obakeng and Ofentse, for keeping the smile on my face even when I felt miserable. To my mother, you always say that I could live to be a hundred years old and even then I would have no idea how much you love me, until I have a child of my own. I have come to slightly comprehend what you mean and now that this is done, I will get started on finding a wife and getting you a grandson or granddaughter. To my extended family I say, 'much love and many thanks'

I am also indebted to my colleagues; Sonwabo, Nicolay, Doreen, Tracey, Conrad, Kubefu, Waldo, Jacobus, just to mention a few; for providing a interesting, fun, stimulating and sometimes fanatical environment in which I could learn grow and develop.

# Presentations and Publications

## Poster Presentations

1. CATSA Conference 2008, Parys, South Africa
   Metal support interactions in Fe-based Fischer-Tropsch catalysts

2. CATSA Conference 2009, Worcester, South Africa
   The effects of Fe-O-Si interactions on the activity and selectivity of Fe-based Fischer-Tropsch catalysts.

## Oral Presentations

1. CATSA Conference 2010, Bloemfontein, South Africa
   Silica as a chemical promoter for Fe-based Fischer-Tropsch catalysts

2. University of the Cape Town Postgraduate Symposium 2009, Johannesburg, South Africa
   Characterization of Fe-O-Si interactions

3. University of the Witwatersrand Postgraduate Symposium 2008, Johannesburg, South Africa
   Characterization of Fe-O-Si interactions



## Publications Resulting From This Work

1. R. P. Mogorosi, N. Fishcer, M. Claeys and E. van Steen, 'Strong-metal-support interactions by molecular design: Fe-silicate interactions in Fischer-Tropsch catalysts' *Journal of Catalysis* (2012), doi:10.1016/j.jcat.2012.02.002

2. R. P. Mogorosi, M. Claeys and E. van Steen, 'The promotion of Fe-based Fischer-Tropsch catalysts via 'the contact effect' induced by TBO modification' (in preparation).

3. R. P. Mogorosi, M. Claeys and E. van Steen, "The effects of Fe-O-Si interactions on the carburization of Fe-based Fischer-Tropsch catalysts' (in preparation).

# SYNOPSIS

‘Metal support interactions’ is a term used to describe a phenomenon whereby the interaction between the active metal and the support material is strong enough to affect the catalytic activity and selectivity of the active phase. Primarily, there are two theories described in literature to explain the manner in which the development of these interactions alters catalytic behavior in supported catalysts. The first theory is ‘the contact affect’, which is generally associated with partially reducible supports such as $TiO_2$ [Tauster et al., 1978]. It is believed that the intimate contact between the partially reduced surface of the support and the surface of the active phase results in the creation of special contact sites at the interface. These sites are thought to be responsible for the improved activity observed in $TiO_2$ supported catalysts [Burch and Flambard, 1982; Vannice and Sudhakar, 1984; Tauster, 1987]. The second theory is ‘the ligand effect’. With this hypothesis, it is proposed that the development of chemical bonds at the interface between the active metal and the support material is responsible for the altered catalytic behavior in supported catalysts [Qing et al., 2011; Sou et al., 2012]. The presence of these bonds is believed to alter the strength of CO and $H_2$ absorption on the surface of the active phase, resulting in different activity and selectivity. These chemical bonds might be viewed as ligand attachments [Haller and Resasco, 1989], holding the active metal in place. The ligand effect is commonly associated with irreducible support material such as silica [Hou et al., 2008; Sou et al., 2012] and alumina [Taniguchi, et al., 1988; Wan et al., 2007].

The aim of this study was to investigate metal support interactions as a ligand effect. The objective was to prepare model catalysts and modify the surface of the iron oxide using alkoxide compounds, viz. tetra ethoxy-silane (TEOS) and titanium butoxide (TBO), to generate the Fe-O-Si and Fe-O-Ti interactions respectively in a controlled and varying manner in order to investigate how these interactions affect the behaviour of the catalysts. The presence of both the surface silicate and surface titanate groups in the calcined catalyst precursor was confirmed using DRIFTS. Characterization of the calcined samples, containing $Fe_2O_3$, showed an overall decrease in the average crystallite size with increasing alkoxide loading (for both TEOS and TBO). However, this effect was more severe for the TEOS modified samples.

The surface silicate groups are preserved after a hydrogen treatment at 350 $^oC$ for 16 hrs. These surface ligands are associated with the residual iron oxide phase, wüstite. During the Fischer-Tropsch synthesis, α-Fe is mostly converted into $Fe_5C_2$, whereas FeO is the main source for hexagonal carbide, $Fe_2C$.The activity per unit surface area of hexagonal carbide,

$Fe_2C$, is ca. 25% higher than that of $Fe_5C_2$. The presence of surface silicate groups on $Fe_2C$ result in a further enhancement of the rate per unit surface area of $Fe_2C$ by a factor of ca. 3. This is being ascribed to the enhanced availability of hydrogen on the surface due to the presence of the surface silicate groups, which also results in an increase in the methane selectivity, a decrease in the olefin content, and a decrease in formation of branched product compounds.

The reduction of the TBO modified samples leads to formation of α-Fe and Fe-Ti mixed oxides, due to the incorporation of the Ti atoms into the iron oxide structure. The α-Fe was converted to $Fe_5C_2$ whilst the high thermal stability of the mixed metal oxide preserved the oxide phase during Fischer-Tropsch synthesis at 250 $^0$C. The $Fe_5C_2$ in the TBO modified sample was ca. 20% more active than that found in the unmodified sample, possibly due the intimate contact sites between that active phase and the mixed metal oxide phase. The presence of these contact sites is also thought to be responsible for the enhanced methane selectivity observed in TBO modified samples. The chain propagation reaction and the formation of olefins, thought to occur at different sites, showed no effects due to TBO modification. However, the Lewis acid sites present on the surface of the Fe-Ti-O mixed oxides, results in the double bond isomerisation of the α-olefins. At high reaction temperature (300 $^0$C), CO induced reduction of the mixed metal oxide was observed, resulting in the migration of the titanium atoms to the surface. The presence of the Ti-ligands on the carbide surface was found to block active sites resulting in a decrease in the normalized activity of the catalytically active phase with increasing TBO loading. The trends obtained in the analysis of the selectivity data were consistent with those obtained at lower operating temperature.

# TABLE OF CONTENTS

# LIST OF FIGURES

## Chapter 2



## Chapter 4



## Chapter 5



## Chapter 6

# LIST OF TABLES

## Chapter 5



## Chapter 6

# NOMENCLATURE

| Abbreviation: | Description |
|---|---|
| FTS | Fischer-Tropsch Synthesis |
| HTFT | High Temperature Fischer-Tropsch process |
| LTFT | Low Temperature Fischer-Tropsch process |
| WGS | Water Gas Shift |
| TEOS | Tetraothoxy-silane |
| TBO | Titanium butoxide |
| TEM | Transmission Electron Microscopy |
| XRD | X-Ray Diffraction |
| FTIR | Fourier Transform Infrared |
| SEM | Scanning Electron Microscopy |
| EDX | Energy Dispersive X-ray |
| DRIFTS | Diffuse Reflectance Fourier Transform Spectroscopy |
| TPR | Temperature Programmed Reduction |
| FIC | Flow controller |
| CV | Flow control valve |
| CWV | 4 way flow control valve |
| NDV | Needle valve |
| AS | Ampoule Sampler |
| PI | Pressure Indicator |
| GC-TCD | Gas Chromatography- Thermal Conductivity Detector |
| GC-FID | Gas Chromatography- Flame Ionisation Detector |
| SASOL | Suid Afrikaanse Steenkool en Olie |
| PI | Pressure Indicator |
| DTF | Density Function Theory |
| SMSI | Strong Metal Support Interactions |
| CUS | Coordinate Unsaturated Sites |
| TOPAS | Total Pattern Analysis Solution |

# 1

# Introduction



*Promoted iron-based catalysts are commonly used in the production of liquid fuels via Fischer-Tropsch synthesis [Dry, 1981]. The active metal (Fe) may interact with the structural promoter (supports or binders) leading to a formation of a covalent bond; Fe-O-Support. These bonds are often referred to as metal support interactions. The effect of these bonds on the resulting catalytic activity and selectivity is largely unexplored. This is due to the complex nature of industrial catalyst; brought about by the presence of other constituents (e.g. chemical promoters) within the catalyst formulation. Therefore, in this study, the catalysts system is simplified by attaching surface ligands (-O-Support) to precipitated iron oxide crystallites to mimic the interactions found in industrial catalysts. The purpose of this study is to investigate the influence of these surface interactions (or ligands) on the catalytic behaviour of iron catalysts in Fischer-Tropsch synthesis.*

# 1.1 Catalysts, activity and selectivity

Fischer-Tropsch synthesis is the catalyzed conversion of synthesis gas ($H_2$ and CO) into a wide range of hydrocarbons. The transition metals Ni, Ru, Fe and Co have significant activity for this process [Vannice, 1977]. Under industrial conditions, Ni produces mostly methane. On the other hand, Ru is expensive, making it uneconomical for industrial application [Dry, 2004a]. Therefore, only Fe and Co are industrially used as practical catalysts for Fischer-Tropsch synthesis. Both Fe-based and Co-based catalysts are used on a commercial scale in low temperature Fischer-Tropsch processes (220-250 $^0$C, 25-40 bar) [Dry, 2004a]. Only Fe-based catalysts are used in high temperature Fischer-Tropsch processes (330-350 $^0$C, 25 bar) for petrol and chemical production, since at those conditions the methane selectivity over Co-based catalysts becomes too high [Dry, 1981].

Industrial Fischer-Tropsch catalysts are generally made up of three components; the active metal, promoter and the support (or binder). The active metal (Fe or Co) constituent in the catalyst is responsible for the catalytic function, i.e. the reaction takes place on the surface of the metal. Other metals such as Cu (used for Fe-based catalysts), Pt, Pd and Ru (used for Co- based catalysts) can be added to the catalyst (as promoters) to improve the reducibility of the active metal. There are no known chemical promoters for the cobalt based catalysts. However, potassium is commonly used as a chemical promoter for Fe-based catalysts. Potassium addition has been shown to improve the activity of the catalyst and its selectivity towards heavier hydrocarbons [Dry, 1981].

The product distribution, for Fischer-Tropsch synthesis, depends on reaction temperature, total pressure, $H_2$/CO feed ratio and the amount of chemical promoter added but, both the activity and selectivity of Fischer Tropsch catalysts depends mainly on the active metal used [Dry, 1981]. Activity is a function of the total active metal (or metal carbide for Fe-based catalysts) surface area available. A high catalytically active surface area can be achieved with small crystallites of the active phase. Therefore, the active metal is distributed on irreducible metal oxide such as $SiO_2$, $TiO_2$ and $Al_3O_3$ to stabilize these small crystallites [Moulijn et al., 2001; Yang et al., 2005] and also to minimize loss of activity due to crystalline growth (sintering) [Dry, 1981]. These irreducible metal oxides are referred to as supports (or binders). All support materials show no activity for the Fischer-Tropsch synthesis on their own. They are believed to be inert since they were previously assumed to be irreducible under typical reduction and reaction conditions applied to the catalysts [Dry, 1981]. However, interactions between the active metal and the support may occur, hampering the reducibility of the active metal precursors. These interactions are often referred to as metal-support interactions [Tauster et al., 1978; Tauster et al., 1981; Tauster, 1987].

## 1.2 Metal-support interactions

Metal-support interactions have been extensively investigated in the past [Tauster et al., 1978; Raupp and Dumesic, 1984; Vannice and Sudhakar, 1984; Tauster, 1987] and are still of interest in recent work [Riva et al, 2000; Puskas et al., 2006; Qing et al., 2011; Sou et al., 2012]. The active metal can bond to the support through the formation of a surface chemical bond ('the ligand effect') [Qing et al., 2011; Sou et al., 2012] or through electronic exchange with a partially reduced support compound ('the contact effect') [Tauster, 1987; Riva et al., 2000]. These interactions occur for both Fe-based [Wan et al., 2006, Zhang et al., 2006; Hou et al., 2008; Qing et al., 2011; Sou et al., 2012] and Co-based catalysts [Puskas et al., 2006; Jacobs et al., 2007]. The nature of these interactions depends on the combination of the active metal and the type of support used. The strength of interaction, for both Fe and Co catalyst, increases in the order $SiO_2 < TiO_2 < Al_2O_3$ [Choi et al., 1997].

The development of these interactions generally has a negative influence on the reducibility of active metal precursors [Tauster et al., 1978; Puskas et al., 2006; Hou et al., 2008]. Moreover, these interactions also impact the activity and selectivity of the catalyst [Tauster, 1987; Puskas et al., 2006; Qing et al., 2011] by changing CO (and $H_2$) adsorption behavior on the modified surface [Tauster et al., 1978; Wan et al., 2006; Sou et al., 2012]. However, in Fe-based catalysts, the presence of chemical promoters (K or Na) has dominant influence on the overall Fischer-Tropsch activity and selectivity of the catalysts [Dry, 2004b]. Therefore, it is difficult to determine whether the support material present in the catalyst formulate has any influence on the resulting catalytic behavior. Furthermore, the presence of structural promoters stabilizes the catalyst phase during Fischer-Tropsch synthesis [Dry, 1981; Bukur et al., 1990; Bartholomew, 2001] and also affects crystallite size, which in turns affects the catalyst activity and selectivity [Barkhuizen et al., 2006; Bezemer et al., 2006]. Hence, the effects of metal support interaction on the activity and selectivity of promoted Fe-based catalysts are possibly masked by the presence of these promoters.

Recent research in Fischer-Tropsch synthesis has been aimed mainly at improving catalytic activity and maximizing the selectivity towards the $C_{5+}$ cut (i.e. minimizing the formation of light hydrocarbons, $C_1$-$C_4$). This is due to the increasing demand for liquid products such as petrol and diesel [Dry, 2004a]. Work done in the past was aimed at optimizing the support and promoter loading to achieve high activity [Yang et al., 2005], improving selectivity towards long chain hydrocarbons [Hou et al., 2008; Bukur et al., 1990] and understanding the influence of metal crystallite size on catalytic behavior [Mabaso, 2005; Barkhuizen et al., 2006; Bezemer et al., 2006]. However, optimization of catalytic activity and $C_{5+}$ selectivity can only be fully achieved if the influence of all the constituents within the catalyst formulation is understood. This includes the role metal support interactions play on the resulting activity of

the catalyst and the development of the product spectrum. The documented effects of these interactions are clouded by the influence of other constituents in the catalyst formulation (e.g. chemical and structural promotion). Thus, in order to isolate the effects of metal support on the catalytic behaviour of iron-based Fischer-Tropsch catalysts, a new approach is needed.

## 1.3 Metal support interactions as a ligand effect

The chemical bond anchoring the active metal to the support (or binder) material might be viewed as a ligand [Cheng et al., 1991b]. These anchors (ligands) are resistant to reduction [Puskas et al., 2006; Yang et al., 2005; Hou et al., 2008; Sou et al., 2012] and are Therefore, present during Fischer-Tropsch synthesis. The effect of this anchor-type of structures on the resulting catalytic activity is largely unexplored. In this study, the effect of the modification of the surface of iron nanoparticles with surface silicate (or titanate) ligands on the catalytic activity in CO hydrogenation is investigated. This can be regarded as a model for the anchors present when using silica (or titania) as a binder [Pham and Datye, 2000] or support [Egiebor and Cooper, 1985; Duvenhage and Coville, 2002].

Metal-support interactions are typically investigated by putting the catalytically active phase on some support followed by heat treatment or, in the case of iron-based Fischer-Tropsch catalysts, by varying the amount of binder in the sample. In this study, a novel approach is taken by modifying the surface of the catalyst precursor with covalently bonded ligands mimicking the metal-support interactions. This will serve as model systems for interactions present in industrial iron-based Fischer-Tropsch catalysts. The effect of these ligands anchored to the surface of the catalyst precursor on the activation step and on the resulting activity and product formation in the Fischer-Tropsch synthesis will be reported.

# 2

# Background



*Fischer-Tropsch synthesis (FTS) is a practical way of converting synthesis gas (CO + $H_2$) derived from coal and natural gas to gasoline, diesel oil, wax and chemicals such as olefins, alcohols and aldehydes [Dry, 2004a]. The enormous reserves of coal deposits and low value methane (natural gas) represent a major potential source of liquid transport fuels [Steynberg, 2004]. Fischer-Tropsch synthesis is relevant because the fuel derived from this process is very clean, since the synthesis gas used in the process may only contain a few parts per billion of sulphur [Schulz, 1999]. Furthermore, the high oil prices and developments in Fischer-Tropsch technology make this process more viable for the production of cheaper and cleaner fuels.*

## 2.1 Relevance of the Fischer-Tropsch process

Fischer-Tropsch synthesis involves the hydrogenation of CO over a catalyst, mainly group VIII metals, to produce a spectrum of hydrocarbons and oxygenates with water and/or $CO_2$ as co-products. The objective of the Fischer-Tropsch (FT) process is to produce transportation fuels and other chemicals from synthesis gas ($CO + H_2$) derived from coal, biomass or natural gas [van Steen and Claeys, 2008]. The fuel derived from this process may be used as a substitute for crude oil derived products. The fuels derived from the FISCHER-TROPSCH synthesis have high environmental value because they are sulphur and nitrogen free [Steynberg, 2004]. This property is recognized as very valuable in the ongoing drive towards cleaner fuels. Furthermore, the diesel produced from this process has excellent combustion properties (cetane number > 60).

Oil prices are very volatile. In 2008, the oil price was 150 US$/barrel in July and dropped to 30 US$/barrel in December of the same year [www.oil-price.net/index.php?lang=en; accessed 15/12/2010]. The volatility of the oil prices has raised concerns about the production of liquid fuels all over the world. Focus is, therefore, being directed towards alternate methods of liquid fuel production. Steynberg and Dry (2004) determined that the Fischer-Tropsch process is commercially viable when the price of crude oil exceeds 20 US$/barrel, since at this price Fischer-Tropsch products compete with liquid fuels produced from crude oil. The high oil prices (ca. 90 US$/barrel in 2011)[a] and the relatively low cost of production of synthetic fuel have presented the Fischer-Tropsch process with opportunity to place a significant claim in the global energy scene [Khodakov et al., 2007]. Another driving force has been the environmental pressure to minimize the flaring gas associated with oil recovery [Vosloo, 2001]. Improvements in the cost effectiveness of Fischer-Tropsch technology, in particular the development of more active catalysts [Khodakov et al., 2007], and improved reactor design [Vosloo, 2001], can make production of petroleum based products from non-traditional feedstock utilizing the Fischer-Tropsch process economical.

Sasol has more than 50 years[b] of proven commercial experience in producing synthetic fuels using Fischer-Tropsch synthesis. The Fischer-Tropsch process has recently seen the commissioning of Fischer-Tropsch plants in different locations all over the world. A methane-based plant, aimed at producing waxes, high quality diesel fuels and kerosene, is already operational in Malaysia with, a capacity of $3.7 \times 10^6$ bbl per year [Eilers et al., 1990]. A joint venture between SASOL and Chevron has seen the development of a similar plant in Nigeria[b]. Exxon and SASOL, in a joint venture, have recently started production in a new plant in Qatar[b]. This shows that this process will remain relevant for years to come.

a: http://inflationdata.com/inflation/inflation_rate/historical_oil_prices_table.asp: accessed 7/10/2011

b: http://www.sasol.com/sasol_internet/downloads/GTL_brochure12_6_1150180264478.pdf: accessed 3/02/2012

## 2.2 Industrial application and other reactions associated with Fischer-Tropsch synthesis

The reaction mechanism for the Fischer-Tropsch synthesis involves a series of complex and parallel reactions. There are secondary reactions involved. The basic description of the reaction is that it is a polymerization type reaction that involves the growth of $CH_x$ monomers to form longer chains (see Equation 2.1).

$$n\,CO \quad + \quad 2n\,H_2 \quad \Longrightarrow \quad C_n\,H_{2n} \quad + \quad n\,H_2O \qquad (2.1)$$

Two modes of Fischer-Tropsch synthesis are applied industrially: High Temperature Fischer-Tropsch (HTFT) and Low Temperature Fischer-Tropsch (LTFT) processes.

The HTFT is used for the production of chemicals and petrol range hydrocarbons. This requires high temperature. The temperatures for the HTFT process range from 300 to 350 $^0$C and the reactor is operated at 20 to 40 bar. At these conditions methane selectivity over Co-based catalysts is too high [Dry, 1981] and Therefore, only Fe-based catalysts are used for this process. The yield of hydrocarbons, for iron-based catalysts is mainly in the $C_1$ – $C_{15}$ range [Khodakov et al., 2007]. The products are mostly used as liquids fuels but other valuable chemicals such as α-olefins, can be extracted from the crude synthetic oil [Khodakov et al, 2007]. Furthermore, chemicals such as ketones, alcohols and acetic acid can be obtained from aqueous product stream of this process [Khodakov et al, 2007].

Contrary from the HTFT, the LTFT process is aimed at the production of long chain hydrocarbons and is thus operated at lower temperatures, ranging from 200 to 260 $^0$C. The reactor pressures for both systems are comparable as LTFT is operated at 20 to 45 bar. Both cobalt and iron based catalyst are used for LTFT synthesis. However, water generated in the Fischer-Tropsch process slows down the reaction rate on iron based catalyst a lot more than in cobalt catalyst [Khodakov et al, 2007]. Hence a higher conversion per pass can be obtained with Co-based catalysts [van Berge and Everson, 1997]. Most of the Fischer-Tropsch technologies developed in the last two decades are mainly for the LTFT process using a Co-based catalyst [Khodakov et al, 2007]. However, because Fe is cheap, the operational cost associated with the use of Fe-based catalysts makes these catalysts economically relevant.

The main disadvantage of using LTFT synthesis is that the $H_2$/CO feed ratio for Co-based catalysts has to be high (1.7 – 2.15) and this normally involves the use an upstream water gas shift reactor to adjust the $H_2$ deficit [Steynberg, 2004], if coal or biomass are used as a carbon source. However, Fe-based catalysts support the water gas shift reaction (see Equation 2.2).

$$CO + H_2O \Longrightarrow H_2 + CO_2 \qquad (2.2)$$

The water gas shift reaction produces hydrogen and carbon dioxide as products. For this reason iron catalyst are able to handle feed ratios below 2. The iron catalysts use the water gas shift reaction to adjust the $H_2$ deficit. Thus only Fe-based catalyst are used is the HTFS mode of operation.

Although the WGS reaction allows Fe-based catalyst to deal with coal derived synthesis gas, the production $CO_2$ results in lower carbon efficiency (carbon is lost as $CO_2$). Carbon dioxide gas can also be produced through the disproportionation of CO (Boudouard reaction):

$$2CO \Longrightarrow C + CO_2 \qquad (2.3)$$

The carbon that is formed may coke the catalyst and may results in deactivation of the catalyst. The effects of the Boudouard reaction is more significant for High Temperature Fischer-Tropsch synthesis (HTFT) and less so at low temperatures (LTFT) [Khodakov et al, 2007].

## 2.3 Product formation in the Fischer-Tropsch synthesis

The Fischer-Tropsch synthesis is a polymerization process resulting in a distribution of different chain lengths of the products [Anderson, 1984]. Numerous reaction pathways have been proposed to explain the observed product distribution in the Fischer-Tropsch synthesis (see Figure 2.1).

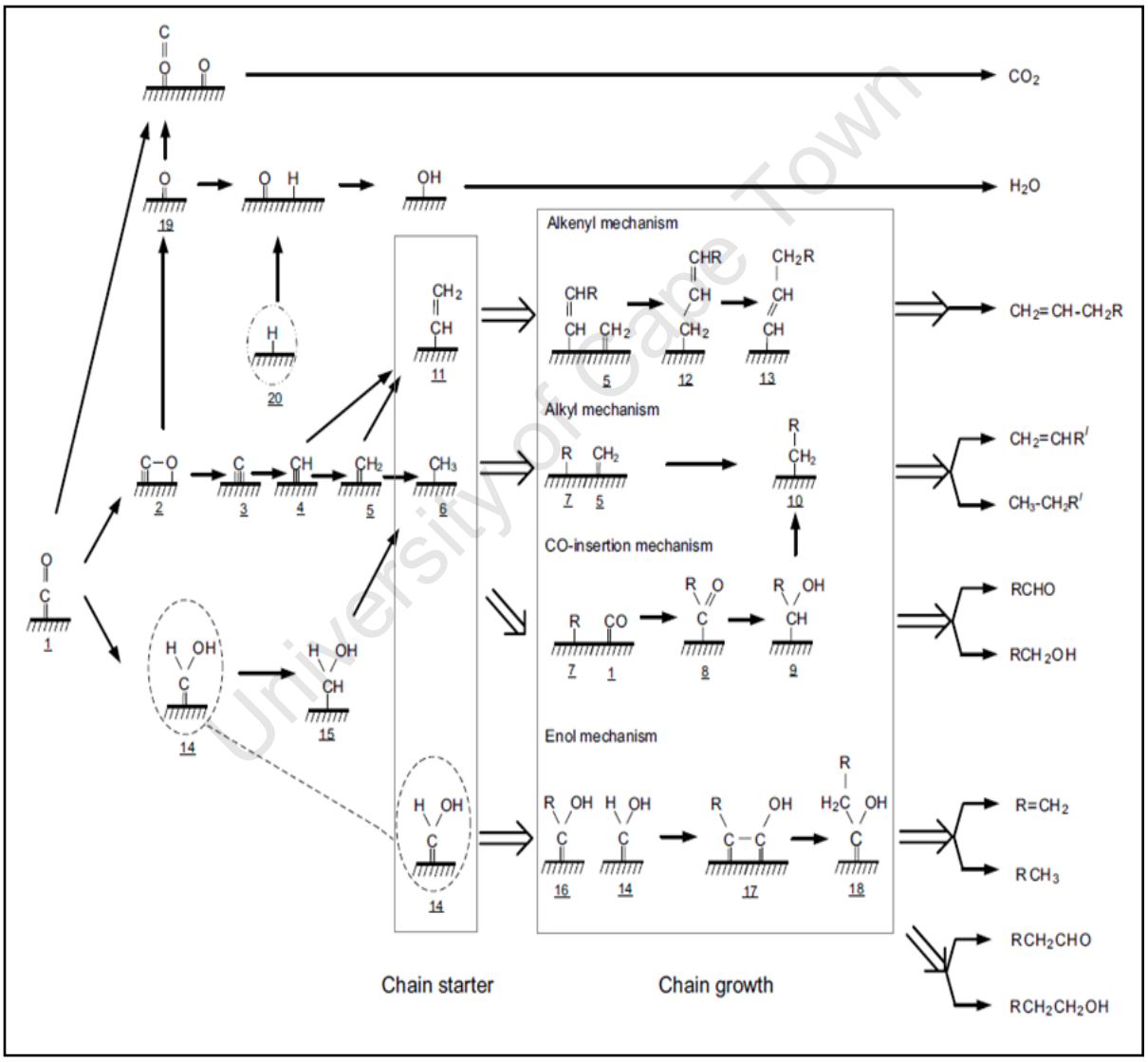


**Figure 2.1:** Overview of Fischer-Tropsch reaction pathways [adopted from Mabaso, 2006].

### 2.3.1 Adsorption of CO and $H_2$

All Fischer-Tropsch catalysts are able to dissociatively absorb the CO and $H_2$. This property is the basis of all mechanisms explaining the formation of Fischer-Tropsch products. The beginning of all the proposed pathways is the same and involves the reactants, $H_2$ and CO, adsorbing onto the active sites of the catalyst. This forms dissociated H species (20) and absorbed CO surface species (1), which can also dissociate to absorbed C surface species (3) and O surface species (19).

Water is the main (co-) product of the Fischer-Tropsch synthesis. The removal of surface oxygen (19), formed via the dissociation of the absorbed CO (1) is required to complete the catalysts cycle. The O species (19) can be hydrogenated to absorbed OH species, followed by reaction with H surface species (20) results in the formation of water. Furthermore, the reaction of absorbed O (19) with absorbed CO (1) results in the formation of $CO_2$.

### 2.3.2 Mechanisms for organic product formation

As in any polymerization reaction, the Fischer-Tropsch surface polymerization requires chain starters and monomers. The various mechanisms proposed for the formation of organic Fischer-Tropsch products are based on this principal. The mechanisms include: the surface carbide mechanism [Fischer and Tropsch, 1926], a mechanism involving an alkenyl intermediate [Maitlis et al., 1999] and an enolic intermediate mechanism [Storch et al., 1951]. Extensive reviews of these mechanisms can be found in literature [Dry, 1981; Anderson, 1984; Claeys and van Steen, 2004].

#### 2.3.2.1 Alkyl mechanism

In the alkyl mechanism, the $CH_3$-species is thought to be the chain starter and the surface $CH_2$-spicies is the monomer initiating chain growth. The monomers (5), formed near the growing chain surface species (7), migrate towards it through surface diffusion [Erley et al., 1983]. The reaction of the two absorbed species results in the formation of a metal-alkyl species (10). Alkenes are formed via β-H-elimination of the metal-alkyl species (10), while methane and higher alkanes form by reductive elimination of the alkyl group [Anderson, 1956]. The relative rate of β-H-elimination and the reductive elimination plays a role in product selectivity which is altered by re-adsorption and further reaction.

### 2.3.2.2 Alkenyl mechanism

Maitlis et al. (1999) proposed the alkenyl mechanism in which vinyl surface species (11) is thought to be formed via the coupling of methylidyne (4) and methylene (5). This is considered to be the chain initiator and the $CH_2$ surface species (5) is believed to be the monomer. Product desorption in the alkenyl mechanism involves the addition of hydrogen to an alkenyl (13) species yielding *α*-olefins. This mechanism fails to explain the primary formation of n-paraffins and does not explain the formation of oxygenates [Claeys and van Steen, 2004]. Furthermore, there is no experimental evidence for the isomerisation reaction of the allyl species (12) to form the vinyl species (13).

### 2.3.2.3 CO-insertion mechanism

This mechanism can explain the formation of oxygen containing organic product compounds. Chemisorbed *CO* is the monomer in the case of the CO-insertion mechanism and $CH_3$ is the chain starter. Chain propagation involves CO-insertion into a metal-alkyl species (7) bond leading to a surface acyl species (8), which is subsequently hydrogenated to form an alcohol species (9). Chain termination reactions of these oxygen containing species leads to the formation of oxygenates (aldehydes and alcohols). Oxygen elimination from the alcohol surface species via formation of water leads to the formation of the alkyl species (10), identical to the species formed via the alkyl mechanism. Chain termination of this species (alkyl) may occur via H-addition yielding n-paraffins or via *β*-H-elimination yielding *α*-olefins.

### 2.3.2.4 Enol mechanism

Another mechanism, the enolic mechanism, was proposed by workers at the Bureau of Mines (Storch et al., 1951). In this mechanism, chemisorbed CO (1) is hydrogenated to form an enolic surface species (14), which is both the chain initiator and monomer. Chain growth occurs via a condensation reaction between two enol species under formation of water and chain termination yields oxygenates, α-olefins or n-paraffins. Further hydrogenation of the enolic species (14) will lead to the formation of surface species (15) which in turn can be converted to methyl species (6), the chain initiator for alkyl and CO-insertion mechanisms.

### 2.3.2.5 Formation of branched compounds

A primary formation of branched compounds, analogous to the alkyl mechanism, was proposed by Schulz et al. (1970, 1988, and 1990). In this reaction pathway, it was proposed that the formation of branched hydrocarbons (see Figure 2.2) involves the reaction of an alkylidene surface species (21) and a methyl surface species (6) to form species (22).

Following the additions of a $CH_2$ group, desorption of surface species (23) yields a methyl branched compound.

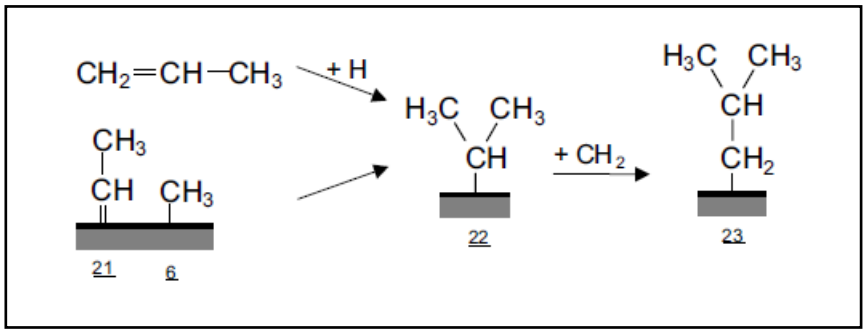


**Figure 2.2:** Formation of branched hydrocarbons [proposed by Schulz et al., (1970, 1988, 1990)].

Schulz et al. (1970, 1988, and 1990) also proposed the partial formation of branched hydrocarbons via olefins, such as propene, which can re-adsorbed on the penultimate carbon atom (22) and then react with methylene to form a branched surface species (23).

### 2.3.3 Product distribution

The product distribution of the Fisher-Tropsch, in particular the steady state chain length distribution, can be described by the Anderson–Schulz-Flory (ASF) equation:

$$\lg(x_N) = N\lg(\alpha) + \lg\frac{(1-\alpha)}{\alpha} \quad (2.4)$$

Where $x_N$ is the mole fraction of a product compound consisting of N carbon atoms and α is the chain growth probability (the derivation, assumptions and limitations of the equation above are given in Appendix A). The polymerization characteristic of the Fischer Tropsch synthesis implies that it is not selective to a single product or specific carbon number range. The chain growth probability (α) gives an indication on the catalysts probability to form longer chain hydrocarbons and is an indication of the rate at which monomers are incorporated into growing chains relative to the rate of desorption of growing chains from the surface. The probability (α) value can be used to compared catalyst performance and selectivity.

# 2.4 Catalysts for Fischer-Tropsch synthesis

The requirements of a good Fischer-Tropsch catalyst is high activity, high selectivity towards the desired product, active sites of the catalysts easily available to the reactants, suitable shape, strength and low costs involved in using the specific catalyst. Fischer-Tropsch catalysts consist of four components namely: An active metal (Fe or Co), oxide chemical promoters, small amount of second metal (reduction promoters), and support or binder [Dry, 1981].

Low temperature Fischer-Tropsch catalysts are commonly prepared using impregnation and precipitations methods, whilst the Fe-based catalyst used in high temperature Fischer-Tropsch synthesis is prepared by fusion [Dry, 1981]. The prepared catalysts are commonly calcined in an inert [Mabaso, 2005; Puskas et al., 2006] or in an oxidizing atmosphere [Wanke and Flynn, 1975; Puskas et al., 2007], resulting in the oxide phase of the metal precursors [Mabaso, 2005; Puskas et al., 2006; Wanke and Flynn, 1975; Puskas et al., 2007].

## 2.4.1 Phase of the catalytically active material

Prior to Fischer-Tropsch synthesis, oxide catalyst precursors are activated in $H_2$, CO or a mixture thereof. Depending on the conditions used metallic Fe (or Co) or iron carbides are formed [Dry, 1981; Bukur et al., 1995a; de Smit et al., 2009; de Smit et al., 2010]. The catalytically active phase for the Fischer-Tropsch synthesis in Co-based catalysts has been reported to be metallic $Co^0$ [Ernst et al., 1999; Sadeqzadeh et al., 2011]. For Fe-based catalyst, both metallic Fe and iron carbides are considered catalytically active for Fischer-Tropsch synthesis because of their ability to dissociate and hydrogenate CO [Gracia and Prinsloo, 2009; Petersen et al., 2010]. However, under Fischer-Tropsch conditions, carbides readily form due to the proposed similarity between activation barriers of carbon diffusion into the metallic Fe body centered cubic (bcc) structure and hydrogenation and polymerization at the surface [Niemantsverdriet and van der Kraan, 1981]. There are two main types of carbides found in Fischer-Tropsch catalysts; octahedral (O) carbides ($\varepsilon$-$Fe_2C$, $\varepsilon$-$Fe_{2.2}C$) and Trigonal Prismatic (TP) carbides ($\chi$-$Fe_5C_2$, $\theta$-$Fe_3C$, $Fe_7C_3$). These carbides are classified according to the site occupation of the carbon atoms in the carbide structures [de Smit et al., 2010]. During Fischer-Tropsch synthesis both the TP-carbides and O-carbides, together with magnetite ($Fe_3O_4$), have been observed [Niemanstverdriet et al., 1980; Dry, 1981; Bukur et al., 1995a; O'Brien et al., 1995; Dry, 2004b; de Smit et al., 2009; de Smit et al., 2010]. Metallic iron and both types of iron carbides are thought to be active for Fischer-Tropsch

synthesis while the oxides, in particular $Fe_3O_4$, are thought to be inactive or at least less active for the Fischer-Tropsch reaction [Dry, 1981; Anderson, 1984; Li et al 2002a].

de Smit et al., (2010) showed, via Spin-Polarized Density Function Theory (DTF) calculations, that O-carbides are energetically more stable than the TP-carbide over the entire range of low Fischer-Tropsch synthesis and high Fischer-Tropsch synthesis conditions. However, TP carbides, more specifically $\chi$-$Fe_5C_2$, are commonly found in low temperature Fischer-Tropsch spent catalysts [Niemanstverdriet et al., 1980; Dry, 1981; Bukur et al., 1995a; O'Brien et al., 1995; Lox et al., 1988; Dry, 2004b; de Smit et al., 2009; de Smit et al., 2010]. O-carbides ($\varepsilon$-$Fe_2C$ and $\acute{\varepsilon}$-$Fe_{2.2}C$) typically form under low temperature conditions (<200 $^0$C). O-carbides have been observed to transform into $\chi$-$Fe_5C_2$ above 250 $^0$C and subsequently to $\theta$-$Fe_3C$ above 350 $^0$C [de Smit et al., 2010]. Moreover high CO partial pressure in the gas phase also favors the formation $\chi$-$Fe_5C_2$ either through the transformation of the O-carbide [de Smit et al., 2010] or through the conversion of $Fe_2O_3$ [Bukur et al., 1995b; O'Brein et al., 1995] or metallic Fe [de Smit et al., 2010]. The transformation of the O-carbides to $\chi$-$Fe_5C_2$ phase at higher temperatures, or higher CO partial pressure, is thought to be due to the combination of lower strain, carbon diffusion limitations, and lower vibrational entropy, ultimately resulting in a higher relative thermodynamic stability and kinetic preference for $\chi$-$Fe_5C_2$ [de Smit et al., 2010]. On the other hand, the presence of other materials, such as $SiO_2$ and $TiO_2$, within the catalyst make up, has been shown to stabilize the O-carbides during Fischer-Tropsch synthesis [Amelse et al., 1977; Niemantsverdriet et al., 1980; Lox et al., 1988].



## 2.4.2 Active metal crystallite size and size distribution

Previous work has indicated that the activity and selectivity of Fischer-Tropsch catalysts, both Fe and Co based, are dependent on the average crystallite size and size distribution of the active metal [Mabaso 2005; Barkhuizen et al., 2006; Bezemer et al., 2006;].

Mabaso (2005) prepared Fe crystallites of different crystallite sizes (3 - 30 nm) and supported them on activated carbon and alumina respectively. Catalysts starting with an average $Fe_2O_3$ crystallite sizes less than 7 nm (dx) were shown to indicate lower activity per unit mass; the activity decreased with decreasing crystallite size for both the $Al_2O_3$ and activated carbon supported catalysts. However, the turn over frequency over catalysts containing $Fe_2O_3$ crystallites larger than 7 nm was found to be comparable. Similar results were found by Bezemer et al. (2006) for active cobalt supported on carbon nanofibers. The turnover frequencies attained over cobalt catalysts with average crystallite sizes that are larger than 6 nm were found to be independent of size.

The active metal crystallite size was also found to impact on the selectivity in the CO hydrogenation reaction. Mabaso (2005) found that crystallites smaller than the optimum ($d_x$ = 7 nm) produced higher selectivity towards methane and lighter hydrocarbons ($C_{1-4}$). Smaller crystallites also produced fewer olefins and showed a larger degree of branching, however, the selectivity of crystallites larger 7 nm was found to be the same [Mabaso, 2005]. Similar effects were observed by Bezemer et al. (2006) over Co based catalysts.

## 2.4.3 Promotion

Apart from the active metal (Fe or Co) industrial Fischer-Tropsch catalyst also contain: a metal oxide chemical promoter (only for Fe), a small amount of second metal (reduction promoters) and support (or binder) material [Dry, 1981].

### 2.4.3.1 Chemical promoters

Potassium is the most commonly used chemical promoter for Fe-based catalysts [Dry, 1981]. Potassium enhances strength of CO adsorption and facilitates CO dissociation while lowering the strength of metal-hydrogen and metal-oxygen bonds, thus resulting in increase in CO consuming reactions [Dry 1981]. Therefore, low degrees of potassium promotion results in an increase in Fischer-Tropsch activity and water gas shift activity. The addition of potassium also enhances the formation of carbides and free surface carbon [Dry, 1981], thus high loadings results in high carbon deposition, which may lead to a decrease in activity. Potassium promotions favors higher olefin selectivity and higher chain growth and consequently all industrial Fe-based catalysts are potassium promoted.

### 2.4.3.2 Reduction promoters

Reduction promoters are added to Fischer-Tropsch catalysts to enhance the reduction of the active metal from oxide to metallic form. Cu is generally used for Fe-based catalysts whilst noble metals such as Pt, Pd or Ru are often used for cobalt based catalysts. The reduction promotion is believed to occur via hydrogen-spill over. These promoters are generally believed to directly impact the catalyst activity by improving the degree of reduction, and hence the amount of catalytically active material in the catalyst.

### 2.4.3.3 Structural promoters (supports and/or binders)

Structural promoters, also known as supports (or binders), are micro-porous metal oxides which usually have high surface area, high thermal and chemical stability and high mechanical strength [Dry 1981]. The primary function of structural promoters is to minimize sintering of the catalytically active material within the catalyst formulation. Sintering is the loss of catalysts active surface due crystal growth. The sintering of small particles often results from the movement of atoms rather than particles [Moulijn et al., 2001]. Upon temperature increase the mobility of atoms increases and at sufficiently high temperatures, larger aggregates of atoms also become mobile [Moulijn et al., 2001]. These particles might move via surface migration and coalesce, then grow into larger ones [Moulijn et al., 2001]. This results in a loss of catalytic active surface. Therefore, structural promoters are used to stabilize small active metal crystallites and to prevent sintering of the active metal during high temperature processes such as pretreatment and Fischer-Tropsch synthesis [Bukur et al., 1990; Moulijn et al., 2001]. The most common materials used as support/binder are silica ($SiO_2$), titania ($TiO_2$) and alumina ($Al_2O_3$) [Choi et al., 1997].

Commercial Fe-based catalyst, used for low temperature Fischer-Tropsch, only contain small amounts of structural promoters whereas the high temperature iron catalyst, is virtually free of support material [Dry, 1981; Anderson, 1984; Dry, 2004b].

**Iron-silica ($Fe/SiO_2$)**

$SiO_2$ has been widely proven to be the most preferable structural promoter for Fe-based Fischer-Tropsch catalysts in both catalytic activity and selectivity [Dlamini et al., 2002; Yang et al., 2005; Zhang et al., 2006; Wan et al., 2006; Sou et al., 2012]. The addition of this support/binder to the Fe-based catalyst is of great interest because it has been shown to impact the catalytic activity of the active phase as well as the selectivity of the promoted catalyst. Pham and Datye (2000) showed that both the amount of $SiO_2$ and method used for $SiO_2$ addition, had an effect on the attrition resistance of the Fe/Cu catalysts. Dlamini et al. (2002) investigated the effects of silica addition on precipitated 100Fe/5Cu/0.2K catalysts. Silica was added during different stages of catalyst preparation. They found that the $SiO_2$ incorporation step influenced the degree Fe-$SiO_2$ interaction and $K_2O$ distribution, and consequently decreases the extents of reduction and carburization.

Generally, the incorporation of $SiO_2$ into Fe-based catalysts results in a decrease in Fischer-Tropsch activity per unit mass of catalysts [Anderson, 1984; Jothimurugesan et al., 1998; Basu et al., 1998]. Bukur et al. (1990) reported that upon increasing $SiO_2$ loading from 24 to 100 g per 100 g Fe, the degree of reduction decreased (with increasing $SiO_2$ content). As a

result, the CO-conversion, per unit mass of iron loaded, decreased. Furthermore olefin selectivity was reduced. Busa et al. (1998) reported comparable results. Similar finding were shared when the silica content was varied in promoted, Fe-based, catalyst [Yang et al., 2005; Hou et al., 2008]. Yang et al. (2005) investigated the influence of varying silica content in precipitated 100Fe/12Mn/1.2K/x$SiO_2$ (x = 0, 5, 10, 15 or 20) catalyst and Hou et al. (2008) used a precipitated 100Fe/5Cu/4.2K/x$SiO_2$ (x = 15, 20, 25, 30 or 40) catalyst. Additionally, both studies found a decrease in carbon deposition rate and improved stabilization of the Fe crystallites with increasing $SiO_2$ content [Yang et al., 2005; Hou et al., 2008].

Wan et al. (2006) compared Fischer-Tropsch activity of a precipitated silica containing (100Fe/5.9Cu/4.6K/25$SiO_2$) and silica free (100Fe/5.9Cu/4.6K) Fe catalyst. For the Fischer-Tropsch synthesis experiments, 5 ml of each catalyst was loaded into a fixed bed reactor. It was not mentioned whether or not the Fe content in the loaded catalysts was the same. They reported that the catalyst with no $SiO_2$ had a slightly higher initial activity but deactivated quickly with time on stream, whereas the CO-conversion of catalyst with silica was stable or even increased slowly. This was accompanied by an increase in $CO_2$ selectivity and lower olefin selectivity for the $SiO_2$ containing catalysts. They also reported an increase the strength of $H_2$ adsorption upon addition of $SiO_2$ to the catalyst formulation, coinciding with a decrease in the strength of CO adsorption. Furthermore, the work showed that the addition of $SiO_2$ suppressed carbon deposition and re-oxidation of the active metal during Fischer-Tropsch synthesis.

**Iron-Titania (Fe/$TiO_2$)**

$TiO_2$ supported catalysts are often observed to be more resistant to reduction when compared to their $SiO_2$ supported counterparts. However, $TiO_2$ supported catalysts have better dispersion of the active metal [Tauster et al., 1978; van der Kraan et al., 1986; Duvenhage and Coville, 1997; Riva et al., 2000]. This is because $TiO_2$ interacts more severely with the active metal [Tauster et al., 1978; Choi et al., 1997; Riva et al., 1999]. Tauster (1987) showed that, at elevated temperatures, the $TiO_2$ surface can be reduced to a lower valency; the species appearing atop of the metal was found to be "$TiO_x$" with x<2. It was indicated that the $TiO_x$ species then interacts with the active metal surface to form strong $TiO_x$-metal interactions which are difficult to reduce [Tauster, 1987]. Santos et al. (1983) also reported transport of titanium species during catalyst preparation, reduction, and oxidation of metallic iron particles supported on titania, prepared by aqueous incipient wetness impregnation, nonaqueous impregnation, and thermal decomposition of iron pentacarbonyl. Riva at el. (2000), using a Co/$TiO_2$ prepared using incipient wetness technique, also reported formation a surface compound between cobalt and titania that is more resistant to reduction.

Duvenhage and Coville (2002) investigated the effects of varying calcination temperature (200, 300 and 400 $^0$C) on 10 wt-% Fe/$TiO_2$ catalyst prepared via incipient wetness. They found that the degree of reduction decreased with increasing calcination temperature. It was implied that this occurred due to stronger interactions between the active metal and support, induced by increasing calcination temperature [Duvenhage and Coville, 2002]. The same effects were observed with a bimetallic Fe/Co (5 wt-% Fe + 5 wt-% Co) catalyst supported on $TiO_2$; i.e. that the catalyst was more difficult to reduce with increasing calcination temperature [Duvenhage and Coville, 2002].

The catalytic effect of titania on metals is, in general, neutral or deactivating, but an important exception is the reaction of CO with $H_2$ to form methane or higher hydrocarbons [Vannice and Sudhakar, 1984; Tauster et al., 1987; Ishihara et al., 1988]. The rate of methanation was observed to increase by an order of magnitude or more when $TiO_2$ was used as a support [Tauster, 1987; Ishihara et al., 1988]. Similar, although smaller, effects were observed with other metals, including Fe [Vannice and Sudhakar, 1984; Tauster, 1987]. Moreover, the CO-conversion and selectivity of light hydrocarbons ($C_1$-$C_4$) was observed to increase with $TiO_2$ addition and the olefin selectivity is generally shown to decrease [Vannice and Sudhakar, 1984; Ishihara et al., 1988; Duvenhage and Coville, 2002]. Temperature Programmed Desorption studies of $TiO_2$ supported catalyst indicated enhanced ability of $H_2$ to compete with CO for the metal surface [Raupp and Dumesic, 1984; Vannice and Sudhakar, 1984; Tauster, 1987; Ishihara et al., 1988; Duvenhage and Coville, 2002].



## 2.5 **Remarks**

It has been reported that the activity of the active phase should not depend on the nature of the support, i.e. the support material is thought not to have any chemical effect on the turn over frequency of the active sites [Iglesia, 1997]. In the case where ‘mild’ conditions were used during pre-treatment of the supported catalysts this was found to be true [Tauster et al., 1978]. The difference in the reported catalytic behaviour of supported and unsupported Fe-based catalysts is believed to results from an interaction of the iron active phase with the support material. This is a phenomenon referred to as metal support interactions.

# 3

# Metal-support interactions



*When an active metal phase is supported, it is a well known that depending on the pretreatment and/or reaction conditions, the active metal may interact with the support. This process is usually referred to as the development of metal-support interactions. The existence of these interactions within a catalysts formulation impacts on the catalytic behavior of the supported active metal phase. This chapter provides a brief background on the history of metal support interactions. It also looks at the different ways in which the active metal phase can interact with a specific support, considering that different support material behave differently under pretreatment conditions*

# 3.1 Background on metal-support interaction

Conventional industrial catalysts generally consist of an active metal distributed over a structural promoter (support or binder), whose primary function is to provide good dispersion of the catalytically active phase [Dry, 1981] and to prevent sintering through minimizing direct contact between the catalytically active crystallites. However, during high temperature catalyst pretreatment, such as calcination and reduction, even supported materials may sinter. This may occur due to the migration of active metal crystallites [Moulijn et al., 2001] and this process is generally accelerated by the presence of water vapour; which is formed (e.g. during calcination and $H_2$ reduction [Dry, 1981; Bartholomew, 2001]). The active metal phase may sinter to a large extent when it is not supported. It is thought that the interaction between the active metal and the supports holds the active metal crystallites in place and minimizes migration, thus decreasing sintering and resulting in higher dispersion of the active metal [Moulijn et al., 2001; Khodakov et al., 2007].

Historically structural promoters were believed to be 'inert' material and thus the interaction with the active metal was perceived to be weak and not detrimental to the activity and selectivity of the active metal [Tauster et al., 1978]. However, Tauster et al. (1978) discovered that due the close proximity of the active metal and the support and exposure to elevated temperature during pretreatment, the active metal particles bonded to the support either through the formation of a surface compound or through electronic exchange with a partially reduced support material [Tauster et al., 1978; Tauster et al., 1981; Tauster, 1987]. The development of these interactions is characterized by the formation of (active metal)-O-(support) covalent bonds (e.g. Fe-O-Si or Fe-O-Ti). These interactions are usually referred to as *strong metal support interactions* (SMSI) [Tauster, 1987].

In the past, the existence of metal support interactions was viewed with a negative eye because it was thought that these interactions cover the catalyst surface, blocking active sites and resulting in lower activity [Tauster, 1987]. Furthermore, it is generally accepted that the decrease in the degree of reduction associated with the incorporation of $TiO_2$ (or $SiO_2$) into Fischer-Tropsch catalysts is due to metal support interactions [Tauster et al., 1978; Yang et al., 2005; Hou et al., 2008; Wan et al., 2006; Busa et al., 1998] indicating that these interactions would be present during Fischer-Tropsch synthesis [Bukur et al., 1990; Basu et al., 1998; Yang et al., 2005; Zhang et al., 2006; Hou et al., 2008; Wan et al., 2006]. In his early work, Tauster et al. (1978) showed that the effects of these interactions varied with the active metal used. Some of the noble metals showed enhanced activity for CO hydrogenation while other noble metals showed no effect. Similar effects have been reported for bimetallic [Duvenhage and Coville, 1997 and 2002;] and ternary alloy catalysts [Ishihara et al., 1988].

Nowadays, strong metal support interaction (SMSI) seems to be ascribed to the effects introduced by the intimate contact of the support and the metal. The presence of metal support interactions affects Fischer-Tropsch activity and selectivity by altering the manner in which CO and $H_2$ are adsorbed on the surface of the active metal [Raupp and Dumesic, 1984; Vannice and Sudhakar, 1984; Tauster, 1987; Wan et al., 2006]. The term "Strong metal support interaction" was originally introduced to describe the drastic changes in chemisorption properties of group VIII noble metals when supporting these metals on $TiO_2$ after high temperature treatment [Tauster et al., 1978; Tauster, 1981], and in particular the decrease in the strength of adsorption of CO and $H_2$ [Vannice et al., 1985; Tauster, 1987]. The change in the adsorption energies was originally ascribed to electron transfer from a partially reduced $TiO_X$ (where x<2) surface to the metal particle [Tauster, 1981]. However, changes in CO and $H_2$ adsorption behavior, due to strong-metal support interactions, have also been reported for nonreducible supports, such as alumina [Taniguchi, et al., 1988; Wan et al., 2007] and silica [Wan et al., 2006; Sou et al., 2012].

Past work provides evidence of metal support interaction in Fischer-Tropsch catalysts [Bukur et al., 1990; Basu et al., 1998; Yang et al., 2005; Hou et al., 2008; Wan et al., 2006]. However, not all supported catalysts display the presence of these interactions, which appears to a function of the type of active metal (i.e. Fe or Co) used and the nature of the support material (e.g. reducibility) on which the metal is supported [Tauster, 1987; Choi et al., 1997; Wan et al., 2007]. Support materials that are easier to reduce (e.g. $TiO_2$) interact more severely with the active metal than support material which are thermally more stable under a given sets of preparation conditions [Tauster, 1987; Choi et al., 1997; Wan et al., 2007]. Generally the addition of both $SiO_2$ [Bukur et al., 1990; Yang et al., 2005; Zhang et al., 2006; Wan et al., 2006] and $TiO_2$ [Vannice and Sudhakar, 1984; Ishihara et al., 1988; Duvenhage and Coville, 2002] into Fe-based Fischer-Tropsch catalysts has been observed to favor selectivity towards lighter hydrocarbons and to have a negative impact on olefin selectivity. These changes in Fischer-Tropsch selectivity are thought to occur because the addition of $SiO_2$ [Wan et al., 2006; Sou et al., 2012] and $TiO_2$ [Raupp and Dumesic, 1984] to Fe-based Fischer-Tropsch catalysts increases the strength of $H_2$ adsorption and decreases the strength of CO adsorption. The changes in adsorption behavior are accredited to the presence of Fe-O-Si (Ti) interactions in the catalysts. However, the mechanism explaining these changes in adsorption properties is not well understood. Primarily, there are two theories described in literature to explain the manner in which the development of these interactions alters catalytic behavior in supported catalysts, viz. 'the ligand effect' and 'the contact effect'.

## 3.2 The ligand effect

When an active metal particle interacts with the support surface, it might be chemically bonded to the support [Moulijn et al., 2001]. The formation of this bond may be caused by specific type of pre-treatment, e.g. alloy formation [Lamber et al., 1990; Min et al., 2003] or electronic effects [Benvenutti et al., 1999]. This bond may act as a ligand to the metal anchoring the particle to the support material [Cheng et al., 1991b] (see illustration below). These anchors may be created during catalyst preparation, due to the coordination of the ionic metal precursors to the support [Che, 1993; van Steen et al., 1996] or during the thermal pre-treatment of the catalyst [Puskas et al., 2006]. With most supports, these interactions are believed to only occur at the interface where the metal is in direct contact with the support [Tauster, 1978]. Thus, smaller active metal crystallites, which have larger surface area exposed, may exhibit greater degrees of metal support interactions [Riva et al., 2000; Hou et al., 2008].

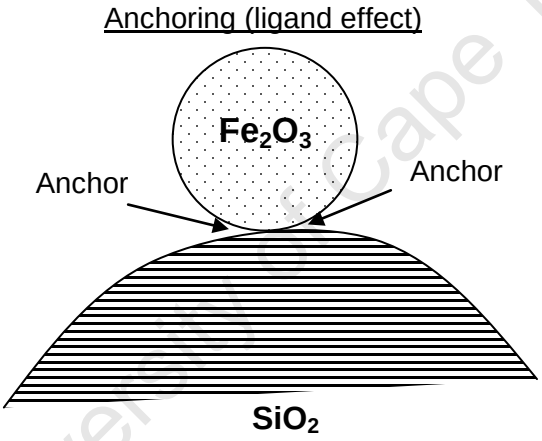




These anchors are usually generated during catalyst synthesis. The interaction of support material with the iron oxide precursors depends on the mode of addition of the support material [Dlamini et al., 2002], with the addition of the structural promoter prior to calcination imparting the largest effect. During the early stages of preparation, the interaction between the active metal precursor and the support material is believed to be dependent on the concentration of surface hydroxyl groups. Qing et al. (2011) proposed that the interaction between iron and silica, in the form of Fe-O-Si bonds, may form in a hydrolysis reaction involving surface hydroxyl groups on iron oxide/hydroxide and silica. Thus, the extent to which the active metal interacts with the support may be decreased by calcination of the active metal precursor or the support material (or both) prior to mixing them together [Dlamini et al., 2002; Puskas et al., 2006]. On the other hand, the degree of metal-support interactions can be improved by activating the support surface prior to metal loading or by preparing the catalyst under a reducing environment [Puskas et al., 2006; Puskas et al., 2007]. Calcination temperature also plays a role in the generation of these interactions. It has been reported that

a high calcination temperature improves the degree of metal support interactions [Duvenhage and Coville, 2002]. Therefore, the most ideal conditions to generate these interactions would be to disperse the metal precursor on the support material prior to calcination, then calcine at high temperatures under hydrothermal conditions. The metal-support interactions generated during calcination might also be in the form of Fe-O-Si anchors [Qing et al., 2011; Sou et al., 2012]. These Fe-O-Si anchors are not easily cleaved during standard catalyst pre-treatment steps (such as hydrogen activation) and thus these interactions are thought to be present during Fischer-Tropsch synthesis. This is the basic principle behind 'the ligand effect'.

With the ligand effect, it is proposed that the development of these chemical bonds between the active metal and the support material is responsible for the altered catalytic behavior in supported catalysts [Qing et al., 2011; Sou et al., 2012]. The presence of Fe-O-support interactions is believed to alter the electronic distribution on the surface of the active phase, hence impacting the manner in which the reactants ($CO + H_2$) are adsorbed. The surface of the support material remains inert and plays no role in the development of products. Hence, 'the ligand effect' is commonly associated with irreducible support material such as silica [Hou et al., 2008; Sou et al., 2012] and alumina [Taniguchi, et al., 1988; Wan et al., 2007].

## 3.3 The contact effect

'The contact affect', which is generally associated with partially reducible supports such as $TiO_2$ [Tauster et al., 1978], is commonly observed to develop during the reduction of the active metal precursors [Tauster et al., 1978; Riva et al., 2000; Vannice and Sudhakar, 1984]. The presence of these interactions in the catalyst is believed to occur at the interface where the active metal is in contact with the support (see illustration on next page). The generation of these interactions is highly dependent of pretreatment conditions.

During the reduction process, partially reducible supports ($TiO_2$ in particular) have been shown to incorporate iron atoms into their structure (see illustration on next page). This occurs at elevated reduction temperatures [Rayner, 2011; Yang et al., 2011] and leads to the formation of mixed metal oxides (e.g. $FeTiO_3$). The incorporation depends on both the temperature of reduction and the hydrogen partial pressure. The extent of incorporation was observed to increase with reduction temperature and declines with increasing hydrogen partial pressure [Rayner, 2011]. The mixed metal oxides (i.e. Fe-Ti-O) are thermally stable and much harder to reduce in comparison to the pure active metal oxides [Yang et al., 2009; Rayner, 2011, Yang et al., 2011]. Furthermore, the formation of these compounds is irreversible under normal pretreatment conditions [Rayner, 2011]. This results in a permanent loss in active metal activity.

At higher temperatures, the reduction of the $TiO_2$ surface has also been shown to result in the formation of mobile $TiO_x$ species (where x<2) [Tauster et al., 1978; Santos et al., 1983; Tauster et al., 1987]. These species have been observed to migrate from the $TiO_2$ surface and form overlayers surrounding the active metal [Tauster et al., 1978; Santos et al., 1983]. These overlayers block the active metal and prevent its reduction. The $TiO_2$ overlayers protect the active metal from sintering during pretreatment, resulting in a loss of catalytic activity. However, this process can be reversed simply by exposing the catalysts to oxygen [Tauster et al., 1978]. In the case of $SiO_2$ supported catalysts, the formation of iron silicate has been observed [Zhang et al., 2006].

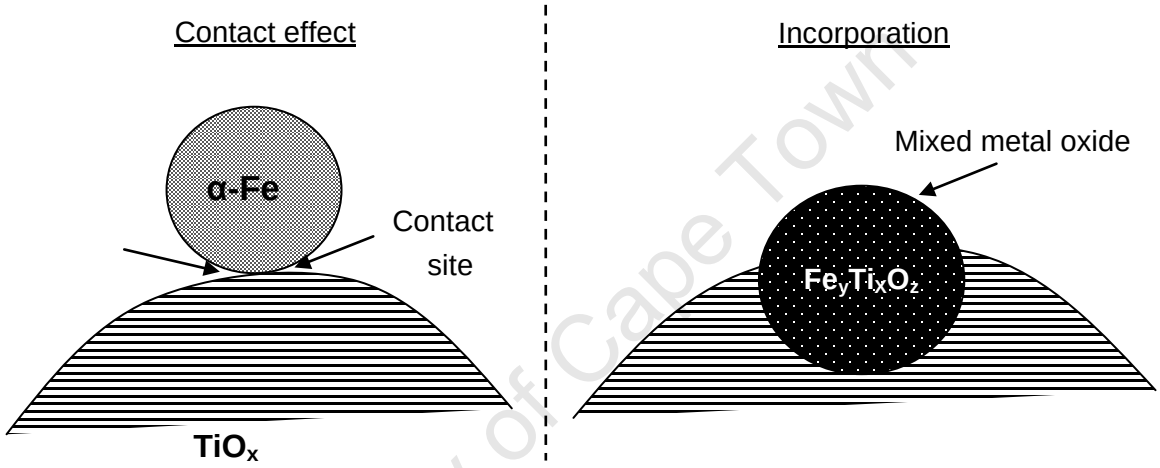


The contact effect is generally believed to occur when reduction temperature is high enough to induce partial reduction of the $TiO_2$ surface but not severe enough to facilitate the migration of $TiO_x$ species, which might result in surface coverage [Vannice and Sudhakar, 1984; Tauster, 1987]. In those conditions, it is believed that the intimate contact between the partially reduced support surface and the surface of the active phase results in the creation of special contact sites at the interface. These sites are thought to be responsible for the improved activity observed in $TiO_2$ supported catalysts [Burch and Flambard, 1982; Vannice and Sudhakar, 1984; Tauster, 1987]. The contacts sites are also believed to be conducive to hydrogen absorption, resulting in higher methane selectivity and lower olefin formation [Vannice and Sudhakar, 1984; Tauster, 1987]. Contrary to the ligand effect, the partial reduction of the support surface, resulting in oxygen vacancies and in $Ti^{3+}$ cations, is thought to play a role in product formation [Vannice and Sudhakar, 1984]. The oxygen end of a CO molecule adsorbed on the active phase surface at the interface can interact with the vacancies on the support surface, facilitating its dissociation. This is believed to result in higher activity [Vannice and Sudhakar, 1984] but this theory has not been conclusively proven.

# 4

# Novelty of this work



*The intent of this study is to investigate 'the ligand effect'. This chapter discusses the design of a model catalyst, modified to mimic the presence of these metal support interactions in industrial catalysts. The modification is based on the reaction of alkoxide compounds (which are precursors for silica and titania) with surface hydroxyl groups on the active metal precursor (FeOOH). The novel aspects of this work are discussed and an overview of the experimental procedure required for the modification process, including pretreatment conditions used for the model catalyst, is presented.*

# 4.1 Relevance and application of this research

Research into metal support interactions is a very broad one. The effects of $TiO_2$ and $SiO_2$ addition on Fischer-Tropsch catalysts have been well documented [Bukur et al., 1990; Basu et al., 1998; Duvenhage and Coville, 2002; Yang et al., 2005; Hou et al., 2008; Wan et al., 2006; Qing et al., 2011; Sou et al., 2012]. However, in a conventional Fischer-Tropsch catalyst where the active metal (Fe or Co) is distributed over the support it is difficult to monitor the development of these interactions or even quantify the extent or degree to which they occur. Furthermore, the changes observed cannot be exclusively assigned to the presence of metal support interaction because the addition of structural promoters affects the catalyst stability. Conventional catalyst medium is complex because of the addition of reduction and chemical promoters. The interaction of these constituents with the support has also been proven to affect catalyst activity and selectivity as well [Yang et al., 2005; Hou et al., 2008]. It is difficult to separate the effects of the other factors on the catalyst system and exclusive view changes brought about by metal support interactions. Moreover, literature provides little information on how the formation of these interactions can be controlled, monitored or manipulated and thus limiting the applications. Metal-support interactions are typically investigated by putting the catalytically active phase on some support followed by heat treatment or in the case of iron-based Fischer-Tropsch catalyst by varying the amount of binder in the sample.

Haller and Resasco (1989) argued that ligand effect, i.e. modification of the (inter)metallic surface with support-like structures, may also impart a change in the adsorption properties. In this study, a novel approach is taken by modifying the surface of the catalyst precursor with covalently bonded ligands mimicking the metal-support interactions. This is done to study ‘the ligand effect’ and will serve as model systems for interactions present in industrial iron-based Fischer-Tropsch catalysts. The novel aspect of this work advances work done in the past and hinges predominantly on the design of a model catalyst that provides three aspects of metal support interactions that have not been fully understood before this point. The first aspect is the ability to control of the level or degree of metal support interactions present in a specific catalyst; although, past research has shown the existence of metal support interaction [Tauster et al., 1978; Qing et al.,. 2011; Sou et al., 2012], no work has been able to control the extent or degree of metal support interactions generated. Secondly, it is possible of quantifying these interactions; i.e. in this study we were able to estimate the amount of active metal atoms affected by these interactions. This has not been done before and thus highlights the unique aspect of this research. Lastly, through the design of the model catalyst we were able to isolate the effects of metal support interactions on catalyst. The effect of these ligands anchored to the surface of the catalyst precursor on the activation step and on the resulting activity and selectivity in the Fischer-Tropsch synthesis are of interest.

This is relevant because attempts continue to elucidate factors that affect the catalytic performances (activity, selectivity and stability) of Fischer-Tropsch catalysts and to improve the catalyst potential capability for applications. For Fe-based catalyst, most of these attempts have been focused on addition of chemical promoters such as potassium and copper [Anderson, 1984, Bukur et al., 1990]. The role of structural promoters ($SiO_2$, $Al_2O_3$ and $TiO_2$) is also of importance [Anderson, 1984; Wan et al., 2006]. Understanding how metal support interactions affect the catalytic activity and selectivity of Fischer-Tropsch active metals could influence the manner in which support material are chosen in industrial processes. Support material that favors improved activity could be chosen strategically to enhance the catalyst performance and, in case of Fe, additional chemical promoters can be used to offset the changes in selectivity. If the support material cannot be changed, then understanding how its interaction with the metal affects Fischer-Tropsch synthesis, could allow for counter measures to be taken (e.g. addition reduction promoter) to adjust the catalyst behavior to meet specification.



## 4.2 Design of a model catalyst

There are three main stages in the preparation of the model catalyst. The first step is the precipitation of the active metal using the microemulsion technique. Secondly, the modification of the active metal surface with the respective alkoxide compounds. Finally, the conditions used for pretreatment of the modified samples prior to Fischer-Tropsch synthesis. The three steps of modification are considered in more detail in the next sections. A general overview of the preparation process is presented in Figure 4.1.

The proposed design is aimed at creating the metal-support (e.g. Fe-O-Si) interactions but instead of having the active metal interacting with bulk support, the interaction is created and attached to the surface of the metal like a ligand**.** If the modification process is successful, then after calcination, the metal oxide crystallites will have support interactions on the surface (see Figure 4.1).

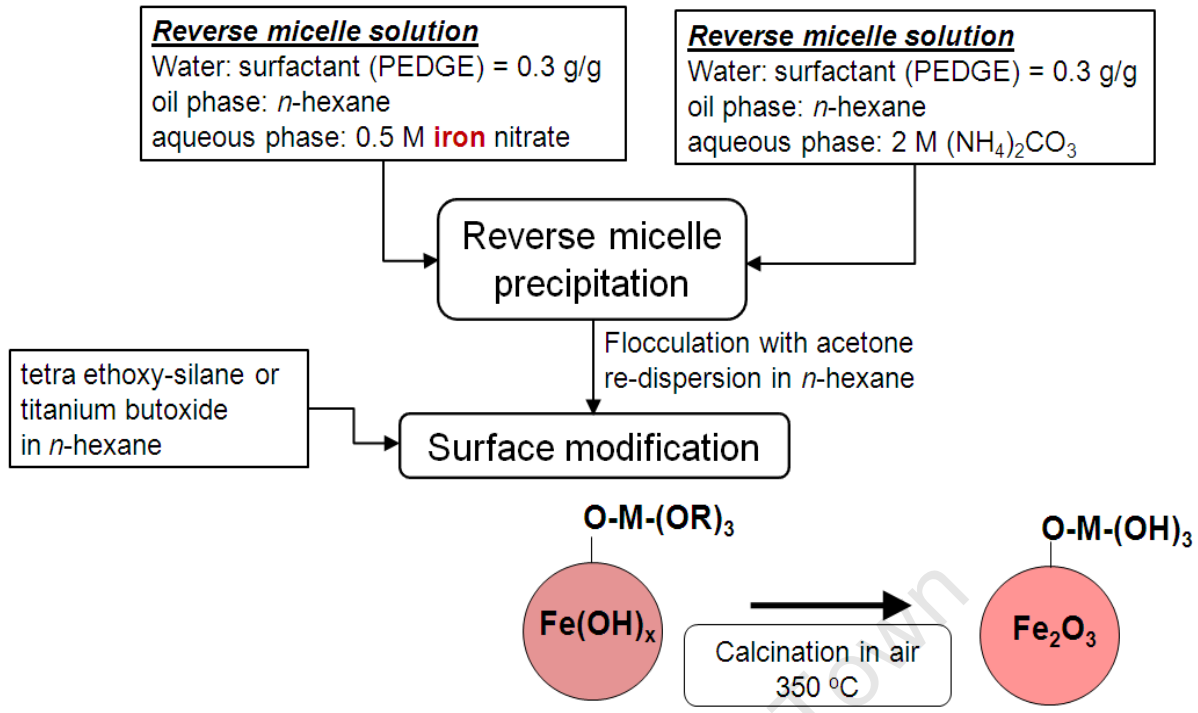


**Figure 4.1:** The experimental overview of the design and modification process of the active metal with the respective alkoxide compounds



## 4.2.1 Active metal precipitation

The microemulsion method provides great potential for controlling the size and shape of crystallites. This allows for the elimination of these factors on the catalyst activity and selectivity. Extensive reviews of this preparation method can be found in literature [Mabaso, 2005; Eriksson et al., 2004]. The technique is referred to as the water-in-oil microemulsion because it involves an aqueous phase (water) encapsulated by a surfactant and surrounded by an oil medium. When a soluble metal salt is dissolved in the aqueous phase of the microemulsion, it resides in micro droplets surrounded by oil. This droplet is referred to as a micelle. The size of these micelles is determined by the ratio of the oil /surfactant/water present in the system [Mabaso, 2005]. The proposed microemulsion mechanism is presented in Figure 4.2. This technique involves confining precipitation or reduction of precursors in a tiny aqueous droplet. To precipitate, a droplet containing the metal salt has to collide with a droplet containing a precipitating agent also in an aqueous phase of a second microemulsion micelle.

The droplets then act as nanosized reactors. The crystallite size is also affected by parameters such as reaction time, chemical nature of the precursors and their composition [Mabaso, 2005]. All these parameters were kept constant for all prepared catalysts. After reaction, the microemulsions are broken by adding acetone. The precipitated metal hydroxide is then recovered. The metal oxide prepared using this method showed a high preference to a spherical morphology and contains large percentage of surface metal ions that are coordinate unsaturated sites (CUS), which can react with $SiO_2$ (or $TiO_2$) to from M-O-Si(Ti) [Qing et al., 2011].

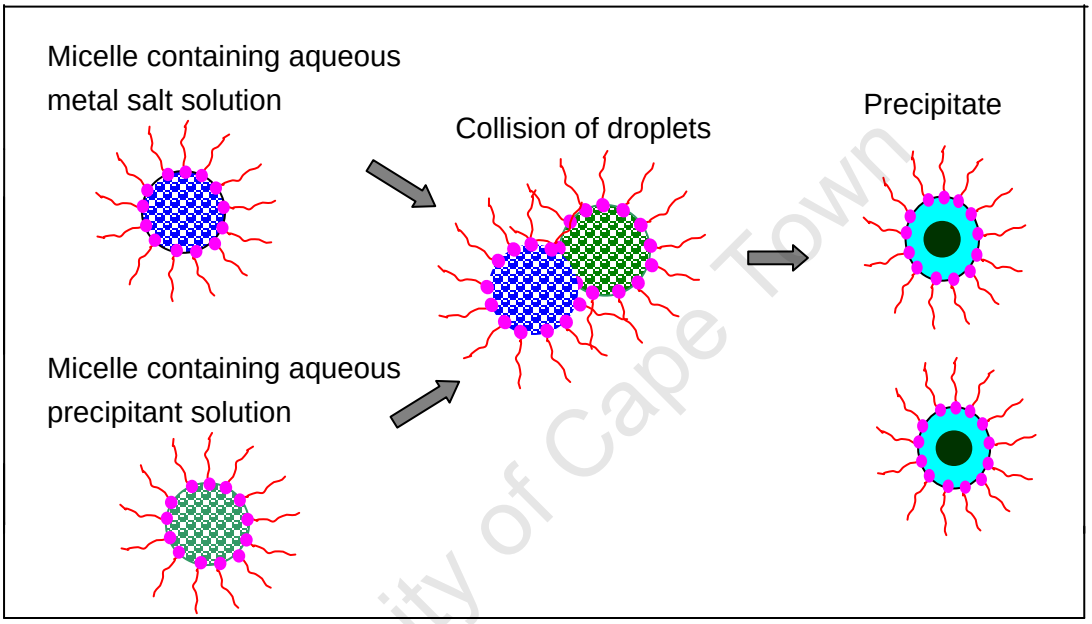


**Figure 4.2:** Proposed microemulsion mechanism (Pileni, 1989; Eriksson et al, 2004)



## 4.2.2 Surface modification

The scope of this work includes the modification of active catalyst surfaces and this was achieved using precursors of support. The two main support materials that are focused on for this study are silica ($SiO_2$) and titania ($TiO_2$). The precursor of $SiO_2$ is tetra ethoxy-silane (TEOS) and the precursor used for $TiO_2$ modification was titanium butoxide (TBO). The bond formed during modification was designed to be similar to that which might be formed when the active metal catalyst interacts with the support/binder medium (for example Fe-O-Si). Since the active metal precipitate from the microemulsion technique was in hydroxide form, the reaction of the metal alkoxides with hydroxide groups was studied carefully. Due to recent developments in sol gel a technique, the hydrolysis of inorganic compounds has been studied extensively [Honda et al., 2001; Phillipp, 1990; De Andrade Lima Coêlho et al., 2003]. Metal alkoxides (TEOS and TBO) are known to react with hydroxyl containing compounds, resulting

in the release of the alkoxide groups as alcohols [Honda et al., 2001; Phillipp, 1990; De Andrade Lima Coêlho et al., 2003]. Generally, the reaction is facilitated by an acid (or base) and may occur at room temperature. The precipitated metal hydroxides have acidic properties. Thus, in the modification process additional acid was not required. Adopting from the hydrolysis of the metal alkoxide compounds, the proposed reaction steps for the modification are represented by Equations (4.1) and (4.2).

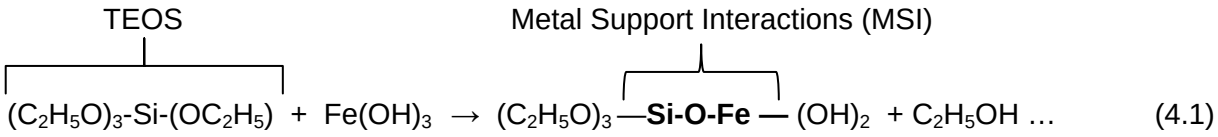


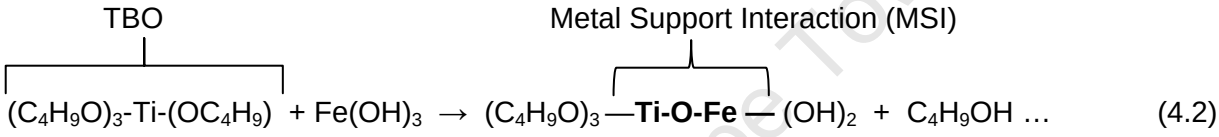


The reaction of the $Fe(OH)_3$ with the respective metal alkoxide will results the formation Fe-O-Si or Fe-O-Ti bonds which are believed to characterize the formation of metal support interaction. These bonds only exist at an interface due to incompatibility of metal atoms and cations within a solid lattice [Tauster, 1987].

There is a possible side reaction associated with this modification process, the condensation polymerization of the alkoxide compounds (see Equation 4.3 and 4.4).

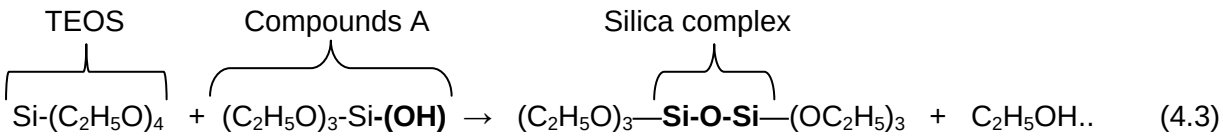


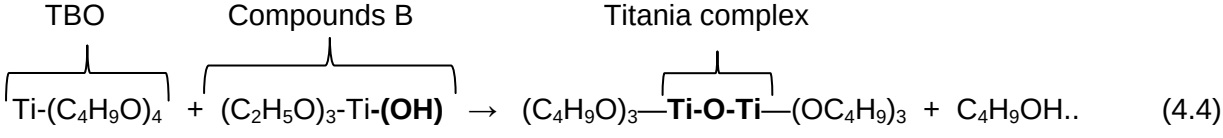


The polymerization reactions are highly dependent on the initial hydrolysis of the alkoxide compounds [Honda et al., 2001] which is accompanied by the release of the corresponding

alcohols. The hydroxyl groups **-(OH)** formed during hydrolysis reaction become functional groups driving the condensation polymerization reactions [Phillipp, 1990]. The alkoxide compounds are very susceptible to hydrolysis and thus the possibility of the condensation reaction should be taken in account for the modification process. However, the polymerization reaction is much slower than the reaction of the alkoxide compounds with the OH groups in the metal hydroxide [Phillipp, 1990] and the extent of polymerization can be controlled by diluting the concentration of the alkoxide compound. Furthermore the precipitated metal hydroxides can be dried prior to modification in order to remove all water from the system and thus preventing the hydrolysis reaction, i.e. the formation of the **-(OH)** functional groups. The dried metal hydroxide could then be resuspended in water free reaction medium.

By varying the amounts of alkoxide compound exposed to the metal hydroxide different degree of interaction can be achieved, i.e. different amounts of ligands can be attached.

### 4.2.3 Calcination and reduction

The modified catalyst will then have to be calcined to convert the modified metal hydroxide to their respective oxide forms. Figure 4.1 shows the overview of the modification and also indicates the reaction condition for the calcination process. After modification the Fe-based catalyst are calcined in flowing air at 350 $^{0}$C.

Figure 4.3 shows the proposed modified catalysts after the calcination step. Also displayed, in the same figure, is a cross-sectional zoom of the modified catalyst surface. The atomic view of the proposed modified catalyst surface indicates the support hydroxide (-O-Si$(OH)_3$ or –O-Ti$(OH)_3$) attached to the metal oxide surface. The bond between the attached ligand and the active metal represents the MSI interaction (M-O-Si or M-O-Ti) which is has been shown to exist in conversional catalysts.

Before the catalysts are tested for Fischer-Tropsch synthesis the oxides have to be reduced to a catalytically active phase [Dry, 1981; Bukur et al., 1995a]. The metal support interactions are hard to reduce [Hou et al., 2000] and require very high temperatures to be removed. If the model catalysts are reduced at a relatively low temperature, the ligand may survive reduction step. Figure 4.3 shows the final catalyst surface prior to Fischer-Tropsch synthesis.

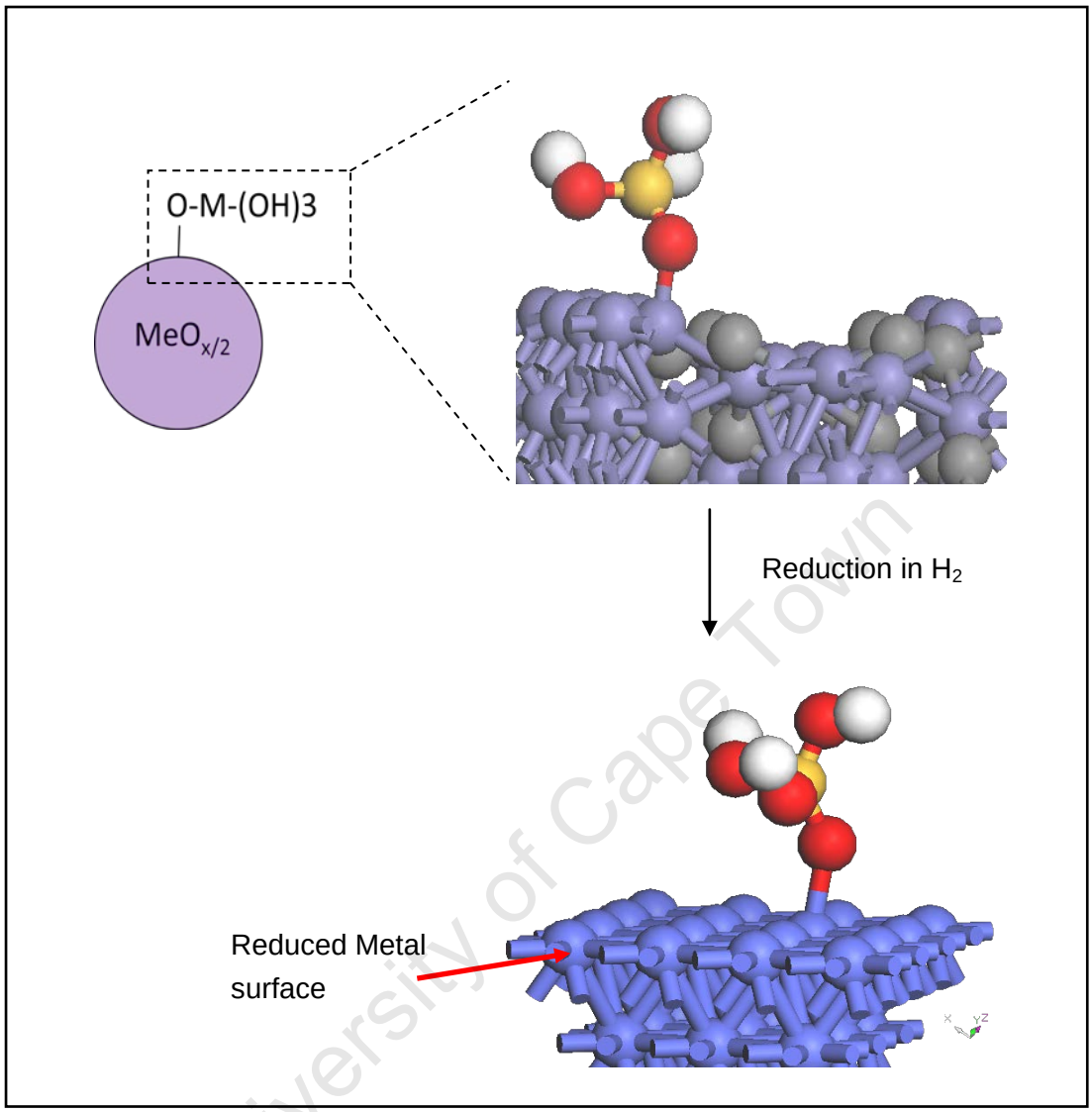




**Figure 4.3:** Proposed calcined metal oxide (top) and reduced (bottom) metal surfaces with attached alkoxide ligand

# 5

# Experimental Procedure



It has been shown that the crystallite size and size distribution have an effect on the activity and selectivity of a catalyst [Maboso, 2005; Hota et al., 2004] and thus to eliminate these effects, the first objective of this work was to generate iron oxide crystallites having a controlled crystallite size and size distribution. This could be achieved by using the water in oil microemulsion technique which allows great control over size and shape of inorganic nanocrystallites [Eriksson et al., 2004; Mabaso, 2005]. Secondly, the different injection methods used in the modification process are explained. The prepared catalysts were then characterized using various analytical techniques prior to Fischer-Tropsch Synthesis. The spent catalysts were also analyzed.

# 5.1 Catalyst precipitation using microemulsion technique

The first step of the microemulsion technique is the preparation of the emulsion solution by mixing 250 grams n-hexane (HPLC grade, Aldrich Chemical Company) and 40 grams of (surfactant) Berol 050[a] (Akzo Nobel) in a one liter volumetric flask. The stability of this microemulsion system is discussed in Appendix B (section B.1). The resulting oil-surfactant microemulsion solution was stirred for thirty minutes to ensure that the Berol mixes with the n-hexane, then sealed using parafilm and left for 24 hours to equilibrate. Two sets of solutions are required to produce one catalyst.

Two aqueous phase solutions were then prepared using de-ionized water. The first solution containing a metal salt (i.e. 0.5 M iron nitrate solution ($Fe(NO_3)_3.9H_2O$, 99%, Sigma-Aldrich Inc.)) and the second consisting of the precipitating agent (i.e. 2M ammonia carbonate ($(NH_4)_2CO_3$, 30-33% as $NH_3$, Fluka)). 12 grams of the prepared 0.5 M aqueous metal salt solution was added to the first microemulsion solution (microemulsion 1). Similarly 12 grams of the 2 M aqueous precipitating agent was added to the second microemulsion solution (microemulsion 2). Figure 5.1 demonstrates the microemulsion systems and shows the metal salt solution and precipitating agent trapped in microemulsion droplets (micelle). The size of the micelle is determined by the mass ratio of oil(250 g) /surfactant (40g) /aqueous phase (12 g), and according to past work [Mabaso, 2005], the ratios used in this work result in a micelle size of 18.1 nm.

A 2 liter beaker was then positioned under a turbine stirrer. The microemulsion solution containing the metal salt solution is poured into the 2 liter beaker first. The solution is stirred at 800 revolutions per minute for ten minutes before the second microemulsion, containing the precipitating agent, is added (see Figure 5.1). The beaker was then sealed and the mixture is allowed to stir for three hours.

Figure 5.1 shows the collision and coalescence of the droplets. The reactants from the metal precursor and the precipitating agent come into contact with each other, react and form precipitate. The precipitation process is accompanied by a colour change, from light orange to brick red, indicating the precipitation of FeOOH [Mabaso, 2005]. The precipitate remained confined to the interior of the microemulsion droplets until they were separated from the liquid phase by flocculation with acetone ($CH_3COCH_3$, 99%, Kimix) [Mabaso, 2005] and settled at the bottom of the beaker.

a: Berol 050 is a nonionic organic surfactant, the chemical name being: Pentaethyleneglycoldodecylether.

The precipitate was washed with acetone until most of the surfactant was removed. The excess acetone was then decanted (see Figure 5.1). This process was repeated until the precipitate does not stick to the bottom of the beaker.

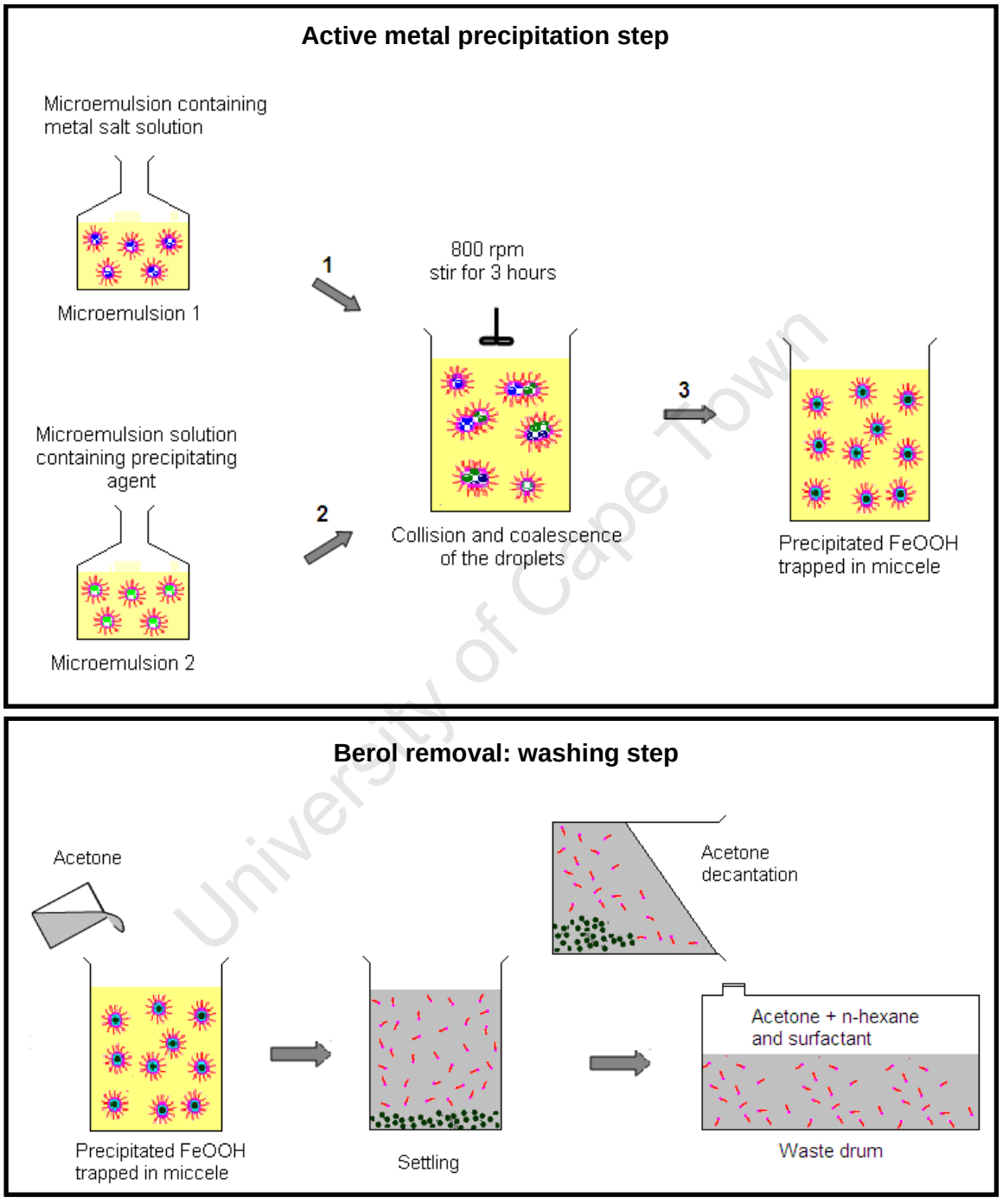


**Figure 5.1:** Schematic representation of the metal hydroxide precipitation in a water-in-oil emulsion and washing steps

The precipitate is then allowed to dry at room temperature until all the acetone is removed after which point the samples are placed in an oven at 120 $^{0}$C for 12 hours. This was done to remove water and other volatiles prior to the catalyst modification.

Following the drying, the samples were weighted. On average 0.46 grams FeOOH was precipitated corresponding to a Fe recovery of ca. 60 %. The samples are then dispersed in 500 ml of n-hexane which serves as the reaction medium for the modification process. The suspension is stirred at 600 rpm using a magnetic stirrer for 1 hour to ensure resuspension of the precipitated metal hydroxide prior to the injection of the respective solutions containing the alkoxide compounds.

## 5.2 Catalyst modification

The modification of the catalyst was done by addition of the support precursors which were tetraethoxy-silane (TEOS) for the silica system and titanium butoxide (TBO) for the titania system.

Only small amounts of the precursors are required for modification, ranging from 0.01 ml to 0.1 ml; this corresponds to a Si (or Ti) loading of 10 - 100 mmol per mol Fe. Therefore, a solution containing 1vol-% precursor in n-hexane was prepared, for both the TEOS and TBO separately. This increased the control volumes and ensured consistency in the injection process. The dilution of the support precursors is also done to improve distribution and prevent the auto condensation of the alkoxide compounds. The prepared solutions were put on the magnetic stirrer at 300 rpm for two hours then left overnight to ensure that the solution was well mixed. Due to the difference in chemical nature and reactivity of the precursors (TEOS and TBO), two different methods were used for modification process. The difference between the two methods was the manner in which the precursor was loaded. The volumes of the alkoxide compounds injected and the calculated molar Si or Ti-content are presented on Table 5.1.

### 5.2.1 Method one: instantaneous injection (for Si system)

A syringe was used and the 1% TEOS in n-hexane solution (v/v) was injected instantaneously into the suspended $Fe(OH)_3$ solution. The beaker was sealed using parafilm immediately after injection and left on the stirrer for 24 hours. After 24 hours the samples were removed from the stirrer, uncovered and then left at room temperature to allow the n-hexane to evaporate. The samples were subsequently placed in an oven operating at 120 $^0$C for 1 day.

### 5.2.2 Method two: Infinite dilution (for Ti system)

The control volumes of the 1% TBO in n-hexane (v/v) were diluted further by injection into an additional 100 ml n-hexane. The suspended $Fe(OH)_3$ in n-hexane solution is moved into a 2 liter beaker and diluted by adding an extra liter of n-hexane. The subsequent solution was stirred at 600 rpm. The diluted TBO solution is then injected into the 2 liter beaker systematically and evenly across ten hours. After the last injection, the system was allowed to stir for 24 hours. Preceding that, the samples were removed from the stirrer, uncovered and then left at room temperature to allow the n-hexane to evaporate. The samples were subsequently placed in an oven, which was operating at 120 $^0$C for 1 day.

The dried samples, irrespective of the method of injection used, were calcined under flowing air (at 300 (NTP) ml/min/$g_{sample}$) in a fluidized reactor (see Appendix B; section B.2). The temperature was set to increase from 25 $^0$C to 350 $^0$C at a heating rate of 10 $^0$C/min. The temperature was then maintained at 350 $^0$C for 3 hours.

**Table 5.1:** The control volumes of the metal alkoxides loaded and the corresponding metal to ligand atomic ratios

| System | Sample Code: | **Volume loaded 1% TEOS (TBO) (ml)** | **Calculated molar ratio (mmol Si(Ti)/mol Fe)** |
|---|---|---|---|
| **Fe-O-Si** | FS-0 | 0 | 0 |
| | FS-10 | 1 | 10 |
| | FS-30 | 3 | 31 |
| | FS-100 | 4 | 42 |
| | FS-50 | 5 | 52 |
| | FS-100 | 10 | 105 |
| **Fe-O-Ti** | FT-5 | 1 | 5 |
| | FT-10 | 2 | 10 |
| | FT-30 | 6 | 31 |
| | FT-50 | 9 | 52 |
| | FT-100 | 17 | 104 |



## 5.3 Catalyst characterisation

### 5.3.1 Transmission Electron Microscopy, TEM

The samples were analyzed using a JEM200CX (JEOL, JAPAN) which was operated at 120 kV. The powder samples were ultrasonically suspended in methanol for 3 hours and then a drop of each sample was transferred onto a carbon coated copper grid. The samples were then allowed to dry at room temperature. After drying the samples were placed into the microscope for viewing. A total of five images were taken for each sample.

The TEM images were then analyzed with image analysis tool (ImageJ)[a] to determine the crystallite size and size distribution. A total of 200 crystallites were measured and the mean volume crystallite diameter was calculated using Equation 5.1

$$d_{c\text{-}TEM} = \sum n_i d_c^4 / \sum n_i d_c^3 \quad (5.1)$$

for comparison with the XRD data which is sensitive to volume of crystallites [Bergeret and Gallezot, 1997].

### 5.3.2 X–Ray Diffraction spectroscopy, XRD

The phase composition of the calcined, reduced and spent catalysts was determined using a Bruker AXS D8 Advance X-ray laboratory diffractometer operated at 40 kV and 40 mA utilizing a Co source ($\lambda_{Co\text{-}K\alpha1}$ = 0.178897 nm) and a VÅNTEC position-sensitive detector. Diffraction scans were taken in the range $20^0 < 2\theta < 80^0$ and compared to the standard compounds reported in the JCPDS[b] data file. All diffraction patterns were recorded in the step-scan mode with a step size of 0.05 degrees and a scan rate of 0.5 deg/min.

The average crystallite sizes and phase composition were determined by Rietveld refinement of the XRD spectra in TOPAS[c] 4.2 (Bruker AXS). The structural files for all metal oxides used in the fitting were found in the built-in TOPAS database. The CIF files used in the fitting of carbides were acquired from an *online crystallography open database*[d].

In-situ XRD analysis was also used to analyze the phase transformations of the sample during $H_2$ pretreatment. An in-situ XRD cell (Anton Paar XRK 900) was used and 0.1 grams of the sample was loaded. The samples were reduced in situ at condition identical or Fischer-Tropsch pretreatment i.e., 350 $^0$C (heating rate 1 $^0$C/min) for 16 hrs under pure $H_2$ flowing at 40 ml (NTP)/min. Scans were taken every hour in the ranged from $20^0 < 2\theta < 80^0$ at a step size of 0.01 degrees and a scan rate of 0.5 deg/min.

a: A public domain Java image processing program inspired by National Institute of Mental Health

b: Joint Committee for Powder Diffraction Standards.

c: Total pattern analysis solutions

d: www.crystallography.net/search.html

### 5.3.3 Scanning Electron Microscopy, SEM, and Energy Dispersive X-Ray analysis, EDX

A scanning electron microscope (LEO S444 SEM, La:Ka, UK) equipped with a Four Quadrant Back Scatter Detector and an energy dispersive Fissons Kevex X-ray spectrometer (EDXA) with sigma analysis software was used to investigate the macroscopic distribution of the Si and Ti ligands on the metal oxide crystallites to determine the actual amount of Si and Ti on the catalyst.

Sample preparation involved sprinkling dry powder of the sample on an aluminium stub coated with glue containing graphite. Here, graphite is used to conduct electrons thereby preventing charge build up. The samples were then coated with carbon which does not interfere with the elemental analysis.

### 5.3.4 Fourier Transform Infra Red, FTIR

FTIR spectroscopy was used to observe the presence of metal support interactions (Fe-O-Si and Fe-O-Ti) in the modified catalysts. The unmodified catalysts were used as a baseline. This technique was also used to monitor for auto condensation of the alkoxide compounds, i.e. formation of Si-O-Si and Ti-O-Ti interactions. IR spectra were obtained using an FTIR Nicolet 5700 spectrometer (for the calcined and reduced catalyst in the DRIFTS mode and for the spent catalyst in the transmission mode). A total of 1000 scans were taken in the range between 400 and 4000 $cm^{-1}$ for each sample at a resolution of 4 $cm^{-1}$. A background scan is taken prior to every analysis.

#### Ex-situ analysis

A Diffuse Reflectance Fourier Transform Spectroscopy (DRIFTS) mode accessory was used for all the ex-situ studies for the calcined and reduced catalyst. 10 mg of each sample was diluted with 1 g of KBr and then loaded into a DRIFT cup and the surface was leveled with a glass slide. The cup was then loaded into the holder and placed in the DRIFTS unit for analysis. The passivated spent catalysts were analyzed using transmission mode. 5 mg of each sample was diluted with 1 g of KBr. The spent catalyst was pressed into a translucent wafer for measurement.

### In-situ analysis

In-situ IR analysis was done on the samples to examine the changes that occur on the catalyst interactions during $H_2$-reduction. An in-situ cell with a Germanium (Ge) glass window was used in this analysis. The samples were diluted with the same amount of KBr as described for the DRIFTS mode analysis. 50 mg of the KBr-sample mixture was loaded into the in-situ cell, which was subsequently loaded into the IR machine for analysis. A thermocouple in the cell unit, which was in direct contract with the sample, was used to monitor the temperature. $H_2$ was passed over the sample at a flow rate of 40 ml/min (NTP) and the sample was then heated to 350 $^0$C at a heating rate of 5 $^0$C/min. The temperature is maintained at 350 $^0$C for16 hours during which time a scan is taken every hour. A total of 1000 scans were taken in the range between 600 and 4000 $cm^{-1}$ for each sample at a resolution of 4 $cm^{-1}$

## 5.3.5 Temperature Programmed Reduction, TPR

The reduction behavior of the all the samples (under $H_2$) was investigated using TPR. The analysis was carried out in a quartz reactor on a Micromeritics AutoChem2950 (Micromeritics Instrument Corp., USA) machine. Approximately 40 mg of each sample was loaded but prior to reduction, the catalyst was degassed at 150 $^0$C under 50 ml/min (NTP) nitrogen for 30 minutes. This was done to remove excess moisture and other contaminants from the sample. Following that the samples were treated with of 5% $H_2$/Ar (v/v) following at 50 ml/min (NTP). The temperature was increased from 60 to 900 $^0$C at constant heating rate of 10 $^0$C/min.

The instrument was also used to determine the degree of reduction. The samples were initially reduced in situ at condition identical or Fischer-Tropsch pretreatment i.e., 350 $^0$C (heating rate 1 $^0$C/min) for 16 hrs under pure $H_2$ flowing at 40 ml/min/$g_{cat}$. After reduction the samples were cooled to room temperature under Ar at a flowrate of 25 ml/min (NTP) to remove any excess $H_2$ in the system. Following that normal TPR is run on the pre-reduced samples and the hydrogen consumed to further reduce the samples is used to calculate the degree of reduction. The $H_2$ consumption was regularly calibrated using $Ag_2O$ (see Appendix B; section B.3).

# 5.4 Fischer-Tropsch synthesis

## 5.4.1 The Setup

Figure 5.2 depicts the setup used in this work. The supply of the all gases was received from storage gas cylinders and the flow rates of all gases were controlled using mass flow controllers (FIC-1-4). The flow controllers were calibrated prior to use. All gas streams were fitted with control valves (CV-1-4). The control valves were kept shut unless in use.

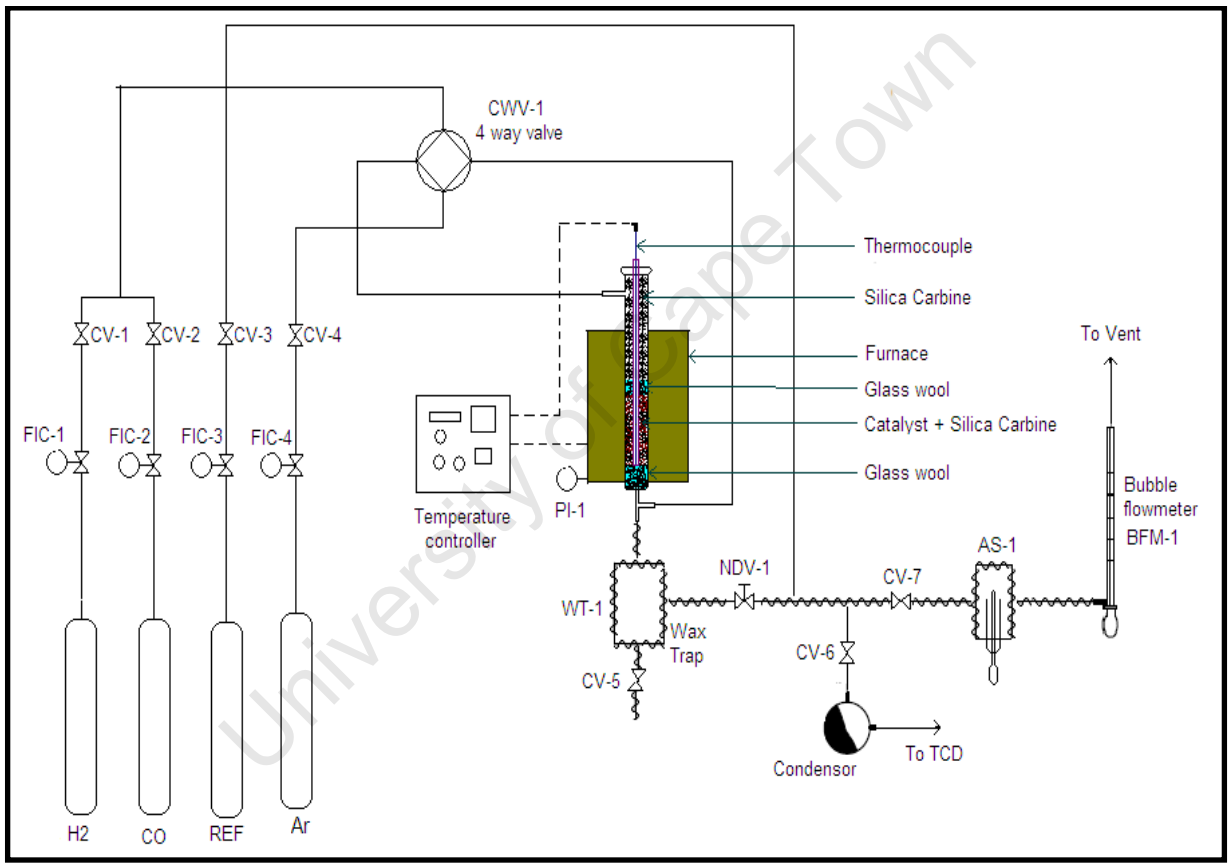


**Figure 5.2:** Setup for Fischer-Tropsch synthesis. CV-1-4: flow control valves; FIC-1-4: flow indicator controllers; AS-1: Ampoule Samples

The setup also included a 4 way valve (CWV-1) which was used to change the flow of the gases between bypass and the reactor. Argon was used to control and maintain the total pressure of the system by pressure controlled addition. A pressure indicator (PI-1) is connected to the reactor to monitor the pressure. A reference gas is used as an internal standard for analysis. The gas is $N_2$/cyclohexane mixture containing 0.05 vol-%

cyclohexane. The mixture is feed directly into the product stream via a flow controller before the product ampoule sampler (AS-1).

The total gas flow out of the reactor is controlled using needle valve (NDV-1) which was fitted after the wax trap (WT-1). The gas flow rate was measured using a bubble flow meter (BFM-1) before being vented off. A heating element was put around the reactor to maintain the reactor at a constant temperature during the reaction. The reactor and heating element are insulated to avoid heat loss to the surroundings. All exit lines from the reactor were heated using heating wires and the temperature was maintained at 180 $^0$C. The wax trap is also heated and normally operated at 180 $^0$C. The wax trap was also insulated using quartz wool. All wax products formed during the reaction collect in the wax trap and were removed using a control valve (CV-5).

The conversion across the reactor was measured using an online Gas Chromatographer (GC) equipped with a Thermal Conductivity Detector (TCD). Control valves CV-6 and CV-7 were used to alternate the flow between the GC-TCD machine and the product ampoule sampler. The product gas passed through the condenser before flowing to the TCD.

The product selectivity is calculated using an offline FID detector. This was done by using ampoules. After sampling (at the ampoule breaker) the ampoules were labeled and collected for analysis. After every 10 ampoules the control valve (CV-7) to the ampoule breaker (AB-1) is closed and the ampoule breaker is opened and the broken glass is removed.



## 5.4.2 The experimental procedure

The loading of the samples was chosen to be 0.1 g, and this was mixed with 6 g silicon carbide. The catalyst dilution with silicon carbide, which has a fairly high thermal conductivity, served to lower the amount of heat released per catalyst volume. The particle size of the SiC (200-250 μm) allows for ideal plug flow behavior. Silicon carbide was found to be inert in the reactor and thus does not affect the results of the experiments [Mabaso, 2005]. The catalyst and silica mixture is then slightly wetted with iso-propanol and then physically mixed to ensure an even distribution of the catalyst. Following the mixing, the sample + SiC is loaded into the reactor (see Appendix B; section B.4.1) which is subsequently connected to the Fischer-Tropsch synthesis setup (see Figure 5.2). The setup is the pressure tested to ensure that there are no leaks. The procedure for the pressure test is also explained in Appendix B (section B.4.2).

Prior to Fischer-Tropsch synthesis all the catalyst samples were reduced. The hydrogen flow controller (FIC-1) was set at 40 ml/min (NTP) and the hydrogen control valve (CV-1) was open. And four way valve (CWV-1) is turned to allow for flow through the reactor. To ensure that there is flow through the reactor the bubble flow meter was used.

The reduction program was started and the heating element was programmed to increase the temperature of the reactor to 350 $^0$C at a heating rate of 1 $^0$C/min. This was done such that the catalyst was reduced at 350 $^0$C for sixteen hours using pure hydrogen. The temperature was then programmed to drop to 250 $^0$C and maintained there for the duration of the experiment. After the reduction process is complete Ar is passed over the reactor to keep the catalyst under an inert environment while the synthesis gas is passed over the bypass. The flow rates of the $H_2$ and CO were set at 40 ml/min (NTP) and 20 ml/min (NTP) respectively (using the flow controllers FIC 1-2). The reference gas was then set at 20 ml/min (using FIC-3). Using pressure controlled addition of Ar in conjunction with the needle valve the system was then pressurized to 20 bar.

A total of five bypass samples were taken to confirm the flow rates and feed ratio. Once the flowrates are confirmed, the four way valve was switched back to reactor flow and reaction was started.

## 5.4.3 Sampling and data work-up

Sampling was divided into two parts. The inorganic gases and methane were analyzed using an on-line method whiles the organic compounds were analyzed using an off-line method.

### 5.4.3.1 On-line Sampling

Nitrogen was used as an internal standard for the on-line analysis where $H_2$, $N_2$, CO, $CH_4$ and $CO_2$ were analyzed using a GC (Varian 4900) equipped with thermal conductivity detector (TCD). The GC-TCD is fitted with 3 columns, which were used to analyzed different gasses in separate channels; channel 1 (CP-4900 Backflush column module, 20 m, MS5), channel 2 (CP-4900 column module, 10 m, PPQ heated in) and channel 3 (CP-4900 Backflush column module, 10 m, MS5). Each channel uses a different carrier gas and is connected to a separate detector. The operating conditions and the gasses detected in each column are given in Table 5.2. Relative errors (repeatability of this analysis technique) are typically ±3 % for TCD analyses.

**Table 5.2:** Conditions for online GC-TCD (Varian 4900) chromatographic analysis

| | Channel 1 | Channel 2 | Channel 3 |
|---|---|---|---|
| Compounds analyzed | CO,$N_2$, $CH_4$ | $CO_2$ | $H_2$ |
| Column temperature ($^0$C) | 80 | 60 | 80 |
| Carrier Gas | $H_2$ | He | Ar |
| Inlet Pressure (KPa) | 150 | 100 | 150 |
| Injection time (ms) | 120 | 120 | 120 |
| Injector temperature ($^0$C) | 40 | 40 | 40 |
| Backflush time (s) | 160 | — | 160 |
| Sampling time (s) | 180 | 180 | 180 |

The TCD setup was calibrated on a monthly basis using calibration gas mixtures with known composition. The peak areas: $A_i$, obtained from the TCD analysis were then used to calculate the relative calibration factors normalized for nitrogen, $f_{TCD}$, for each species (Equation 5.2; Table 5.3).

$$\left(\frac{n_i}{n_{N_2}}\right) = f_{TCD,i}\left(\frac{A_i}{A_{N_2}}\right) \tag{5.2}$$

**Table 5.3:** Typical calibration factors used in this work

| Gas | Calibration Factor |
|---|---|
| $f_{TCD,H_2}$ | 0.108 ± 0.02; |
| $f_{TCD,CO}$ | 1.045 ± 0.031 |
| $f_{TCD,CO_2}$ | 0.969 ± 0.029 |
| $f_{TCD,CH_4}$ | 0.506 ± 0.09 |

Before Fischer-Tropsch reaction bypass sample are taken. The reactants, CO and $H_2$ are analyzed together with the internal standard ($N_2$). Following that, the peak areas for each species present are obtained and used to calculate the molar flow rate of the respective gases.

The molar flow rates of inorganic compounds and methane, ṅ, obtained from TCD analysis are given by:

$$(\dot{n}_i) = f_{TCD,i}\left(\frac{A_i}{A_{N_2}}\right)\dot{n}_{N_2} \tag{5.3}$$

With

$$\left(\dot{n}_{N_2}\right) = \frac{x_{N_2} \cdot \dot{V}_{ref}(NTP)}{\widetilde{V_A}} \tag{5.4}$$

where $x_{N_2}$ is the molar concentration of nitrogen in reference gas; $\dot{V}_{ref}(NTP)$ is the volumetric reference gas flow rate; $\widetilde{V}_A$ is the Avogadro volume. This will then represent the amount of reactants fed into the reactor (i.e. $(\dot{n}_i)_{in}$).

During Fischer-Tropsch synthesis, TCD samples are taken and analyzed (see Figure 5.3). Following that, peak areas for each species present are obtained and used to calculate the molar flow rate of the respective species (see Equation 5.3) out of the reactor (i.e. $(\dot{n}_i)_{out}$). Conversion of a reactant can be calculated as being:

$$X_i = 1 - \frac{(\dot{n}_i)_{out}}{(\dot{n}_i)_{in}} \tag{5.5}$$

The yield, $Y_{i.c}$ and selectivity, $S_{i,c}$ of a product on carbon basis is:

$$Y_{i,c} = \frac{(\dot{n}_i)_{out}}{(\dot{n}_{CO})_{in}} \tag{5.6}$$

$$S_{i,c} = \frac{Y_{i,c}}{X_{CO}} \tag{5.7}$$

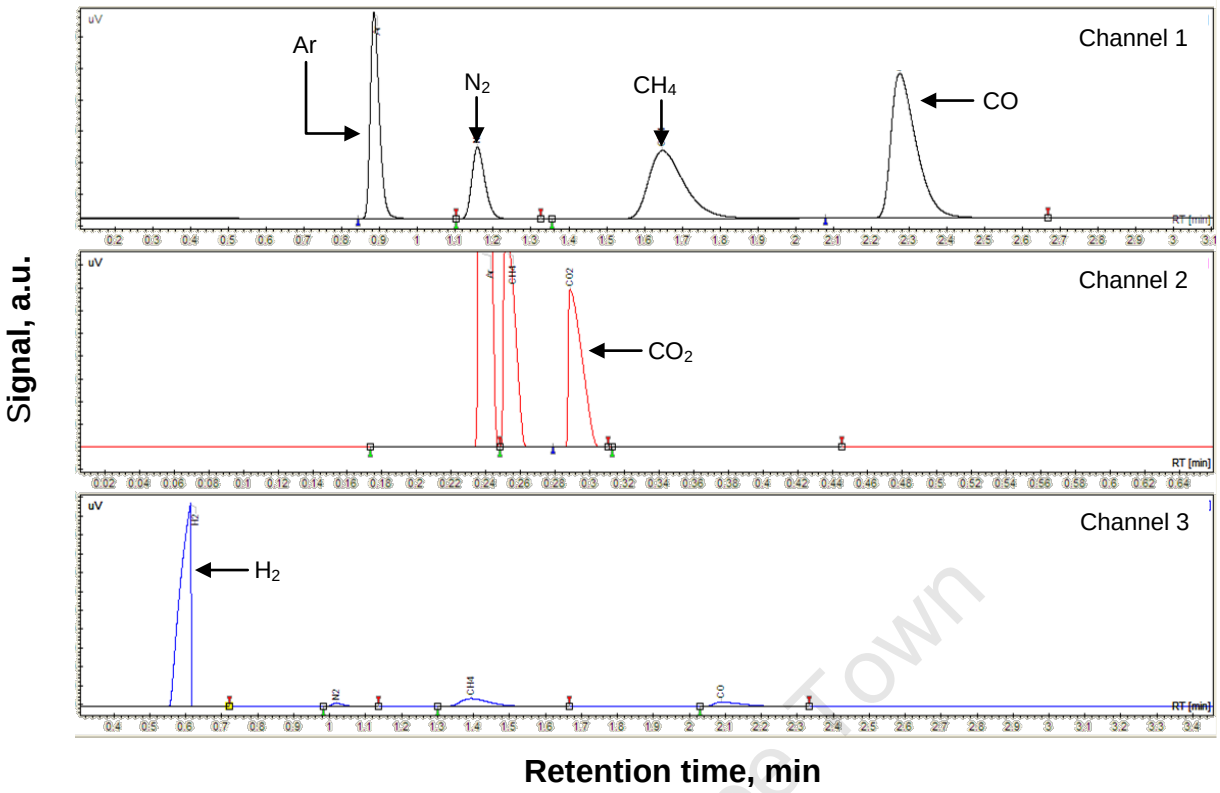


**Figure 5.3:** A typical chromatogram obtained from and GC-TCD analysis during Fischer-Tropsch synthesis (only peaks used in analysis are labeled)

### 5.4.3.2 Offline Sampling

The total composition of the combined stream of product and reference gas was sampled in their vapour state using heated glass ampoules as prescribed by Schulz and Nehren (1986). In this technique, the capillary end of an evacuated glass ampoule is inserted, through the septum of a sampling device, into the effluent stream. The capillary is broken in the sampling device, so drawing a total vapour phase sample into the ampoule after which the capillary is partially withdrawn and sealed with a butane flame. This is illustrated in Figure 5.4.

These ampoules are later crushed within an ampoule breaking device so releasing the sample contents into an off-line chromatograph for analysis of organic compounds. Cyclohexane, which is not a product of Fischer-Tropsch synthesis at the conditions applied, was used as an internal standard for the off-line analysis of organic compounds using a temperature programmed gas chromatograph (Varian 3400) equipped with a flame ionization detector (FID). Conditions of the gas chromatographic analyses are given in Table 5.4 and a typical FID chromatogram is shown in Appendix B (Figure B.6). The

internal standards, which were accurately fed to the product stream, were used for calculation of flow rates of organic components and subsequently yields and selectivity.

The response of a FID detector is strictly carbon specific; however, oxygen containing components give a weaker response. In order to account for this, theoretical mass specific response factors have been used following an incremental approach suggested by Kaiser (1969). Here the response of all carbon atoms which are not bonded to an oxygen atom is 1, the response of carbon atoms with a single bond to an oxygen atom is 0.55 and those carbon atoms with C=O double bonds are considered to give no response. The resulting factor for a component is then calculated using Equation 5.8.

$$f_i = \frac{N_C}{N_{C(no\ O)} + 0.55N_{C(O)}} \tag{5.8}$$

where $N_C$ is the total number of carbon atoms in a molecule, $N_{C(no\ O)}$ is the number of carbon atoms not connected to oxygen and $N_{C(O)}$ is the number of carbon atoms connected to one oxygen atom with a single bond.



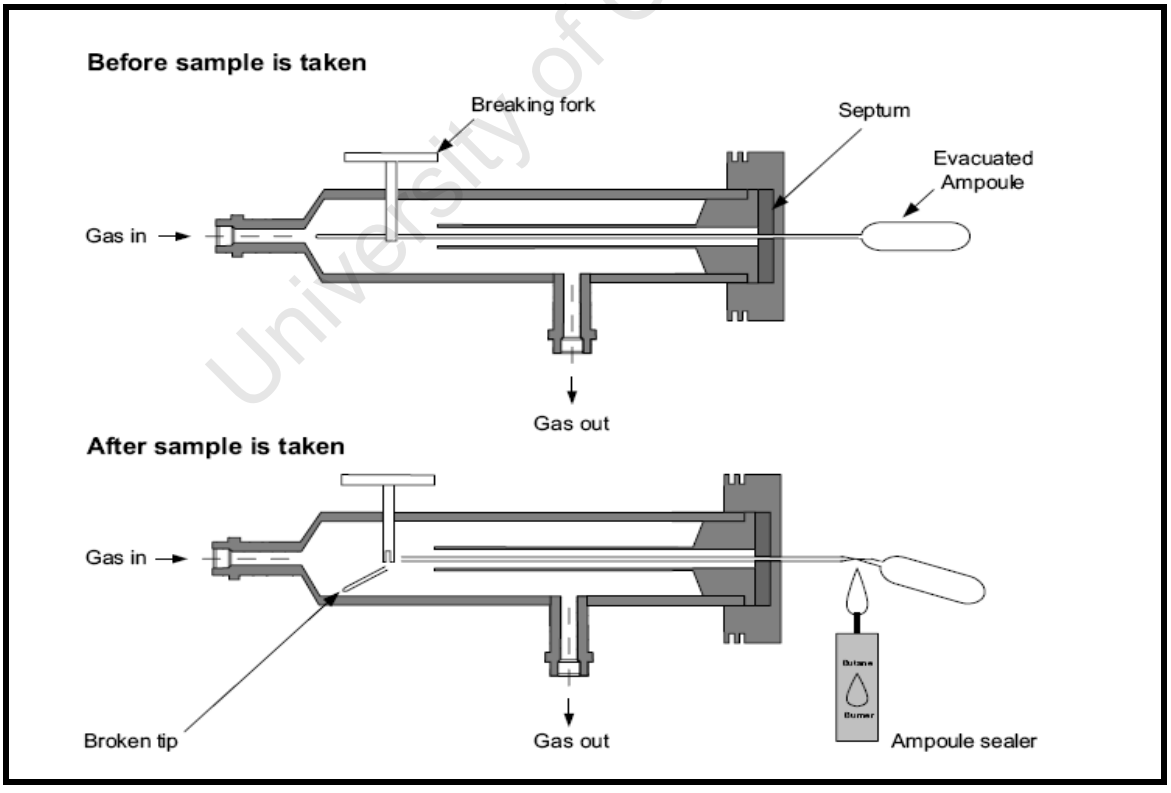


**Figure 5.4:** Ampoule sampling procedure [adopted from Mabaso (2005)]

The molar flow rate of an organic compound, $n_i$, can be derived from results of FID analyses as follows:

$$\dot{n}_i = \frac{N_{CH_X}}{N_i} \cdot \frac{f_i \cdot A_i}{f_{CH_X} \cdot A_{CH_X}} \cdot \dot{n_{CH_X}} \tag{5.9}$$

with $N_{CHx}$, the carbon number of cyclohexane and $n_{CHx}$ the molar flow rate of the reference compound, cyclohexane, equaling:

$$\left(\dot{n}_{N_2}\right) = \frac{x_{N_{CHx}} \cdot \dot{V}_{ref}(NTP)}{\widetilde{V_A}} \tag{5.10}$$

The yields and selectivity of the organic compounds are then calculated using Equation 5.6 and Equation 5.7.

**Table 5.4:** Conditions for offline GC-FID (Varian 3400) chromatographic analysis

| | |
|---|---|
| Gas chromatograph | Varian 3400 (off line)<br>**(adapted to ampoule technique)** |
| Detector | flame ionization detector (FID), T = 250 $^{o}$C |
| Column | Column RTx-1 (Restek)<br>fused silica capillary column, 60 m x 0.25 mm<br>stationary phase: 0.5 µm dimethyl siloxane<br>(crosslinked) |
| Carrier gas | Hydrogen |
| Introduction gas | Nitrogen |
| Column head pressure | 2.9 bar (absolute) |
| Injector | Split injector, T= 250 0C<br>Split ratio 1:20 |
| Temperature programme | -60 oC, 3 min, isothermal<br>at 15 $^{o}$C/min to -35 $^{o}$C, 0 min isothermal<br>at 10 $^{o}$C/min to -5 $^{o}$C, 2 min isothermal<br>at 2.5 $^{o}$C/min to 25 $^{o}$C, 0 min isothermal<br>at 5 $^{o}$C/min to 250 $^{o}$C, 10 min isothermal |
| Temperature | 250 $^{0}$C |

# 6

# Results and discussion



*The results section is divided into four main sub-sections. Firstly, it centers on the development of the metal support interactions during the calcination process; focusing on the identification and quantification of the respective interactions also discussing the effects these interactions have on the crystallite size of the calcined samples. Secondly, the reduction behavior of the modified catalyst was investigated. Thirdly, Fischer-Tropsch synthesis runs revealed changes in activity and selectivity of the modified catalyst, followed by the post reaction analysis of the spent catalysts.*

# 6.1 Catalyst preparation

## 6.1.1 Analysis of the drying method

All the samples were prepared using the microemulsion precipitation technique [Mabaso, 2005; Eriksson et al., 2004]. Prior to modification the samples were dried to remove water so as to prevent auto condensation of the metal alkoxide precursors (TEOS and TBO). Since the modification process was modeled on the reaction of the metal alkoxides compounds with a precipitated metal hydroxide phase, it was important to ensure that during drying, the metal hydroxides were not converted to oxide form.

A test sample was prepared (also using the microemulsion technique) and dried in an oven at 120 $^0$C for 24 hours and then examined using XRD (see Figure 6.1). After the drying, the sample is shown to be two-line ferrihydrite (β-FeOOH). The two-line ferrihydrite is built from $Fe(O,OH)_6$ octahedra sharing corners and edges and is a form of iron hydroxide [Liu et al., 2004; Combes et al., 1989].



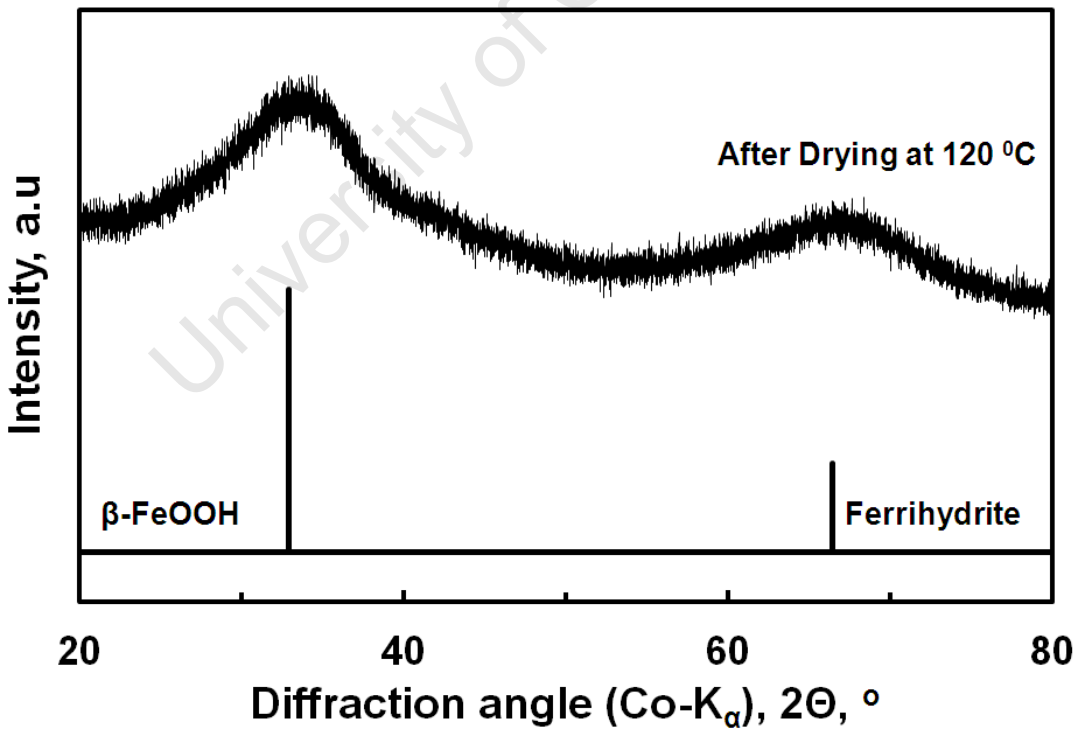


**Figure 6.1:** XRD patterns of an unmodified iron oxide catalyst prepared using micro-emulsion precipitation technique after drying at 120 $^0$C in an oven for 24 hrs (also shown is the reference spectra for ferrihydrite (β-FeOOH))

Before drying, the sample weighed 0.42 g. After 24 hours of drying the sample mass had decreased by 12 %. Since the oven was operated at 120 $^{0}$C, it can be deduced that the change in sample mass indicates the removal of water and other impurities. XRD analysis indicates that prior to modification the samples are in the required dried hydroxide phase.

## 6.1.2 Analysis of the modification techniques

Prior to calcination the modified catalysts are doped with metal alkoxide compounds to produce the desired metal support interactions. To generate the Fe-O-Si interaction tetraethoxy-silane (TEOS) is used and to generate Fe-O-Ti, titanium butoxide (TBO) was injected. Two different methods were used for the modifications, i.e. the instantaneous injection technique for the Si system, and the infinite dilution technique for the Ti system. The slow addition of highly diluted titanium butoxide was used to avoid the auto-condensation of the alkoxide compound [Orlović et al., 2005].

### 6.1.2.1 Method one: instantaneous injection (for Si system)

The TEM technique was used to investigate the crystallite formation of the catalysts after modification. This method was also used to observe the morphology of the nanocrystallites. Additionally, the co-current use of Electron Density Scan (EDS) allowed for the study of the silicon (Si) distribution across the crystallites. The results of the EDS analysis for a selected catalyst (FS-56), prepared using the instantaneous injection method, are presented in Figure 6.2.

The contrast EDS scan, also depicted in Figure 6.2, shows the silicon distribution as blue spots. It can be deduced from the image that the silicon is homogeneous distributed across the sample. There are no isolated clusters of the silicon atoms, which would be expected if there were large amounts of amorphous silica present in the sample. Furthermore there are no silicon free patches on the iron oxide crystallites. This is an indication that the instantaneous injection technique, used for TEOS modification, resulted in an even distribution of the ligands on the sample.

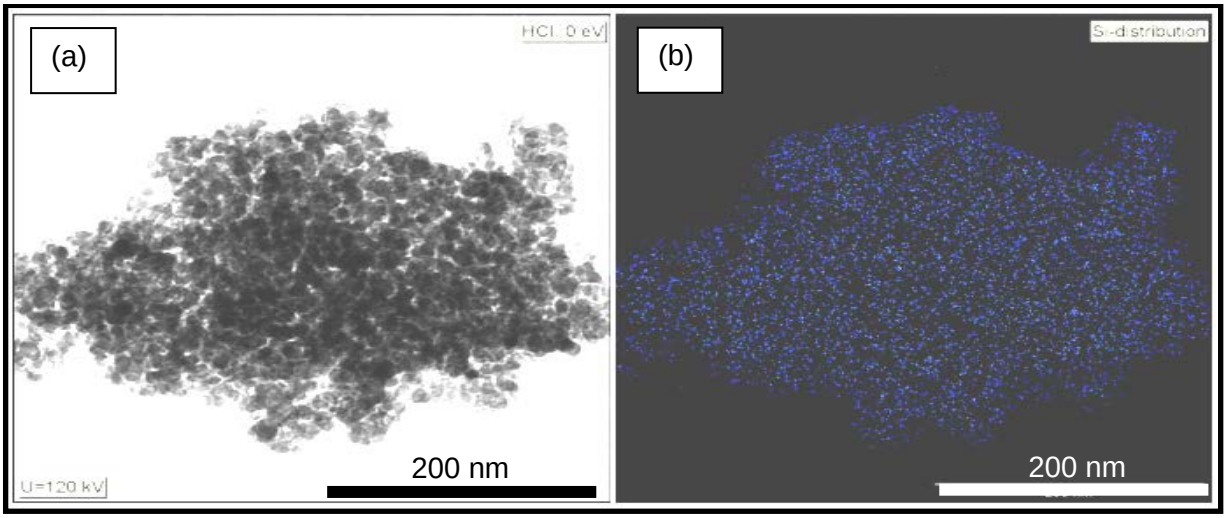


**Figure 6.2:** TEM image of a calcined, TEOS modified iron oxide nano-crystallites (FS-56) prepared using micro-emulsion technique and modified by the instantaneous injection method

(a) TEM micrographs of modified iron oxide crystallites

(b) A contrast EDS scan showing the distribution of the silicon (indicated by the blue dots) across the crystallites



### 6.1.2.2 Method two: infinite dilution (for Ti system)

To ascertain the validity of the infinite dilution method used in the preparation of TBO modified catalyst, EDS was used to study Titanium (Ti) distribution across the calcined iron crystallites prepared using both the instantaneous injection and the infinite dilution method.

Figure 6.3(a) shows TEM scan of a catalyst modified with TBO prepared using the instantaneous injection method (as described for the preparation of the TEOS modified samples). Uneven distribution of the titanium is observed. There appears to be areas with a high density of titanium atoms (see Figure 6.3(a); titanium shown as red spots), which might indicate the formation of crosslinked Ti-O-Ti interactions (highlighted on Figure 6.3(a) by area A). The large titanium rich crystallites have no specific shape or size, indicating a random agglomeration of the $TiO_x$ species in the sample. The titanium free crystallites (highlighted on Figure 6.3(a) by area B), show spherical morphology. The size of the titanium free crystallites appears to be considerably smaller than the titanium rich crystallites. It can be concluded that TBO modification using the instantaneous injection methods results in a non-homogeneous distribution of titanium in the sample, possibly due to auto condensation of the TBO compound.

(a)

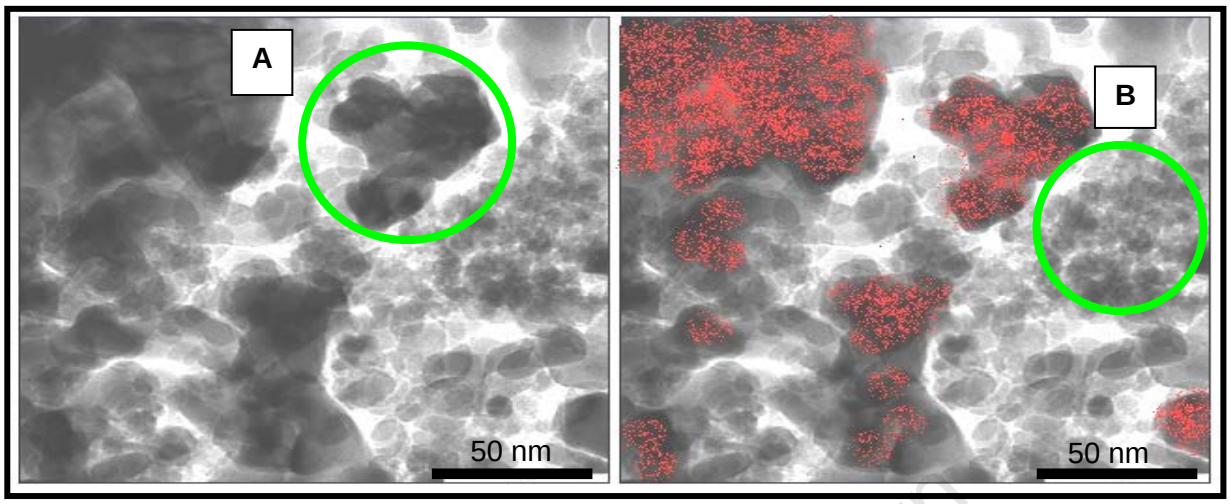


*A: Area on the sample showing a high density of titanium*

*B: Area on the sample that showing titanium free crystallites*

(b)

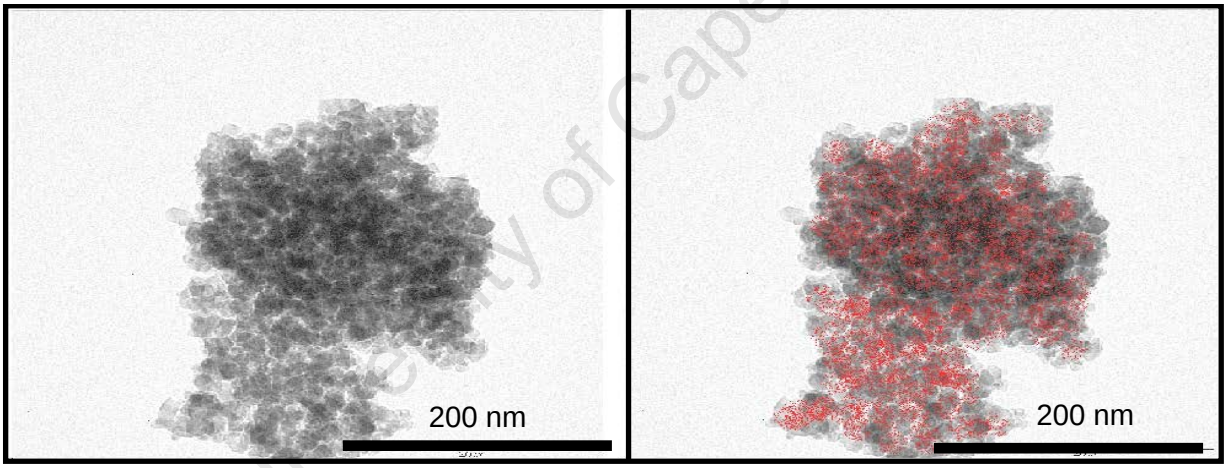




**Figure 6.3:** TEM images of a calcined, TBO modified iron oxide nano-crystallites prepared using micro-emulsion technique (FT-21)

(a) A contrast EDS scan showing the distribution of the titanium (indicated by the red dots) across the iron oxide crystallites prepared using the instantaneous injection method

(b) A contrast EDS scan showing the distribution of the titanium (indicated by the red dots) across the iron oxide crystallites prepared using the infinite dilution method

Figure 6.3(b) shows a TEM scan of a sample modified with an identical amount of TBO as the sample described before, but prepared using the infinite dilution method. The EDS analysis shows titanium as red spots (see Figure 6.3(b)). The distribution of titanium appears to be homogeneous across the sample. There are no isolated clusters of the titanium, which would be expected if there was a large amount of titania present in the sample. Furthermore, there are no titanium free areas on the image. Thus, from the results, it is clear that the infinite dilution method was successful in preventing the formation of large amounts of titania in the sample.

The EDS data indicated that after calcination the silicon (or titanium) was homogeneously distributed in the sample. However, the analysis technique provided no information on the type of interactions that were formed or the quantity of these interactions. Once the EDS analysis validated the modification methods, it was essential to identify and quantify the generated interactions. The quantification of ligand content was done using Energy Dispersive X-ray (EDX).



### 6.1.3 Quantification of surface modification

An iron oxide sample was prepared and used as a standard. Varying amounts of tetraethyl orthosilicate (TEOS) and titanium butoxide (TBO) were loaded. The prepared samples are listed in Table 6.1 (the EDX analysis of the silicon and titanium content, relative to the iron content in the samples, are also displayed). The sample codes correspond to the EDX measured silicon (or titanium)-content (rounded off to the nearest 1). The second column shows the expected silicon (or titanium) contents calculated from the amount of TEOS (or TBO) loaded (assuming 100 % recovery). The amounts of alkoxide precursor added in each sample are shown in the experimental section (see Table 5.1).

The calculated molar ratios are given in millimole of silicon (or titanium) relative to moles of iron present in the catalyst. Assuming a 10 nm reduced α-Fe crystallite, which was the intended crystallite sizes prescribed by the use of the micro-emulsion ratios [Mabaso, 2005], which has a dispersion of 10% [Wise et al., 2001], the expected modification surface coverage ranges from 4-42%. Total surface coverage was not desired because blocking of all active site would hinder the study of the ligand effect, since no iron atoms would be available for reaction. Thus a maximum surface coverage of 42% was used.

The preparation techniques used were successful at loading the respective ligands. However, the modification process is more efficient at low loadings, with the calculated values corresponding reasonably well with the experimental data (see Table 6.1). At high loadings of the alkoxide compounds, the EDX measured silicon (or titanium)-contents deviates considerably from the calculated values. This was observed for both the TEOS and the TBO modified samples (see Figure 6.4), indicating that reaction between the metal hydroxide and the alkoxide, irrespective of which compound, might get saturated at which point no further modification can take place. This could be due the steric hindrance (blocking) effects of the surface ligands or repulsions between the ligands attached to other silica or titania. Surface saturation is influenced by steric hindrance that is imposed by the ligands, limiting the number of bonding sites [Puurunen, 2003]. This effect would not be significant at low loading, since there is a high number of iron surface atoms available, but will increase with increasing ligand addition and thus resulting in the a larger variation at high loading.



**Table 6.1:** EDX analysis of prepared samples

| System | Sample Code: | Calculated (loading) Molar Ratio mmol Si(Ti)/mol Fe | EDX analysis Molar Ratio mmol Si(Ti)/mol Fe |
|---|---|---|---|
| **Fe-O-Si** | FS-0 | 0 | 0.0 |
| | FS-10 | 10 | 9.9 ± 0.7 |
| | FS-19 | 31 | 19.4 ± 0.9 |
| | FS-38 | 42 | 37.8 ± 2.9 |
| | FS-56 | 52 | 56.3 ± 4.9 |
| | FS-88 | 105 | 87.9 ± 4.4 |
| **Fe-O-Ti** | FT-4 | 6 | 4.4 ± 0.4 |
| | FT-9 | 10 | 8.8 ± 1.7 |
| | FT-21 | 31 | 21.4 ± 1.4 |
| | FT-39 | 52 | 38.6 ± 1.0 |
| | FT-70 | 104 | 70.0 ± 2.2 |

At high alkoxide loading, an average silicon recovery of ca. 90 % was observed for the TEOS modified samples and only ca. 70 % of the titanium is recovered in the samples modified with TBO (see Figure 6.4). Steric hindrance is largely influenced by size of the ligands, with larger ligands resulting in greater hindrance [Ratzinger et al., 2009]. The butoxide -$(OC_4H_9)_3$ groups on the titanium ligands are larger than the ethyl -$(OC_2H_5)_3$ groups on the silicon ligands. Therefore, steric hindrance would be expected to be larger in the TBO modifies samples, resulting in lower recovery. Moreover, the presence of pre-attached surface ligands (achieved using infinite dilution method for TBO modification), increases the overall steric repulsion on the surface [Jin et al., 1994], resulting a lower ligand concentration at which saturation occurs.

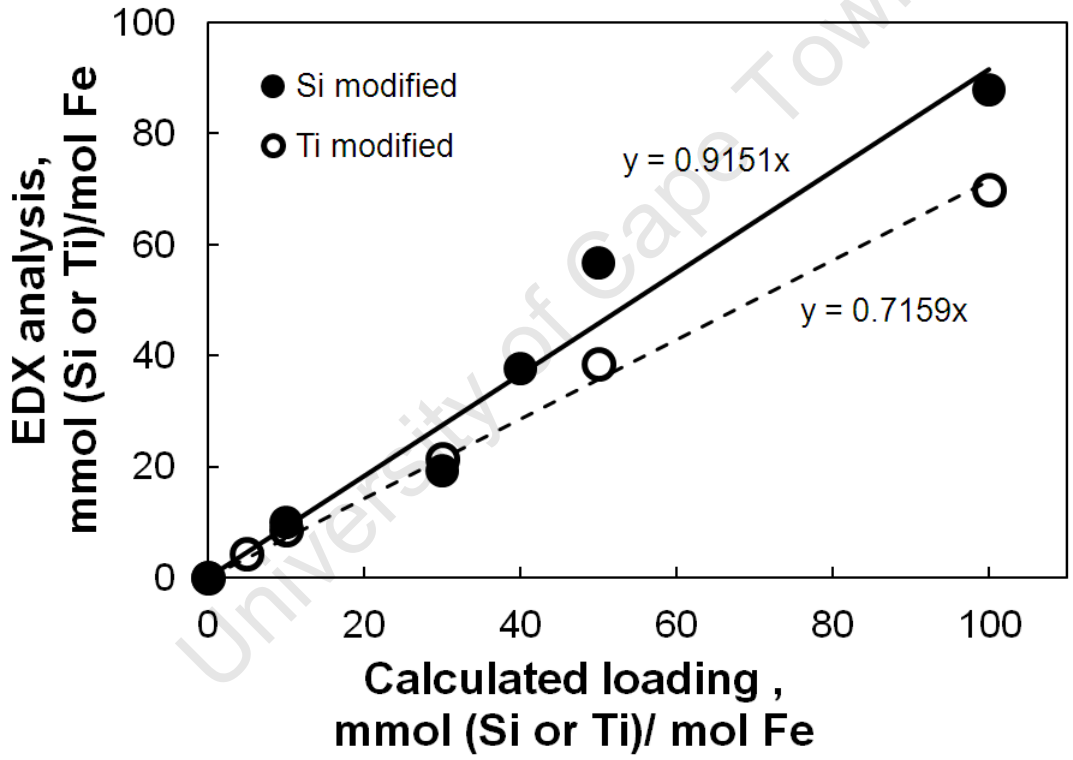




**Figure 6.4:** The comparative analysis of the Si and Ti-contents loaded during modification and the contents recovered after calcination (as given by EDX analysis)

# 6.2 Iron silica system (Fe-O-Si)

## 6.2.1 FTIR (DRIFTS mode) analysis of TEOS modified calcined catalysts

The type of interaction generated during TEOS modification on the calcined samples was determined by FTIR (DRIFTS mode). The results showing the full range of analysis (400 – 4000 $cm^{-1}$) are displayed in Figure 6.5.

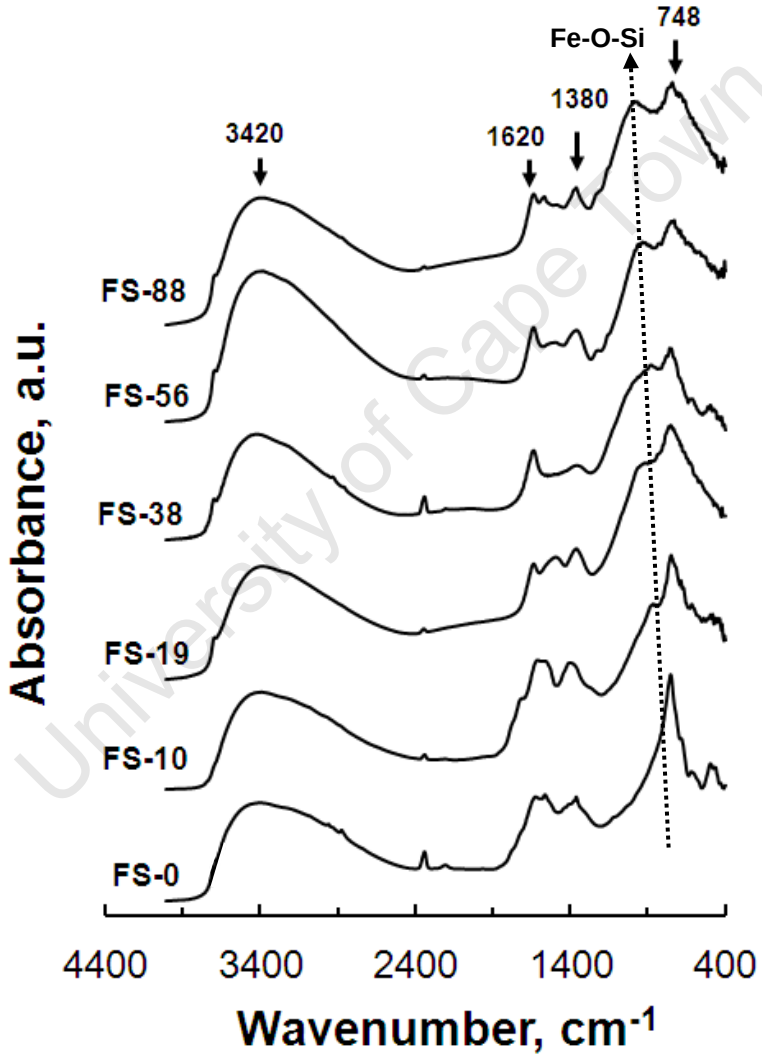


**Figure 6.5:** FT-IR (DRIFTS mode) analysis of calcined iron oxide nano-crystallites prepared using microemulsion technique and modified with TEOS using instantaneous injection method.

All the analyzed samples show absorption bands at 3420 $cm^{-1}$, due to the stretching of hydroxyl groups (-OH) [Walters, 2006; Darezereshki, 2011] generally associated with the presence of water. This is accompanied by a band at 1620 $cm^{-1}$ due to the (-OH) bending of water [Walters, 2006; Darezereshki, 2011]. The small absorption bands at ca. 2380 $cm^{-1}$ represent the asymmetric vibration of $CO_2$ from the atmosphere [Darezereshki, 2011]. The bands at 1380 $cm^{-1}$ might be assigned to C-H stretching modes due to the presence of residual surfactant in the catalyst, commonly observed with catalyst prepared via microemulsion technique [Morsy et al., 2009]. It is important to note that the absence of strongly crosslinked Si-O-Si interactions, which yield an adsorption band at ca. 1110 $cm^{-1}$ [Qing et al., 2011; Manceau et al., 1995, Vempati et al., 1990], excludes the formation of amorphous silica (see Figure 6.5).

**Identifying the iron oxide phases present in the calcined samples**

FTIR analysis of the calcined samples over the full range of 400 – 4000 $cm^{-1}$ (see Figure 6.5) does not show the details of the smaller absorption bands associated with the iron oxide phase in the range < 1000 $cm^{-1}$. Therefore, in order to identify the $Fe_2O_3$ phases present in the calcined samples, this region is highlighted (see Figure 6.6).

Sample FS-0 indicates a mixture of hematite ($\alpha$-$Fe_2O_3$) and maghemite ($\gamma$-$Fe_2O_3$). The absorption bands at 430, 560, 590, 630, 690 and 748 $cm^{-1}$ are due to the vibration of Fe-O bonds, consistent with the presence of nano-sized well ordered maghemite [Veintemillas-Verdaguer et al., 1998; Belin et al., 2002; Jarlbring et al., 2005; Darezereshki, 2011]. The two absorption bands at ca. 460 and 500 $cm^{-1}$ result from Fe-O stretching in hematite [Woo et al., 2003; Hiremath and Venkataraman, 2003; Darezereshki, 2011]. The higher intensity of the $\gamma$-$Fe_2O_3$ absorption bands indicates that this is the dominant phase.

The intensity of absorption bands associated with Fe-O bonds is compromised by the presence of Fe-O-Si interactions [Qing et al., 2011]. This explains the high signal to noise ratio observed for samples FS-10 (see Figure 6.6). FTIR spectra obtained for samples with higher silicon content (FS-19 to FS-88) are similar to the spectrum for sample FS-10. Therefore, the absorption bands for the TEOS modified samples, in the region 400-1000 $cm^{-1}$, could not be clearly discerned and thus could not be identified. However, the all the TEOS modified samples clearly show an absorption band at 748 $cm^{-1}$ (see Figure 6.5), consistent with the presence of $\gamma$-$Fe_2O_3$.

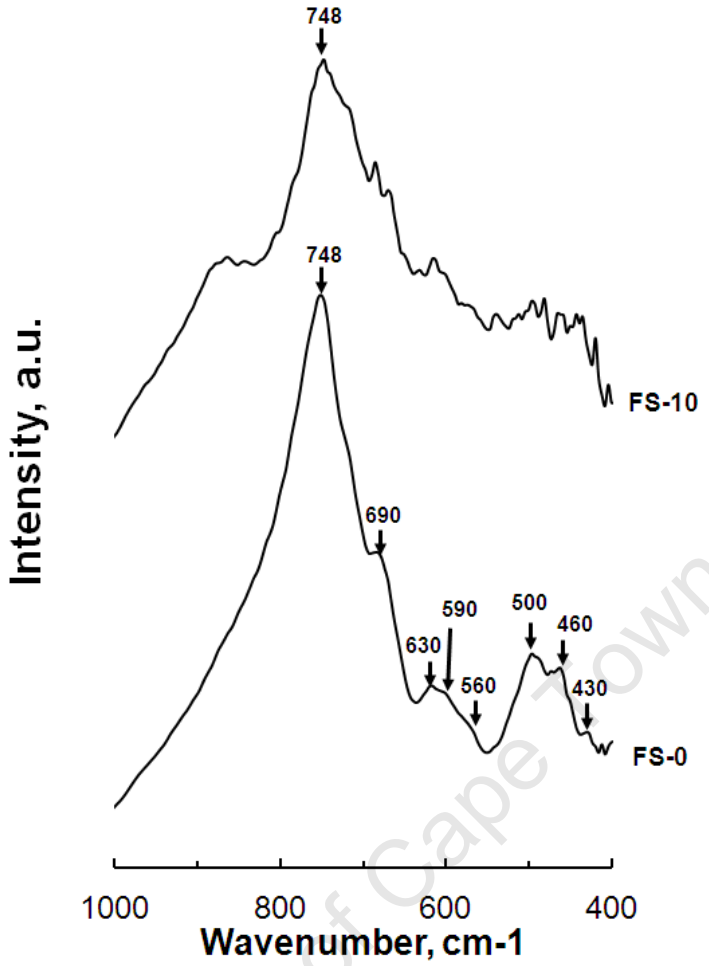


**Figure 6.6:** FT-IR (DRIFTS mode) analysis of sample FS-0 and FS-10 focusing on the range 400-1000 $cm^{-1}$



**Identifying the Fe-O-Si interaction in the samples**

All the TEOS modified catalyst show an additional absorption band between 890 $cm^{-1}$ and 1010 $cm^{-1}$ (see Figure 6.5 and Figure 6.7). This is region where absorption band due to stretching of the Fe-O-Si interaction occurs [Barraclough et al., 1961; Qing et al.,2011; Day, 1981; Vempati et al., 1990; Yang et al., 2008; Swedlund et al., 2009]. The broad nature of the observed peak is also consistent with what has been reported before. The allocated frequencies for the Fe-O-Si interaction ascribed in literature (see Table 6.2) are consistent with FTIR assignment for the Fe-O-Si interaction in this study (see Table 6.3).

The position of the additional absorption band appears to be a function of TEOS loading. At low loading (FS-10), the silicon surface coverage is expected to be low, i.e. a high number of Fe surface atoms available for interaction. This may result in the formation of tridentate interactions, corresponding to a low absorption frequency (896

$cm^{-1}$) due to the lack of vibrational freedom (see Figure 6.7). An increasing the silicon content, FS-19 to FS-56, introduces electronic repulsion and steric hindrance between the surface ligands. This results in the blue shift of the adsorption frequency from 896 $cm^{-1}$ to 990 $cm^{-1}$. The adsorption band at 990 $cm^{-1}$ is ascribed to bidentate $(\equiv FeO)_2$-$Si(OH)_2$) interactions [Yang et al., 2008; Swedlund et al., 2009]. A further increase of the adsorption frequency to 1020 $cm^{-1}$ is observed for the sample with the highest silicon content (FS-88), consistent with monodentate interactions $(\equiv FeO)$-$Si(OH)_3$ [Yang et al., 2008].

**Table 6.2:** FTIR frequency assigned to Fe-O-Si and the corresponding Si content as established in literature

| Frequency ($cm^{-1}$) | (Si/Fe) molar ratio (mmol/mol) | Reference |
|---|---|---|
| 900 | not given | Barraclough et al. (1960) |
| 1000 | 200 | Qing et al. (2011) |
| 1000 | 500 | Day (1981) |
| 1010-1030 | 1400 | Manceau et al. (1995) |

**Table 6.3:** FTIR frequency assigned to Fe-O-Si present in prepared catalysts

| Sample code | Frequency ($cm^{-1}$) |
|---|---|
| FS-10 | 896 |
| FS-19 | 990 |
| FS-38 | 990 |
| FS-56 | 990 |
| FS-88 | 1020 |

The TEOS modified samples also show and additional absorption band at ca. 3740 $cm^{-1}$ (see Figure 6.5), which is assigned to the *v* -OH vibrations of free/isolated silanol groups [ van Roosmalen and Mol, 1978; Chuckin and Malevich, 1977; Takei et al., 1999]. The adsorption band at 3740 $cm^{-1}$ is attributed only to free surface hydroxyl groups and is not consistent with hydrogen bonding and also excludes the presence of internal hydroxyl groups in the sample [Takei et al., 1999]. Silanol groups are resistant to thermal treatment up to 1000 $^0$C [Takei et al., 1999]. Thus it is not surprising that after calcination at 350 $^0$C, these interactions are still present in the analyzed catalysts. The presence of these hydroxyl groups is not clearly evident on the sample FS-10 because of the low concentration of the silanol groups (due to low TEOS loading) and might also be compromised by the presence of water [Takei et al., 1999].

It can thus be concluded that the surface modification of the iron oxide nano-particles with TEOS was successful. Furthermore, the silicon ligands are attached to (-OH) groups.



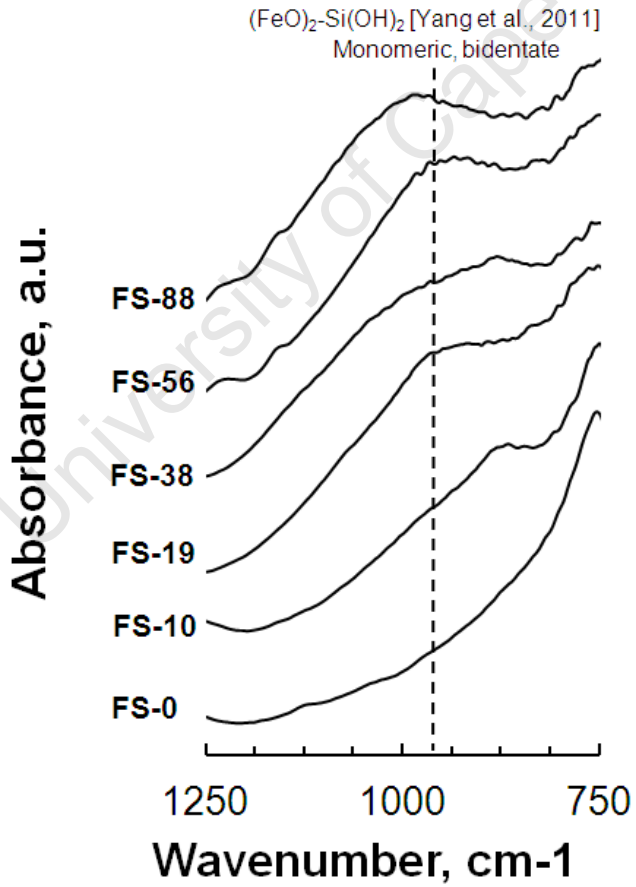


**Figure 6.7:** FT-IR (DRIFTS mode) analysis of calcined iron oxide nano-crystallites prepared using microemulsion technique and modified with TEOS focusing on the range 750-1250 $cm^{-1}$

## 6.2.2 TEM analysis of TEOS modified calcined samples

TEM was used to ascertain the average crystallite size and size distribution of the TEOS modified samples. This method was also used to observe the morphology of the nanocrystallites. The TEM images of the TEOS modified calcined samples are shown in Figure 6.8. The TEM micrographs show that the prepared catalyst nanocrystallites have a well defined and uniform structure with a predominantly spherical morphology. The presented TEM images also indicate, visually, a change in crystallite size with increasing silicon content (also see Table 6.4). The TEM images of samples FS-0 and FS-10 show two types of crystallites. The TEM images show mostly light crystallites that appear to be smaller in size and dominant in number whiles the darker crystallites seem to be larger.

Two hundred crystallites, for each sample, were then measured using imageJ software. The average crystallite diameters estimated from the TEM-images are given in Table 6.4 and the associated crystallite size distributions are displayed in Figure 6.9.



**Table 6.4:** Average crystallite sizes (in nm) estimated from TEM-images (n = 200)[a]

| Catalyst | FS - 0 | FS - 10 | FS - 19 | FS-38 | FS - 56 | FS - 88 |
|---|---|---|---|---|---|---|
| $d_{AVG\_TEM}$ | 12.4 ± 2.8 | 13.9 ± 4.8 | 11.6 ± 2.2 | 10.8 + 2.1 | 9.1 ± 1.8 | 6.9 ± 1.1 |

*a: 200 crystallites were measured from the TEM images using J-image software*

*b: The values presented are mean volume average diameters displayed also are the standard mean deviations*

The average crystallite size distributions are narrow (see Figure 6.9), with standard deviations of 15-32 % (when expressed as a percentage of the mean crystallite diameter; see Table 6.4). The standard deviations are directly proportional to the average crystallite diameters, i.e. the largest deviation is obtained for the sample with the largest average crystallite size and vice versa. Similar results were reported by Catlow et al. (1997) and Mabaso (2005).

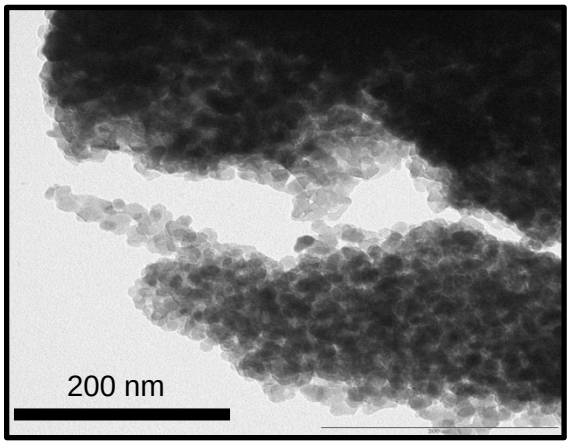


FS-0

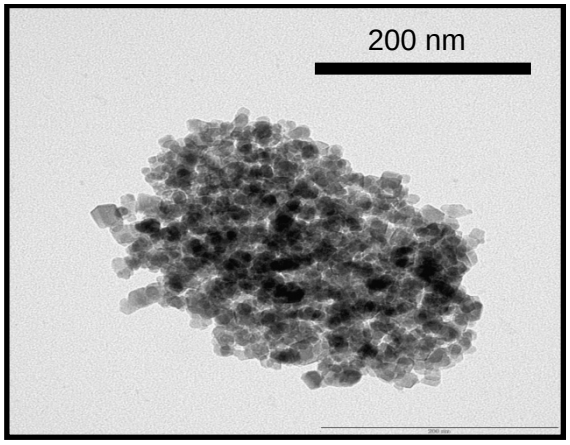


FS-10

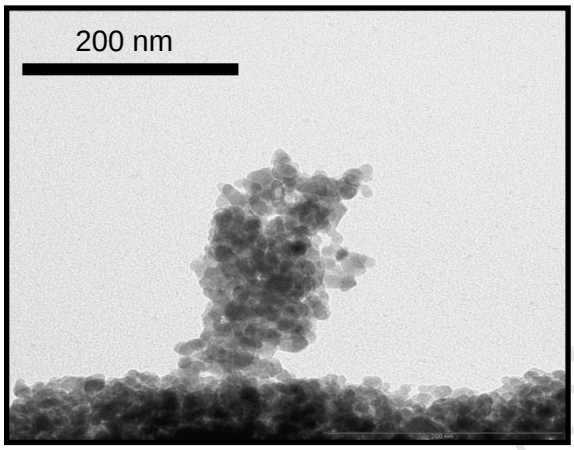


FS-19

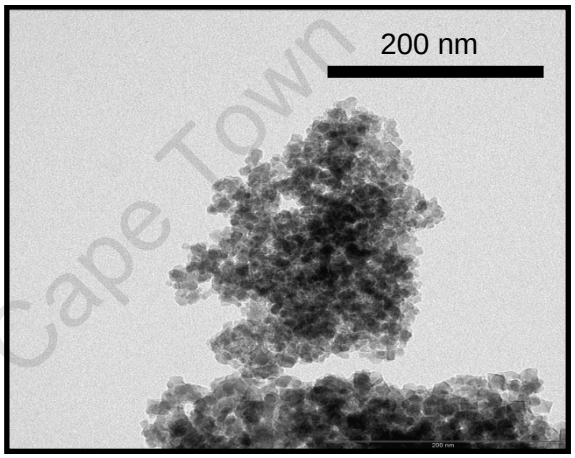


FS-38

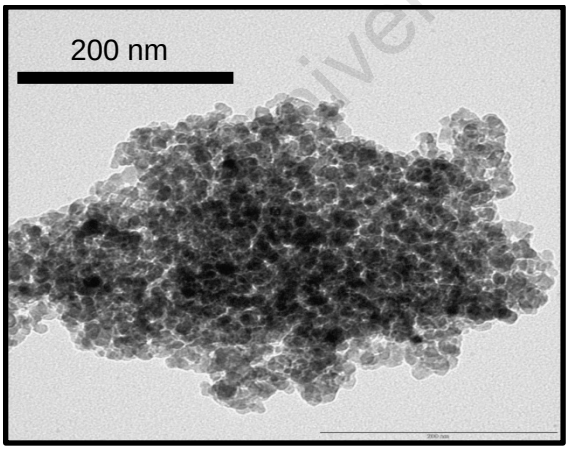


FS-56

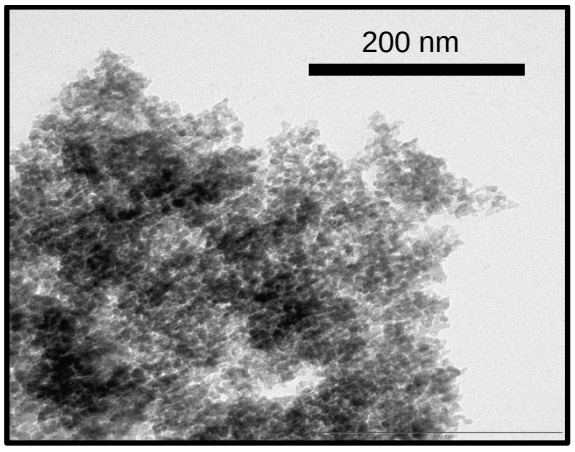


FS-88



**Figure 6.8:** TEM micrographs of calcined iron oxide nano-crystallites prepared using microemulsion technique and modified with TEOS using instantaneous method.

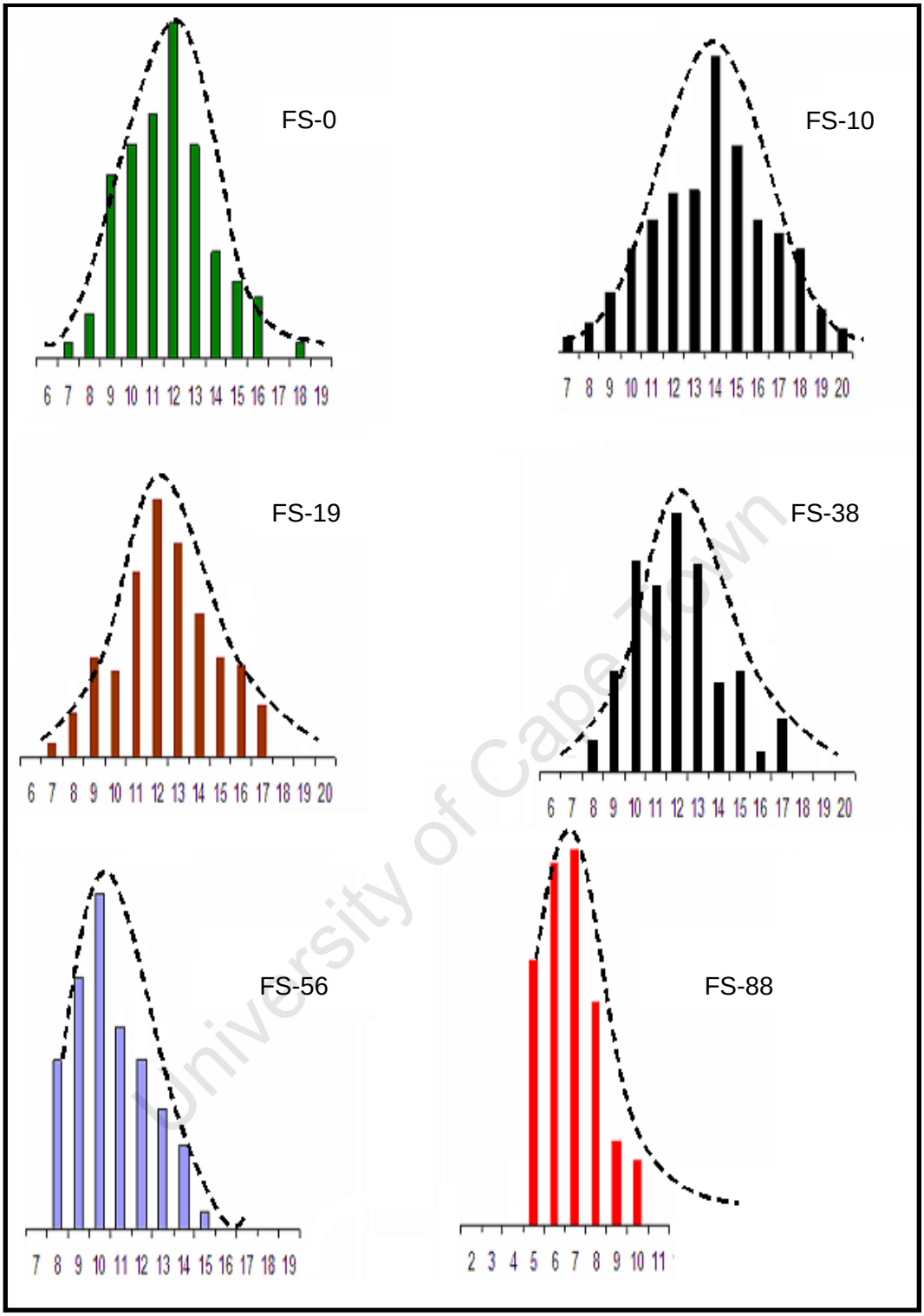




**Figure 6.9:** Crystallite size distribution of the calcined iron oxide nano-crystallites prepared using microemulsion technique and modified with TEOS using instantaneous method (also displayed in broken lines are the types of distributions associated with each histogram).

The crystallite size distributions, displayed by the histograms, are shown in Figure 6.9. The characterization of the calcined samples also showed different types (shapes) of distributions. The unmodified sample (FS-0) and the sample with the lowest silicon content (FS-10), with standard deviations of 23% and 32% respectively, showed normal distributions, i.e. the highest concentrations of the measured crystallites are centered on the mean value. Samples FS-19 and FS-38 showed the same type of distribution but with a narrower mean deviation of ca.18%. On the other hand, the crystallite size distribution for samples with higher silicon content (FS-56 and FS-88) showed a log-normal distribution, i.e. the majority of the crystallites that were measured were small and concentrated around the mean value while the frequency of the larger crystallites decreased with increasing size. The histograms also indicate that the distribution of the highly modified catalysts is very narrow with standard deviations of ca. 15 %. Thus, it may be concluded that with increasing TEOS loading, the concentration of smaller crystallites in the samples increases.

### 6.2.3 XRD analysis of TEOS modified calcined samples

XRD characterization was performed on the TEOS modified samples to assess the average crystallite sizes the phase compositions (see Figure 6.10)**.** Samples FS-(0 to 38) contain a mixture of maghemite (γ-$Fe_2O_3$) and hematite (α-$Fe_2O_3$), indentified using reference patterns. However, the hematite content appears to decrease with increasing TEOS loading. This is indicated by the disappearance of the major hematite diffraction peak at $2\theta = 33.6^0$. The samples with higher silicon content (FS>38) only contain maghemite. The XRD diffraction patterns also show an increase in peak broadening with increasing TEOS loading (see Figure 6.10), indicating a decrease in the average crystallite size.

The average crystallite diameters and phase composition (determined by Rietveld refinement) are displayed in Table 6.5. Maghemite is the dominant phase in all the analyzed samples. The iron oxide phase content appears to be influenced by the crystallite size rather than TEOS modification. The average crystallite size of the hematite phase appears to be larger than that of the maghemite phase in all catalyst containing a mixture of both phase (FS-0, FS-10, FS-19 and FS-38; see Table 6.5). This result is consistent with the study by Mabaso (2005) who observed that samples with a large average crystallite size consist predominantly of hematite, α-$Fe_2O_3$, whereas small crystallites were mainly present as maghemite, γ-$Fe_2O_3$.

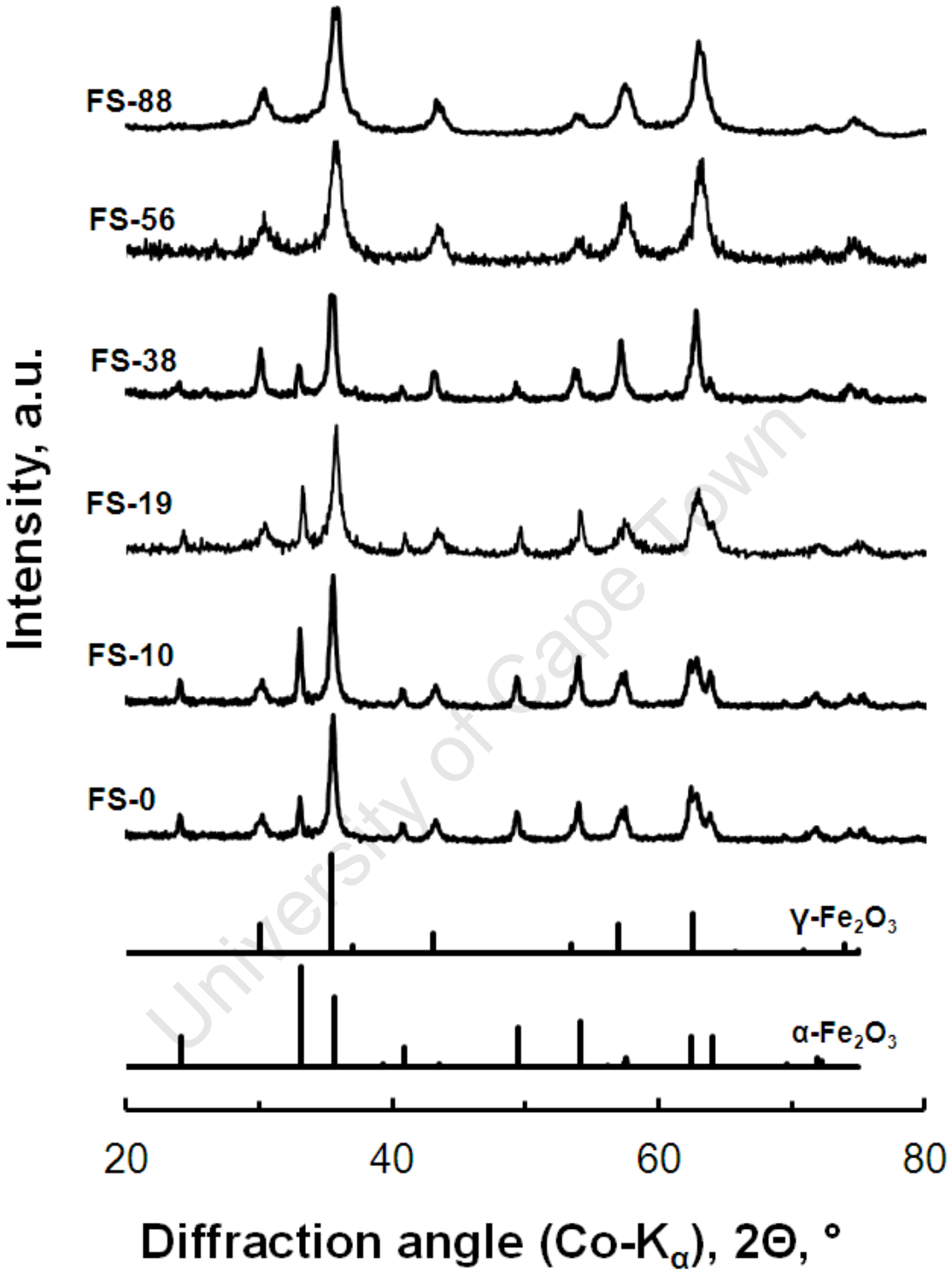


**Figure 6.10:** X-ray diffraction patterns of the calcined TEOS modified catalysts. Also shown are reference patterns of hematite (α-$Fe_2O_3$) and maghemite (γ-$Fe_2O_3$)

The average crystallite sizes of the calcined samples, as determined from both TEM (see Table 6.4) and XRD (see Table 6.5) analysis, are presented in Figure 6.11. TEM results correspond well with XRD analysis for the γ-$Fe_2O_3$ phase. This is expected, since γ-$Fe_2O_3$ is the dominant phase in all analyzed samples. The average crystallite diameter passes a maximum as a function of the amount of silicon in the samples. It appears that at lower loading, TEOS assists or promotes agglomeration of the iron oxide resulting in a higher average crystallite diameter. The reason for this behavior is not clear. It might be caused by the nature of the interaction between silicon and iron oxide at low loading. The average crystallite size for samples with higher silicon content (samples FS≥19) decreases with increasing silicon content, reaching a minimum of ca. 7 nm at the highest TEOS loading (FS-88). This represents a 44% decrease in the average crystallite size between the unmodified sample (FS-0; $d_{AVG\_TEM}$ = 12.4 nm) and the sample highest silicon content (FS-88; $d_{AVG\_TEM}$ = 6.9 nm).

Factors known to impact the average size of the crystallites are: preparation method, the use of support material and the calcination temperature. The micro-emulsion technique was used to prepare all catalyst. No support was added and the calcination temperature was constant at 350 $^0$C. With the effects of all these factors eliminated, it is clear, based on XRD and TEM results, that the resulting average crystallite size is affected by the silicon content in the samples.



**Table 6.5:** Average crystallite sizes and the phases present in the TEOS modified samples after calcination at 350 $^0$C (calculated using Rietveld refinement)

| **Component** | **FS-0** | **FS-10** | **FS-19** | **FS-38** | **FS-56** | **FS-88** |
|---|---|---|---|---|---|---|
| **α-$Fe_2O_3$**: content (wt %): | 12 | 24 | 9 | 11 | none | none |
| Size (nm): | 17 | 23 | 15 | 16 | n/a | n/a |
| **γ-$Fe_2O_3$**: content (wt %): | 88 | 76 | 91 | 89 | 100 | 100 |
| Size (nm): | 13 | 16 | 11 | 11 | 9 | 8 |

The decrease in average crystallite size with increasing silicon content observed in this study may be explained by a chemical and by a physical property of the modified surface. The formation of a surface is energetically not favored. In equilibrium the system (crystal or set of crystals) tends to reduce the surface energy by formation of specific crystallite shapes [Wise et al., 2001], by reconstruction of the surface [Titmuss, 1996], or by crystal growth (sintering). The development of Fe-O-Si interaction stabilizes the catalyst [Hou et al., 2008; Qing et al., 2011] by lowering the surface energy and thus minimizing the driving force for sintering during calcination [Dlamini et al., 1997]. Thus, surfaces with increasing Fe-O-Si interaction will have a lower surface energy and be more stable. Hence the average crystallite size would decrease with increasing TEOS loading. Another reason to explain the decrease in crystallite diameter with increasing surface coverage could be that the modification stabilizes the iron oxide by capping the surface of the nanoparticle with the inorganic –O-Si$(OH)_3$ ligands. This behavior promotes the formation of nanoparticles with narrow sizes, which has been proven using organic ligands [Morsy et al., 2009].



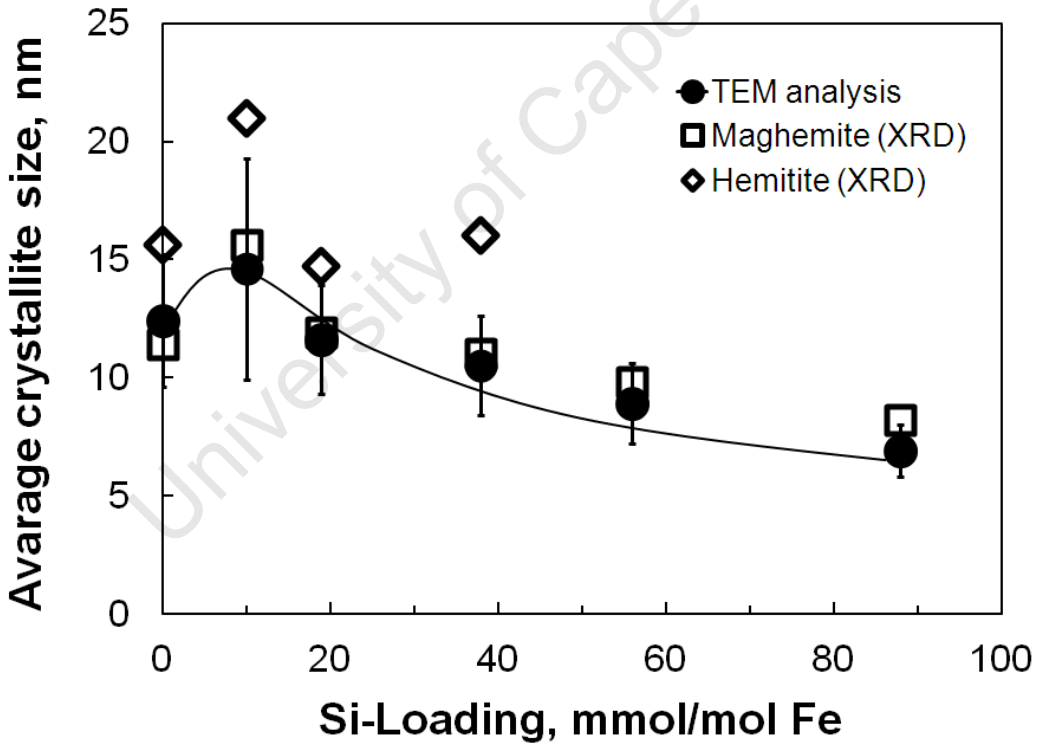


**Figure 6.11:** Average crystallite diameters the of calcined TEOS modified samples obtained using TEM and XRD analysis represented as a function of Si loading

### 6.2.4 Ligand surface Coverage in calcined samples

It might be assumed that Fe-O-Si interactions are only at the surface, since the incompatibility of the two metal (i.e. Fe and Si) cations makes incorporation of the silicon atoms into the iron oxide structure highly unlikely under the preparation conditions [Tauster, 1978]. Surface area available for TEOS attachment was estimated from the crystallite sizes determined using TEM. Then, the total number of Fe surface atoms was calculated from the surface area of maghemite (assuming a surface density of 4.80 Fe/nm$^2$ for γ-$Fe_2O_3$ (110)). EDX data was used to determine the Si content in every sample, and then surface ratio (the ratio of the total iron surface atoms to total silicon atoms) was plotted against Si-loading (see Figure 6.12).

The surface ratio decreased with increasing TEOS loading. The sample with lowest silicon content (FS-10) shows a ratio of 1 Si atom for every 8 Fe surface atoms. With increasing Si loading the ratio drops until it reaches a ratio of 2 Fe surface atoms for every Si atom present in the sample at the highest TEOS loading (FS-88). It can thus be estimated that a surface coverage of between ca. 12-50 %, which is increasing with silicon content in the samples, is achieved during TEOS modification.



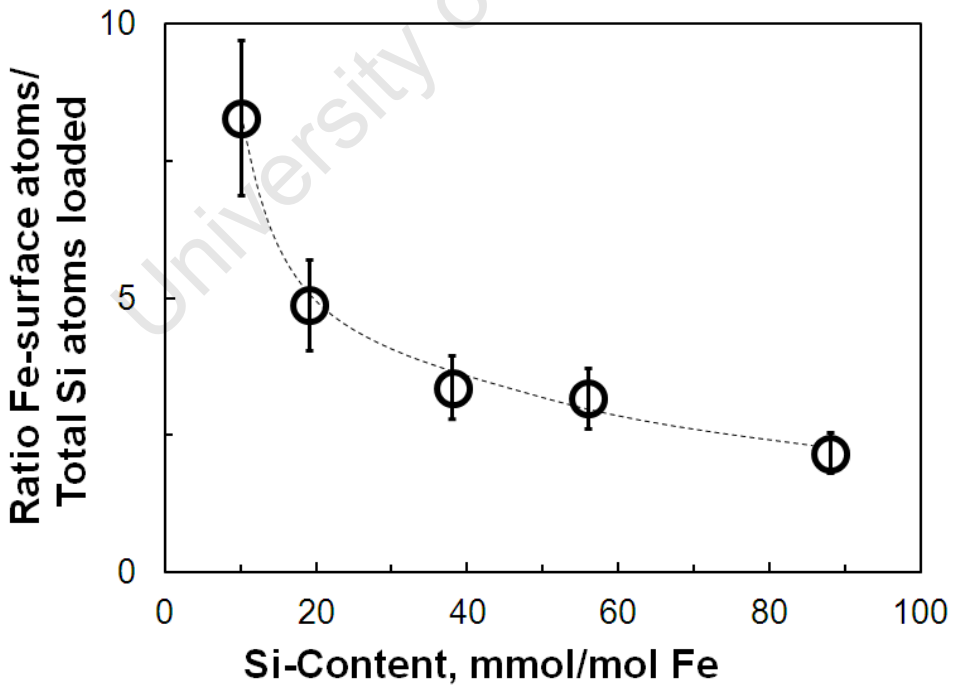


**Figure 6.12:** Calculated Si surface coverage based on the crystallite sizes of the iron oxide from TEM analysis and Si contents (EDX) together with FTIR information (ensuring surface interaction)

## 6.2.5 Reduction behaviour of TEOS modified calcined samples

### 6.2.5.1 $H_2$-TPR analysis

The reduction behavior of the TEOS modified calcined samples was analyzed using Temperature Programmed Reduction (TPR) in a 5% (v/v) hydrogen/argon mixture (see Figure 6.13)**.** Based on the TPR profiles, the hydrogen consumed during reduction was calculated by integrating the area of the curves. The calculated hydrogen consumptions were normalized to the total moles of iron loaded (see Table 6.6). The total $H_2$ consumed during reduction in 5% $H_2$ at 900 $^0$C, per mole of iron in the samples, decreases with increasing TEOS loading, indicating a decrease in the degree of reduction.

The unmodified sample (FS-0) shows two reduction peaks (see Figure 6.13), indicating the two steps reduction process of $Fe_2O_3$ to metallic Fe (see Equation 6.1) [Iglesia et al., 1993; Lin et al., 2003]:

$$Fe_2O_3 \rightarrow Fe_3O_4 \rightarrow Fe \qquad (6.1)$$

The hydrogen consumption of the first reduction peak (maximum at ca. 340 $^0$C) was 0.15 mol $H_2$/mol Fe (see Table 6.6), which was the consistent the theoretical value (0.17 mol $H_2$/mol Fe) of the transformation of $Fe_2O_3$ to $Fe_3O_4$ [Hou et al., 2008; Yang et al., 2005]. The second reduction peak (maximum at 580 $^0$C) showed a hydrogen consumption of 1.32 mol $H_2$/mol Fe which also corresponded well with the theoretical value (1.33 mol $H_2$/mol Fe) for the conversion of $Fe_3O_4$ to metallic Fe [Hou et al., 2008; Yang et al., 2005].

The reduction profiles of all the TEOS modified samples show three reduction peaks, indicating an additional reduction step (see Figure 6.13). The appearance of a third reduction peak (ca. 700 $^0$C) is typically observed in the reduction of silica supported iron oxide catalyst and is believed to represent the reduction of FeO to metallic Fe. According to literature [Wan et al.,2006; Hou et al., 2008; Yang et al., 2005; Zhang et al., 2006; Herranz et al., 2006], the $H_2$ reduction of a sample containing Fe-O-Si interactions can be represent by Equation 6.2.

$$Fe_2O_3 \rightarrow Fe_3O_4 \rightarrow FeO \rightarrow Fe \qquad (6.2)$$

The TPR profiles of the TEOS modified samples were divided into three sections each representing a reduction step. The first region [60-440 $^0$C] represents the conversion of $Fe_2O_3$ to $Fe_3O_4$. The second region [440-610 $^0$C] represents the reduction of $Fe_3O_4$ to FeO and the third region [610-900 $^0$C] shows the conversion of FeO to Fe [Herranz et al., 2006, Yang et al., 2005; Zhang et al., 2006].

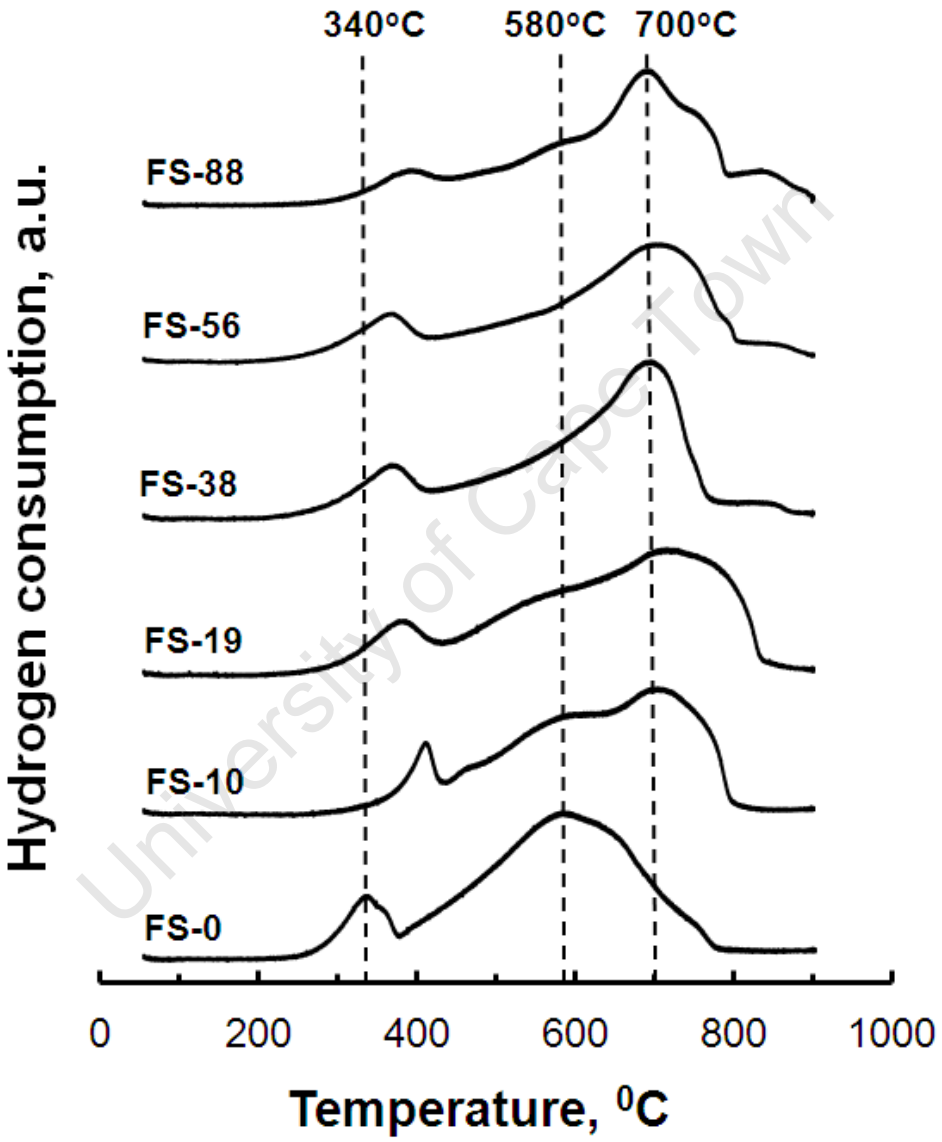


**Figure 6.13:** TPR profiles of the calcined iron oxide nano-crystallites prepared using microemulsion technique and modified with TEOS using instantaneous method.

The hydrogen consumption in the first region [60 - 440$^0$C] decreases with increasing silicon content (see Table 6.6). The existence of Fe-O-Si interactions in a sample has been shown to retard the conversion of $Fe_2O_3$ to $Fe_3O_4$, i.e. the reduction occurs at higher temperatures as compared to unsupported samples [Yang et al., 2005; Zhang et al., 2006]. Therefore, with increasing silicon content this effect would become more severe results in lower hydrogen consumption in this region.

The $H_2$ consumption in the second region [440 – 610 $^0$C] also decreases with increasing silicon content. For samples FS-10 and FS-19, the hydrogen consumption (0.46 and 0.37 mol $H_2$/mol Fe) is higher than the theoretical value (0.33 mol $H_2$/mol Fe) required for the reduction of $Fe_3O_4$ to FeO. The theoretical hydrogen consumption value for the conversion of $Fe_3O_4$ to α-Fe is 1.33 mol $H_2$/mol Fe, indicating that a fraction of the $Fe_3O_4$ is converted directly to α-Fe and thus consuming more $H_2$ than it is required for a complete conversion $Fe_3O_4$ to FeO (see Equation 6.3). The amounts of $H_2$ consumption in the same temperature range for samples FS-38 and FS-56 were similar to the theoretical values associated with a three step reduction process. This shows that with increasing silicon content, the formation of FeO becomes more favored compared to the reduction of $Fe_3O_4$ to α-Fe. Whilst, the $H_2$ consumption for sample FS-88 (0.19 mol $H_2$/mol Fe) was much lower than the theoretical value, indicating that with increasing silicon loading, the overall reduction of the catalysts is hindered.

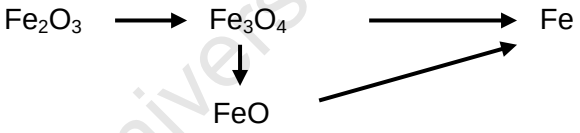


(6.3)

The $H_2$ consumption in the last region [610 – 900 $^0$C] increases with increasing silicon content. This suggests that the FeO content in the samples increases with increasing TEOS loading. There are two possible reasons. Firstly, FeO might be more stabilized with increasing TEOS loading, thus becoming more resistant to reduction (even to temperature as high as 900 $^0$C). Herranz et al. (2006) observed that with increasing $SiO_2$ content in a catalyst, the FeO phase can be stabilized to temperatures as high as 1000 $^0$C. Secondly, given the high reduction temperatures, silicon might get incorporated into the crystal lattice forming irreducible iron silicates.

**Table 6.6:** Quantitative results of $H_2$ consumption for the TEOS modified calcined samples during temperature programmed reduction

| Sample Code: | Hydrogen consumption | | | |
|---|---|---|---|---|
| | Step 1 $Fe_2O_3 \rightarrow Fe_3O_4$ mol $H_2$/mol Fe [60 – 440 $^0$C] | Step 2 $Fe_3O_4 \rightarrow FeO$ mol $H_2$/mol Fe [440 – 610 $^0$C] | Step 3 $FeO \rightarrow Fe$ mol $H_2$/mol Fe [610 – 900 $^0$C] | **Total[a]** $Fe_2O_3 \rightarrow Fe$ mol $H_2$/mol Fe |
| ***Theoretical[b]*** | ***0.17*** | ***0.33*** | ***1.00*** | ***1.50*** |
| **FS-0[c]** | 0.15 | n/a | 1.32 | 1.48 |
| **FS-10** | 0.14 | 0.46 | 0.83 | 1.45 |
| **FS-19** | 0.13 | 0.37 | 0.92 | 1.44 |
| **FS-38** | 0.13 | 0.33 | 0.93 | 1.41 |
| **FS-56** | 0.12 | 0.33 | 0.94 | 1.39 |
| **FS-88** | 0.11 | 0.19 | 1.00 | 1.31 |

*a:The total hydrogen consumed during reduction to 900 $^0$C*

*b: Hou et al., 2008; Yang et al., 2005*

*c: the regions for FS-0 were 60-380$^0$C and 380-900 $^0$C*

### 6.2.5.2 $H_2$ reduction using an in-situ XRD cell for the calcined samples

To investigate the phase transformations of the catalyst during reduction selected samples were reduced in-situ with $H_2$ (40 ml(NTP)/min) at 350 $^0$C (1 $^0$C/min heating rate) for 16 hours (conditions similar to reduction conditions prior to Fischer-Tropsch synthesis) and analyzed using XRD. The samples selected for the analysis were FS-0; to establish a baseline form which deviations could be measured. The other catalyst selected was the sample with the maximum silicon loading, FS-88. The results from the XRD analysis are presented in Figure 6.14.

The reduction process of the unmodified catalyst, FS-0, starts as early as 160 $^0$C with the conversion of $Fe_2O_3$ to $Fe_3O_4$, following which there is coexistence of the two phases. As the temperature increases, the intensity of the diffraction peaks attributed to $Fe_3O_4$ increases at the expense of the $Fe_2O_3$. $Fe_3O_4$ is subsequently converted to metallic Fe. It is important to note that no metallic Fe was formed until all the $Fe_2O_3$ is converted to $Fe_3O_4$. After the reduction process was complete, no diffraction peaks attributed for $Fe_3O_4$ were observed, implying complete reduction. This indicated that the reduction process follows the steps represented by Equation 6.1, and supports the data obtained from the TPR analysis

The first reduction step of the TEOS modified sample is the reduction of $Fe_2O_3$ to $Fe_3O_4$. Subsequently, at a temperature of ca. 325 $^o$C both FeO and α-Fe are formed in an apparently parallel process. It should be noted that the transformation of magnetite is not severely hindered by the modification of the sample with TEOS. However, silicon in the sample stabilizes the FeO phase at temperatures substantial below its critical temperature for disproportionation of wüstite into magnetite and metallic iron (570 $^0$C). The disproportionation of FeO (4 FeO → $Fe_3O_4$ + Fe) is kinetically feasible at temperatures higher than 150 $^0$C in hydrogen containing atmospheres, and at temperatures higher than 200 $^0$C in inert atmospheres [Jozwaik et al., 2007]. The silicon-containing samples were left at 350 $^0$C for 16 hours in hydrogen. It must thus be concluded that the disproportionation is either severely kinetically hindered by the silicon modification or that the ligands introduced by the silicon modification lower the surface energy of nano-sized FeO and thus rendering the disproportionation into magnetite and α-Fe thermodynamically no longer allowed.

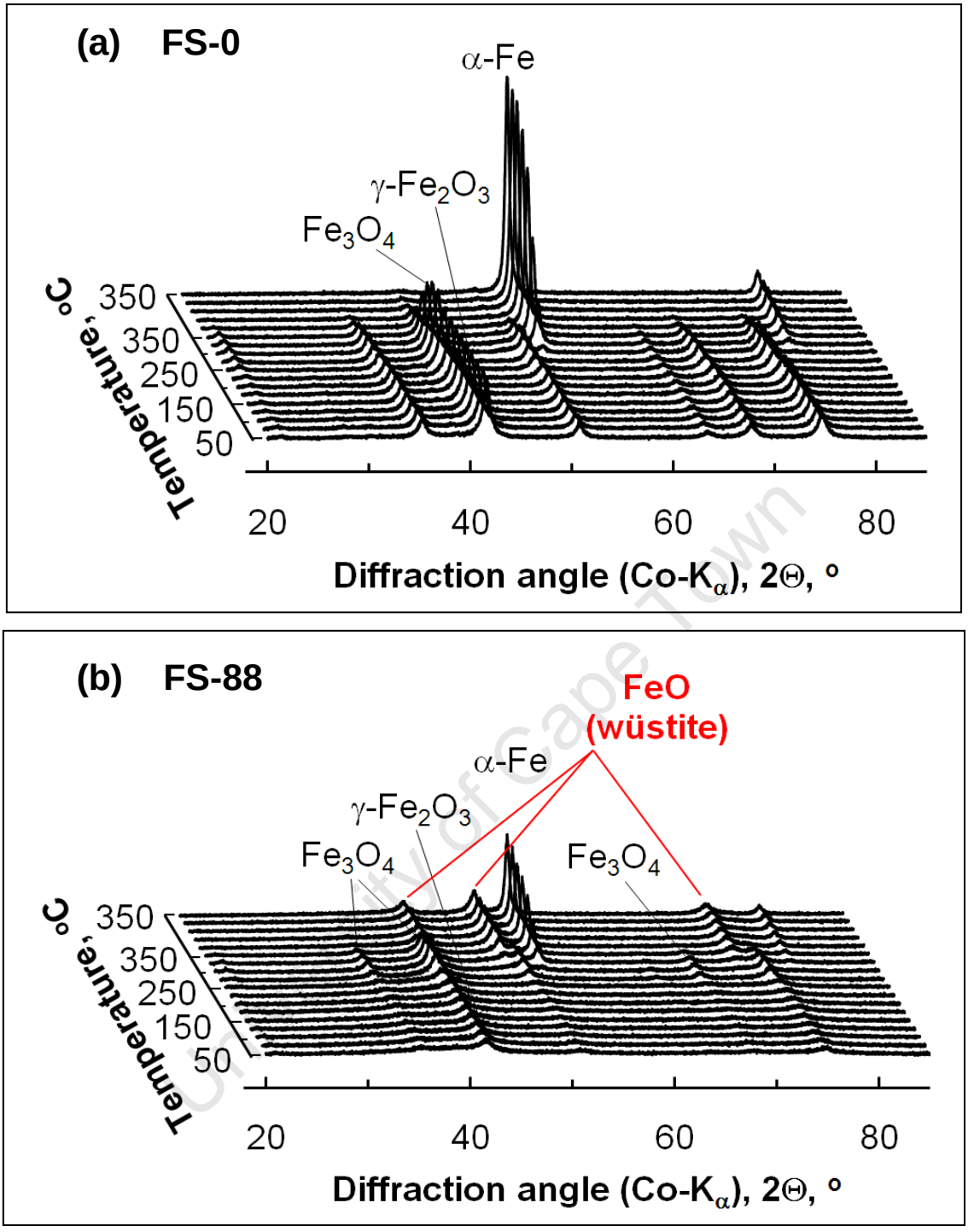




**Figure 6.14:** In-situ XRD analysis of the phase transformations occurring during $H_2$ reduction of TEOS modified samples at 350 $^0$C (1 $^0$C/min heating rate) for 16 hours

(a) Reduction analysis of unmodified sample, FS-0

(b) Analysis of sample with highest TEOS loading, FS-88

## 6.2.6 Analysis of the reduced TEOS modified samples

### 6.2.6.1 $H_2$-TPR analysis

To investigate the degree of reduction, the calcined catalysts were reduced with $H_2$ (40 ml(NTP)/min) at 350 $^0$C (1 $^0$C/min heating rate) for 16 hours (conditions similar to reduction conditions prior to Fischer-Tropsch synthesis). Following the reduction, the temperature was dropped to 100 $^0$C. The samples were then reduced in a hydrogen/argon mixture using a temperature program. The TPR profiles were divided into three section: The first region [60-500 $^0$C], the second [500-680 $^0$C] and third region [680-900 $^0$C] (see Figure 6.15). The degree of reduction was calculated by relating the moles of Fe loaded to the theoretical hydrogen consumption required for total reduction. Thus every mole of $H_2$ that is consumed during TPR analyses can be related to a mole of Fe that is not reduced during reduction at 350 $^0$C for 16 hours. After reduction, the unmodified sample does not contain any $Fe_2O_3$, as indicated by the in situ XRD analysis (see Section 6.2.5.2). Thus, the reduction peak presented by sample FS-0 (see Figure 6.15) can be assigned to the conversion of residual $Fe_3O_4$ to metallic Fe. The $H_2$ consumption calculated for this region (0.13 mol $H_2$/mol Fe) compared to the theoretical value of 1.33 mol $H_2$/mol Fe indicates that only small amounts of $Fe_3O_4$ are present after reduction (see Table 6.7).

The catalyst with the lowest silicon content (FS-10) showed a one broad peak which starting at 280 $^0$C. Since there was no clear separation between the reduction steps no clear conclusion can be made about the reduction of this sample. It is possible to assign this peak to the overlapping effect of the transition of the remaining $Fe_3O_4$ to α-Fe and FeO which would occur at temperatures below 680 $^0$C, coupled with the transformation of FeO, which is then harder to reduce, to α-Fe, resulting in the broad peak reaching 780 $^0$C. At higher TEOS loading (FS-19 till FS-88) the reduction patterns can be divided into three stages. In the first region [60 to 500 $^0$C], the hydrogen consumption for sample FS-19 (0.19 mol $H_2$/mol Fe) was higher than the theoretical for the conversion of $Fe_2O_3$ to $Fe_3O_4$ (0.17 mol $H_2$/mol Fe). Moreover no $Fe_2O_3$ is expected to be present since the catalysts were pre-reduced at 350 $^0$C for 16 hours. Therefore, the first peak can be assigned to the conversion of a fraction of $Fe_3O_4$ directly to metallic Fe. This is supported by the reduction behavior of the unmodified catalyst (FS-0) that indicates that this reduction step occurs in this region. Furthermore, the $H_2$ consumption in this region decreases with increasing TEOS modification, similar to the calcined samples (see section 6.2.5.1).

The second region [500 and 680 $^0$C] may indicate the conversion of the remaining $Fe_3O_4$ to α-Fe and FeO. The hydrogen consumption in this region decreases with increasing TEOS loading. The direct conversion of conversion of $Fe_3O_4$ to Fe requires more hydrogen (1.33

mol $H_2$/mol Fe) than the conversion of $Fe_3O_4$ to Fe (0.33 mol $H_2$/mol Fe). The decrease in this value might indicate that the formation of FeO is preference for with increasing TEOS loading. This is also observed with $H_2$-TPR of the calcined samples (see section 6.2.5.1).

The final region, representing $H_2$-comsumption at temperatures greater than 680 $^0$C, can be assigned to the conversion of FeO to Fe [Wan et al.,2006; Hou et al., 2008; Yang et al., 2005; Zhang et al., 2006; Herranz et al., 2006]. The $H_2$ consumption in this region increases with increasing TEOS modification. This is consistent with the increased stabilization of FeO that is brought about by Fe-O-Si interactions [Wan et al.,2006; Hou et al., 2008; Yang et al., 2005; Zhang et al., 2006; Herranz et al., 2006] and explains the observed decrease on the degree of reduction observed with increasing TEOS loading (see Table 6.7).

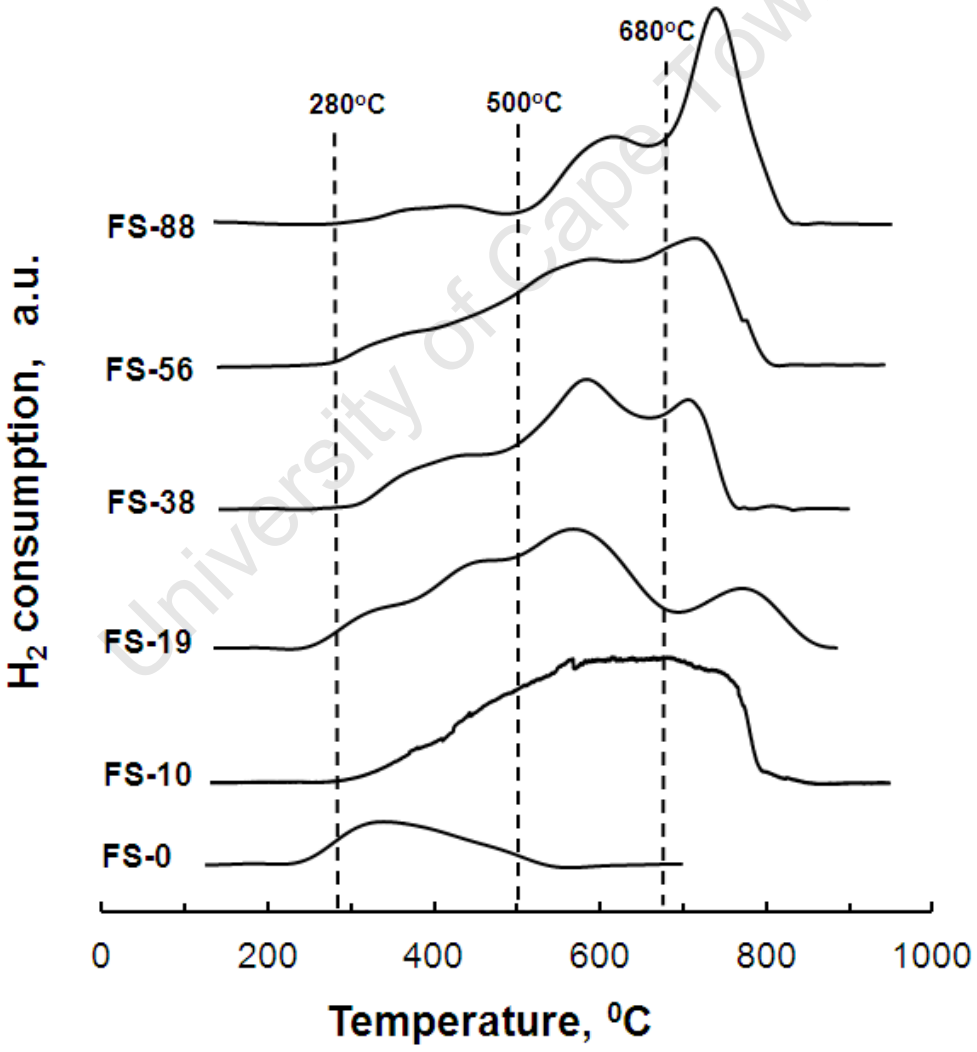


**Figure 6.15:** TPR profiles of the TEOS modified samples after reduction in $H_2$ (40 ml (NTP)/min) at 350 $^0$C (heating rate 1 $^0$C) for 16 hours

**Table 6.7:** Quantitative results of $H_2$ consumption for the pre-reduced (at 350 $^0$C for 16 hours) TEOS modified samples

| Sample Code: | Hydrogen consumption | | | |
|---|---|---|---|---|
| | Step 1 [60-500$^0$C] mol $H_2$/mol Fe | Step 2 [500-680$^0$C] mol $H_2$/mol Fe | Step 3 [680-900$^0$C] mol $H_2$/mol Fe | **Degree of reduction (%)** |
| **FS-0**[a] | 0.13 | 0 | 0.0 | **91** |
| **FS-10**[b] | n/a | n/a | 0.44 | **70** |
| **FS-19** | 0.19 | 0.31 | 0.15 | **66** |
| **FS-38** | 0.11 | 0.24 | 0.22 | **61** |
| **FS-56** | 0.08 | 0.27 | 0.28 | **61** |
| **FS-88** | 0.03 | 0.27 | 0.35 | **58** |

*a: the regions for FS-0 were 0-580$^0$C*

*b: The peaks could not be separated: only the total consumption is given*



### 6.2.6.2 Phase analysis of $H_2$ reduced samples using XRD

The $H_2$ reduced, TEOS modified samples, were analyzed using XRD to determine the phase composition and crystallite size of the samples prior Fischer-Tropsch synthesis (see Figure 6.16 and Table 6.8). After reduction, the samples were passivated in 20 ml (NTP)/min of $CO_2$ for three hours prior to analysis. The unmodified sample only contained α-Fe whilst the TEOS modified samples also contain FeO (with the exception of sample FS-10 which shows small amounts of contained $Fe_3O_4$).With increasing amount of tetra ethoxy-silane added to the sample, the amount of metallic iron and the average crystallite size decreases. The average crystallite size of α-Fe is much larger than the original hematite/maghemite crystallite sizes implying severe sintering during the $H_2$-activation step. However, the sintering process is somewhat impeded for the samples containing silicon. This might be ascribed to the physical separation of the metallic iron crystallites due to the presence of the oxide phase.

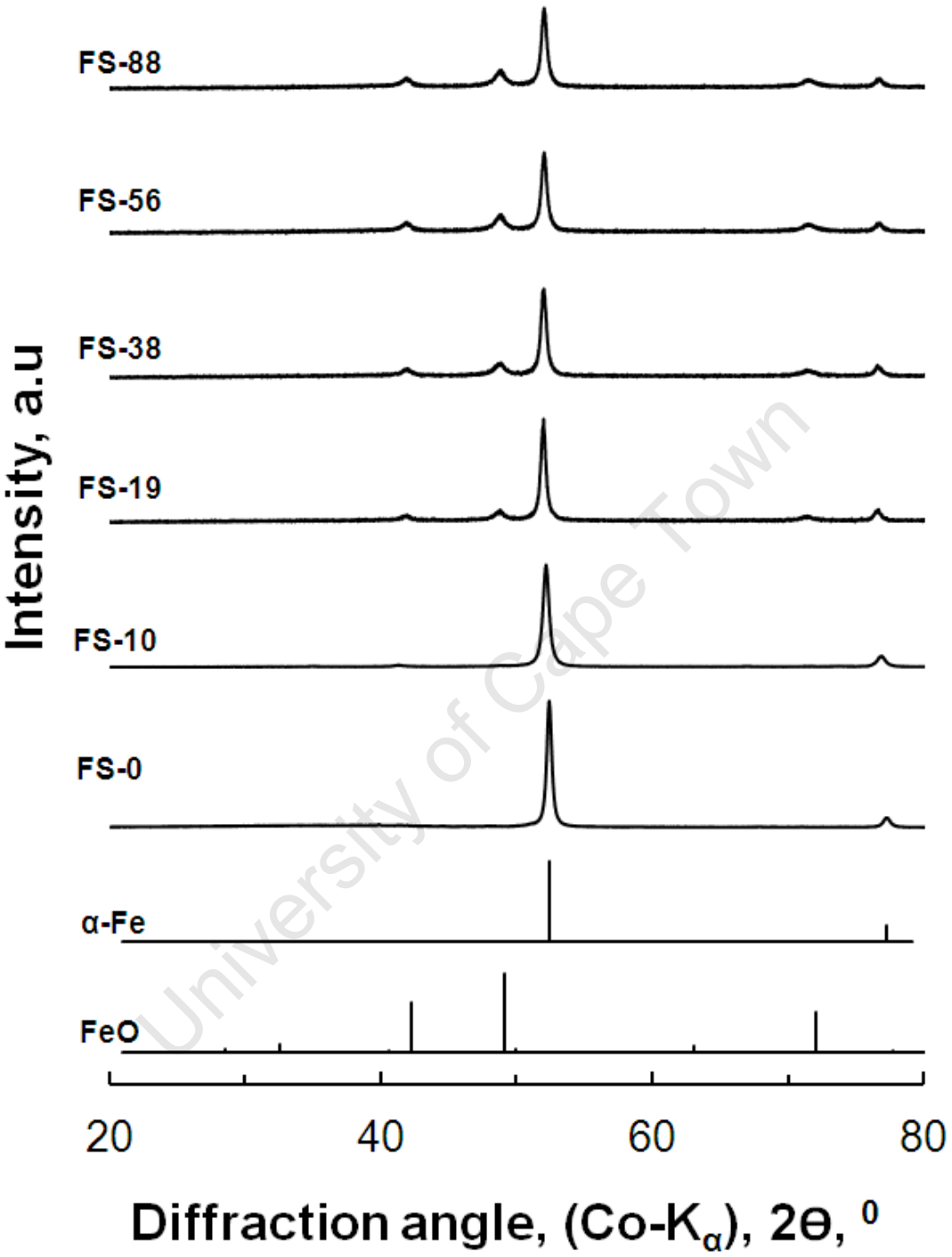




**Figure 6.16:** XRD analysis of the TEOS modified samples after reduction in $H_2$ (40 ml (NTP)/min) at 350 $^0$C (heating rate 1 $^0$C) for 16 hours (samples were passivated in $CO_2$ prior to analysis)

The relative amount of iron oxide in the sample increases with increasing silicon loading showing that the silicon modification leads to a retardation of the reduction process. The resulting crystallite sizes of the iron oxide phases decrease with increasing silicon content and correlate reasonably with the average crystallite size of maghemite in the original sample, taking the size reduction due to oxygen removal into account. This implies that the iron oxide phases are residuals of individual maghemite crystallites in the original sample. If all silicon is associated with the iron oxide phases, the ratio of silicon to surface iron for the samples containing FeO as the iron oxide phase is ca. 1.20 ± 0.06 (assuming an surface iron density of 10.7 Fe/nm$^2$ for FeO(100)), which can be taken as an indication that the wüstite crystallites can be fully covered with surface silicate structures (in addition to possibly some amorphous silica).

**Table 6.8:** Average crystallite sizes (in nm) and the phase quantitative analysis of the $H_2$ reduced (at 350 $^0$C for 16 hours) catalyst, estimated using Rietveld refinement

| Component | **FS-0** | **FS-10** | **FS-19** | **FS-38** | **FS-56** | **FS-88** |
|---|---|---|---|---|---|---|
| **α-Fe**: content (wt %): | 100 | 94 | 81 | 69 | 61 | 52 |
| Size (nm): | 39 | 33 | 30 | 31 | 29 | 27 |
| **$Fe_3O_4$**: content (wt %): | none | 6 | none | none | none | none |
| Size (nm): | n/a | 10 | n/a | n/a | n/a | n/a |
| **FeO**: content (wt %): | none | none | 19 | 31 | 39 | 48 |
| Size (nm): | n/a | n/a | 12 | 10 | 11 | 7 |

### 6.2.6.3 IR analysis of $H_2$ reduced samples

IR analysis was done on the TEOS modified catalysts after reduction in $H_2$ (40 ml (NTP)/min) at 350 $^0$C (heating rate 1 $^0$C) for 16 hours. The catalysts were reduced ex-situ and then passivated with 20 ml (NTP)/min $CO_2$ for 2 hours at 30 $^0$C prior to being analyzed using DRIFTS mode (see Figure 6.17). The presence of the Fe-O stretching is represented by the absorption band at 590 $cm^{-1}$. This also represents the presence of partially reduced iron oxide [Bruce et al., 2004]. The intensity of this peak increases with increasing TEOS loading showing an increase in the Fe-O content in the reduced catalyst. This is in agreement with the XRD analysis of the reduced samples which also showed an increase in the FeO content with increasing TEOS loadings (see Section 6.2.5.2). The bands at 3420 $cm^{-1}$ and 1620 $cm^{-1}$ are due to the presences of absorbed water [Darezereshki, 2011, Walters, 2006].

With increasing silicon loading, an adsorption band at ca. 900 $cm^{-1}$ starts to become more intense. This might be ascribed to the Fe-O-Si stretching frequency, with iron incorporated in different iron oxide phases. The Fe-O-Si stretching with Fe incorporated into $Fe_2O_3$ yields an adsorption band at 940-952 $cm^{-1}$ [Qing et al., 2011; Yang et al., 2008; Swedlund et al., 2009]. A lowering in the oxidation state of iron will result in a shift in the Fe-O-Si stretch toward lower frequency. The adsorption band becomes wider with increasing silicon loading, possibly due to Si-O-H stretch in isolated silanol groups [Morrow and McFarlan, 1992]. The typical adsorption band for the asymmetric Si-O-Si vibration at ca. 1120 $cm^{-1}$ [Qing et al., 2011] is absent implying that at even after reduction at most a minimal amount of cross-linked silica is present. Hence, it can be concluded that silicon is still (mostly) present as surface ligands possibly attached to the remaining iron oxide phase in the sample.

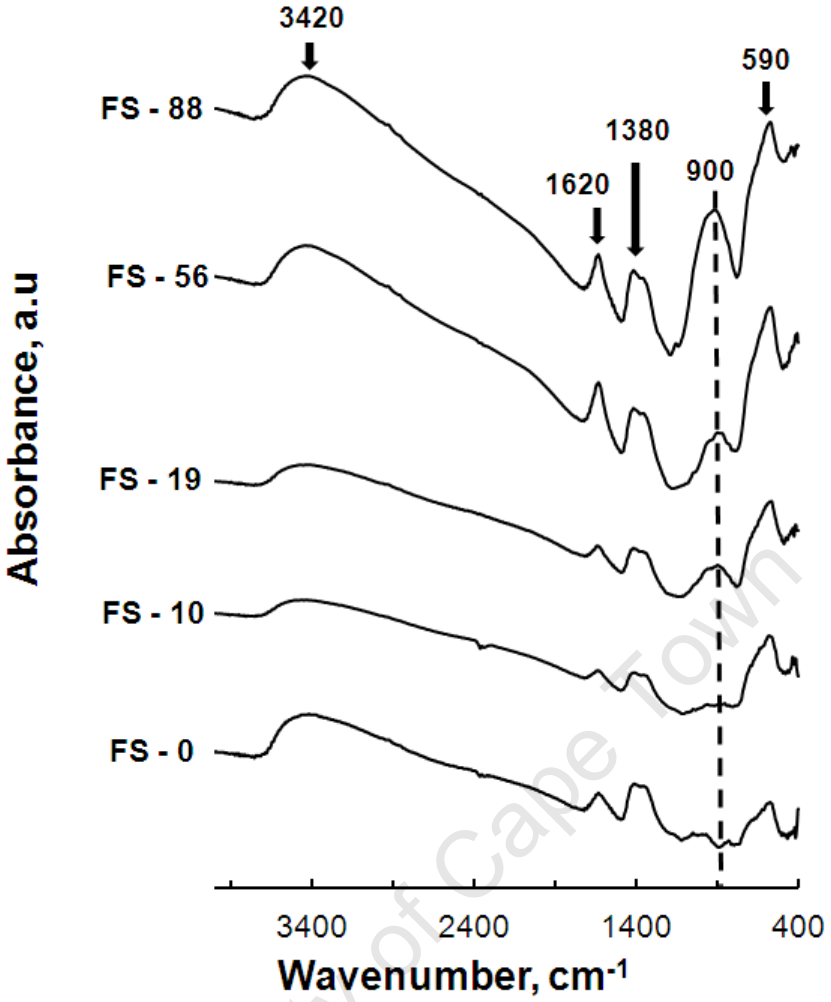


**Figure 6.17:** FTIR analysis of the $CO_2$ passivated TEOS modified samples after reduction in $H_2$ (40 ml (NTP)/min) at 350 $^0$C (heating rate 1 $^0$C) for 16 hours



## 6.2.7 Characterization of spent catalyst

### 6.2.7.1 XRD analysis of spent catalysts

After the Fischer-Tropsch synthesis, the catalysts were passivated in 20 ml (NTP)/min of $CO_2$ for 3 hours. Following that the samples were recovered and separated from the silica carbide using a 100 um sieve. The recovered spent catalyst was then analyzed using XRD (see Figure 6.18). The mass content and the crystallite sizes of the iron containing phases present were calculated using Rietveld refinement are shown on Table 6.9 (all the other phases present, i.e. SiC, wax and graphite, were left out).

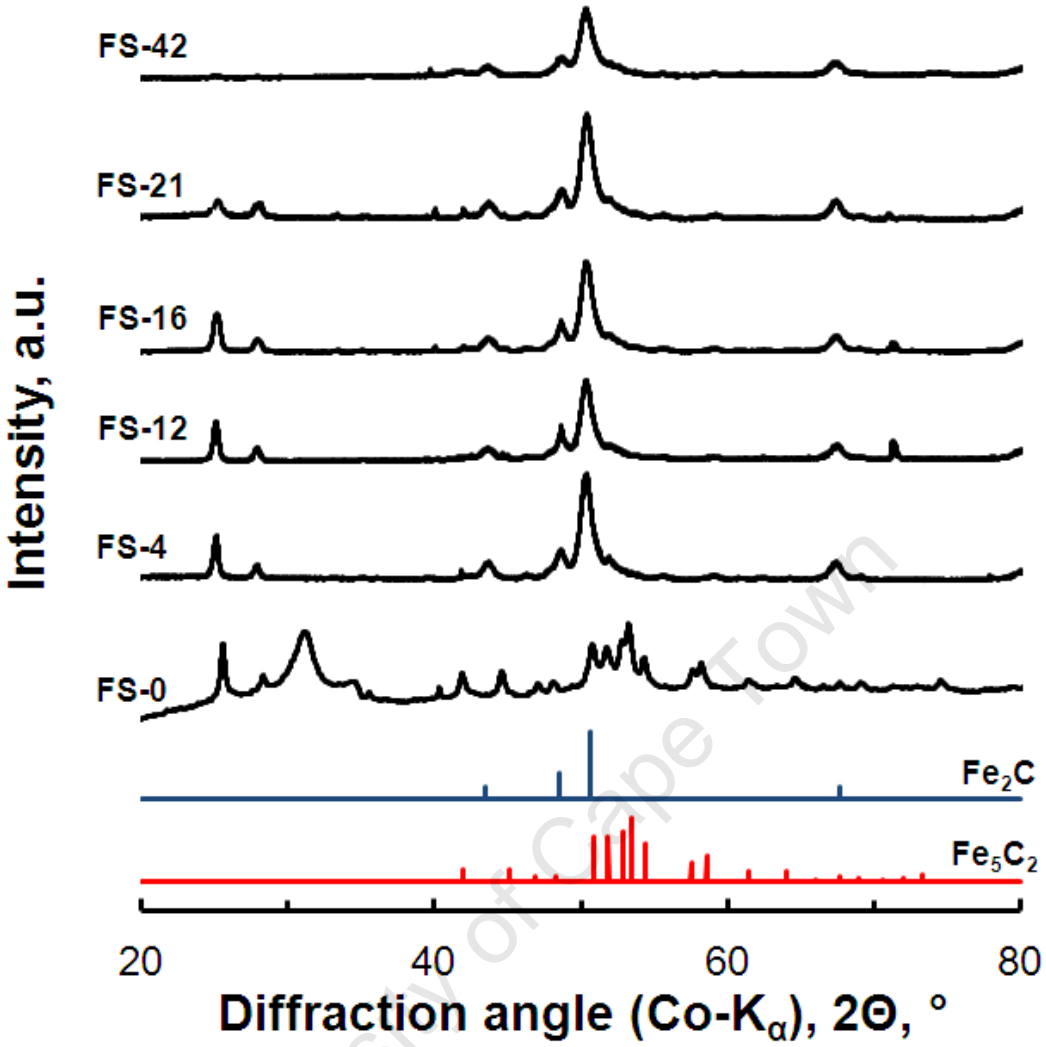


**Figure 6.18:** X-ray diffraction patterns of the spent samples of the TEOS modified catalysts after 24 hours time on stream. (Also shown are reference patterns of $Fe_2C$ and $Fe_5C_2$).

A zero background sample holder was used since only small amounts, 40 to 60 mg, of the spent catalyst was recovered. When the catalysts were removed from the reactor the volume of the unmodified sample, FS-0, appeared to be larger than all the TEOS modified samples. The recovered catalyst, FS-0, was much darker, fluffier and was 1.2 times the mass that was loaded in the reactor, indicating the formation of free carbon (graphite). This was confirmed by the high intensity of the graphite peak at $2\Theta = 30^0$ which was observed for this catalyst (see Figure 6.18). Carbon formation was not observed for the TEOS modified catalysts (FS-10 till FS-88). The results from the XRD analysis also revealed a residue of long chain hydrocarbons (wax), found on the spent catalyst after Fischer-Tropsch synthesis. This is shown by the two diffraction peaks at diffraction angles $2\Theta$ between 20 and $30^0$. However, the intensity of these peaks decreases with increasing

TEOS loadings. This indicates that less wax is generated when the catalyst is modified with TEOS.

**Table 6.9:** Average crystallite sizes (in nm) and the phase quantitative analysis of the Fischer-Tropsch spent catalyst after 24 hours time on stream, estimated using Rietveld refinement

| Component | **FS-0** | **FS-10** | **FS-19** | **FS-38** | **FS-56** | **FS-88** |
|---|---|---|---|---|---|---|
| **$Fe_3O_4$**: content (wt %): | none | none | trace | 3 | 7 | 22 |
| Size (nm): | n/a | n/a | n/a | 9 | 9 | 7 |
| **$Fe_5C_2$**: content (wt %): | 100 | 62 | 61 | 59 | 62 | 53 |
| Size (nm): | 13 | 17 | 15 | 14 | 13 | 14 |
| **$Fe_2C$**: content (wt %): | none | 38 | 39 | 37 | 31 | 25 |
| Size (nm): | n/a | 22 | 17 | 22 | 23 | 22 |



**Analysis of the iron oxide phase present in the spent catalysts**

Magnetite was not detected in the spent sample of the unmodified catalysts (FS-0) using XRD analysis. The reduced unmodified catalyst, FS-0, contained pure α-Fe prior to exposure to synthesis gas at reaction conditions (see Section 6.2.6.2). Both the formation of magnetite and iron carbide are thermodynamically feasible at Fischer-Tropsch conditions [Anderson, 1984]. Of the two reactions the formation of iron carbides is thermodynamically and kinetically more favored seeing that the formation of magnetite requires product water, whereas the CO which is required to form carbides is already present in the feed synthesis gas. Thus the formation of magnetite would involve oxidation of the carbides. The oxidation of this carbide by water, as represented by Equation (6.4) and (6.5), was considered.

$$Fe_3C + 5H_2O \leftrightarrow Fe_3O_4 + 5H_2 + CO \qquad K_{PI,eq}(250\,^0C) = 100 \text{ bar} \qquad (6.4)$$

$$Fe_3C + 4H_2O + CO_2 \leftrightarrow Fe_3O_4 + 4H_2 + 2CO \qquad K_{PII,eq}(250\,^0C) = 1.2 \text{ bar} \qquad (6.5)$$

Thermodynamically, the oxidation of the of bulk $Fe_3C$ yielding $Fe_3O_4$ is only feasible is the actual Kp values are smaller than the equilibrium constants; The $K_{PI}$ and $K_{PII}$ of all the Fischer-Tropsch tested catalysts were calculated using the exit stream after 24 hours time on stream. $K_{PI}$ was found to be between $15x10^3$ and $87x10^5$ bar whilst $K_{PII}$ was between $29x10^3$ and $44x10^5$ bar (see Appendix D; Table D.1). These values are much larger than the equilibrium values which implies that oxidation of bulk $Fe_3C$ carbide to $Fe_3O_4$ by product water is not feasible under these conditions. The same considerations would hold true for other carbides since the thermodynamic properties of the various carbides are very similar [de Smit et al, 2010]. This might explain why no magnetite was found in the spent analysis of the unmodified, FS-0, sample.

The analysis of the spent catalysts illustrates improved degree of reduction for all the TEOS modified samples. Moreover, FeO was not found in any for the spent catalysts. This might be due to the presence of water that is generated during Fischer-Tropsch synthesis. Water is known to be an oxidizing agent [Anderson, 1984]. The formation of water during the Fischer-Tropsch synthesis might facilitate the oxidation of FeO to $Fe_3O_4$, which is thermodynamically feasible for the bulk compounds at $P_{H_2}/P_{H_2O} < 890$ (or in the absence of water-gas shift activity at $X_{CO} > 0.2\%$). It was deduced that the original FeO crystallites were fully covered with silicate ligands (vide supra). The average crystallite size of the resulting magnetite crystallites are in accordance with the average crystallite size of the original wüstite crystallites suggesting that the oxidation of wüstite to magnetite occurs without sintering. The silicon cannot be solely associated with the magnetite phase, since the calculated surface coverage, if all silicon was to be associated with the magnetite phase, would result in more than one silicate group being associated with a surface iron in magnetite (assuming a surface density of 9.8 Fe/nm$^2$ for $Fe_3O_4$(111)). CO reduction studies indicated that in the presence of CO, the formation of carbides might be more favored than the reformation of FeO (see Appendix C; Table C.1), which would lead to an increase in the carbide content and a decrease in the oxide phase. An increase in the carbide content would improve the activity of the catalyst. Since the iron oxide phases are believed to be inactive or at least less reactive for Fischer-Tropsch synthesis [Li et al 2002a].

**Analysis of the iron carbides in spent catalysts**

The unmodified sample only contains Hägg carbide ($Fe_5C_2$), whereas the silicon containing catalyst samples also contain hexagonal iron carbide ($Fe_2C$). Hägg carbide is commonly observed as one of the carbide phases in iron-based Fischer-Tropsch catalysts. The molar fraction of iron present as Hägg carbide in the spent catalysts corresponds to the molar fraction of iron present as metallic iron in the reduced catalyst for the catalyst samples with a high silicon content (FS-56 and FS-88) (see Figure 6.19) suggesting that in these samples as well Hägg carbide is formed upon exposing α-Fe to synthesis gas. The molar Fe-content in Hägg carbide is slightly lower than the Fe-content in α-Fe in the corresponding reduced sample for spent samples with a lower Si/Fe-ratio implying that some of α-Fe is transformed into either $Fe_2C$ or $Fe_3O_4$. The average crystallite size of Hägg carbide is, in all cases, substantially smaller than the average crystallite size of the original α-Fe crystallites implying crystallite break-up during carburization due to strain within the crystal introduced by diffusion of carbon into the structure.

Carbides with carbon in trigonal bipyramide interstices (TP-carbides), such as Hägg carbide are enthalpically less stable than carbides octahedral interstices (O-carbides), such as $Fe_2C$ [de Smit et al., 2010]. The formation of $Fe_2C$, or $Fe_{2.2}C$, two phases which are difficult to distinguish by XRD [Bao et al., 2009], can be found in silica-supported systems [Wan et al., 2006; Hou et al., Niemantsverdriet et al., 1980, Amelse et al., 1978]. It seems from our study that a surface modification of the starting iron oxide results in the formation of the enthalpically favored $Fe_2C$. Amelse et al. (1978) reported that the $Fe_2C$ phase is stable up to 400 $^0$C when supported on $SiO_2$. Thus, it might be argued that the surface ligands stabilize the hexagonal carbide further. However, the relatively large size of these carbide crystallites (17-23 nm) would result in a relative small effect of surface modification on the bulk crystal stability. Hence, it is deduced that the formation of $Fe_2C$ is thermodynamically favored and becomes kinetically favored due to a retardation of the carbon diffusing into the iron matrix allowing for sufficient time for lattice expansion leading to formation of O-carbides.

$Fe_2C$ originates, at least for a significant part, from the silicon stabilized FeO phase. The average crystallite size of $Fe_2C$ is larger than the size of the original wüstite phase implying that the transformation is associated with sintering. Hence, the protection of the crystallite by surface silicate ligands must have been lost during the Fischer-Tropsch synthesis. It can be postulated that the product water of the Fischer-Tropsch synthesis may result in hydrolysis of some of the silicate ligands resulting in the formation of amorphous silica. The (partially) naked oxide surface may sinter via condensation between hydroxyl groups [van Steen and Claeys, 2008], which upon carburization yields $Fe_2C$. It might further be argued

that not all silicate groups are removed from the surface, since rapid diffusion of carbon into the oxide structure will lead to Hägg carbide and cementite [Li et al 2002b]. These surface silicate ligands may however, become progressively hydrolysed during the Fischer-Tropsch synthesis.

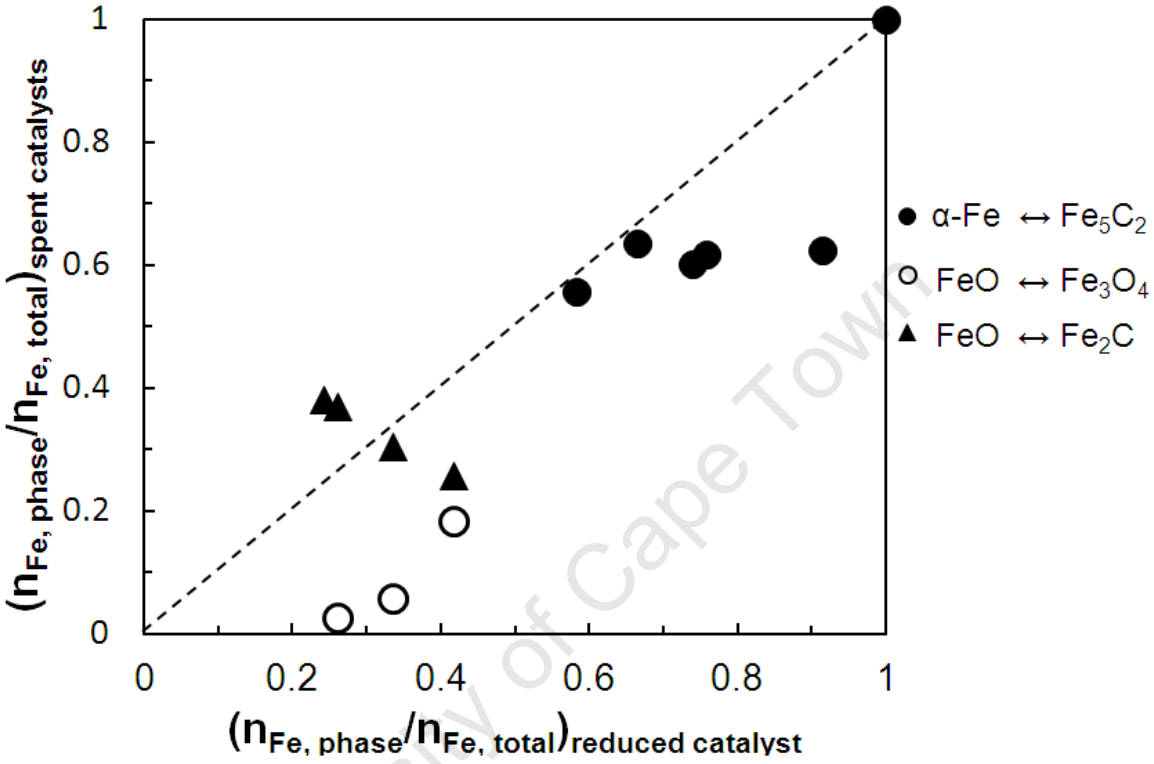




**Figure 6.19:** Correlating the phases present in the reduced catalyst (350 $^0$C, pure hydrogen, 1 atm, SV=400 ml (NTP)/min/g) with the phases present in the catalysts exposed for 24 hours industrially relevant Fischer-Tropsch conditions (250 $^0$C, 20 bar, $(H_2/CO)_{inlet}$ = 2, SV = 600 ml(NTP)/min/g)

### 6.2.7.2 IR analysis of spent catalysts

The recovered spent catalyst was subsequently analyzed using FTIR (transmission mode) spectroscopy to observe if the Si ligands were still present after reaction (see Figure 6.20). The spectra show adsorption bands due to the presence of wax, and the spectra are further complicated due to the presence of amorphous carbon. The spectra for the samples containing silicon do show a feature at ca. 900 $cm^{-1}$, which might be ascribed to silicate groups attached to the carbide phase. The IR-spectrum for the sample FS-88 shows a shoulder at ca. 950 $cm^{-1}$ typically associated with silicate adsorbed on magnetite [Qing et al., 2011; Yang et al., 2008; Swedlund et al., 2009]. Furthermore, an adsorption band at ca.

1025 $cm^{-1}$ starts appearing with increasing silicon loading of the sample, possibly associated with the formation of oligomeric silicate species [Yang et al., 2008]. The presence of amorphous silica is shown by the typical adsorption band for the asymmetric Si-O-Si vibration at ca. 1120 cm-1 [Qing et al., 2011]. The intensity of this peak increases with silicon content thus indicating that an increase in the content of amorphous silica in the samples. Numerically, all silicon modified samples with exception of FS-10 should have some amorphous silica, since the calculated surface coverage of e-Fe2C with silicate ligands would exceed full coverage (assuming a surface iron density of 9.2 Fe/$nm^2$ taking only the top surface Fe-atoms on the ridge of the corrugated $Fe_2C$(111)-surface due to geometric constraints imposed by the silicate ligand and assuming that all $Fe_3O_4$ crystallites are fully covered with silicate ligands). The sample with Si/Fe = 10 mmol/mol would have a coverage of the Fe-atoms on the ridge of the $Fe_2C$(111)-surface of 0.55, if no amorphous silica was formed during the formation of the hexagonal iron carbide phase or the Fischer-Tropsch synthesis.

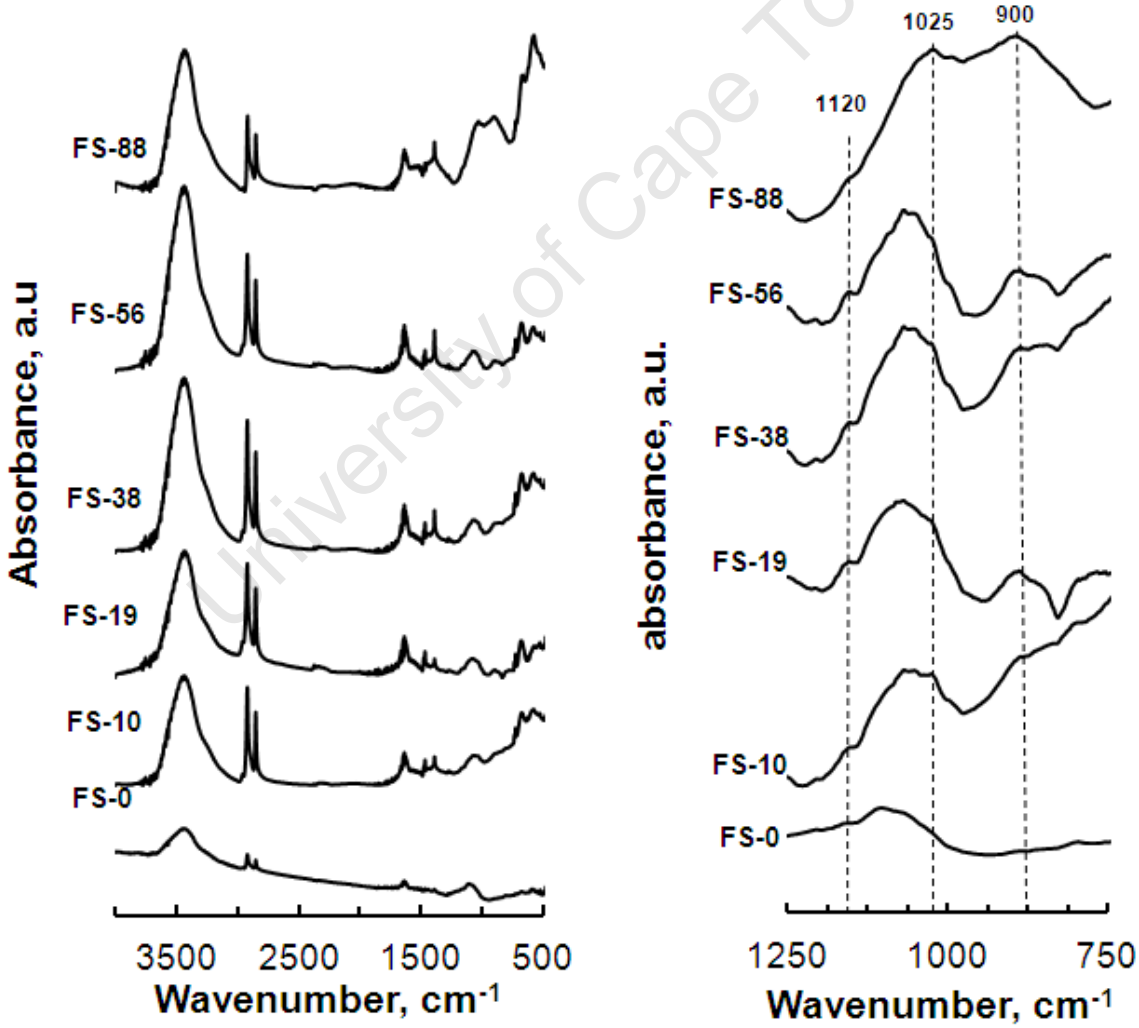




**Figure 6.20:** FTIR analysis of the TEOS modified spent catalysts taken after 24 hours time on stream

## 6.2.8 Fischer-Tropsch synthesis

The Fischer-Tropsch activity of the materials modified by the additions of TEOS were tested in a fixed bed reactor at 250 $^{o}$C, 20 bar and a space velocity for CO, $F_{CO,0}/W$ of 8.2 mmol/(min·g). A total of 0.1 grams of catalyst was distributed over 6 grams of silica carbide. A constant feed gas with a $H_2$ to CO ratio of 2 was passed over the catalyst and the tested for a period of 24 hours. Prior to FT analysis the catalysts were reduced in-situ in 40 ml (NTP)/min $H_2$ at 350 $^{0}$C for 16 hours. The CO-conversion was determined as a function of time on stream (see Figure 6.21).

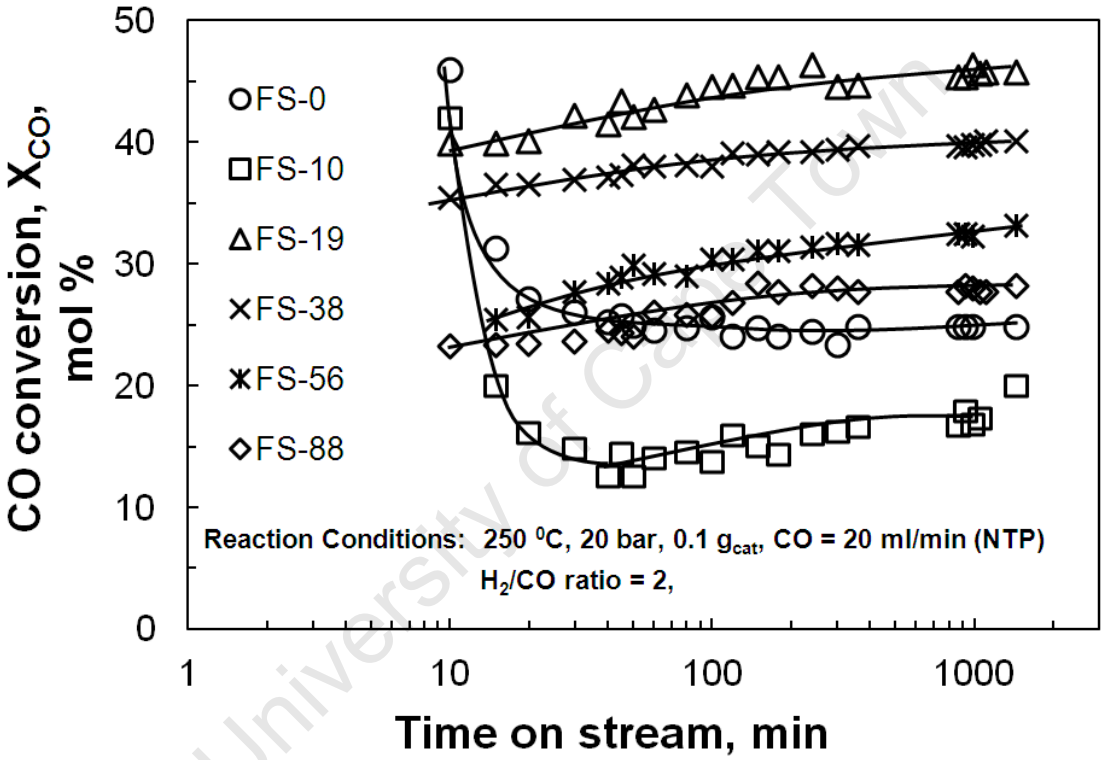


**Figure 6.21:** CO-conversion of TEOS modified catalyst in the Fischer-Tropsch synthesis at 250$^{o}$C, 20 bar, $F_{CO,0}/W$ = 8.2 mmol/(min·g) represented after reduction in $H_2$ (40 ml (NTP)/min) at 350 $^{0}$C for 16 hours.

The unmodified catalyst, FS-0, has high initial activity with $X_{CO}$ = 48 %. Catalyst deactivation was then observed with time on stream for this sample, before the CO-conversion reached steady state at ca. 24 % conversion after ca. 180 min. The same trend was observed for the sample with the lowest silicon content (FS-10), i.e. an initially high CO-conversion of 40 % followed by a decrease of activity with time on stream to a lower, steadier, CO-conversion of ca. 17 %. This observed high initial activity cannot be ascribed

to a residence time behavior (the residence time for the gas was calculated to be 8 minutes and the samples were taken after 15 min time of stream). If the initial decrease in activity was due to residence time, then the effects would be visible on all catalysts since residence time is independent of the chemical nature of the catalyst. However, as indicated in Figure 6.21, the CO-conversion for the samples with higher silicon content, FS-19 to FS-88, did not show this effect. Similar results have been reported by Sou et al. (2012).

The proceeding loss of activity for samples FS-0 and FS-10 could be due to a number of factors. The change to the catalyst due to initial exposure to CO was considered. Catalysts FS-0 and FS-10 showed a degree of reduction of 100% and 94% respectively. The dominant phase in the catalyst prior to reaction is α-Fe. This would then allow these samples to initially have a large amount of FTS sites, which would significantly enhance the adsorption of CO and thus the observed higher initial activity. However, in the case of Fe catalyst, it is well accepted that the carbides are the main active phases for Fischer-Tropsch reaction at steady state [Buker et al., 1995b; Dlamini et al., 2002; de Smit et al., 2010]. Initially there are three possible reaction pathways for the absorbed CO. It may react with α-Fe to form carbides, CO may form carbon through the Boudouard reaction or it may react with the hydrogen, resulting in Fischer-Tropsch products.

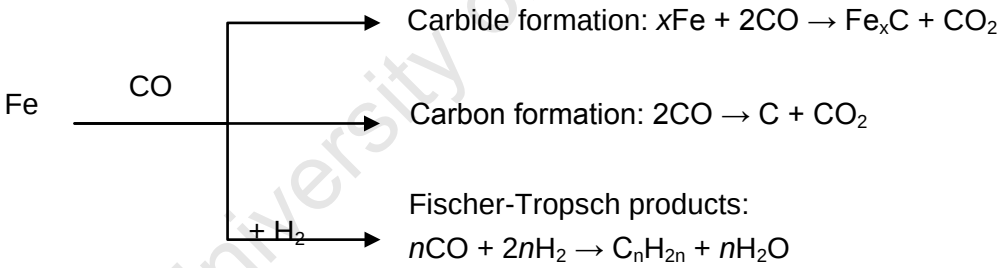


The initial high CO-conversion observed might result from the fast formation of the carbides. This was also indicated by the lower initial activity observed when FS-0 was reduced with CO, where the catalyst would be in carbide form at the start of the reaction (see Appendix C; Figure C.3). Unsupported iron catalyst carburize easier as compared to catalysts that were supported with silica [Wan et al., 2006; Hou et al., 2008]. Therefore, carbide formation might explain the observed deactivation of catalysts FS-0 and FS-10. Furthermore, the formation of free carbon over α-Fe would also results in a loss in 'activity' and thus the deactivation observed for catalysts FS-0 and FS-10. The XRD analysis showed that a larger amount of amorphous carbon was found in the spent catalyst of sample FS-0 (see Section 6.2.7.1) and no carbon was detected for samples with higher TEOS loadings, FS-19 till FS-88.

The samples with higher TEOS loading, FS-19, FS-38, FS-56 and FS-88 show a lower initial activity than the unmodified sample, FS-0 (see Figure 6.21). The low initial α-Fe mass content might result in lower initial CO-conversion. Furthermore, the development of Fe-O-Si interaction in the catalyst might suppress the carburization process [Wan et al., 2006; Hou et al., 2008]. Wan et al. (2006) showed that addition of $SiO_2$ into a Fe-based catalysts suppresses CO adsorption strongly. These findings were consistent with findings from the in-situ XRD analysis of the CO reduction study (see Appendix C) which indicated that the formation of carbides in the TEOS modified samples was delayed, i.e. only started occurring at higher temperatures. This implies that the rate of carbide formation is lower for the TEOS modified samples, resulting in a lower initial CO-conversion since initially less CO will be used for carbide formation. The suppression of CO adsorption is also supported by the analysis of the spent catalyst that indicated carbon formation was suppressed by TEOS addition (see section 6.2.7.1).

The CO-conversion for the higher silica loading catalysts, FS-19, FS-38, FS-56 and FS-88, is stable and even increases slowly with time on stream (see Figure 6.21). This implies that the catalyst becomes more active with time. This might be explained by an increase in the amount of iron associated with the carbide phase. XRD analysis of the reduced samples, FS-19 to FS-88, indicated that between 4 and 41 mol-% of Fe is associated with the oxide phase (see Table 6.8) whereas in the spent catalyst analysis it is reduced to between 0 and 28 mol-% (see Table 6.9). It can be further noted that the increase in the CO-conversion level seems to shift towards longer time on line with decreasing levels of CO-conversion. This might be attributed to a slow three-step transformation process of silicate covered wüstite (FeO) to $Fe_2C$ under the applied Fischer-Tropsch conditions (see Scheme 1), with the first step being the oxidation of wüstite to magnetite by the product water. Furthermore the average crystallite sizes of the iron carbide found in the spent catalyst ($Fe_2C$ = 17-22 nm; $Fe_2C_5$ = 14-15 nm) were smaller than the α-Fe present at the beginning of the Fischer-Tropsch run (27-33 nm). This indicates that the available surface area increases with time on stream and thus might explain the observed increase in activity.

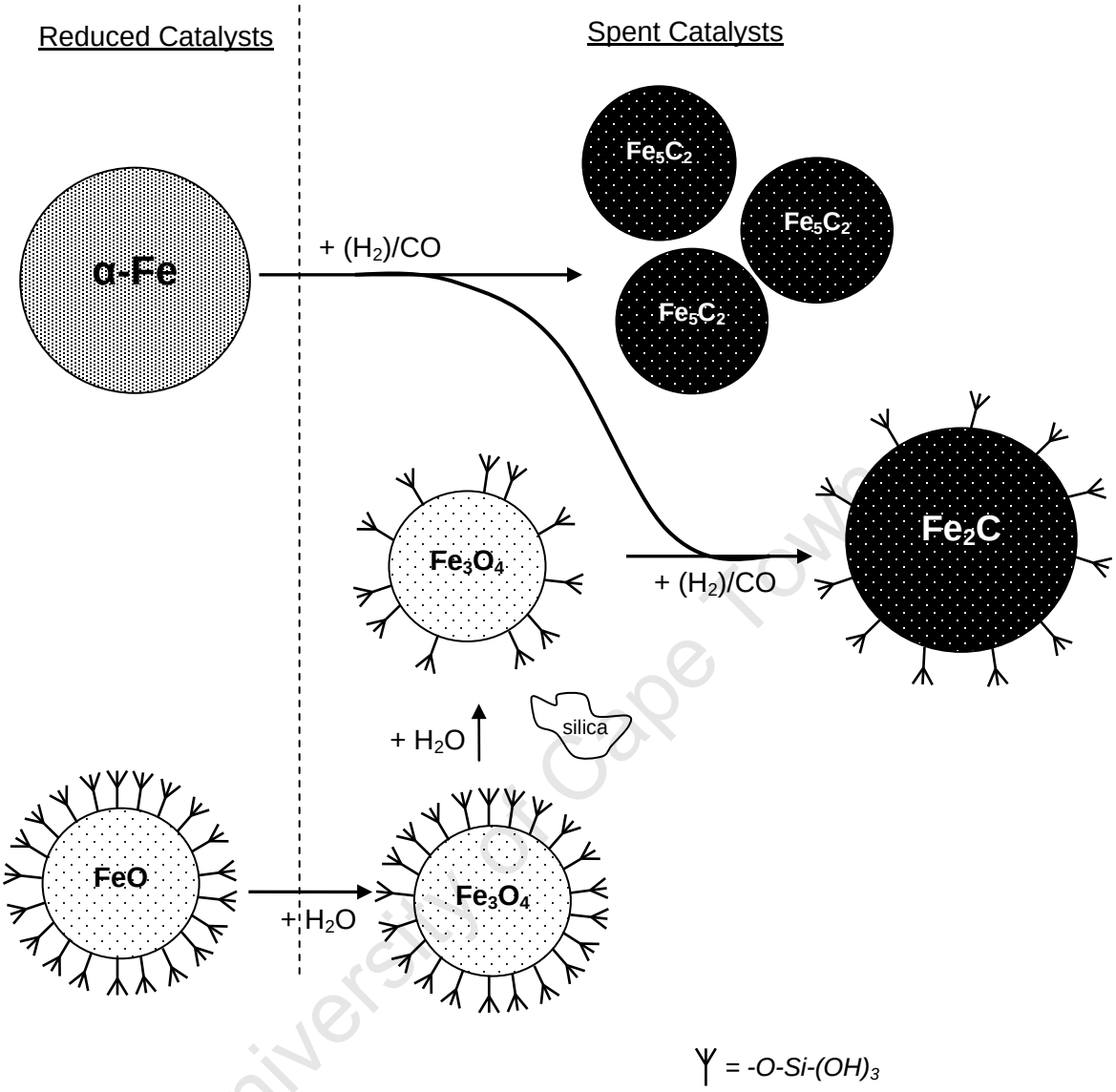


**Scheme 1:** Transformation of $\alpha$-Fe and FeO stabilised by silicate surface ligands during Fischer-Tropsch synthesis

### 6.2.9 $CO_2$ selectivity

The Fischer-Tropsch synthesis requires the removal of oxygen from the surface active for the formation of organic product compounds, leading to the formation of the co-products water or carbon dioxide [van Santen et al., 2011; Krishnamoorthy et al., 2002]. The product water may, in a secondary reaction, react further with CO in the water-gas shift reaction yielding $CO_2$. The latter is typically linked with the presence of magnetite in the catalyst sample [Rao et al., 1995; Newsome, 1980].

Figure 6.22 shows the $CO_2$-selectivity as a function of the silicon loading. The Fischer-Tropsch synthesis over the unmodified catalyst resulted in a very low $CO_2$-selectivity (ca. 3 C-%), whereas the reaction over modified catalysts yielded a $CO_2$-selectivity in the range between 6.5 - 8.5 C-%. The higher $CO_2$ selectivity for sample FS-10 compared to the unmodified sample despite the lower level of CO-conversion may reflect a higher probability of oxygen removal via $CO_2$-formation than via $H_2O$ formation. It is estimated that the probability for oxygen removal as $CO_2$ is ca. 3 % for Hägg carbide and ca. 14 % for $Fe_2C$ to remove oxygen on the surface. The $CO_2$-selectivity for sample FS- 19 is only slightly higher than the selectivity obtained over sample FS-10 despite the significantly higher CO-conversion. This implies a lowering of the probability of O-removal as $CO_2$ neglecting secondary formation of $CO_2$. The $CO_2$-selectivity increases further with increasing silicon content with a concomitant lower CO-conversion. The integral rate of $CO_2$ formation over the samples with high silicon content cannot be linked to the increase in the surface area of $Fe_3O_4$, which increases strongly with increasing silicon content, implying a higher probability of O-removal as $CO_2$ possibly due to the interaction of surface OH-groups or product water with surface silicate groups.

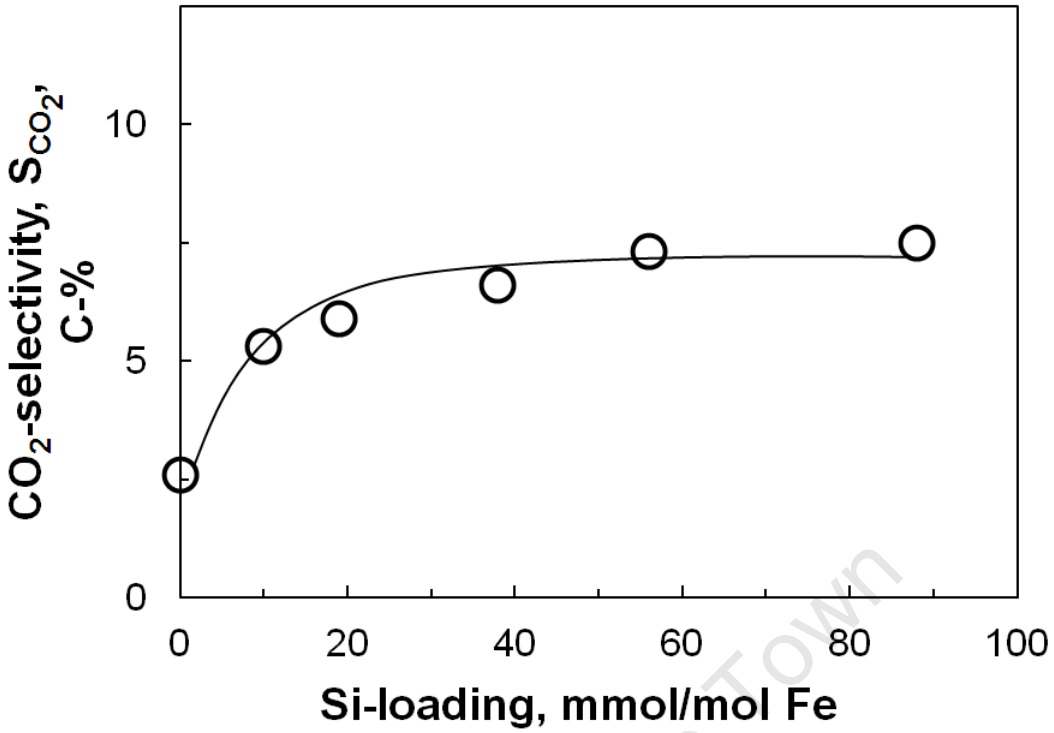


**Figure 6.22:** The steady state Fischer-Tropsch $CO_2$ selectivity of the TEOS modified iron oxide samples taken after 24 hours time on stream represented as a function of Si loading.



## 6.2.10 Selectivity for the formation of organic products

Analyzing product selectivity may give some insight into the surface chemistry on the catalyst. Thus, to obtain a clearer understanding of the effects of TEOS addition to the iron oxide precursor, the organic products were analyzed. All the presented organic product selectivity data was taken after of 24 hours on line. This was done to ensure that steady state conversion was obtained.

**Methane selectivity and chain growth**

The methane selectivity of the TEOS modified catalysts obtained after 24 hours time on stream as a function of Si loading is shown in Figure 6.23. The inhibition of methane formation is considered an essential feature in Fischer-Tropsch synthesis since methane is the least valuable but thermodynamically most favored of the organic products [Schulz, 2003]. Methane is thought to be formed by the interaction methyl species and the surface hydrogen as indicated by the proposed mechanism presented on next page.

Alternatively the methyl species can act as a chain starter and undergo chain growth. Thus the methane selectivity is related to the chain growth probability of a catalyst

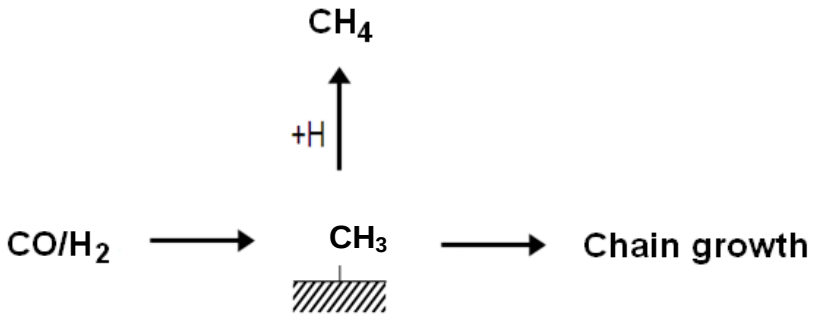


The methane selectivity increases with increasing silicon content. All the TEOS modified samples showed higher methane selectivity as compared to the unmodified sample. The methane selectivity increased from 4 C-% for the unmodified catalyst (FS-0) to about 8 C-% for the highest modification (FS-88). Although the selectivity of the intermediate TEOS loadings, FS-10 till FS-56, was higher than the unmodified catalyst, the change is methane selectivity was still small ranging from 5 C-% till 6 C-%. In commercial processes the methane selectivity is about 4 C-% for low temperature FT synthesis (200 $^0$C – 240$^0$C, 20 – 45 bar) and 8 C-% in high temperature FT synthesis (300 $^0$C – 350$^0$C, 20 – 40 bar) [Dry, 2004a]. From this prospective the methane selectivity obtained in this work for the modified catalysts ranging from 5 C-% to 8 C-% are acceptable. Catalyst crystallite size has been shown to affect methane selectivity but the effects of varying crystallite size on the methane selectivity can be eliminated because previous work has indicated that the methane selectivity remains constant for iron crystallite sizes bigger than 7 nm [Mabaso, 2005]. The analysis of the reduced catalyst showed that the crystal diameter of the metallic Fe found after reduction of the catalyst ranged from 27 nm to 39 nm (see Table 6.8).

Methane selectivity is a complex variable, which is determined by the probability that a surface carbon is transformed into a surface methyl group and the probability that the surface methyl group is hydrogenated yielding methane. Both probabilities increase with increasing hydrogen availability on the surface [Schulz et al., 1994] and hence in methane selectivity increases with increasing higher hydrogen availability on the catalyst surface. The existence of the Fe-O-Si interaction in the catalyst which have previously shown to result in a enhanced hydrogenation properties for the modified catalyst [Hou et al., 2008; Zhang et al., 2006; Wan et al., 2006]. Wan et al. (2006) showed that the addition of $SiO_2$ results in an increase the strength of $H_2$ adsorption whilst having an opposite effect on the adsorption of CO. Hou et al. (2008) also observed higher methane selectivity with high $SiO_2$ addition. This infers that the improved hydrogenation quality of the catalyst might be

due to Fe-O-Si interaction explaining the observed increase in methane selectivity with increasing silicon content (see Figure 6.23).

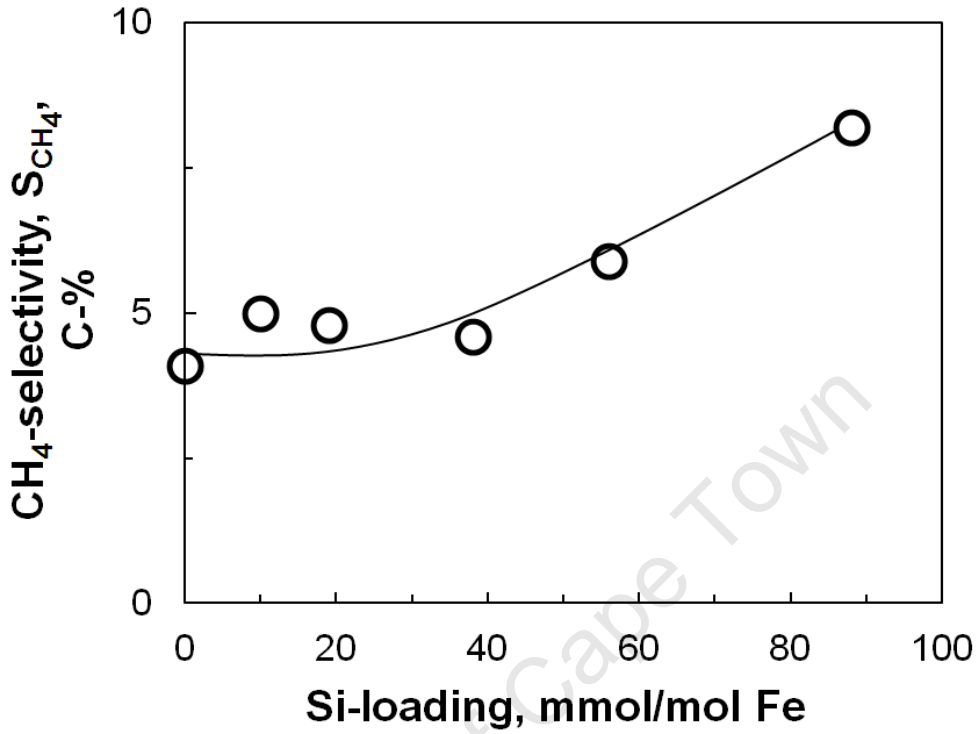


**Figure 6.23:** The steady state Fischer-Tropsch $CH_4$ selectivity of the TEOS modified iron oxide samples taken after 24 hours time on stream represented as a function of Si loading.



**Chain growth probability (α)**

The chain growth probability gives an indication to the inhibition of product desorption in Fischer-Tropsch synthesis allowing for chain growth. A high probability is more desired since long chain hydrocarbons product compounds are formed [Schulz, 2003]. The chain growth probability (calculated between $C_3$ – $C_8$ using the Anderson-Schulz-Flory equation, see Appendix A) of the prepared samples as a function of silicon loading are presented in Figure 6.24. The chain growth probability shows, as expected, an inverse relationship with the methane selectivity, i.e. the growth probability decreases with increasing TEOS loading. The chain growth probability over the pure iron oxide sample,FS-0, was 63% and with increasing Si loading the growth probability decreased to a minimum of 57% for the sample with the highest silicon content, FS-88.

A higher hydrogen availability on the catalyst surface would favor the desorption of surface alkyl species by recombination with surface hydrogen. This would yield paraffins resulting in a decrease in the rate of readsorption. This would have a further negative effect on the chain growth probability. Hence an increase in hydrogen availability with increasing TEOS loading would result in a decrease in chain growth probability.

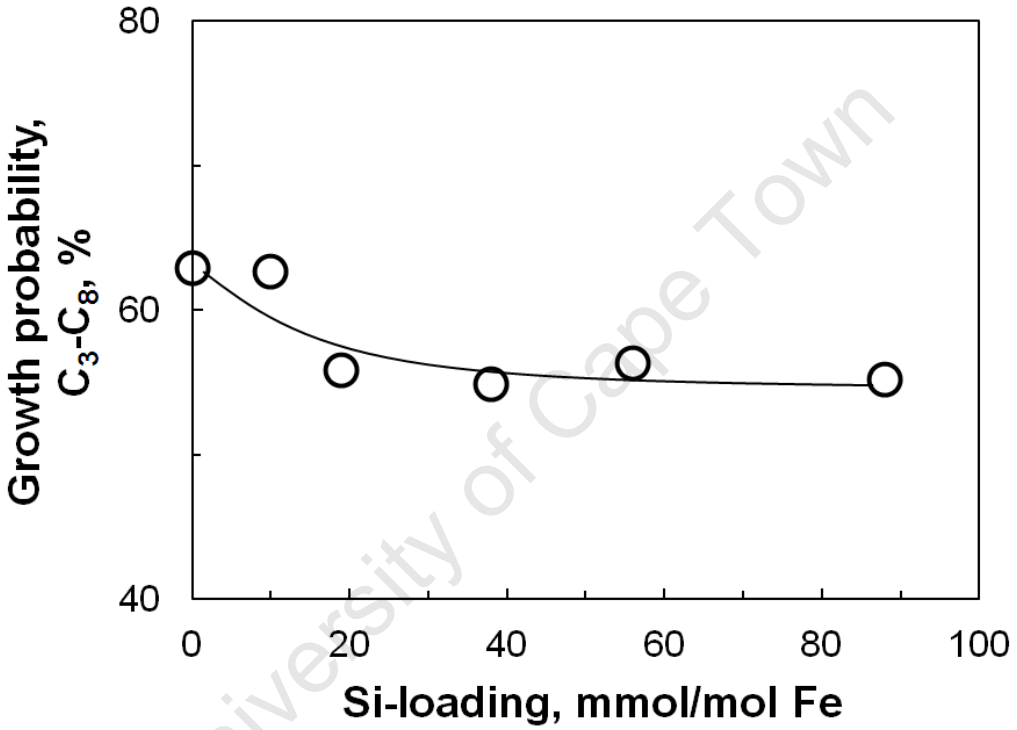




**Figure 6.24:** The chain growth probability ($C_3$-$C_8$) of the TEOS modified iron oxide samples taken after 24 hours time on stream represented as a function of Si loading**.**

**Olefin formation**

Olefins are the primary organic products of FT synthesis [Schulz, 1999]. They are thought to be formed from the dissociative desorption of growing alkyl species. Alternatively, the alkyl species can be hydrogenated to form a paraffin. The hydrogenation reaction is strong inhibited and thus primarily up to 70-90 mol-% olefins are formed in each carbon number of FT products. However, olefins can readsorb and undergo secondary reactions in which the 1-olefin can be can be hydrogenated and undergo double bond isomerisation, or participate in further chain growth.

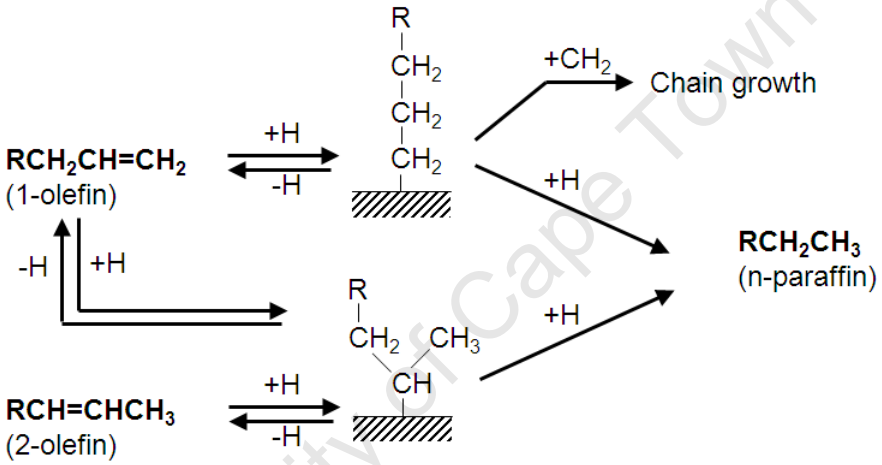




The $C_5$ fraction was used investigate the olefin selectivity. The olefin selectivity of the TEOS modified catalysts obtained after 24 hours time on stream as a function of Si loading are shown in Figure 6.25. The olefin content in the fraction of $C_5$-hydrocarbons decreases with increasing silicon content. The selectivity decreased from 78 C-% for the unmodified catalyst, FS-0, to a minimum of 53 C-% for the sample with the highest silicon content, FS-88. The intermediate loadings (FS-10 till FS-88) showed selectivity ranging from 67 till 56 C-% in descending order. Past studies, done in similar conditions, indicated olefin contents between 70-78 mol-% in the $C_5$ fraction for an unpromoted Fe-based catalyst [Wan et al., 2006; Zhang et al., 2006]. Thus, in that regard, the observed olefin selectivity of the TEOS modified catalyst of 69-56 mol-% was low.

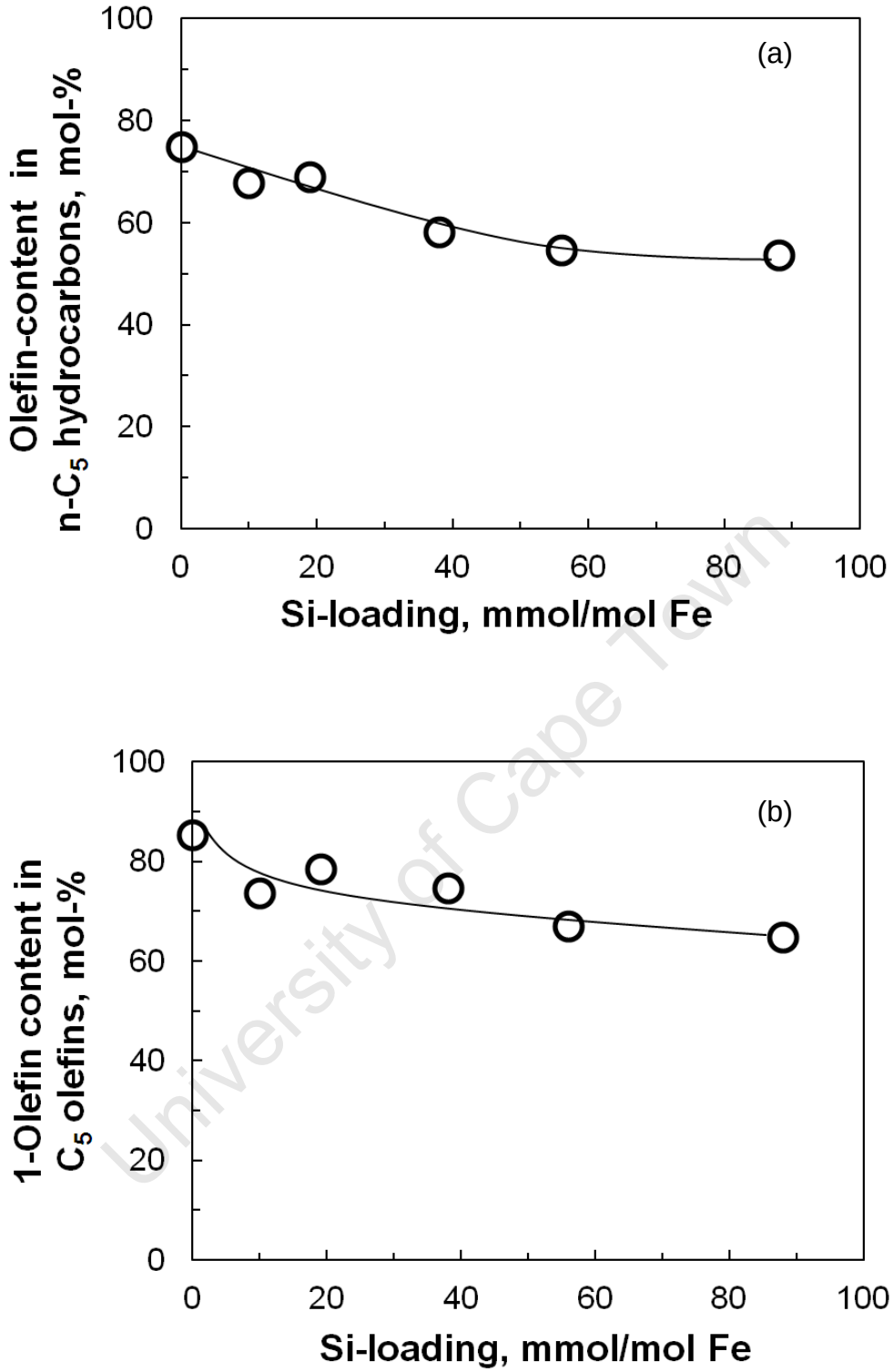




**Figure 6.25**: $C_5$ fraction Olefin selectivity of the TEOS modified catalyst taken at 24 hours time on stream as function of Si content.

(a) The total olefin content of the $C_5$ fraction in the $C_5$ n-hydrocarbons

(b) The selectivity of the 1-olefin expressed as function of the total olefins in the $C_5$ fraction

The 1-olefin content in the $C_5$ fraction total olefins deceases with increasing silicon content (see Figure 6.25(b))**.** Readsorption of the 1-olefin and secondary reactions might also result in a decrease in selectivity. The selectivity decreased from 85 C-% for the unmodified catalyst, FS-0, to a minimum of 65 C-% for the sample with the highest silicon content, FS-88. Although there seems to be a clear relationship between the decrease in 1-olefin content and the increasing Si content, readsorption is also a factor to consider.

The decrease in the 1-olefin selectivity with increasing TEOS modification might also be explained by a increase in the hydrogen avialability on the catalyst surface, which may lead to an increase in the formation of primary paraffins from the absorbed alkyl species hydrogenation as opposed to the desorption of 1-olefins. Moreover, an increase in surface hydrogen will enhance the likelihood of the 1-olefin to readsorbtion leading to further hydrogenation, isomerisation or chain growth. Once the olefin is readsorped the high hydrogen availiability would favor the formation of parrafins and thus have a negative effect on chain growth (see Figure 6.24) and the total oefin content (see Figure 6.25(a))**.** This is consistent with the observed results and supports the agrguement that an increase in silicon content might be accompanied by an increase hydrogen avialiabilty.

**Formation of branched compounds**

Branched compounds can be formed in two reaction pathways [Schulz et al., 1988]. The first reaction pathway involves readsorption of 1-olefin. This was proven co-feeding $^{14}C$ labelled propene by Schulz et al., (1970). The second pathway involves the primary combination of an alkylidene and a methyl species on the surface as presented below.

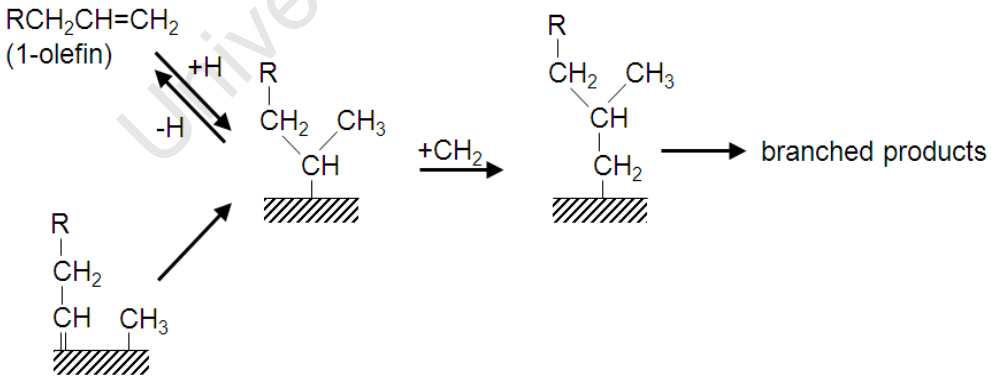


The ratio of branched to linear hydrocarbons in $C_5$ fraction as a function of silicon content is shown in Figure 6.26. The effects of hydrogen availability on the formation of branched compounds are shown in Figure 6.27.

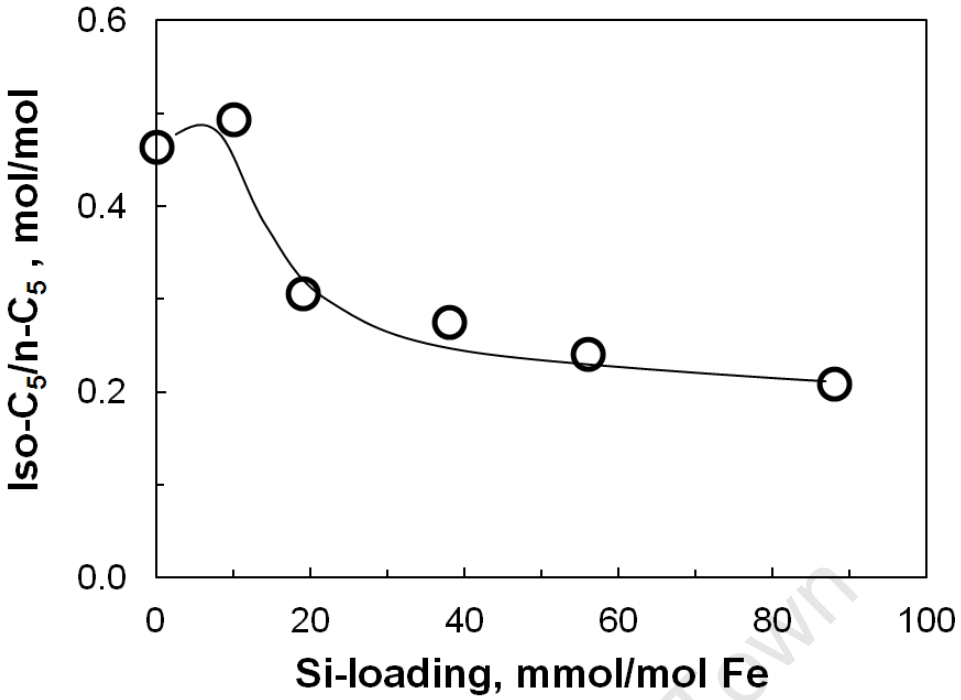


**Figure 6.26**: The molar ratio of branched to linear hydrocarbons in the $C_5$ fraction for TEOS modified iron oxide samples taken after 24 hours time on stream represented as a function of Si loading.



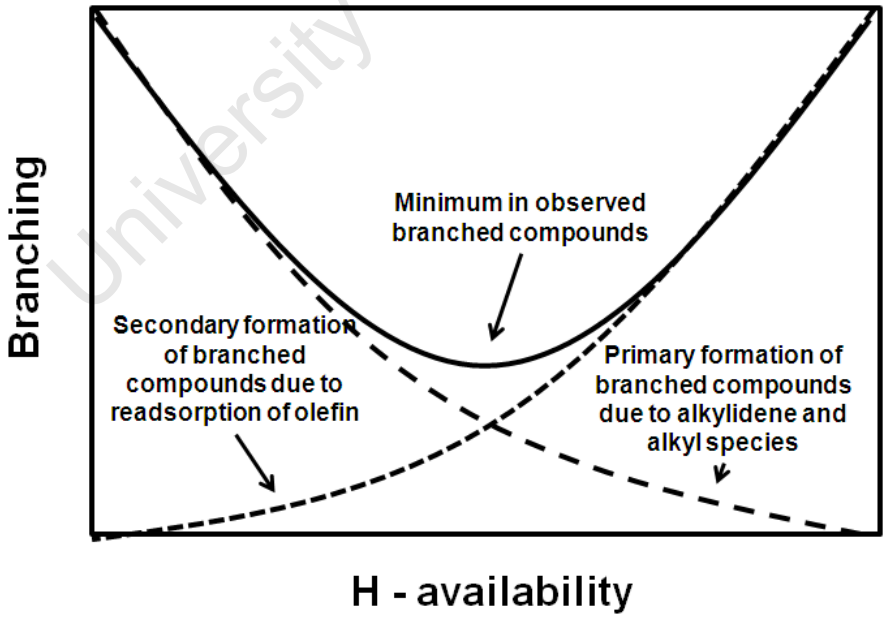


**Figure 6.27:** The effects of hydrogen availability on the formation of branched compounds.

The unmodified catalyst, FS-0, contained up to 46 mol-% branched compounds in the $C_5$ fraction, however, the degree of branching decreased with increasing TEOS modification to approximately 20 mol-% for the silicon content, FS-88. On Fe catalysts, formation of branched compounds passes a minimum with increasing hydrogen availability, see Figure 6.27. Although increasing the hydrogen concentration of the surface improves the readsorption of the olefins, it decreases the primary formations of the branched compounds through the combination of the alkylidene and a methyl species on the surface. This is because the relative concentrations of the alkylidene species is thought to decrease with increasing hydrogen availability thus resulting in a decrease in branched compounds. An increase in hydrogen availability with increasing TEOS modification is consistent with the observed decrease in branched compound content.

**Formation of oxygenates**

According to Pichler and Schulz (1970), oxygen containing surface species can be formed via a CO insertion step. Johnston and Joyner (1993) postulated that the same species could be formed by addition of hydroxyl groups to an alkylidene species. Desorption of this species then leads to formation of alcohols or aldehydes respectively. The total oxygenate content as a function of Si loading is shown in Figure 6.28.



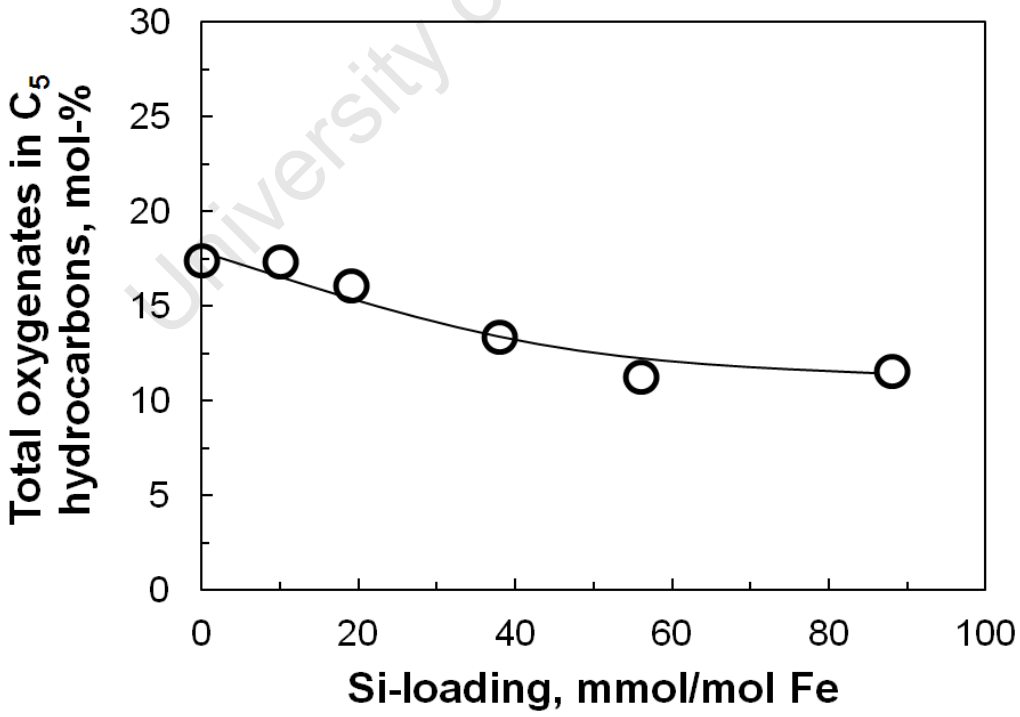


**Figure 6.28:** The total oxygenate content $C_5$ fraction for TEOS modified iron oxide samples taken after 24 hours time on stream represented as a function of Si loading.

Under typical commercial LTFT conditions (230 $^{0}$C, 20-40 bar, fixed bed reactor) the oxygenate content for Fe-based catalysts is low relative to the total amount of hydrocarbons, 6 C-% and is made up mostly 94% alcohols [Dry, 1981]. In this work, higher fractions of oxygenates (17 mol-%), mainly primary alcohols and aldehydes, were found in products of the unmodified catalyst. This is not surprising since commercial Fe catalysts are promoted with potassium which has been shown to affect the selectivity of oxygenates [Dry, 1981]. All the modified, FS-10 till FS-88 catalysts showed lower oxygenate content with a minimum of approximately 10 mol-% reached at the highest silicon content, FS-88.

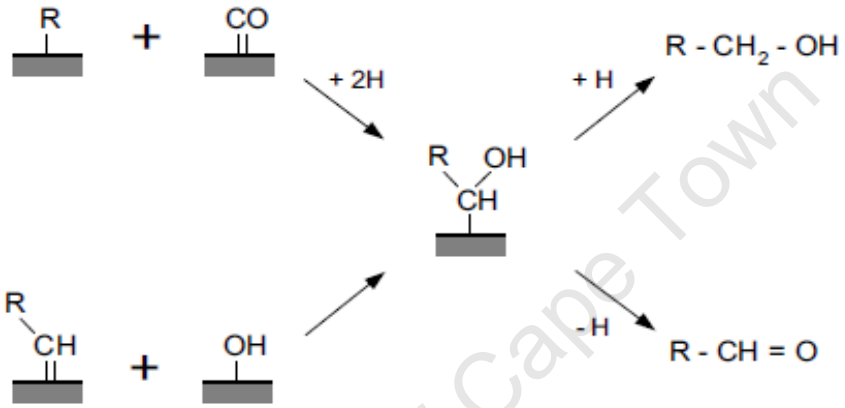


As previously discussed, an increase in hydrogen availability decreases the concentration of alkyldene species on the surface, this would not favour the formation of oxygenates. Moreover the concentration of OH species would decrease with increasing hydrogen availability since the formation of water will be thermodynamically more favoured and thus the oxygenate content will decrease.

## 6.2.11 Discussion of all Fe-O-Si results

**Changes in activity and selectivity**

The integral rate of the Fischer-Tropsch synthesis per unit surface area of carbide ($Fe_5C_2$ or $Fe_2C$) passes a maximum as a function of the silicon content in the sample (see Figure 6.29). The specific rate of $Fe_2C$ can be deduced by assuming that $Fe_5C_2$ in all samples has a similar specific rate per unit surface area. The assumption that the rate of the Fischer-Tropsch synthesis over Hägg carbide is unaffected by the silicon modification in the sample is reasonable since it was made plausible that metallic iron in the reduced catalyst was the source of Hägg carbide, whose surface was not modified with silicate (vide supra).

The specific integral rate of $Fe_2C$ per unit surface area for the sample containing Si/Fe = 10 mmol/mol is ca. 25% higher than that of $Fe_5C_2$, whereas the activity for specific integral rate of $Fe_2C$ per unit surface area for the samples containing more silicon (FS > 10 mmol/mol) is almost four times higher than the specific rate of $Fe_5C_2$. It might be argued that the specific activity of $Fe_2C$ obtained with sample FS-10 represents that of an (almost) bare $Fe_2C$ surface, since the CO-conversion over the catalyst with Si/Fe = 10 mmol/mol was initially high resulting in an initial high water partial pressure. This may have led to removal of almost all silicate surface ligand by hydrolysis. The site density on $Fe_2C(111)$, defined as the number of surface iron atoms per unit area, is ca. 5% higher than on $Fe_5C_2(100)$, which may explain some of the observed enhanced activity. However, the observed rate of the Fischer-Tropsch synthesis is a complex variable depending amongst others on the strength of CO and $H_2$ adsorption, surface coverage of the adsorbed species and the activation barrier for surface $CH_x$-species hydrogenation [van Steen and Schulz, 1999; Hou et al., 2009; Santen et al., 2011]. The samples with high silicon content show a much higher rate of the Fischer-Tropsch synthesis over $Fe_2C$ per unit surface area (ca. 3.2 – 3.5 times higher than the rate per unit surface area of $Fe_2C$ obtained with sample FS-10). This might be ascribed to a promotional effect of the surface silicate groups as ligands. Wan et al. (2006) indicated that the addition of silica to Fe-based catalyst results in a weakening of the CO-adsorption on the pre-carburized catalyst. A weakening of the strength CO adsorption may result in an increase in the rate of Fischer-Tropsch synthesis [Santen et al., 2011, Krishnamoorthy et al., 2002].

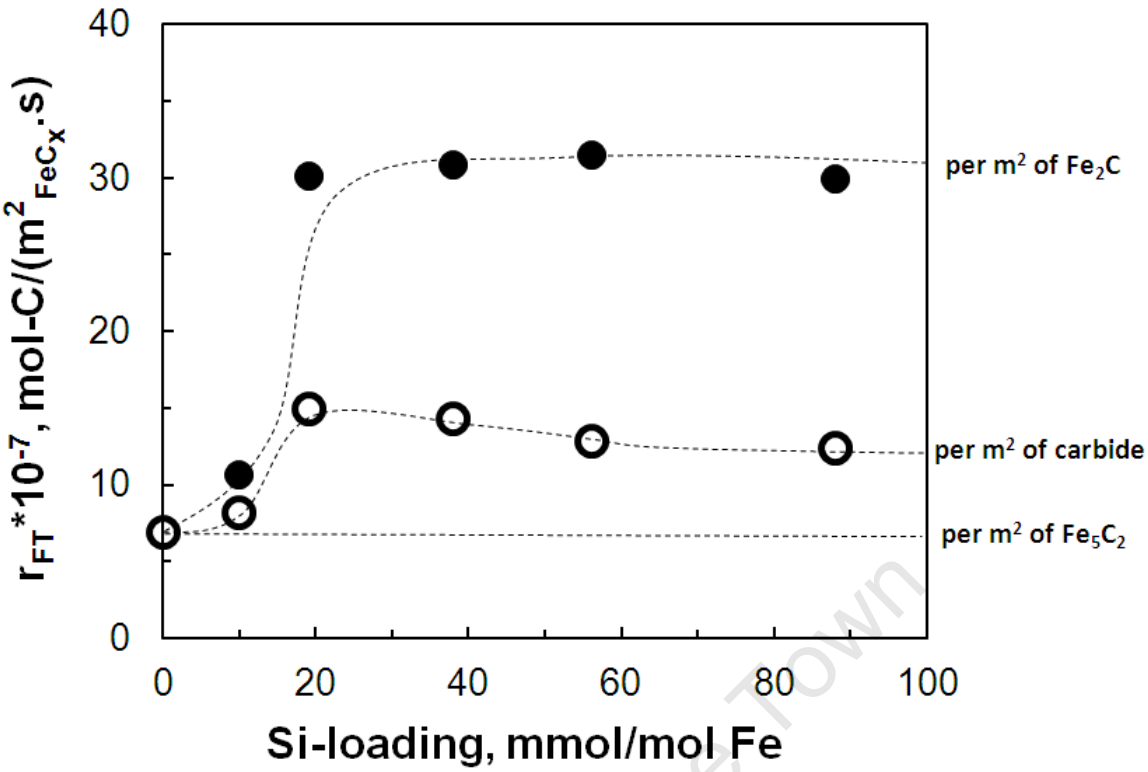


**Figure 6.29:** The integral rate of Fischer-Tropsch reaction for the TEOS modified samples after 24 hours time on stream



To explain how the presence of the Si-ligands on the surface of the carbides is related to the observed result, a simplified theoretical model of the surface electron density of a simple carbide was compared to that of a TEOS modified carbide. The model is schematically represented on Figure 6.30.

The surface electron distribution of an spherical carbide crystallite can be assumed to be homogeneous since the Fe surface atoms in each cell are indistinguishable from each other. Therefore, the manner in which the reactants interact with the surface will the same at any point around the surface. In the case of TEOS modified samples, it has been argued that some of the carbide surface is covered with Si-ligands. The silanol groups (-O-Si) are very electronegative and have been shown to pull electrons away from metals that they are attached too [Barraclough et al., 1961]. The pulling of the electrons will change the surface density and as a result create special contact zones that have different catalytic capabilities [Vannice and Sudhakar, 1984; Tauster, 1987]. Since these contact zones would be electron deficient, they would be more conducive for the absorption of $H_2$ and less favorable to CO. This would result in improved surface hydrogen availability which can then be related to the rate of reaction.

According to the reaction rate developed by Huff and Satterfield (1984) the rate of the Fischer-Tropsch reaction of iron-based catalysts can be represented by Equation 6.6. As indicated by this equation an increase in the surface partial pressure of hydrogen will result in an increase in the rate of reaction. Thus with increasing hydrogen availability the rate of reaction is expected to increase.

$$r_{H_2+CO} = \frac{a \cdot P_{CO} \cdot P_{H_2}^2}{P_{H_2O} + b \cdot P_{CO} \cdot P_{H_2}} \quad (6.6)$$

Furthermore, the products obtained in the TEOS modified samples were in agreement with this theory. The increase in methane selectivity, the decrease in the chain growth, olefin content, oxygenate and lower degree of branching with TEOS modification all indicate a improved surface hydrogen availability.



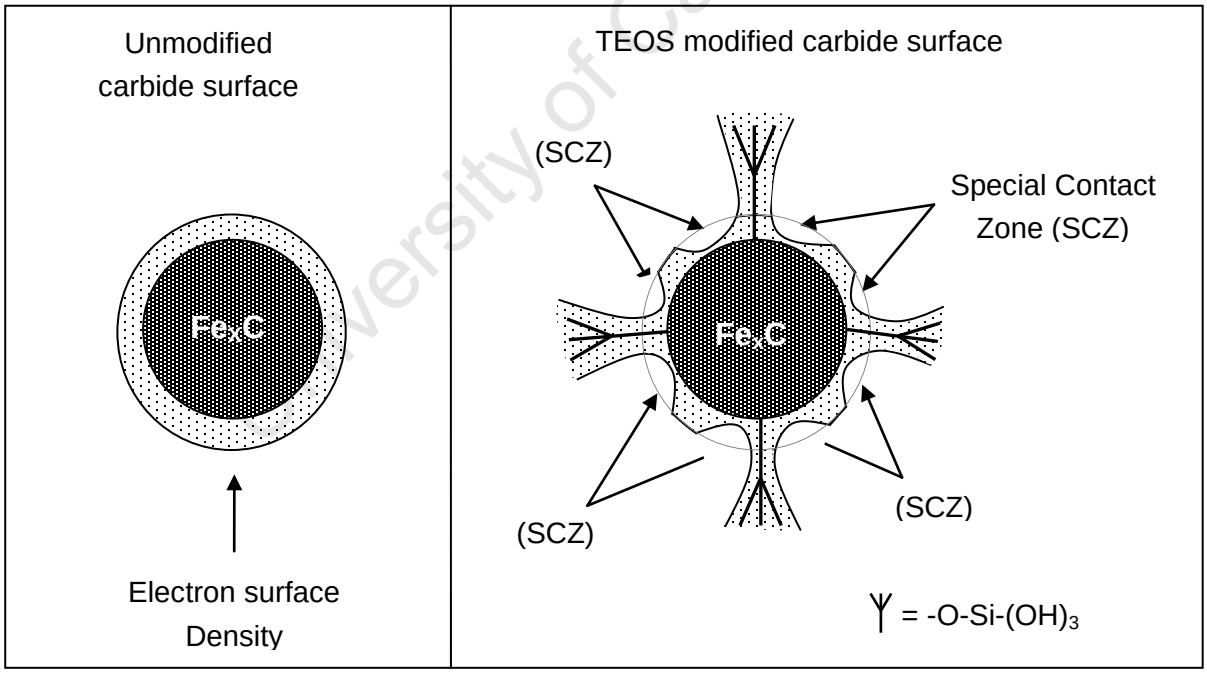


**Figure 6.30:** The proposed change in surface electron density cause by silicate surface coverage of the carbide phase

# 6.3 Iron-titania system (Fe-O-Ti)

## 6.3.1 Characterization of TBO modified calcined samples

### 6.3.1.1 FTIR (DRIFTS mode) analysis of calcined catalysts

The FTIR analysis (in DRIFTS mode) of TBO modified samples over the range 400 – 4000 $cm^{-1}$ is shown in Figure 6.31.

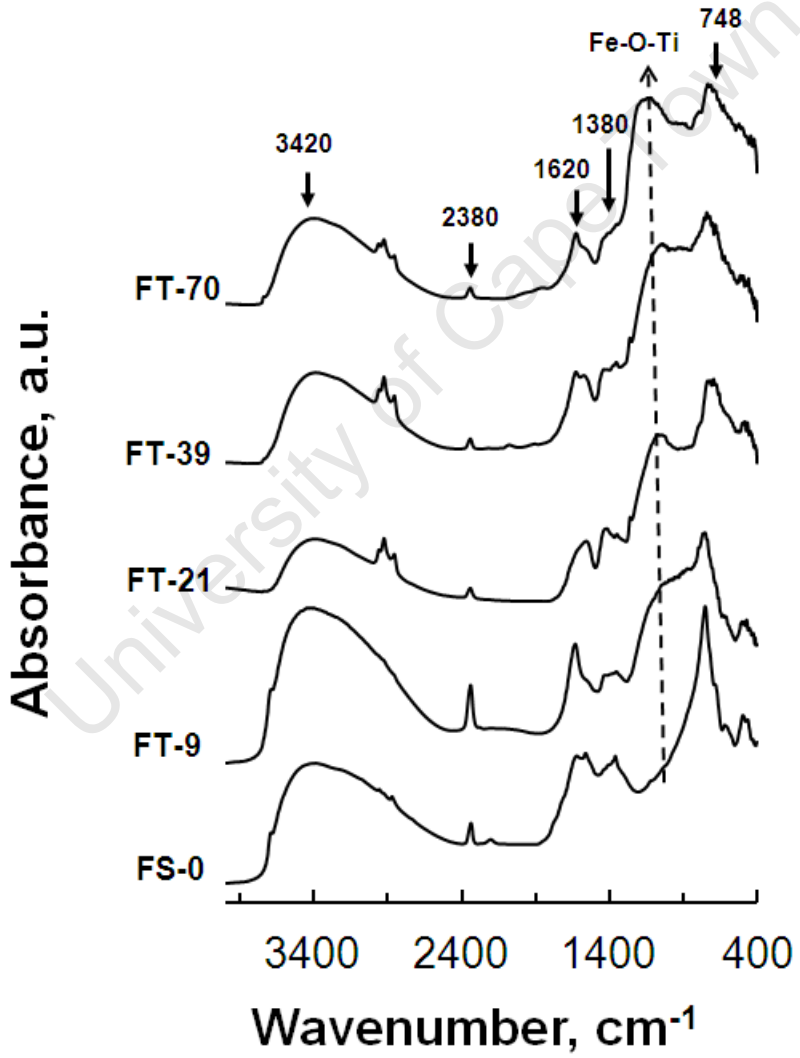


**Figure 6.31:** FT-IR (DRIFTS mode) analysis of calcined iron oxide nano-crystallites prepared using microemulsion technique and modified with TBO using infinite dilution method.

All the analyzed samples show an absorption band at 748 $cm^{-1}$ which represents the vibration of Fe-O bonds consistent with the presence of maghemite [Darezereshki, 2011; Jarlbring et al., 2005]. The absorption band at 3420 $cm^{-1}$ is typical for the stretching frequency in a hydroxyl group (-OH) [Darezereshki, 2011; Walters, 2006]. This might be due to the presence of water and is accompanied by the band at 1620 $cm^{-1}$ due to the bending of the (-OH) group [Darezereshki, 2011; Walters, 2006] and the presence of butoxide groups [Roslov et al., 2010]. The absorption band 1380 $cm^{-1}$ might be assigned to C-H stretching modes attributed to the residual surfactant present in the catalyst [Morsy et al., 2009]. The small peak at 2380 $cm^{-1}$ represents the asymmetric vibration of $CO_2$ from the atmosphere [Darezereshki, 2011]. Due to the high signal to noise ratio observed, absorption bands occurring in the range below 700 $cm^{-1}$ are not discussed in this work.

The TBO modified samples show an additional absorption band between 890 $cm^{-1}$ and 1360 $cm^{-1}$ (indicated on Figure 6.31 with the broken line). This range of frequencies is consistent for all the TBO modified catalysts. However, there appears to be a slight shift in the peak maximum position with increasing Ti-content. Table 6.10 shows the IR frequencies for the additional bands as observed in FTIR analysis of the TBO modified samples.



**Table 6.10:** IR frequency assigned to Fe-O-Ti present in prepared catalysts

| Sample code | Frequency ($cm^{-1}$) |
|---|---|
| FT-9 | 1021-1060 (unclear) |
| FT-21 | 1060 |
| FT-39 | 1040 |
| FT-70 | 1120 |

The intensity of these bands increases with increasing TBO loading but before these bands can be assigned to Fe-O-Ti interactions other alternatives have to be considered. Firstly, the possibility that the Ti atoms are incorporated into the $Fe_2O_3$ structure was considered. The incorporation of Ti atoms into the $Fe_2O_3$ structure leads to the formation of Fe-Ti-O mixed oxide. These oxides have been shown to give a broad absorption band at ca. 540 $cm^{-1}$ [Pal et al., 1999; Glisenti, 2000; Chen et al., 2011; Maček and Orel, 1997; Ishakawa et

al., 2002]. The position of the observed additional bands is inconsistent with that of the mixed metal oxide phase. Secondly, titanium butoxide might undergo auto condensation during calcination (performed at 350 $^0$C) to form anatase ($TiO_2$) [Roslov et al., 2010]. The Ti-O stretching in an organized $TiO_2$ structure gives absorption bands at 430 and 580 $cm^{-1}$ [Pal et al., 1999; López et al., 2002; Wei et al., 2009] which is also inconsistent with the observed additional bands. Furthermore, cross-linked Ti-O-Ti interactions yield an intense band at 1200 $cm^{-1}$ [Hamadanian et al., 2010]. The M-O-Ti stretching frequency is expected to decrease if a Ti atom is replaced by a heavier Fe atom. More specifically the bending vibration of a hydroxyl metal oxide (e.g. M-O-Ti-OH) is observed at frequencies between 900 - 1125 $cm^{-1}$ [Chen at el., 2009; Yang et al., 2009]. Hence the absorption bands between 890 and 1360 $cm^{-1}$ might be assigned to Fe-O-Ti. Past work has indicated that this is region where absorption due to Fe-O-Ti occurs [Gleseni, 2000; Khaleel, 2009; Wei et al., 2009].

The Fe-O-Ti interactions observed for the TBO modified samples show differences in both adsorptions frequency and type of peak broadness with increasing TBO loading (see Figure 6.31). This indicates that these samples possibly contain a mixture of tridentate $(\equiv FeO)_3$-Ti(OH), bidentate $(\equiv FeO)_2$-$Ti(OH)_2$ and/or monodentate $(\equiv FeO)$-$Ti(OH)_3$ linkages. Although there was no clear peak maximum obtained with the samples FT-9 in the range between 890 and 1360 $cm^{-1}$, samples FT-21 and FT-39 showed a sharper peak at frequencies of 1060 $cm^{-1}$ and 1040 $cm^{-1}$ respectively, demonstrating that there might be a high concentration of a specific type of interaction (possibly bidentate linkages). Further addition of TBO (FT-70) results in a blue shift of the maximum to ca. 1120 $cm^{-1}$ and this implies a high concentration of species with more degree of freedom (e.g. monodentate linkages). It can thus be concluded that the surface modification of the iron oxide nano-particles with TBO was also successful.

The TBO modified samples also show a group of absorption bands between 2800 and 3200 $cm^{-1}$. These bands are consistent with C-H stretching modes of the butoxide ($C_4H_9O$) groups [Roslov et al., 2010]. This indicates that the butoxide groups on the attached titanium ligands survive the calcination process. Roslov et al. (2010) observed that during heating of TBO, the decomposition of the organic constituent leading to the formation of titanium dioxide and elimination of the carbon containing products such as butane and butanol only starts to occur at ca. 320 $^0$C. However, the interaction of the titanium ligands with the iron oxide surface (Fe-O-Ti) might stabilize the ligands by preventing the formation of cross-linked Ti-O-Ti interactions. This would prevent the formation of $TiO_2$ which would otherwise be thermodynamically favored [Roslov et al., 2010]. Thus, the ligands might be stable enough to survive calcination (performed at 350 $^0$C). The stretching of the C-C and C-O bonds in the butoxide ($C_4H_9O$) groups yield absorption bands at ca. 800 and ca. 1500

$cm^{-1}$ respectively [Roslov et al., 2010]. It must also be noted that the bending frequency of the C-O bonds appear at 950 $cm^{-1}$ [Roslov et al., 2010]. Therefore, the presence of these interactions might overlap with the Fe-O-Ti interactions and contribute to the broadness of the observed peaks.

### 6.3.1.2 TEM analysis of calcined samples

TEM was used to ascertain the effects of TBO modification on the crystallite size and size distribution. The TEM images of all the TBO modified calcined samples are shown by Figure 6.32 and the histograms depicting crystallite size distribution are displayed in Figure 6.33.

From Figure 6.32, it is apparent that, as depicted by the TEM micrographs presented, the samples, as in the case of the TEOS modified system; consist of well defined, uniform crystallites with a predominantly spherical morphology. The micrographs were used to calculate the average crystallite size. Two hundred crystallites were measured and the volume based average crystallite diameters estimated from the TEM-images and are given in Table 6.11.

**Table 6.11:** Mean volume average crystallite sizes (in nm) estimated from TEM-images (n = 200)[a]

| **Catalyst** | **FS - 0** | **FT - 9** | **FT - 21** | **FT - 39** | **FT - 70** |
|---|---|---|---|---|---|
| **$d_{AVARAGE\_TEM}$[b], nm** | 12.4 ± 2.8 | 13.4 ± 3.9 | 11.1 ± 2.5 | 9.0 ± 1.7 | 8.7 ± 1.4 |

*a: 200 crystallites were measured from the TEM images using J-image software*

*b: The values presented are mean volume average diameters and the standard mean deviations*

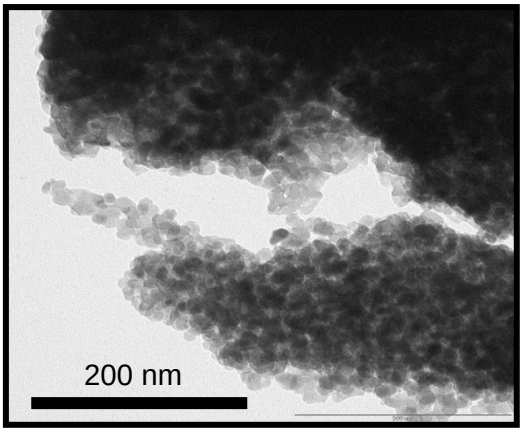


FS-0

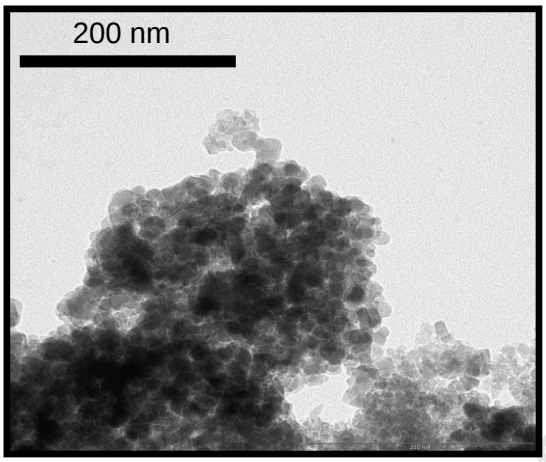


FT-9

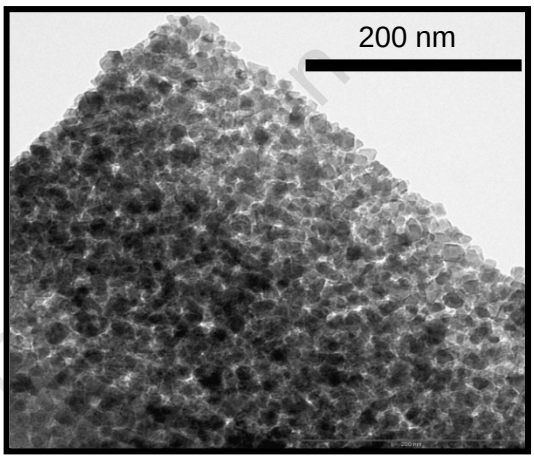


FT-21

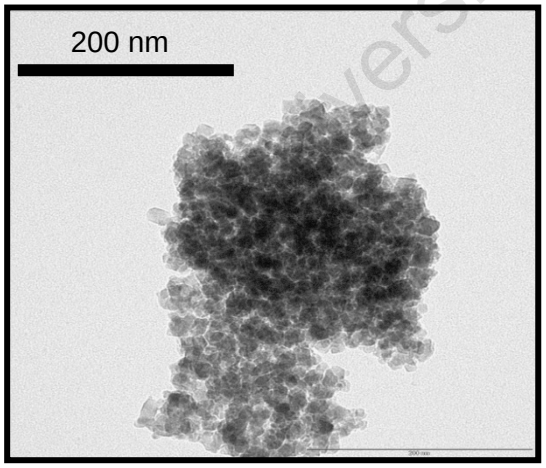


FT-39

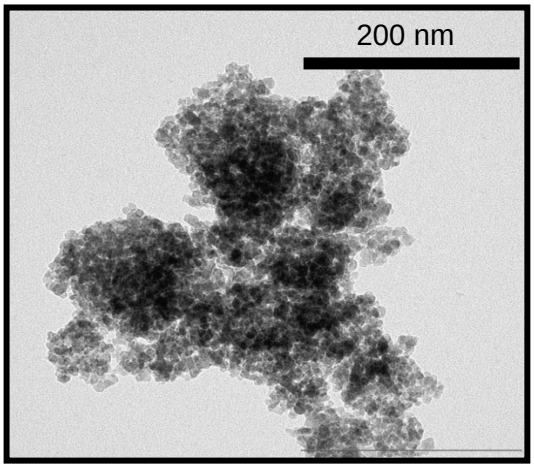


FT-70

**Figure 6.32:** TEM micrographs of calcined iron oxide nanocrystallites prepared using microemulsion technique and modified with TBO using infinite dilution method.

Figure 6.33 shows the crystallite size distribution of the TBO modified catalyst. As already discussed, the unmodified sample (FS-0) has a normal distribution. The lowest TBO loading (FS-9) shows, after deconvolution of the data, two separate normal distributions; the first one having an average crystallite diameter and standard deviation of 10.6 $\pm$ 1.3 nm and the second at 15.2 $\pm$ 2.11 nm. The overall average crystallite diameter for this catalyst is 13.4 $\pm$ 3.9 nm (see Table 6.11). This result indicates that although some of the crystallites might be protected from sintering, giving rise to an average diameter of 10.6 nm, the unmodified crystallites (15.2 nm) sinter in comparison to the unmodified sample (12.4 nm).

Sample FT-21 showed a sharp but normal type of distribution with a long tail (see Figure 6.33). This indicates that there is a cluster of small crystallites centered on the mean diameter giving the distribution its sharp nature and the tail is brought about by the co-existence of much larger crystallites in the analyzed sample. This long tail effects is also displayed by the remaining two samples (FT-39 and FT-70) but to a lesser extent. The existence of the larger crystallites has a negative effect on the standard deviations calculated for the sample modified with TBO. Thus, the standard mean deviations observed are larger as compared to those at similar loading for TEOS modified samples.

The standard mean deviation is between ca. 29-16 % of the mean volume, decreasing with increasing TBO loading (see Table 6.11). It might therefore be concluded that narrower crystallite size distribution are attained when iron crystallites are modified with TBO.

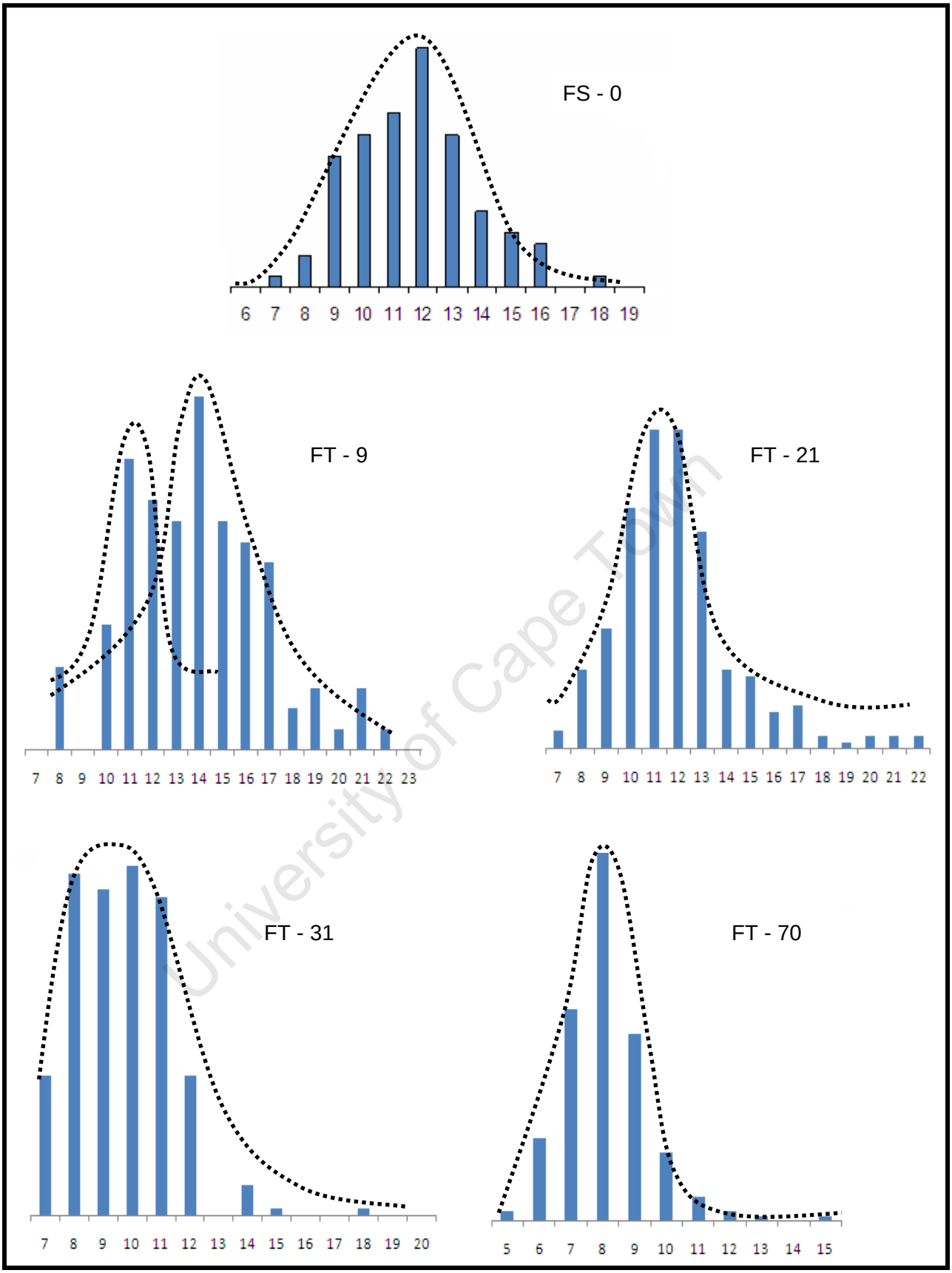




**Figure 6.33:** Crystallite size distribution of the calcined iron oxide nano-crystallites prepared using microemulsion technique and modified with TBO using infinite dilution method (also displayed are the types of distribution)

### 6.3.1.3 XRD analysis of calcined samples

The average crystallite sizes and the phase composition in the calcined samples were analyzed using XRD (see Figure 6.34). When comparing the XRD patterns with literature reference patterns, it can be seen that all the analyzed samples consist of a mixture of hematite (α-$Fe_2O_3$) and maghemite (γ-$Fe_2O_3$). The hematite content in the sample with the lowest titanium content (FT-9) is high. This is indicated by the intensity of the hematite identity diffraction peak at $2\theta = 33.1^0$. The hematite content then decreases with further TBO addition (FT-21). Following that it increases again for highly modified samples (FT-39 and FT-70). The XRD diffraction patterns also show increase in peak broadening at $2\theta = 35.4^0$, for the maghemite phase, which indicates a decrease in size with increasing TBO loading (also see Figure 6.34).

The average crystallite diameters and phase content of the calcined samples were calculated using Rietveld refinement and are displayed in Table 6.12. Maghemite was the dominant phase (89 - 71 %) in all other catalysts excerpt sample FT-9 where the hematite (α-$Fe_2O_3$) is the dominant phase (77 %). There appears to be no clear correlation between the phase contents and the amount of TBO added during synthesis (see Table 6.12). In all the analyzed samples, the calculated hematite crystal diameters (13-19 nm) were larger than the maghemite (8-13 nm).

**Table 6.12:** XRD average crystallite sizes and the phase composition of the FTBO modified sample after calcination, calculated using Rietveld refinement

| Component | FT-0 | FT-9 | FT-21 | FT-39 | FT-70 |
|---|---|---|---|---|---|
| **α-$Fe_2O_3$**: content (wt %): | 12 | 77 | 11 | 29 | 16 |
| Size (nm): | 17 | 18 | 15 | 19 | 13 |
| **γ-$Fe_3O_4$**: content (wt %): | 88 | 23 | 89 | 71 | 84 |
| Size (nm): | 12 | 13 | 11 | 9 | 8 |

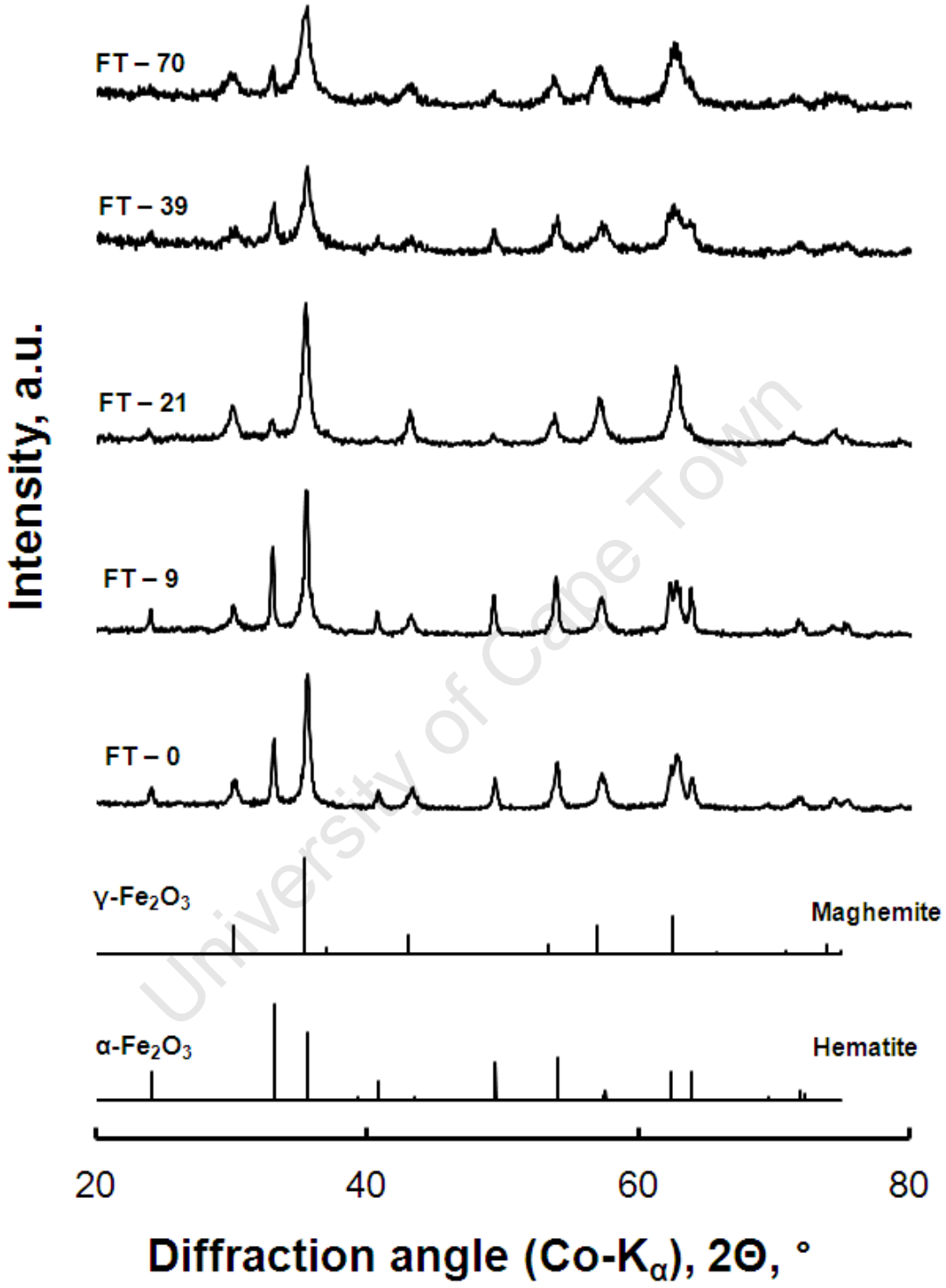


**Figure 6.34:** X-ray diffraction patterns of the calcined TBO modified catalysts. Also shown are reference patterns of hematite ($\alpha$-$Fe_2O_3$) and maghemite ($\gamma$-$Fe_2O_3$)

Hematite is the thermodynamically more stable phase under the conditions applied here [Navrotsky et al., 2008]. However, surface energy contribution modifies the relative phase stability significantly [Navrotsky et al., 2008; van Steen et al., 2005], and maghemite becomes the more stable phase for nano-sized crystallites [Navrotsky et al., 2008], which transforms into hematite upon sintering. The transformation of maghemite to hematite has to obey the thermodynamic constraint that the Gibbs free energy of the system is at a minimum. Hence, the critical diameter for maghemite ($d_{maghemite,c}$) beyond which the transformation to hematite is thermodynamically allowed is given by

$$\mu_{\text{hematite}} - \mu_{\text{maghemite}} = 0$$

$$\mu^0_{\text{hematite}} - \mu^0_{\text{maghemite}} + \frac{6 \cdot \gamma_{\text{hematite}} \cdot M_{Fe_2O_3}}{d_{\text{hematite}} \cdot \rho_{\text{hematite}}} - + \frac{6 \cdot \gamma_{\text{hematite}} \cdot M_{Fe_2O_3}}{d_{\text{maghemite}} \cdot \rho_{\text{maghemite}}} = 0$$

$$d_{\text{maghemite,c}} = \frac{6 \cdot \gamma_{\text{hematite}} \cdot M_{Fe_2O_3}}{(\mu^0_{\text{hematite}} - \mu^0_{\text{maghemite}}) \cdot \rho_{\text{maghemite}}} \cdot \left( \frac{\gamma_{\text{hematite}}}{\gamma_{\text{maghemite}}} \cdot \left( \frac{\rho_{\text{maghemite}}}{\rho_{\text{hematite}}} \right)^{2/3} - 1 \right)$$

It can be estimated using a non-size dependent surface energy that for non-hydrated surfaces this transition at the calcination temperature applied here occurs for maghemite crystallites of ca. 19.4 nm (the corresponding crystallite size of the hematite crystals is 18.9 nm). The high hematite content in the sample FT-9 might be due to the large crystallite size distribution determined after calcination.

The average crystallite size of the calcined samples, as determined from both TEM and XRD analysis as a function of TBO loading, are shown in Figure 6.35 (also represented are the different iron oxides phases present in the analyzed samples). The average crystallite size and content of the hematite phase does not seem to depend on the Ti-content in the samples. However, the average crystallite size of the γ-$Fe_2O_3$ was observed to decrease with increasing Ti-content in the samples. Low loadings of TBO have a negative effect on the average crystallite size, and the mean crystallite diameter increases from $d_{AVG\_TEM}$ = 12.4 nm, for the unmodified catalyst (FS-0), to $d_{AVG\_TEM}$ = 13.4 nm (for FT-9). This effect appears to be limited to low loadings, since addition of more TBO results in a decrease in the average crystallite size. The catalysts, FT-21, FT-39 and FT-70, show an average crystallite diameter, $d_{AVG\_TEM}$ = 11.1 nm, $d_{AVG\_TEM}$ = 9.0 nm and $d_{AVG\_TEM}$ = 8.7 nm

respectively. There is a 27% decrease in average crystallite size between the unmodified catalyst (FS-0, $d_{AVG\_TEM}$ = 12.4 nm) and highest TBO loading (FT-70, $d_{AVG\_TEM}$ = 8.7 nm). The crystallite sizes calculated using XRD analysis for the maghemite (γ-$Fe_2O_3$) phase were consistent with the TEM analysis (see Figure 6.35), which was to be expected since γ-$Fe_2O_3$ is the dominant phase in the synthesized catalysts.

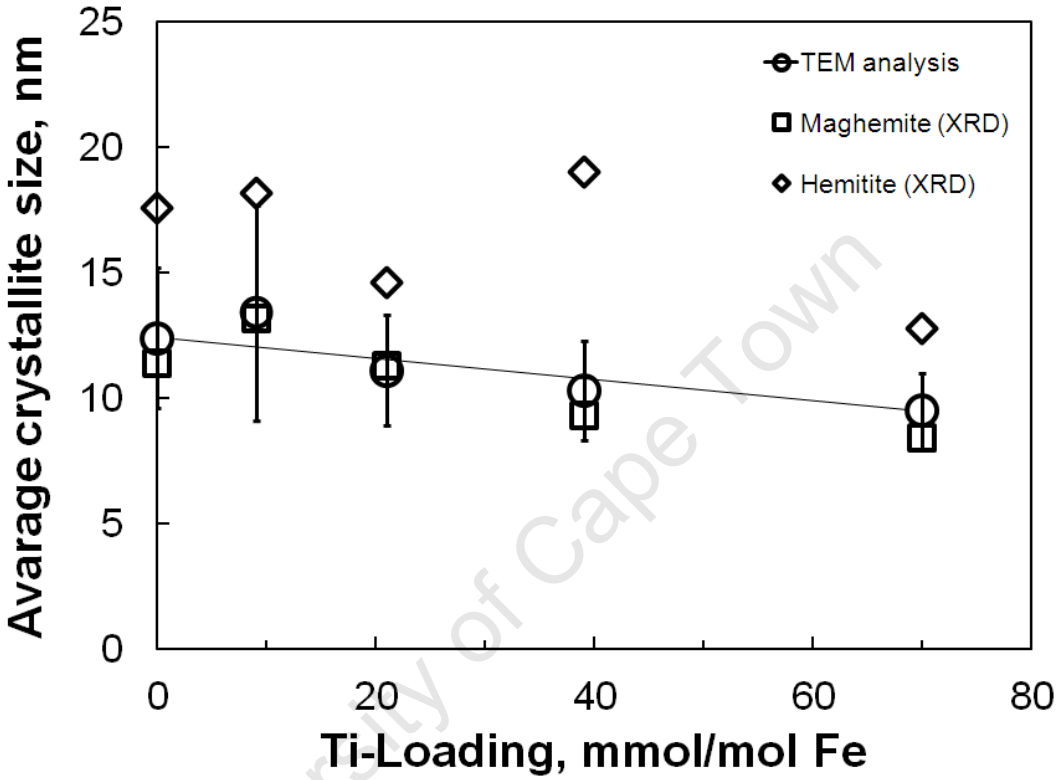


**Figure 6.35:** Volume-based average crystallite diameters the of calcined, TBO modified samples obtained using TEM and XRD analysis represented as a function of Ti-content (also shown are the iron oxide phases corresponding to the calculated crystallite sizes)

One way to explain the decrease in crystallite diameter with increasing TBO loading could be that the modification stabilizes the iron oxide by capping the surface of the nanoparticle with the inorganic –O-Ti($C_4H_9O)_3$ ligands (see illustration on next page). The presence of the –O-Ti-($C_4H_9O)_3$ ligands on the iron oxide surface was shown using FTIR. The ligands keep the iron oxide particles away from each other by steric hindrance, making it physically impossible for the nanoparticle to come into contact with each other. This behavior promotes the formation of smaller nanoparticles with narrow sizes distribution and has been proven using organic ligands [Morsy et al., 2009]. Thus with increasing TBO loading (i.e. more ligands on the surface) the average crystallite size will be expected to decrease.

Therefore, it stands to reason that the observed decline in crystallite size with increasing TBO loading is a function of ligand surface coverage. To investigate this effect the ratio of the total number of Fe surface atoms to the total Ti atoms introduced in the sample was calculated. Titanium atoms are assumed not to be incorporated into the $Fe_2O_3$ structure (as established using FTIR). Therefore, all the Ti present is considered to be interacting with surface Fe atoms. The crystallite sizes of the calcined samples obtained from TEM analysis were used to calculate the dispersion of the iron oxide (assuming a surface density of 4.08 Fe/nm$^2$ for γ-$Fe_2O_3$(110)). Fe surface atoms were then calculated. The titanium content in the samples was obtained from EDX. Following that, the surface Fe to Ti ratio was plotted against Ti loading (see **Figure 6.36)**. The error bars the graphs were established using the standard deviation associated with the average calculated crystallite diameters from the TEM

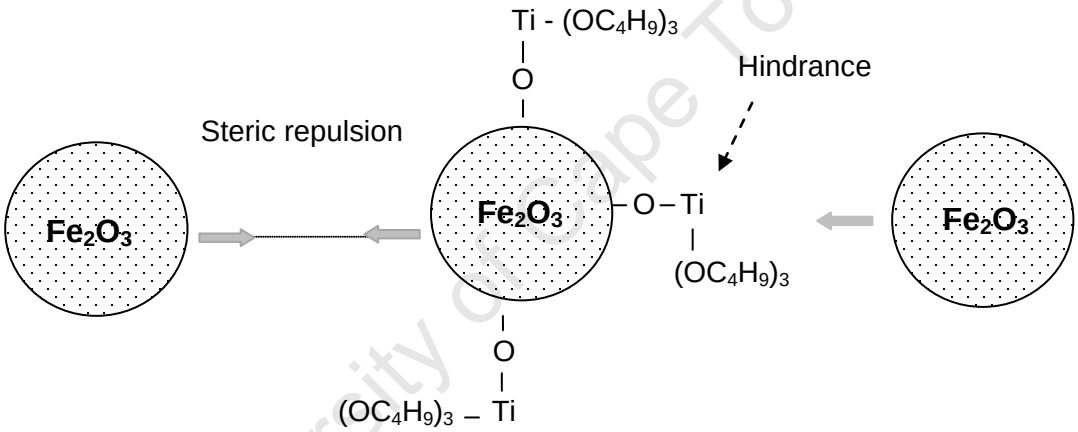




The surface ratio (Fe/Ti) decreased with increasing TBO loading. The lowest TBO loading (FT-9) showed that there is 1 Ti atom for every 11 Fe surface atoms. With increasing Ti loading the ratio drops until it reaches a ratio of 2 surface iron atoms for every Ti atom present in the sample at the highest TBO loading, FT-70 (see **Figure 6.36**). At low TBO loading (FT-9) the surface coverage was calculated to be 10 $\pm$ 3 %; meaning that approximately 90 % of the Fe atoms on the surface are available for reduction and Fischer-Tropsch synthesis. For intermediate loadings (FT-21 - FT-39), the surface coverage came down to 21 $\pm$ 5 % to 31 $\pm$ 6 % respectively, which was still reasonable because over 70 % of the Fe surface atoms were still available. However, the surface coverage for the highest TBO loading (FT-70) was 50 $\pm$ 8 %.

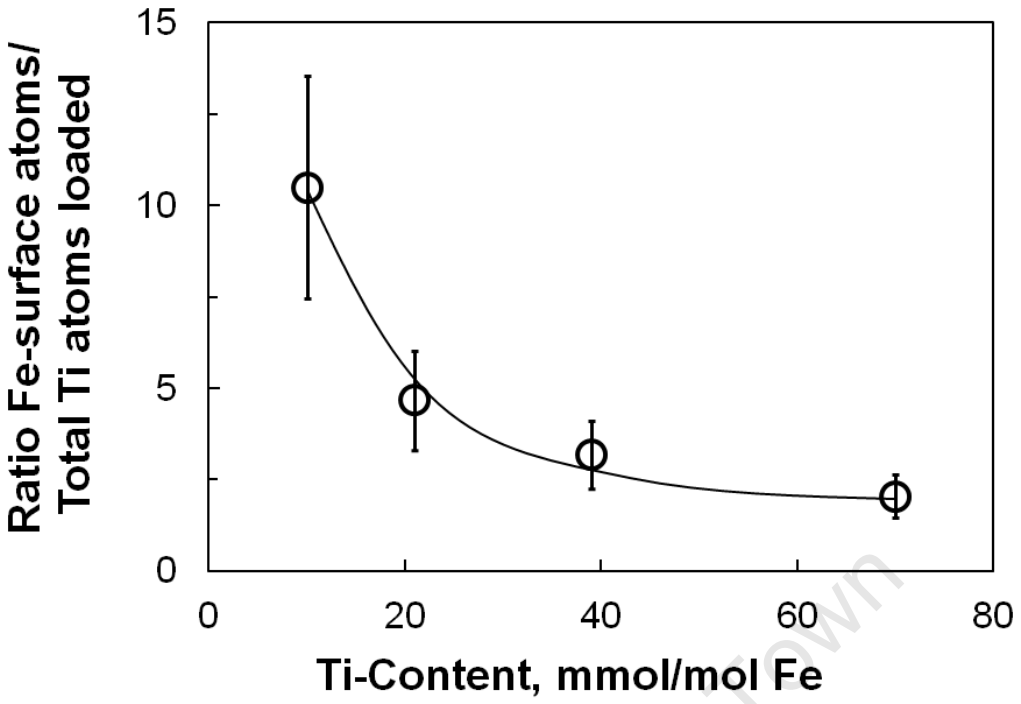


**Figure 6.36:** Calculated Ti surface coverage based on the crystallite sizes of the iron oxide from TEM analysis and EDX Ti-contents together with IR information on the type of interaction



## 6.3.2 Characterization of reduction behaviour and reduced samples

### 6.3.2.1 $H_2$-TPR analysis of calcined samples

Changes in reduction behavior of the iron oxide induced by the presence of various amounts of titanium in the samples were studied using $H_2$-TPR analysis. The samples were initially degassed as described in the experimental section. Following that, the catalysts were reduced in 5% hydrogen in argon (v/v) mixture. Approximately 30 mg of catalyst was loaded and reduced from room temperature to 900 $^0$C (heating rate 10 $^0$C/min). The hydrogen consumption was monitored and the reduction patterns of the TBO modified samples are presented in Figure 6.37.

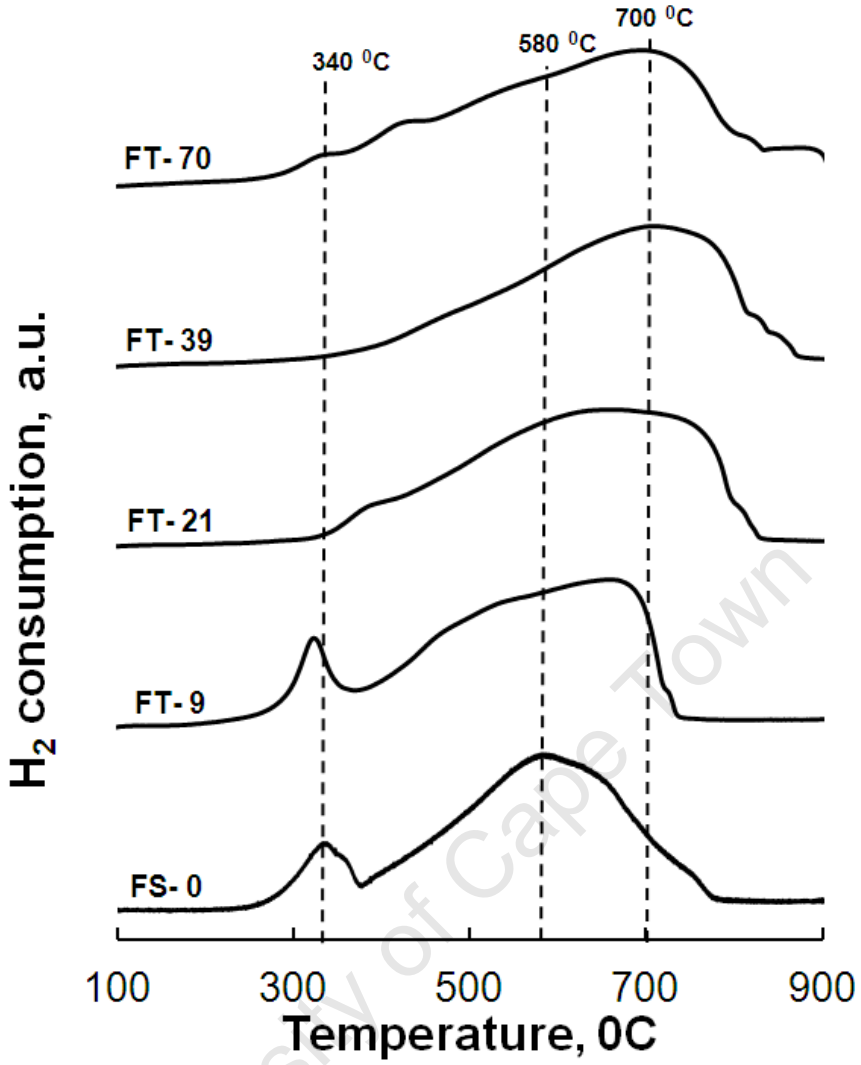


**Figure 6.37:** TPR profiles of the calcined iron oxide nano-crystallites prepared using microemulsion technique and modified with TBO using infinite dilution method.



The reduction of $TiO_2$ supported, Fe-based catalysts, is believed to be hampered by the strong interaction between the active metal and the $TiO_2$ support. The severe nature of this interaction is believed to result in the formation of Fe-$TiO_x$ surface complexes [Tauster et al., 1978; Riva et al., 2000]. It has been shown that the partial reduction of the $TiO_2$ results in a migration of $TiO_x$ species which then interact with the Fe catalyst [Tauster et al., 1978; Tauster et al., 1981]. In light of the data from literature, the proposed reduction steps for TBO modified are depicted in Equation 6.7.

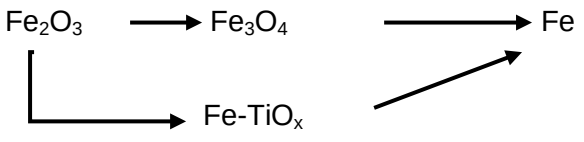


…… (6.7)

Sample FT-9 shows a reduction profile similar to that of the unmodified sample (see Figure 6.37). TEM and XRD data showed that sample FT-9 had a high concentration of small crystallites, which are easy to reduce [Wan et al., 2006; Mabaso, 2005]. Thus, the first reduction peak for sample FT-9 is shifted to a slightly lower temperature when compared to the unmodified sample (FS-0). The peak is much narrower than that of the unmodified catalyst. This indicates that a fraction of the $Fe_2O_3$ might be converted to $Fe_3O_4$ and the remainder is converted directly to the irreducible Fe-$TiO_X$ complexes. The peak maximum for the second reduction peak for sample FT-9 is observed at ca. 580 $^0$C, corresponding to the reduction of $Fe_3O_4$ to α-Fe. This indicates that $Fe_3O_4$ formed in the first step of reduction is reduced to α-Fe at this stage. This is not altered by the presence of titanium in the sample. This supports the hypothesis that the Fe-$TiO_x$ complexes formed in the first stage are difficult to reduce, and also explains the third reduction peak for this catalyst appearing at ca. 700 $^0$C which may represent the reduction of the Fe-$TiO_x$ complex to α-Fe and $TiO_2$ [Yang et al., 2011].

Samples with higher TBO loadings (FT-21 till FT-70) show one reduction step starting at 290 $^0$C and reaching a maximum at ca. 700 $^0$C (see Figure 6.37). This indicates that the iron oxide phase present in these catalysts is hard to reduce. The hydrogen consumption for these samples below 340 $^0$C is very low. This may indicate that the reduction of $Fe_2O_3$ to $Fe_3O_4$ is retarded and that the formation of the Fe-$TiO_x$ species only occurs at high temperatures. The formation and the reduction of these species may overlap resulting in a single broad reduction step. The absence of a clear second reduction peak indicates that once these complexes (Fe-$TiO_x$) are formed, the catalyst can no longer be reduced unless exposed to high temperatures. The conversion of $Fe_2O_3$ to $Fe_3O_4$ appears to be dependent on the Ti-content. It can be deduced from the $H_2$-TPR results that at high TBO loading (FT-21 till FT-70), the formation of the Fe-$TiO_x$ complexes is observed as compared to the conversion of $Fe_2O_3$ to $Fe_3O_4$.

To investigate the extent of reduction in all the catalysts, the total hydrogen consumption for complete reduction at 900 $^0$C was normalized by the mass of the catalyst loaded for $H_2$-TPR analysis. Using the theoretical hydrogen consumption associated with the full reduction of $Fe_2O_3$ to metallic Fe, the degree of reduction of the TBO modified samples was calculated as a ratio of the $H_2$ consumed during reduction to the theoretical $H_2$ required for full reduction of the sample (see Table 6.13).

The unmodified catalyst (FS-0) is almost completely reduced at 900 $^0$C with a degree of reduction of 99%. The TPR analysis indicated that even after 900 $^0$C the modified catalysts were not fully reduced. The overall degree of reduction of the samples declines upon increasing Ti loading. At low TBO loading (FT-9) the degree of reduction dropped slightly to ca. 92%. The remaining catalyst showed a further decline in the degree of reduction with TBO loading. The highest titanium loading (FT-70) has the lowest degree of reduction of 87%.

**Table 6.13:** Quantitative results of $H_2$ consumption up to 900 $^0$C for the TBO modified samples after calcination

| **Sample Code** | **Hydrogen consumption** | |
|---|---|---|
| | **Total** mol $H_2$/mol Fe | **(Percentage Reduction)[a] (%)** |
| **Theoretical[b]** | ***1.50*** | |
| **FS-0** | 1.48 | 99 |
| **FT-9** | 1.38 | 92 |
| **FT-21** | 1.34 | 90 |
| **FT-39** | 1.33 | 89 |
| **FT-70** | 1.31 | 87 |

*a: amount of $H_2$ consumed (mol $H_2$/mol Fe) up to 900 $^0$C relative to the amount of $H_2$ consumed for reduction of $Fe_2O_3$*

### 6.3.2.2 XRD analysis of TBO modified samples after reduction

The TBO modified samples were reduced in $H_2$ (40 ml NTP/min) at 350 $^0$C (heating rate 1 $^0$C/min) for 16 hours. Following that the reduced samples were passivated with $CO_2$ (20 ml/min) for 2 hours and then analyzed with the XRD to monitor the phase composition and crystallite size in the samples prior to Fischer-Tropsch synthesis (see Figure 6.38 and Table 6.15).

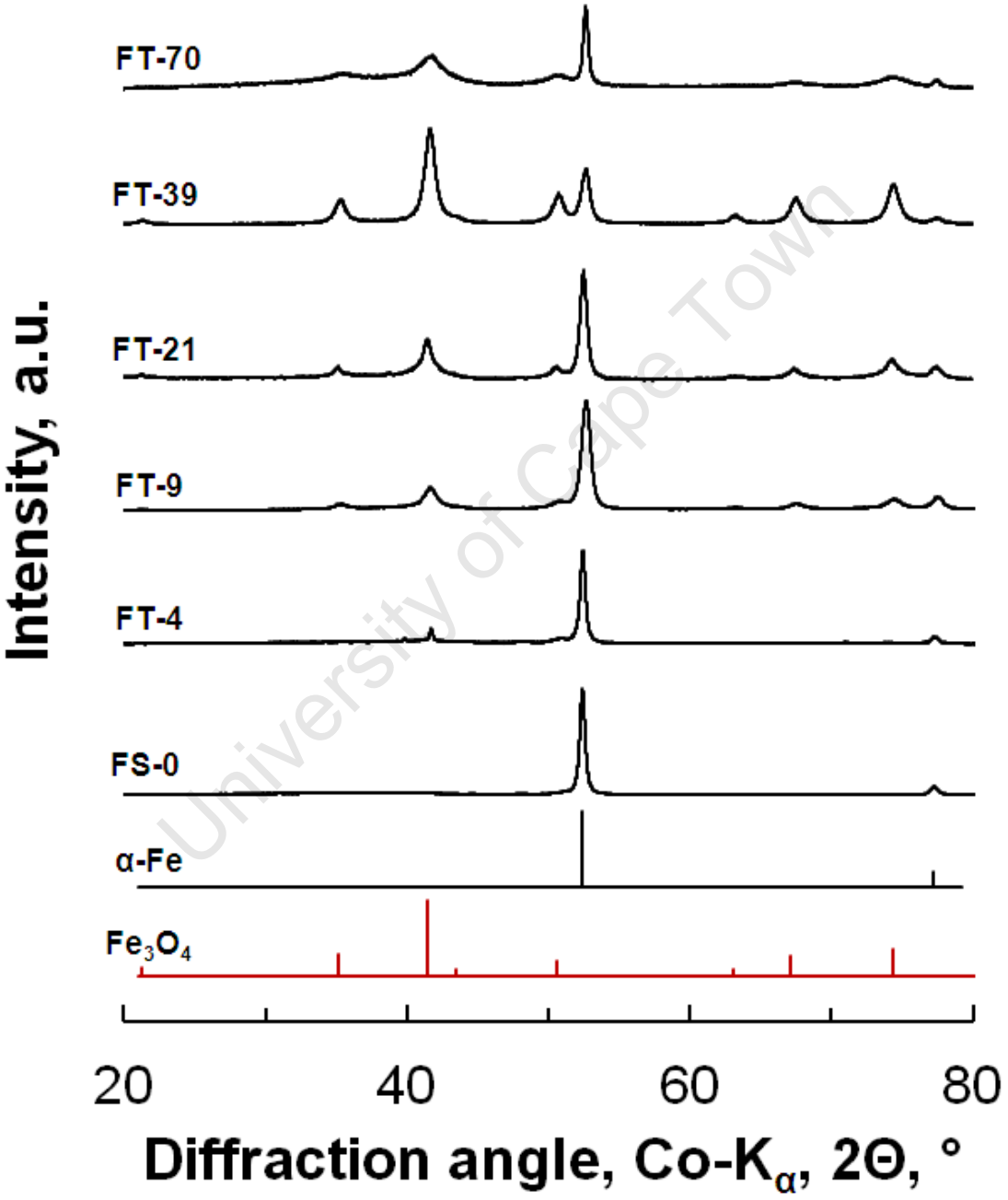


**Figure 6.38:** XRD analysis of the TBO modified samples after reduction in $H_2$ (40 ml (NTP)/min) at 350 $^0$C (heating rate 1 $^0$C) for 16 hours

The XRD patterns of the TBO modified samples indicate the presence of mixed phases, viz. α-Fe and titanomagnetite. Furthermore, XRD analysis also confirmed the absence of a crystalline XRD visible titania phase (as evidenced by the absence of any of the reference diffraction peaks corresponding to both the anatase and rutile phases; see Figure 6.38).

Titanomagnetite occurs as a relic mineral and is stable under room conditions [Broska et al., 2007]. It is formed during reduction of $Fe_2O_3$, when two $Fe^{3+}$ cations are substituted by one $Ti^{4+}$ cation and one $Fe^{2+}$ cation [Yang et al., 2011]. This may occur because the ionic radii of $Ti^{4+}$ and $Fe^{3+}$ are similar (0.68 Å and 0.64 Å respectively) and can, therefore, replace one another via a substitution-type process [Yang et al., 2009]. The iron in the mixed oxide phase can be in the $Fe^{2+}$ state, in which case titanomagnetite $(Fe_{1-x}Ti_x)O_4$ is formed, or in the $Fe^{3+}$ state, where titanomaghemite $(Fe_{1-x}Ti_x)_{\delta-1}O_4$ is formed. The characteristic diffraction peaks for both mixed metal oxide phases are very similar to magnetite. However, the lattice parameters for the two mixed oxide phases are slightly different from that of magnetite. To ensure that the identification of the mixed metal oxide phase in the TBO modified samples was correct, the lattice parameter was calculated at 2θ = 41.4 and are presented in Table 6.14**.** The lattice parameter of synthetic magnetite ($Fe_3O_4$) is 0.840 nm [Yang et al. 2009]. The calculated lattice parameters for the TBO modified sample were ca. 0.835 nm, consistent with both titanomagnetite $(Fe_{1-x}Ti_x)O_4$ [Guigue-Millot et al., 2001] and titanomaghemite $(Fe_{1-x}Ti_x)_{\delta-1}O_4$ [Yang et al., 2011].

**Table 6.14:** Calculated lattice parameters of the reduced TBO modified samples

| Sample Code: | Position of (311) peak 2Θ° | Lattice spacing $d_{311} = n\lambda / (2\sin(\Theta))$ nm |
|---|---|---|
| **Magnetite** | 41.4 | 0.840 |
| **FT-4** | 41.7 | 0.834 |
| **FT-9** | 41.7 | 0.834 |
| **FT-21** | 41.7 | 0.834 |
| **FT-39** | 41.7 | 0.834 |
| **FT-70** | 41.7 | 0.834 |

$\lambda = 1.78*10^{-10}$ m

XRD characterization of the reduced samples showed that TBO addition results in the retardation of the reduction process (see Table 6.15). The titanomagnetite content in the sample increased with increasing TBO loading from 0 % for the unmodified sample to 86 % for the sample with the highest Ti-content (FT-70). The presence of $Ti^{4+}$ cations in the spinel structure of titanomagnetite is believed to improve thermal stability of the oxide making it harder to reduce as compared to magnetite [Yang et al., 2009]. Thus with increasing TBO loading, the amount of titanium available for incorporation will increase, resulting in a decrease in the degree of reduction.

**Table 6.15:** XRD average crystallite sizes and the phase contents of the reduced, TBO modified samples; calculated using Rietveld refinement

| **Component** | | **FT-0** | **FT-4** | **FT-9** | **FT-21** | **FT-38** | **FT-70** |
|---|---|---|---|---|---|---|---|
| **α-Fe** | : content (wt %) | 100 | 73 | 51 | 34 | 15 | 14 |
| | Size (nm): | 39 | 36 | 31 | 33 | 28 | 47 |
| **$(Fe)_{3(1-X)}(FeTi)_XO_4$** | :content (wt %): | none | 27 | 49 | 66 | 85 | 86 |
| | Size (nm): | none | 13 | 8 | 8 | 6 | 4 |
| | **X:** | **-** | **0.07** | **0.12** | **0.15** | **0.18** | **0.24** |



The amount of titanium added to the samples cannot explain the content of mixed metal oxide phases observed. Table 6.16 shows that the Ti-content in the samples prior to reduction (2.10 – 39.1 mg/$g_{sample}$) is too low to account for the formation of bulk mixed-metal oxides ($Fe_2TiO_4$) which require 58.3 – 185.7 mg of Ti per gram of sample. Therefore, it might be speculated that only a fraction of the iron in the crystal structure is substituted with titanium. The partially substituted structure can be formally represented by $(Fe(III)_2Fe(II))_{1-X}(Fe(II)Ti(IV))_XO_4$. The extent of substitution, X, can be calculated from the known elemental analysis (EDX). It can thus be estimated that ca. 7-24 % of the structure is formally titanomagnetite, and the extent of substitution increases with increasing titanium loading (see Table 6.15).

The Ti atoms are interacting with the iron oxide surface prior to reduction. During reduction, cation vacancies are created on the surface allowing for the incorporation of Ti atoms. Therefore, it might be assumed that the mixed oxide phase exist as surface layers surrounding a partially reduced metal oxide phase. To calculate the Ti-contents on these surface layers, the crystallite sizes obtained from XRD (see Table 6.15) were used to calculate the dispersion (assuming a surface density of 9.8 Fe/nm$^2$ for $Fe_3O_4$(111)), which then allows for calculation of the amount of Ti atoms on the surface layers by substitution (X) of Fe atoms (see Table 6.16). The Ti-content in the samples can account for the formation of layers of the mixed oxide phase over an iron oxide bulk (see Table 6.16). At lower TBO loading (FT-4 and FT-9) there is sufficient titanium in the samples to form a monolayer of the mixed metal oxide, given the sizes obtained from the XRD analysis of the samples (see Table 6.15). At higher TBO loadings (FT-39 to FT-70) the results indicate that two layers of the mixed oxide phase can be formed.

**Table 6.16:** The Ti-content in the mixed metal oxide phase calculated based on the XRD analysis of the reduced, TBO modified samples.

| **Sample Code:** | **Calcined EDX-analysis** | **$H_2$ Reduced XRD analysis (Ti-content)** | | |
|---|---|---|---|---|
| | Ti (content) mg/$g_{sample}$ | Bulk $(Fe_2Ti)O_4$ mg/$g_{sample}$ | Mono-layer $(Fe_{3-X}Ti_X)O_4$ mg/$g_{sample}$ | Two-layers $(Fe_{3-X}Ti_X)O_4$ mg/$g_{sample}$ |
| **FT-4** | **2.10** | 58.30 | **1.6** | 3.3 |
| **FT-9** | **5.10** | 114.4 | **5.2** | 10.5 |
| **FT-21** | **13.7** | 142.5 | 6.5 | **13.1** |
| **FT-39** | **24.5** | 183.5 | 11.2 | **22.4** |
| **FT-70** | **39.1** | 185.7 | 17.0 | **34.0** |

The size of the α-Fe seems to decrease with increasing TBO loading from 39 nm for sample FS-0 to 28 nm for the second highest TBO loading (FT-39). However, the average crystallite size (47 nm) of the α-Fe in sample FT-70 is larger. The average α-Fe for all the samples is 36 $\pm$ 8 nm. This indicates that the although Equation 5.3 is correct for the reduction of the sample at temperatures as high as 900 $^0$C, the $H_2$ reduction of the TBO modified samples at 350 $^0$C for 16 hours can be better expressed by Equation 6.8.

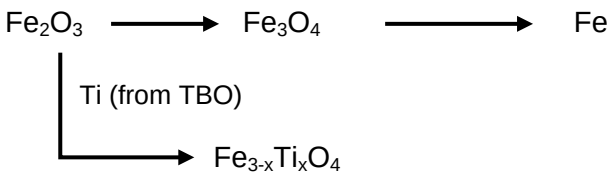


(6.8)

It has been shown that total surface coverage is not reached on any of the modified samples (see Figure 6.36). It can be argued that the unmodified parts of the samples behave similar to sample FS-0 (i.e. reduced from $Fe_2O_3$ to $Fe_3O_4$ to metallic Fe). This explains why the average crystallite size of the α-Fe phase in the samples phase was similar (with a size difference of only 20%).

The presence of titanium in the sample during reduction results in the formation of titanomagnetite. The size of the titanomagnetite was found to decrease with increasing TBO loading from 13 nm for the lowest TBO loading (FT-4) to 4 nm for the highest (FT-70). It has been shown that the size of the mixed oxide phase decreased with an increase in the content of Ti incorporated into the magnetite structure [Diamandescu et al., 2007; Yang et al., 2011]. With increasing TBO loading the Ti-content increases and thus more titanium can be incorporated in the structure resulting in smaller titanomagnetite sizes.

### 6.3.2.3 IR analysis of $H_2$ reduced samples

To investigate the phase transformations of the catalyst during reduction a selected samples, FT-39, was reduced in-situ from at 350 $^0$C (heating rate 1$^0$C/min) for 16 hours and analyzed using FTIR and the results are presented in Figure 6.39.

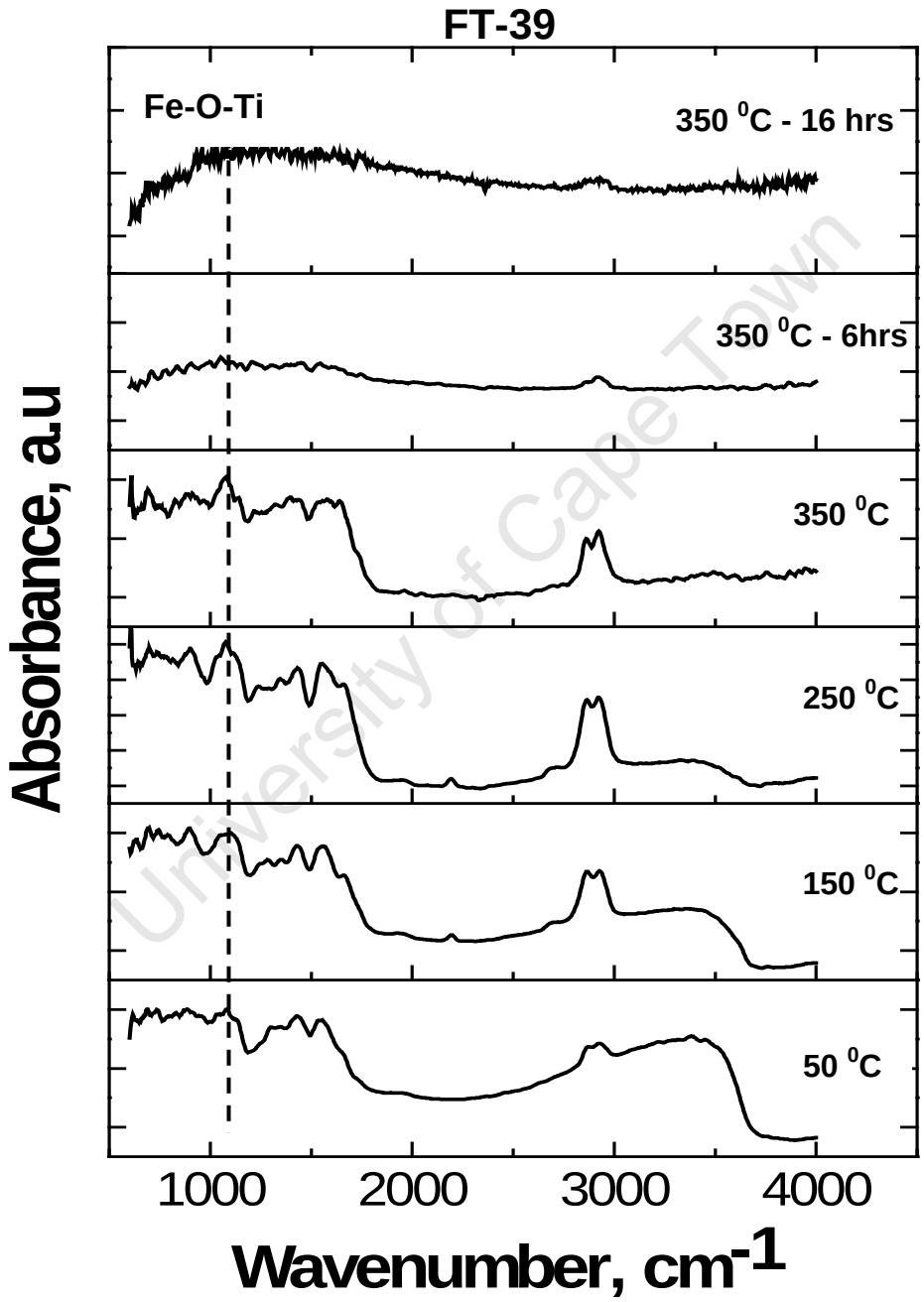


**Figure 6.39:** In-situ FTIR analysis of sample FT-39 during reduction in $H_2$ (40 ml NTP/min) at 350 $^0$C (heating rate of 1 $^0$C/min) for 16 hours.

As the temperature was increased from 50 $^0$C to 250$^0$ C, the -(OH) groups in the samples are removed. This is most likely due to the removal of adsorbed water and is shown by disappearance of the absorption bands at ca. 3460 and ca. 1620 cm$^{-1}$. As the water is removed, the absorption bands at 2800-3000 cm$^{-1}$ due to C-H stretching modes of the butoxide groups, become more visible. The Fe-O-Ti interaction at frequency 1040 cm$^{-1}$ also becomes more pronounced (see Figure 6.39). The intensity of the Fe-O bands is compromised by the visibility limit of the Ge window (600 cm$^{-1}$) used in the in-situ cell. Other absorption bands associated with the butoxide groups; at ca. 900 cm$^{-1}$ and ca. 1500 cm$^{-1}$ (due to the bending and stretching of the C-O bond respectively) and at ca. 890 cm$^{-1}$ (due to stretching of C-C bond), show similar behavior as the C-H stretching modes at ca. 2800-3000 cm$^{-1}$.

The position of the Fe-O-Ti interaction does not change as the temperature is increased from 50 $^0$C to 250 $^0$C. This indicates that at this stage of the reduction the manner in which the Ti is interacting with $Fe_xO_y$ phase in the catalyst is same as in the calcined state, i.e. that the Ti interacts with the iron oxide surface. At temperatures between 250 $^0$C and 350 $^0$C the Fe-O-Ti surface interactions and the butoxide groups are being eliminated. This is shown by the decrease in intensity of the absorption bands at ca. 1040 cm$^{-1}$ and ca. 2800-3000 cm$^{-1}$ respectively. XRD analysis indicates the formation titanomagnetite during $H_2$ reduction of TBO modified samples. This suggests that the decrease in intensity of the Fe-O-Ti absorption band (1040 cm$^{-1}$) is due to incorporation of the Ti atoms into the iron oxide structure. However, the butoxide groups would have to be removed before the Ti atoms can be incorporated thus explaining the shrinking of the absorption bands at ca. 2800-3000 cm$^{-1}$ together with all other bands associated with the butoxide group. The substitution of the butoxide groups with -(OH) constituents can also account for the decrease of intensity. However, that would result in the formation of Ti-OH bonds which yield an adsorption band at ca. 900 - 1125 cm$^{-1}$ [Chen at el., 2009; Yang et al., 2009]. This was not observed.

After 16 hours exposure to $H_2$ at 350 $^0$C there are no peaks visible in the range 600 cm$^{-1}$ to 4000 cm$^{-1}$ for sample FT-39 (see Figure 6.39). All the TBO modified samples show the same trend (see Figure 6.40). Therefore, none of the titanium ligands, in any of the TBO modified samples, are left on the surface after reduction. However, small amounts of butoxide are still present after reduction, indicated by the weak absorption bands at 2800 – 3000 cm$^{-1}$. The oscillations of Ti-O bonds (in $TiO_2$) results in absorption bands at 500-700 cm$^{-1}$ and 1600 cm$^{-1}$ [Roslov et al., 2010]. No absorption bands are visible at these frequencies, indicating that no $TiO_2$ (or possibly a small amount) is formed. XRD analysis also showed the presence of only α-Fe and titanomagnetite in the reduced samples. The absorption bands consistent with titanomagnetite are at 470 and 585 cm$^{-1}$ [Yang et al.,

2009]. This explains why no peaks were found in the IR analysis of the reduced samples since the range was 600-4000 $cm^{-1}$.

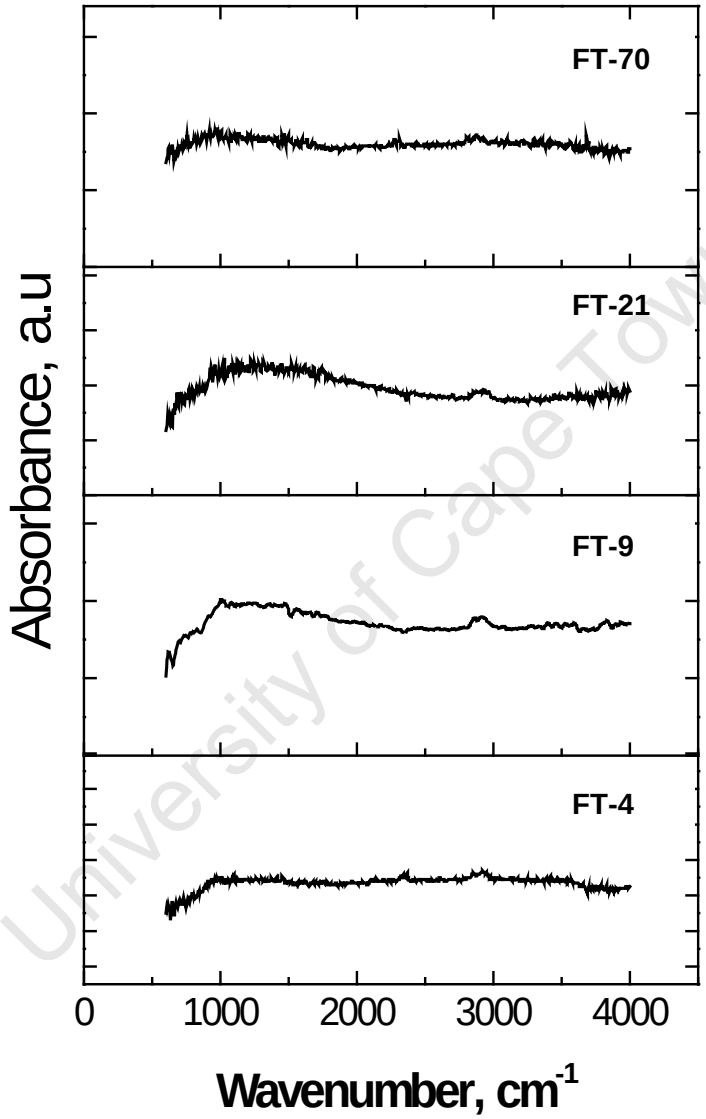




**Figure 6.40:** FTIR analysis of TBO modified samples after reduction in $H_2$ (40 ml NTP/min) at 350 $^0$C (heating rate of 1 $^0$C/min) for 16 hours.

### 6.3.2.4 $H_2$-TPR analysis of reduced samples

The reduction of magnetite ($Fe_3O_4$) and titanomagnetite ($Fe_{3-X}Ti_X)O_4$ is very different since the incorporation of the titanium atoms into the oxide structure improves its thermal stability and makes the mixed metal oxide harder to reduce [Yang et al., 2011]. To confirm the identification of the titanomagnetite as the oxide phase in the catalysts after reduction at 350 $^0$C for 16 hours, these samples were further reduced in a hydrogen/argon mixture using a temperature program (see Figure 6.41). This was done to monitor the reduction behavior of the oxide phases in the reduced samples and also to determine the degree of reduction.

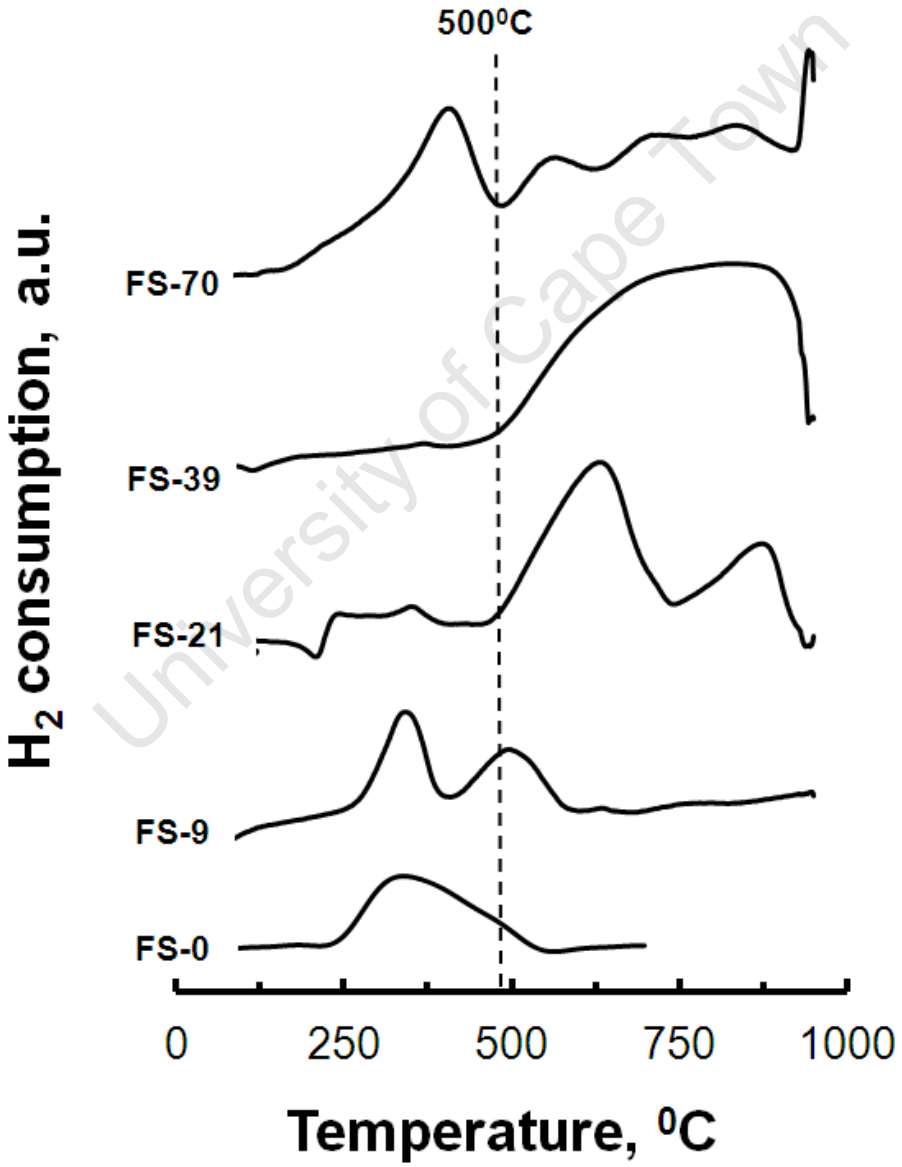




**Figure 6.41:** TPR profiles of the TBO modified samples after reduction in $H_2$ (40 ml (NTP)/min) at 350 $^0$C (heating rate 1 $^0$C) for 16 hours

The shape and nature of the reduction profiles presented by the TBO modified samples are consistent with that reported for the reduction of titanomagnetite $(Fe_{3-x}Ti_x)O_4$ [Yang et at., 2011].

The unmodified sample, FS-0, showed one reduction peak at 360 $^0$C and as previously discussed it represents the conversion of some residual $Fe_3O_4$ to metallic Fe. Sample FT-9 shows a reduction peak at the same temperature (i.e. $Fe_3O_4 \rightarrow Fe$). However, the catalyst also shows an additional reduction peak at 520 $^0$C indicating a reduction of an oxide phase which is harder to reduce. The reduction of samples FT-21 and FT-39 show a broad reduction peaks beginning at 500 $^0$C to higher temperatures. This is consistent with what has been reported for the reduction behavior of $(Fe_{3-x}Ti_x)O_4$ to α-Fe and $TiO_2$ [Yang et al., 2011]. In the case of FT-21, the separation of the peak indicates the formation of transitional phases (e.g. $FeTiO_3$) during the reduction process. The lower temperature reduction of the titanomagnetite in sample FT-9 might be because the reaction is catalyzed. Due to the high α-Fe content in the sample (73 %), hydrogen might be absorbed dissociatively on the iron phase and then spill over to the assist in the reduction process. This would result in a shift of the reduction peak to a lower temperature. A similar behavior has been reported for $Co/SiO_2$ catalysts where with increasing Co content in a sample, the reduction of cobalt silicate moved to a lower temperature [Puskas et al., 2009].

The reduction of the sample with the highest TBO loading (FT-70) was not consistent with the rest of the TBO modified samples. Due to the high ligand coverage (50 %) of the $Fe_2O_3$ surface atoms calculated for this sample in the calcined state, it can be argued that the Ti-ligands would prevent the reduction of the $Fe^{3+}$ cation to $Fe^{2+}$ during the reduction process. However, the conditions used for reduction (350 $^0$C) still facilitate for the incorporation of titanium atoms into the iron oxide structure since preparation of $(Fe_{3-x}Ti_x)O_4$ can be done via thermal treatment at 350 $^0$C [Yang et al., 2011]. However, the incorporation of the Ti atoms into the iron oxide phase whiles it is still in the $Fe^{3+}$ state does not result in the formation of $(Fe_{3-x}Ti_x)O_4$ but rather $(Fe_{3-x}Ti_x)_{1-\delta}O_4$ where (1-δ) is the cation vacancy (δ = (1+x)/(9+x)) [Yang et al., 2011]. The reduction behavior of sample FT-70 is more consistent with what has been reported in literature for the reduction of $(Fe_{3-X}Ti_X)_{1-\delta}O_4$ [Yang et al., 2011]. The first reduction peak at approximately 410 $^0$C represents the reduction of the $Fe^{3+}$ $(Fe_{3-x}Ti_x)_{1-\delta}O_4$ to $Fe^{2+}$ $(Fe_{3-X}Ti_X)O_4$. The broad peak from 500 $^0$C to higher temperatures indicates the reduction of $(Fe_{3-x}Ti_x)O_4$ to α-Fe and $TiO_2$ [Yang et al., 2011]. Furthermore the peaks at 550 $^0$C and 700 $^0$C are believed to indicate the formation of transitional phases during the reduction process [Yang et al., 2011].

The degree of reduction was calculated by normalizing the total hydrogen consumption of the reduced samples to the mass of the $Fe_2O_3$ loaded and the (see Table 6.17). Modification of the iron oxide samples with TBO has a negative effect on the degree of reduction which decreased significantly with increasing Ti-content in the samples. The TBO modified samples showed a degree of reduction between 72-33 %. This is much lower than the unmodified sample which was almost completely reduced.

**Table 6.17:** Quantitative results of $H_2$ consumption for the pre-reduced (350 $^0$C for 16 hrs) TBO modified samples

| Sample Code | Hydrogen consumption | |
|---|---|---|
| | **Total[a]** $Fe_2O_3 \rightarrow Fe$ mol $H_2$/mol Fe | **(Degree of Reduction)[b] (%)** |
| **FS-0** | 0.13 | 91 |
| **FT-9** | 0.41 | 72 |
| **FT-21** | 0.49 | 67 |
| **FT-39** | 1.00 | 33 |
| **FT-70** | 0.93 | 37 |

*a: total hydrogen consumption from 60 $^0$C to 900 $^0$C*

*b: amount of $H_2$ consumed (mol $H_2$/mol Fe) during reduction up to 900 $^0$C of the pre-reduced samples (reduced at 350 $^0$C for 16 hours) relative to the amount of $H_2$ consumed for reduction of $Fe_2O_3$*

### 6.3.2.5 Discussion of the mixed metal oxides formed during the reduction of the samples

It is important to note that the $H_2$-TPR analysis of the reduced samples revealed that although titanomagnetite $(Fe_{3-X}Ti_X)O_4$ is formed at lower TBO loading (FT-4 till FT-38), at high TBO loading titanomaghemite $(Fe_{3-X}Ti_X)_{1-\delta}O_4$ was formed. To explain the results obtained, a simplistic model of the reduction process was designed

**Formation of titanomagnetite $(Fe_{3-X}Ti_X)O_4$ at lower TBO loading (FT-4 till FT-39)**

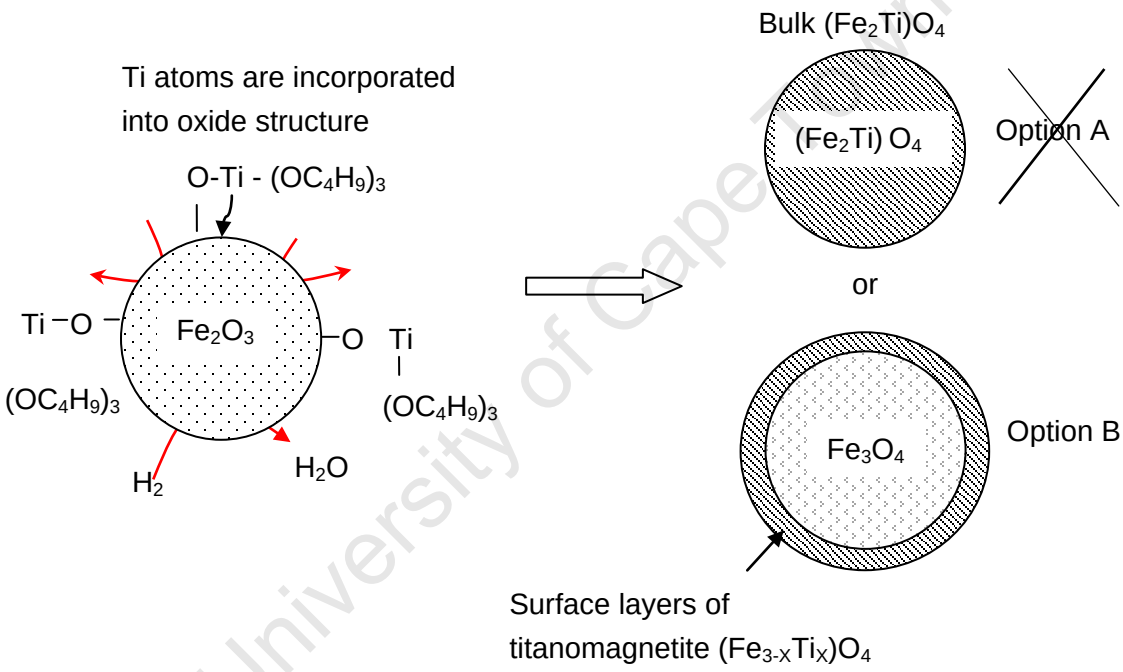




At lower TBO loading, samples FT-4 till FT-21, the calculated ligand surface coverage in the calcined samples was relatively low; from 10 – 31 %. This means that a larger fraction of the surface oxygen was available to be removed by hydrogen during reduction. The reduction of $Fe_2O_3$ to $Fe_3O_4$ involves an increase in the Fe atoms per unit cell from 21.3 in $Fe_2O_3$ to 24 in $Fe_3O_4$. Oxygen is removed from the surface forcing the oxygen in the centre of the structure to migrate outwards and the reduced $Fe^{2+}$ to move into the structure creating cation vacancies. Since the atomic radii of $Fe^{3+}$ (0.64 Å) and that for $Ti^{4+}$ (0.68 Å) are similar, the Ti atoms on the surface can be incorporated into the reduced oxide structure forming a rim of titanomagnetite. However, the bulk phase in the oxide would be magnetite.

**Formation of titanomaghemite $(Fe_{3-x}Ti_x)_{1-\delta}O_4$ at high TBO loading (FT-70)**

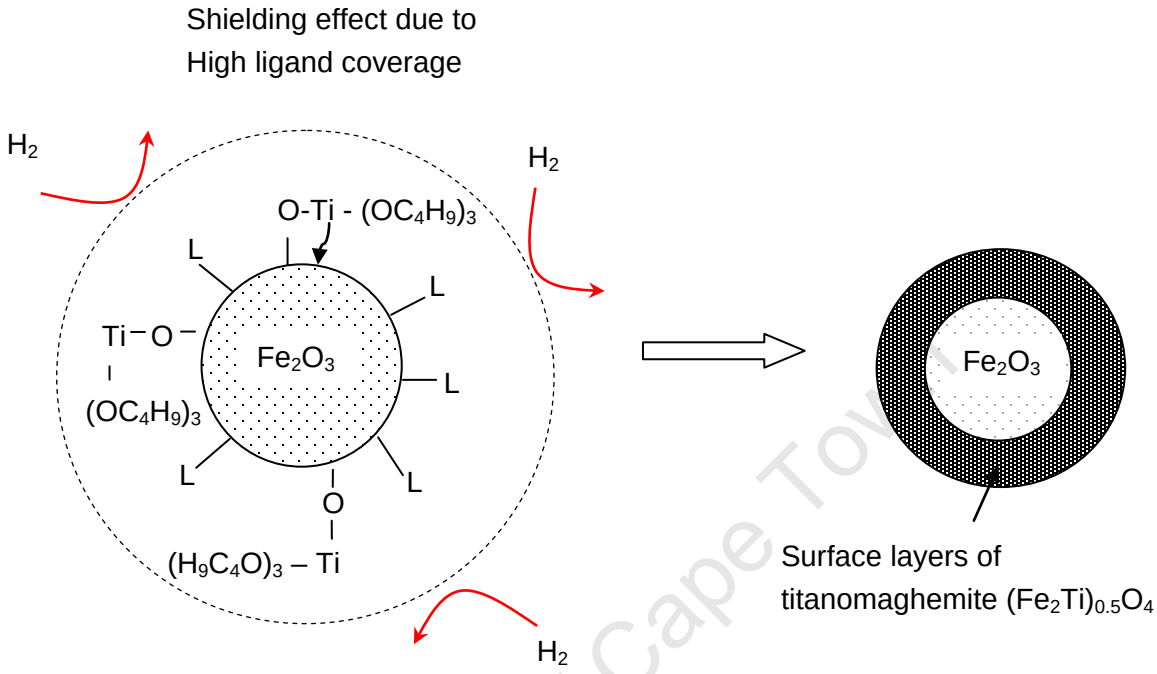


L→ -O-Ti-$(OC_4H_9)_3$

After calcination, at high TBO loading (FT-70), the Ti-ligand surface coverage is high (approximately 50 %). The butoxide groups attached to the ligands are bulky. Therefore, the ligands on the surface of the $Fe_2O_3$ crystallites create a shielding effect, limiting the access of $H_2$ to the surface oxygen during reduction. As a result the reduction of the $Fe_2O_3$ to $Fe_3O_4$ is prevented. However, partial reduction of the surface is still possible, allowing for the incorporation of the Ti into the iron oxide structure. Due to the high concentration of Ti atoms in the sample, once the incorporation occurs no further reduction can take place and the bulk of the Fe atoms in the structure will remain in the $Fe^{3+}$ state. Studies have indicated that an increase in the amount of Ti incorporated into a mixed oxide phase results in a decrease in the crystallite size [Diamandescu et al., 2007; Yang et al., 2011] and this is consistent with the obtained results (see Table 6.15).

### 6.3.3 Characterization of spent catalyst

The degree of reduction of the TBO modified samples was low (see Table 6.17). Therefore, low conversions were expected. As a result, TBO modified samples were tested at two separate temperatures: 250 $^0$C (for comparative analysis with the Fe-O-Si system) and 300 $^0$C (to induce higher activity). All other reaction conditions were kept constant: fixed bed reactor, 20 bar and a space velocity for CO, $F_{CO}$/W of 8.2 mmol/(min·g), 0.1 grams catalyst loading and a feed ratio of 2 ($H_2$/CO). After the Fischer-Tropsch synthesis the catalyst was recovered, passivated and separated from the silica carbide using a 100 µm sieve. The recovered spent catalyst was weighed then analyzed using XRD to determine the phase compositions. (No results for samples FT-39 and FT-70 were obtained for Fischer-Tropsch synthesis due to very low CO-conversion (< 0.5 %) obtained with these catalysts. Therefore, only samples FS-0, FT-4, FT-9 and FT-21 are presented both for Fischer-Tropsch synthesis and spent catalyst analysis)

The spent catalysts recovered from the different operating conditions were analyzed separately. Figure 6.42 shows the XRD analysis for the samples tested at 250 $^0$C whilst Figure 6.43 shows the samples tested at 300 $^0$C. The mass content and the crystallite sizes of the phases present were calculated using Rietveld refinement (see Table 6.18 and Table 6.19). The phase contents presented in these tables were normalized with respect to Fe containing phases. All the other phases present (SiC, wax and graphite) were ignored.

#### 6.3.3.1 XRD analysis samples tested at 250 $^0$C

The analysis of the spent catalyst for the system tested at 250 $^0$C proved a bit problematic. There were large quantities of SiC dust in the spent catalyst of samples FT-4 and FT-9 (see Figure 6.42). Although the SiC phase present in the spent catalysts was identified, its large content, the crystallite size and the overlap of the peaks with the diffraction peak for titanomagnetite at 2θ = 41.4 $^0$ made analysis very difficult. The average crystallite sizes (18 – 32 nm; calculated using Rietveld refinement) for the titanomagnetite phase in these samples were much larger than what was expected (see Table 6.18).

Therefore, the crystallite size for the titanomagnetite was estimated at 2θ = 35.2 $^0$C using the Debye-Scherer equation:

$$d_{XRD} = \frac{k\lambda}{\beta\cos\theta} \quad (6.9)$$

Where λ (0.178 nm) is the X-ray wavelength, k is the shape factor (0.9) and β is the line at full width and half the maximum intensity.

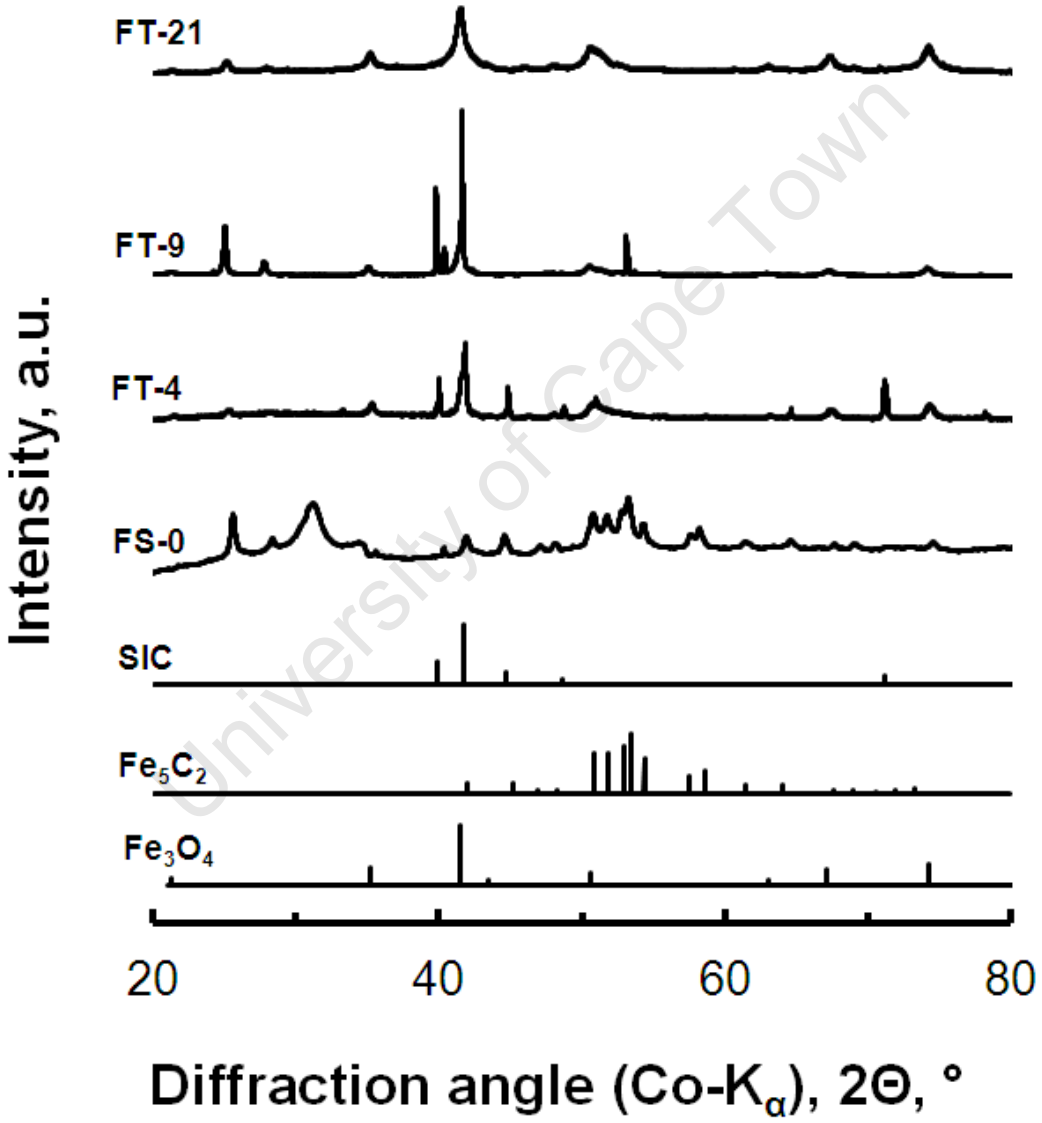




**Figure 6.42:** X-ray diffraction patterns of the spent samples of the TBO modified catalysts tested at 250 $^0$C after 24 hours time on stream. (Also shown are reference patterns of SiC, $Fe_5C_2$ and $Fe_3C_4$).

The average crystallite sizes estimated using the Debye-Scherrer equations were more consistent with the trend observed with the reduced samples, i.e. the average crystallite size of the titanomagnetite phase decreased (14-11 nm) with increasing TBO loading (see Table 6.18).

**Table 6.18:** Average crystallite sizes (in nm) and the quantitative phase analysis of the spent catalyst after 24 hours time on stream at 250 $^{0}$C, estimated using Rietveld refinement

| Component | | FS-0 | FT-4 | FT-9 | FT-21 |
|---|---|---|---|---|---|
| **$Fe_5C_2$:** | content (wt %): | 100 | 67 | 38 | 25 |
| | Size (nm): | 14 | 14 | 11 | 15 |
| **$(Fe_{3-X}Ti_X)O_4$**: | content (wt %): | trace | 33 | 62 | 75 |
| | **X:** | **—** | **0.04** | **0.07** | **0.09** |
| | Size (nm): | n/a | 31 | 18 | 11 |
| | | n/a | *14*[a] | *12*[a] | |

*a: crystallite sizes calculated using the Debye-Scherrer equation.*

Only $Fe_5C_2$ was observed as the carbide phase in all the spent samples (see Table 6.18). The size of the carbide phase (13 $\pm$ 2 nm) is similar in all catalysts. This indicates that the iron carbide crystallites are not affected by the TBO modification. The titanium in the samples is associated with mixed oxide phase. The two phases exist separately. Therefore, the fraction of the sample that is not affected by TBO modification reduces and carburizes in the same manner as the unmodified sample, (FS-0).

The content of titanomagnetite found in the spent catalyst (33-75 wt-%) was higher than that in the reduced samples (27-66 wt-%). In the reduced catalysts, the mole fraction of Fe associated with the α-Fe phase (i.e. $n_{Fe,\alpha\text{-}Fe}/ n_{Total\text{-}Fe,\ reduced\ sample}$) is between ca. 42-79 mol-%. The Fe content decreased with increasing TBO loading. Assuming that the degree of substitution (X) does not change during Fischer-Tropsch synthesis, the mole fraction of Fe in the carbides phase (i.e. $n_{Fe,\ Carbies} / n_{Total\text{-}Fe,\ spent\ catalysts}$) is lower (31-72 mol-%) than the mole fraction of Fe in the active phase prior to reaction. This implies that some of the

metallic iron is transformed into the oxide phase during Fischer-Tropsch synthesis, possibly due to oxidation with water. The increase in the number of moles associated with the oxide phase results in a decrease in the degree of substitution (X). It decreases to ca. 4-9% (see Table 6.18) as compared to reduced samples (ca. 7-15%; see Table 6.15). This shows that there is relatively more $Fe_3O_4$ in the oxide phase than titanomagnetite.

### 6.3.3.2 XRD analysis of samples tested at 300 $^0$C

The separation of the SiC dust and the samples tested at 300 $^0$C was much better. The phases identified using the reference patterns were titanomagnetite $(Fe_{3-X}Ti_X)O_4$, $Fe_2C$ and $Fe_2C_5$ (see Figure 6.43). The unmodified sample only showed trace amounts of magnetite (less than1 wt-%).

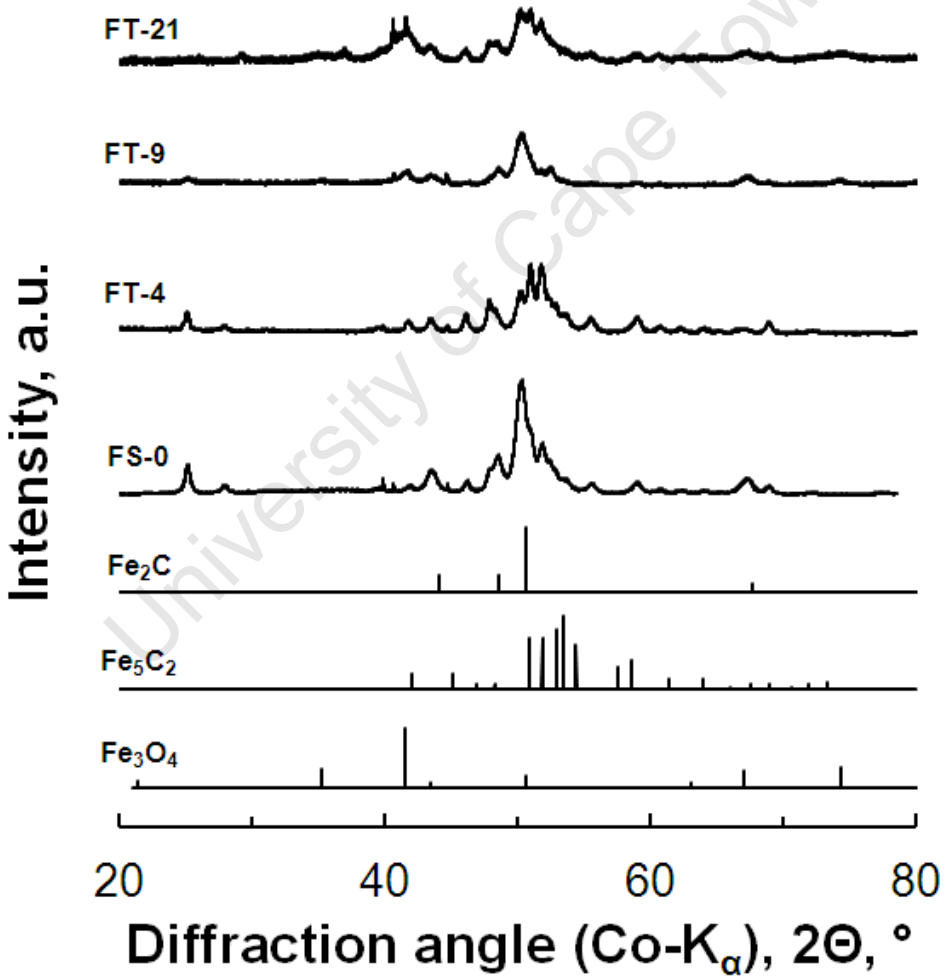




**Figure 6.43:** X-ray diffraction patterns of the spent samples of the TBO modified catalysts after 24 hours time on stream at 300$^0$C. (Also shown are reference patterns of $Fe_2C$ and $Fe_5C_2$ and $Fe_3O_4$).

An improved degree of reduction was observed for all the TBO modified samples after Fischer-Tropsch synthesis at 300 $^0$C. This is indicated by the decrease in the oxide content in TBO modified samples. The reduced samples contained between 27- 66 wt-% of the oxide phase which decreases to 8-44 wt-% (see Table 6.19). CO is a stronger reducing agent than $H_2$. Therefore, CO in the system at 300 $^0$C might improve the degree of reduction.

The amount of Fe associated with the oxide phase decreases from ca. 21-57 mol-% in the reduced samples to ca. 9-45 mol-% in the spent catalysts. As a result, the degree of substitution (X) in the samples increases from ca. 7-15 % (in the reduced samples) to 12-17 % for the spent catalysts (see Table 6.19). If the degree of Ti substitution (X) is assumed to remain the same during Fischer-Tropsch synthesis (this is based on $H_2$-TPR analysis which showed that these oxide are hard to reduce), it can then be suggested that a fraction of the titanium in the sample might be removed from the mixed oxide phase during the reaction. This may occur either through the formation of $TiO_2$ or, the Ti atoms in the mixed oxide phase might be pushed back out to the surface. These possibilities are discussed in detail in the FTIR analysis of the samples (see Section 6.3.3.3).

**Table 6.19:** Average crystallite sizes (in nm) and the phase quantitative analysis of the spent catalyst after 24 hours time on stream at 300$^0$C, estimated using Rietveld refinement

| Component | FS-0 | FT-4 | FT-9 | FT-21 |
|---|---|---|---|---|
| $Fe_5C_2$: content (wt %): | **76** | **88** | **51** | **52** |
| Size (nm): | **22** | **23** | **13** | **16** |
| $Fe_2C$: content (wt %): | **24** | **4** | **14** | **4** |
| Size (nm): | **15** | **15** | **15** | **17** |
| $(Fe_{3-X}Ti_X)O_4$: content (wt %): | **trace** | **8** | **34** | **44** |
| Size (nm): | **n/a** | **5** | **7** | **5** |
| X: | **-** | **0.12** | **0.09** | **0.17** |

The unmodified sample (FS-0) contained 76 wt-% $Fe_5C_2$ carbide and 24 wt-% $Fe_2C$ (see Table 6.19). The TBO modified samples also showed a mixture of the same carbides. However, the $Fe_2C$ content is less in these catalysts (4 - 14 wt-%) and the dominant carbide phase in all the TBO modified samples is $Fe_5C_2$ (88- 51 wt-%). Past work has indicated that, during carburization of α-Fe, O-carbides (e.g. $Fe_2C$) are initially formed prior to being converted to TP-carbides (e.g. $Fe_5C_2$) [de Smit et al., 2010]. This is because O-carbides are thermodynamically more stable than TP-carbides under Fischer-Tropsch conditions used here [de Smit et al., 2010]. Thus, the incomplete conversion of the $Fe_2C$ to $Fe_5C_2$ during Fischer-Tropsch synthesis can explain the co-existence of both carbide phases in the spent catalysts. $Fe_2C$ makes up 24 % (wt/wt) of the carbide phases in the unmodified sample. Sample FT-9 contains 22 % (wt/wt) of the same carbide. This indicates that the formation of the $Fe_5C_2$ in this sample is similar to that of the unmodified sample, implying that the presence of the titanium in the sample has no impact in the phase transformation.

On the other hand, the $Fe_2C$ content in the carbide phase of samples FT-2 and FT-21 is observed to be ca. 4 and 7 % respectively. For the sample with high titanium loading (FT-21), 93 mol-% of the Fe in the carbide phase in the spent catalyst is $Fe_5C_2$. If the α-Fe phase in the reduced samples of this catalysts is assumed to carburize normally (using unmodified sample (FS-0) as a reference point) then only 88 mol-% of the Fe in the carbides should be associated with the $Fe_5C_2$ phase. Assuming that the moles of iron gained by the carbide phase during Fischer-Tropsch synthesis (due to improved degree of reduction) are converted to $Fe_5C_2$, the content of this phase in the spent samples increases to 92 mol-%, consistent with what is observed. This implies that the reduction of titanomagnetite only yields $Fe_5C_2$ carbide under the applied reaction conditions. The increase in the $Fe_2C_5$ content in the TBO modified samples might result from stabilization of this phase by the presence of Ti atoms during reduction. The presence of other material (e.g. $TiO_2$) within the catalyst formulation has also been shown to impact the type of carbides that are formed during Fischer-Tropsch synthesis [Niemanstverdriet et al., 1980]. $Fe_2C_5$ is typically found as the dominant carbide phase in $TiO_2$ supported Fe-based catalysts after Fischer-Tropsch synthesis [Duvenhage and Coville, 2002].

The average crystallite size (16 $\pm$ 1 nm) for the $Fe_2C$ phase was found to be consistent for all the samples. There appears to be no effects due to TBO modification. The average crystallite size of $Fe_5C_2$ was a function of the phase content. Samples with large $Fe_5C_2$ contents (FS-0 and FT-4) have a large average crystallite size for this phase (see Table 6.19). The majority of the $Fe_5C_2$ in the spent sample is formed by carburization of the α-Fe in the reduced samples. Therefore, the sizes of the $Fe_5C_2$ can be related to the α-Fe phase from which they were formed. Samples FT-9 and FT-21 show smaller α-Fe average

crystallite sizes (31 and 33 nm) after reduction and this correlated to $Fe_5C_s$ crystallite seizes of 13 and 16 nm respectively. Whilst samples FS-0 and FS-10 had larger α-Fe average crystallite sizes (39 and 36 nm) which might result in larger $Fe_5C_2$ average crystallite sizes (22 and 23 nm respectively). Therefore, it may be suggested that TBO modification plays no role in the average crystallite sizes of the carbide phase. A point of noticeable interest was that the size of the titanomagnetite was similar for all the modified catalyst, approximately 6 $\pm$ 1 nm, despite the difference in the Ti-content.

### 6.3.3.3 IR analysis of spent catalysts

The recovered spent catalyst was then analyzed using FTIR (transmission mode) to observe if the Ti ligands were present after reaction (see Figure 6.44). The cluster of sharp adsorption bands in the region between 2700 $cm^{-1}$ and 3000 $cm^{-1}$ are due to various types on C-H stretching [Roslov et al., 2010]. This indicates the presence of wax in all the spent catalysts. The broad absorption band at 580 $cm^{-1}$, for sample FS-0, corresponds to the stretching Fe-O bond which consistent with the presence of small amounts of magnetite [Koneracká et al., 2008; Yang et al., 2009].



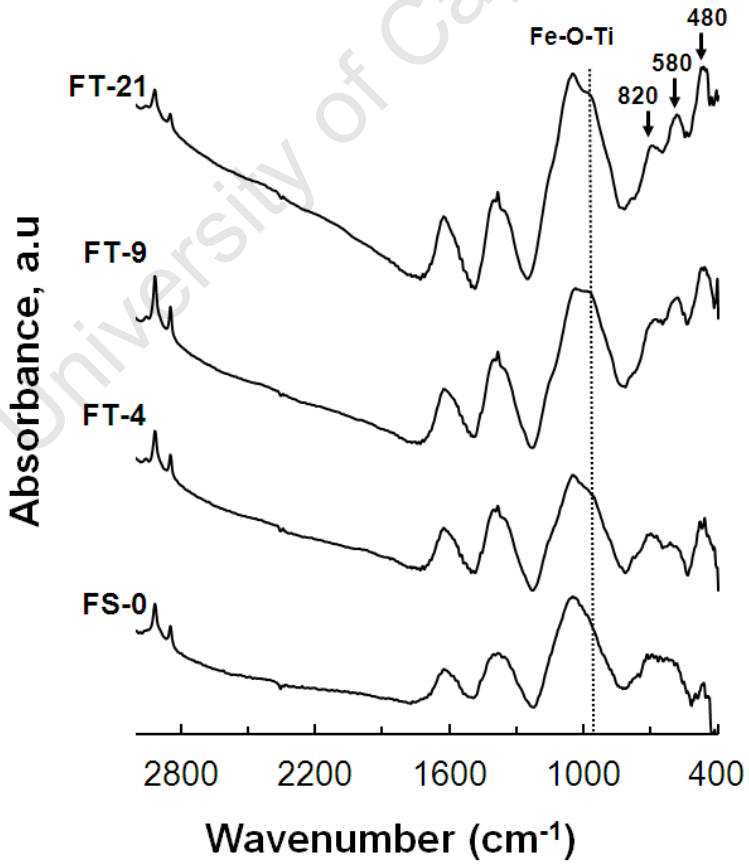


**Figure 6.44:** FTIR analysis of the TBO modified spent catalysts taken after 24 hours time on stream at 300$^0$C.

The absence of an adsorption band at a frequency of 1200 $cm^{-1}$ implies the lack of strongly crosslinked Ti-O-Ti interactions [Hamadanian et al., 2011]. This shows that the Ti ligands did not interact with each other to form $TiO_2$ complexes.

There two main differences between the IR spectrum of the unmodified, FS-0, and the spectra of all the TBO modified catalyst. The first dissimilarity is that all the modified catalysts show three absorption bands at 480, 580 and 820 $cm^{-1}$ which characterize the presence of titanomagnetite, $Fe_{3-X}Ti_XO_4$, [Yang et al., 2009]. The intensity of the absorption band at ca. 480 appears to increase with increasing TBO loading. The vibration that occurs at this frequency is attributed to the presence of titanium in the magnetite structure [Yang et al., 2009]. This shows that the titanomagnetite content in the analyzed samples increases with increasing TBO loading. The band at ca. 580 $cm^{-1}$ is characteristic to the vibration of magnetite [Koneracká et al., 2008; Yang et al., 2009]. This was to be expected since the bulk of the titanomagnetite structure consists of the magnetite phase, i.e. the degree of substitution is only ca. 12-17% in the TBO modified samples (see Table 6.19). The band at 820 $cm^{-1}$ is ascribed to M-OH bending mode. It has been shown that the intensity of this band becomes enhanced with increasing Ti-content in synthetic $Fe_{3-X}Ti_XO_4$ [Yang et al., 2009], consistent with the observed results.

The second dissimilarity is an additional absorption band at ca. 980 $cm^{-1}$. The intensity of this band was also observed to increase with increasing Ti-content the samples. The FTIR results of the reduced catalysts (see Figure 6.44) shows that the Fe-O-Ti interactions in a mixed metal phase do not give any absorption bands at frequencies higher than 600 $cm^{-1}$. XRD analysis of the spent catalysts shows an increase the degree of substitution in titanomagnetite phase (this is assuming that all the titanium in the sample is associated with the oxide phase; see Table 6.19). However, if the extent of substitution is considered to remain constant throughout the catalyst life then the titanium content in the oxide phase could not account for the total titanium loaded. Ti-O-Ti interactions were excluded using FTIR. Therefore, some of the titanium could be associated with the carbide phase. Based on this assumption, the absorption band at 980 $cm^{-1}$ might be ascribed to the interaction between the Ti-ligands and Fe surface atoms on carbide phase of the spent catalysts. This assignment is also supported by the position of this absorption band, which is consistent with the position of the absorption bands for surface Fe-O-Ti interactions (1040 -1120 $cm^{-1}$) found in the calcined samples. The red shift in frequency might result from the change in the ligand constituents. In the calcined sample the titanium ligands were attached to butoxide groups whiles in the spent catalyst they are most likely attached to -(OH) groups.

### 6.3.4 Fischer-Tropsch synthesis

Prior to Fischer-Tropsch synthesis all the catalysts were reduced in-situ in 40 ml (NTP)/min $H_2$ at 350 $^0$C for 16 hours. The Fischer-Tropsch activity of the materials modified by addition TBO were tested in a fixed bed reactor at 20 bar and a space velocity for CO, $F_{CO}$/W of 8.2 mmol/(min·g). A total of 0.1 grams of catalyst was distributed over 6 grams of silica carbide. A feed gas with a $H_2$ to CO ratio of 2 was passed over the catalyst and the tested for a period of 24 hours. The samples were tested at two separate temperatures; firstly at 250 $^0$C and then again at 300 $^0$C. The CO-conversion was determined as a function of Ti-loading (see Figure 6.45). Note that results for samples FT-39 and FT-70 are not presented since the CO-conversion attained with these catalysts was too low. This can be explained by the low degrees of reduction (FT-39 = 33 % and FT-70 = 37 %; see Table 6.17) that were attained for these samples.



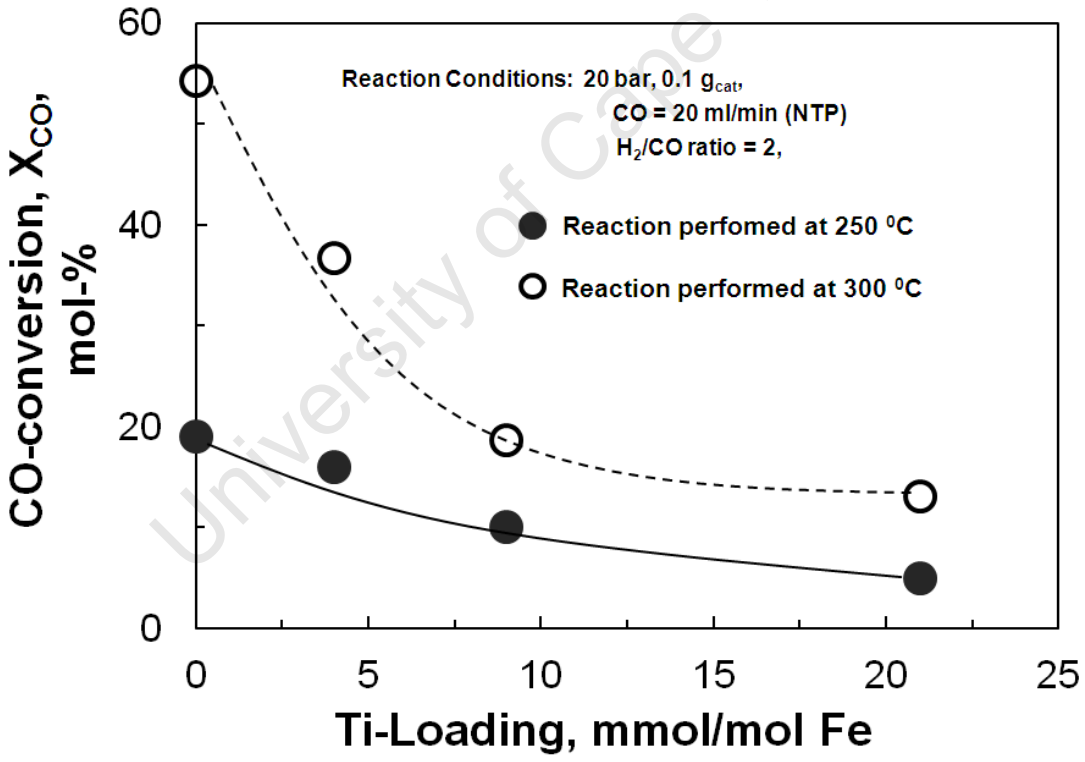


**Figure 6.45:** The steady state Fischer-Tropsch CO-conversion of the TBO modified iron oxide samples taken after 24 hours time on stream represented as a function of Ti loading (Operating temperature: ● 250 $^0$C , ○ 300 $^0$C)

As expected, Fischer-Tropsch synthesis at a higher temperature (300 $^0$C) yielded higher conversions compared to the lower operating temperature (250 $^0$C). The steady state CO-conversion decreases with increasing TBO loading for both the operating temperatures. For the system operated at 250 $^0$C, the conversion drops from 19 % for the unmodified iron oxide sample (FS-0) to 5 % for the sample with highest TBO loading that was tested (FT-21). Whilst at an operating temperature of 300 $^0$C, the conversion drops from 54 % to 13% for the respective samples (see Figure 6.45**)**.

The results for the steady state CO-conversion are consistent with the observed decrease in the degree of reduction with increasing TBO loading. The iron oxide phase is believed to be inactive or at least less reactive for Fischer-Tropsch synthesis [Li et al 2002a]. At the beginning of the Fischer-Tropsch testing, after reduction in $H_2$ for 16 hours, the degree of reduction is 100 wt-%, for the unmodified iron oxide sample (FS-0) and decreases with increasing TBO loading to 67 % for highest tested TBO loading, sample FT-21. Furthermore the analysis of the spent catalysts showed the same trend in carbide content which decreased from 100 wt-% (FS-0) to 25 wt-% (FT-21) for the catalysts tested at 250 $^0$C and decreases from 100 wt-% (FS-0) to 56 wt-% (FT-21) for the samples tested at 300 $^0$C. The decrease in the carbide content is consistent with the observed decrease in CO-conversion with increasing TBO loading.



### 6.3.5 $CO_2$-selectivity for TBO modified catalysts

The steady state $CO_2$ selectivity of the TBO modified samples tested at 250 $^0$C and at 300 $^0$C is presented in Figure 6.46. $CO_2$-selectivity increases from 5-21 mol-% with increasing TBO loading, for the samples tested at 250 $^0$C. Conversion decreases with increasing TBO loading, indicating a higher probability of oxygen removal via $H_2O$ formation compared to $CO_2$ formation. Analysis of the spent catalyst for the system tested at 250 $^0$C showed that the phase content of the titanomagnetite increases with increasing TBO modification form 0 % in sample FS-0, to 75 % in the highest tested TBO loading (FT-21). Since magnetite is believed to responsible for water gas shift activity [Rao et al., 1995; van der Laan, 1999; Newsome, 1980], it stands to reason that the titanomagnetite might have similar catalytic capabilities. Therefore, the increase in $CO_2$ selectivity with increasing TBO loading might result from secondary formation via the water gas shift reaction occurring on the titanomagnetite surface. However, sample FS-0 does not contain titanomagnetite. Hence, at least some of the $CO_2$ must be formed in the carbide phase.

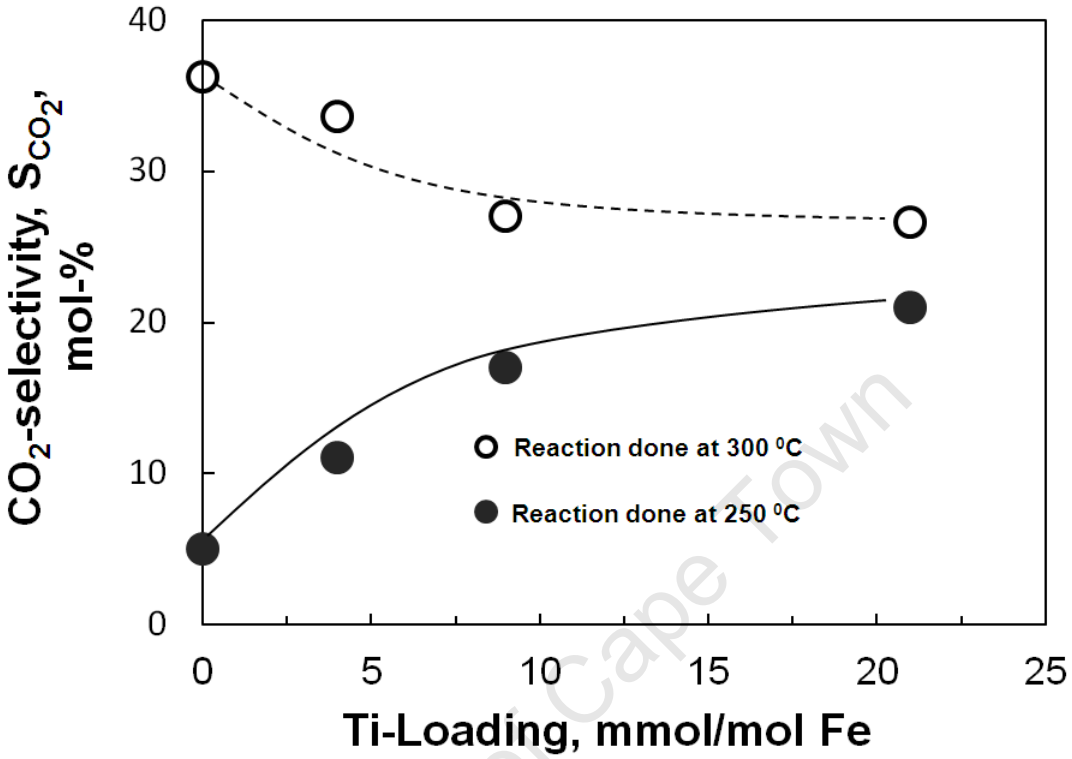


**Figure 6.46:** The steady state Fischer-Tropsch $CO_2$ selectivity of the TBO modified iron oxide samples taken after 24 hours time on stream represented as a function of Si loading.



The $CO_2$ selectivity obtained when the catalysts were tested at 300 $^0$C is higher than the selectivity obtained at 250 $^0$C. Furthermore, the $CO_2$ selectivity decreases from 38 to 26 % with increasing TBO loading. This related to the CO-conversion, which decreases with increasing TBO loading, implying that at these conditions, the primary formation of $CO_2$ from the removal of surface oxygen becomes more dominant compared to the formation of $CO_2$ as a consecutive reaction via the water gas shift reaction. Therefore, as conversion increases the $CO_2$ selectivity is expected to increase despite the increase in titanomagnetite content in the samples, which is observed with increasing TBO loading.

## 6.3.6 Selectivity for the formation of organic products

**Methane selectivity and chain growth probability for the TBO modified samples**

The methane selectivity is of great significance because methane is the least valuable product of the Fischer-Tropsch process and from an economic point of view methane selectivity should be kept as low as possible. The methane selectivity of the TBO modified catalysts obtained after 24 hours time on stream for both operating temperatures (250 $^0$C and 300 $^0$C) as a function of Ti loading are shown in Figure 6.47.

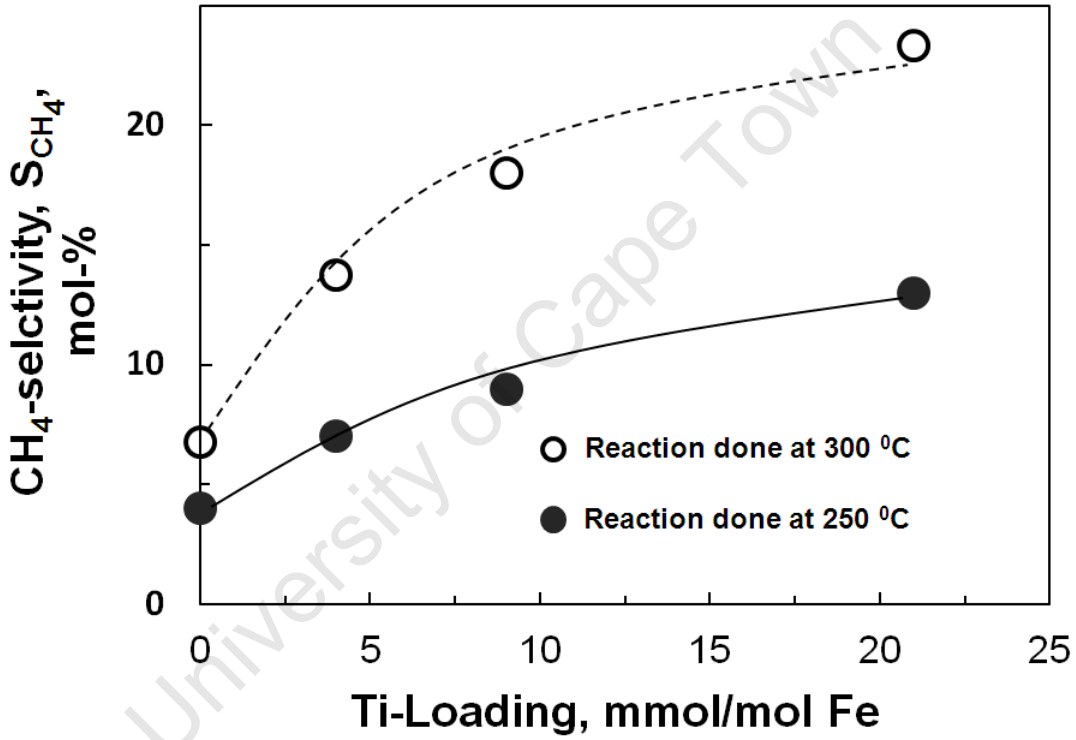




**Figure 6.47:** The steady state Fischer-Tropsch $CH_4$ selectivity of the TEOS modified iron oxide samples taken after 24 hours time on stream represented as function of Si loading.

The methane selectivity, for both operating temperatures, was found to increase with increasing TBO loading (see Figure 6.47). All the modified catalyst showed higher methane selectivity as compared to the unmodified iron oxide sample, FS-0. The methane selectivity for the samples tested at 250 $^0$C increased from 4 mol-% for the unmodified catalyst (FS-0) to ca. 13 mol-% for the highest modification (FT-21). Whilst the samples tested at 300 $^0$C was found to increase from 7 mol-% for the unmodified samples (FS-0) to 23 mol-% for the

highest tested TBO loading (FT-21). With such a significant change in the methane selectivity, the most obvious explanation would be that the enhanced methane selectivity resulting from a higher hydrogen availability on the catalyst surface [Schulz et al., 1994] induced by TBO loading.

Hand in hand with the methane selectivity is the catalyst ability to make long chain hydrocarbons. The chain growth probability was used to estimate the probable yield of long chain hydrocarbons in the product spectrum. The chain growth probability (α), calculated between $C_3$ – $C_9$ using the Anderson-Schulz-Flory equation (see Appendix A), of the TBO modified samples as a function of Ti loading are presented in Figure 6.48.

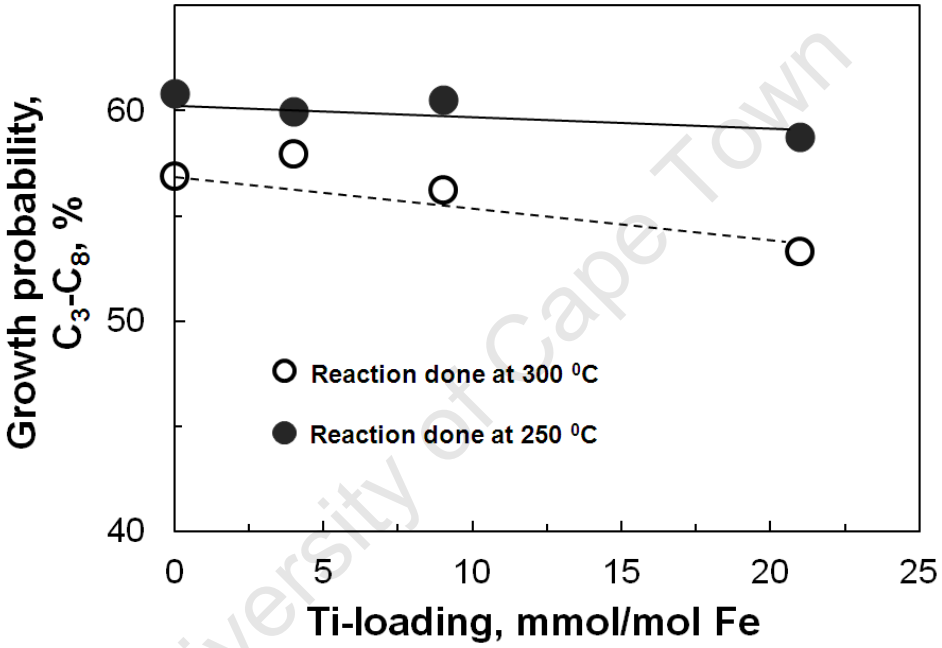


**Figure 6.48:** The chain growth probability ($C_3$-$C_8$) of the TEOS modified iron oxide samples taken after 24 hours time on stream represented as a function of Si loading**.**

The results also show that the chain growth probability ($C_3$-$C_8$) decreases only slightly with increasing TBO loading (see Figure 6.48). For the samples tested at 250 $^0$C, the unmodified iron oxide sample (FS-0) showed a chain growth probability of 61 % and the highest tested TBO loading (FT-21) showed a chain growth probability of 59 %. Samples with lower TBO loadings (FT-4 and FT-9) both show a growth probability of approximately 60 %. The samples tested at 300 $^0$C also show a decrease in chain growth probability from 57 to 52 % with increasing TBO loading. From these results it may be deduced that the effect of TBO modification on the chain growth probability is not significant. This was puzzling considering the difference in the methane selectivity of these samples. This led to

the conclusion that the changes in selectivity might not be caused by hydrogen availability but some other factor relating to TBO modification.

**Olefin selectivity of the TBO modified system**

To investigate the possible increase in hydrogen availability due to TBO modification the total olefin selectivity in the $C_5$ cut of the TBO modified catalysts obtained after 24 hours time on stream for both operating temperatures were calculated and are presented as a function of Ti loading and shown in Figure 6.49. Also shown in the same figure is the selectivity of the alpha olefin for all the tested samples as a function of Ti loading.

TBO loading does not seem to affect the total olefin selectivity in the $C_5$ cut significantly. For the sample tested at 250 $^0$C, the unmodified iron oxide sample, FS-0, show a total olefin selectivity of 88 mol-% and the selectivity of the highest tested TBO loading, FT-21, showed a selectivity of 82 mol-%. The intermediate TBO loadings, FT-4 and FT-9, were covered by a difference of $\pm$ 4 mol-%. The samples tested at 300 $^0$C showed similar trends. Both the total olefin and α-olefin selectivity decreased with increasing TBO loading. The total olefin selectivity decreased from 81 to 74 mol-% with increasing TBO loading. The slight decrease (6 % drop) in total olefin content with increasing TBO loading, for both operating temperatures, highlighted a slight improvement in the hydrogenation capabilities of the catalysts with increasing TBO loading.

The α-olefin selectivity of these catalysts shows a more significant change. The α-olefin content in the fraction of linear olefins decreases from 70 % to 51 % with increasing TBO loading when the samples were tested at 250 $^0$C. The α-olefin selectivity declines from 52 % to 31 % for the respective catalysts when tested at 300 $^0$C. The significant change in the between the total olefin and the 1-olefin selectivity indicates a high degree of double bond isomerization.

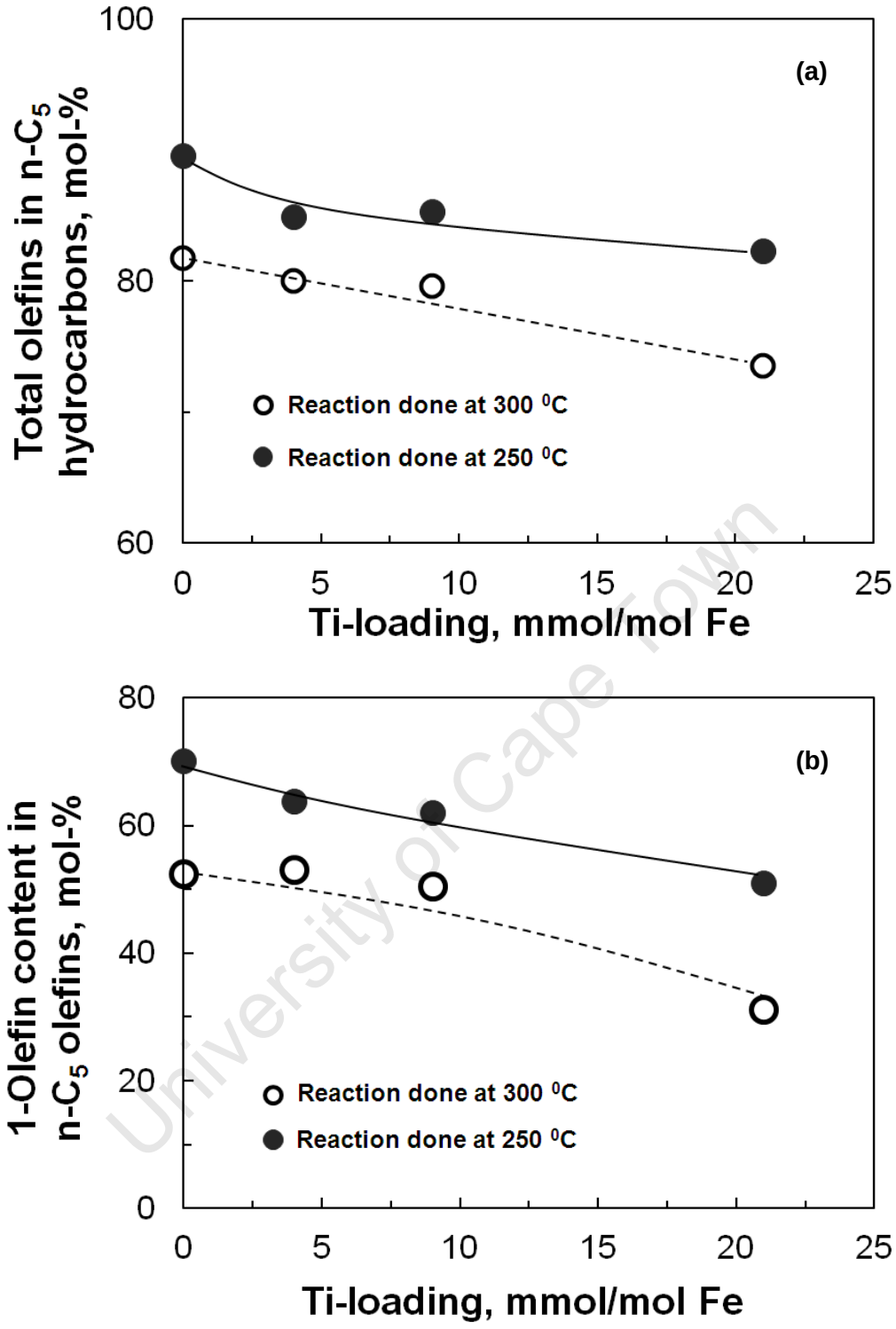




**Figure 6.49**: $C_5$ olefin selectivity of the TBO modified catalyst taken at 24 hours time on stream as function of Ti content.

(a) The total olefin content of the $C_5$ cut in n-$C_5$ hydrocarbons

(b) The selectivity of the 1-olefin expressed as function of the total linear olefins in the $C_5$ cut

Since the total olefin selectivity of the catalysts were similar but the selectivity of the different olefins within the $C_5$ group was so different, it can be seen that TBO modofication promotes double bond isomerisation of the 1-olefin. The next step would be to investigate the degree of branching as an indicator of skeletal isomerisation.

**Degree of branching selectivity for the TBO modified samples**

To investigate the effects of TBO addition in the degree of branching, the ratio of branched to linear hydrocarbons in the $C_5$ fraction as a function of Ti loading for both operating temperatures are shown in Figure 6.50. The unmodifed sample showed a higher degree of braching than all the titanium containing samples. The degree of branching increases with conversion [Claeys, 1997]. The coversion decreases significantly with increases TBO loading (see Figure 6.45), which may contribute to the observed decrease in the degree of branching with between the sample FS-0 and the TBO modified samples. However, amongst the TBO modifies samples, selectivity towards brached compounds increases from 20 to 24 mol-% with titanium content despite the decrease in conversion.

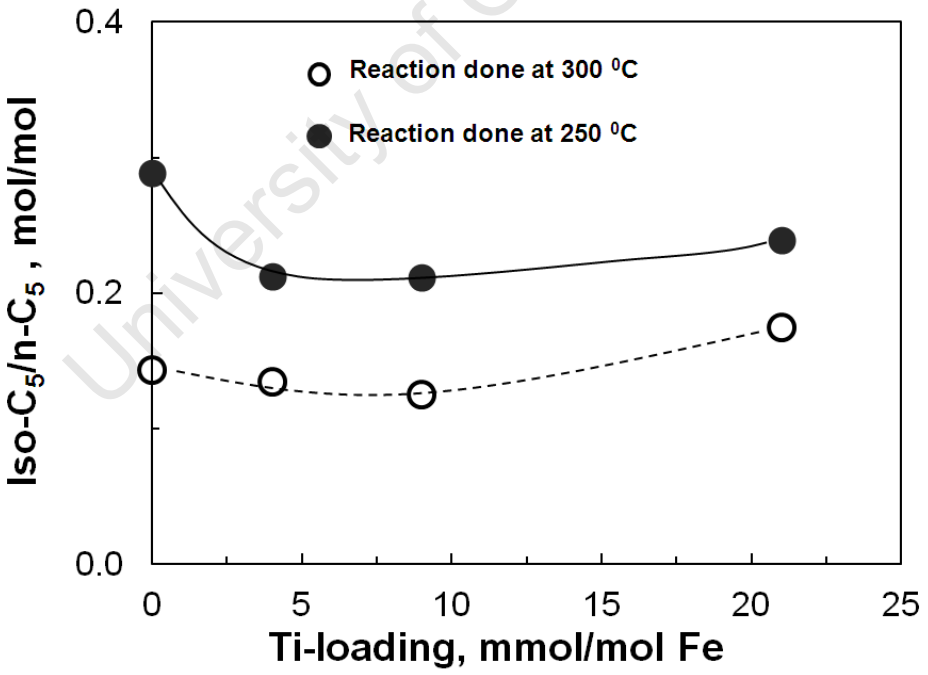


**Figure 6.50:** The total oxygenate content $C_5$ fraction for TBO modified iron oxide samples taken after 24 hours time on stream represented as a function of Ti loading.

This effect is more evident at high temperatures where the degree of branching is similar for the unmodified sample (FS-0) and the sample with low TBO loading (FT-4 and FT-9) at approximately 13 % despite the significant difference in conversion and at the highest tested TBO loading, FT-12, the selectivity increases to 17%. The increase in degree of braching with TBO loading might also highlight an increase in isomerisation.

**Oxygenate selectivity for the TBO modified samples**

The total oxygenate content as a function of TBO loading is shown in Figure 6.51. The oxygenate selectivity decreases with increasing TBO loading for both operating temperatures. The selectivity decreased from 9 to 6 mol-% at low temperature (250 $^0$C) and 7 to 5 mol-% at high temperature (300 $^0$C). Oxygenates are considered to be primary products. The selectivity of oxygenates is affected negatively by enhanced hydrogen availability on the surface. This is believed to result from a decrease the concentration of surface alkyldene species, which are thought to be responsible for the formation of these compounds [Johnston and Joyner, 1993]. An increase in hydrogen availability with increasing TBO loading was shown by the methane selectivity. This is also consistent with the selectivity of oxygenates in the samples.



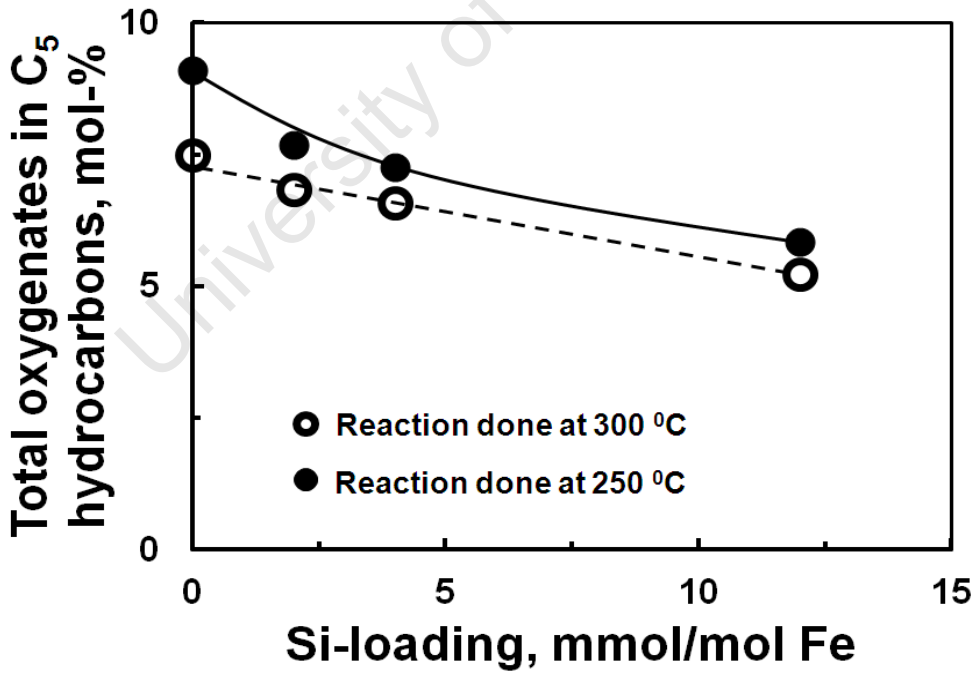


**Figure 6.51:** The total oxygenate content $C_5$ fraction for TBO modified iron oxide samples taken after 24 hours time on stream represented as a function of Si loading.

## 6.3.7 Collaborating the activity, selectivity and spent catalyst data

**Activity of the TBO modified samples at 250 $^0$C**

The assumption that the titanium in the TBO modified samples remains in the oxide structure during Fischer-Tropsch synthesis at 250 $^0$C is reasonable since $H_2$-TPR of the reduced samples indicates that the oxide phase present after reduction is thermal stable and resistant to reduction up to 512 $^0$C (see Figure 6.41). Moreover, the mole fraction of Fe associated with the oxide phase increases by 7-11 mol-% after Fischer-Tropsch synthesis when compared with the reduced samples, resulting in a decrease in the degree of titanium substitution (X) (see Table 6.18) This may be due to the reoxidation of the α-Fe by water during Fischer-Tropsch synthesis, highlighting that the magnetite content in the mixed oxide phase increases (see Scheme 2). It then follows that the $Fe_5C_2$ that is found the spent catalyst results from the carburization of the α-Fe phase. The titanium in the sample does not influence this process.

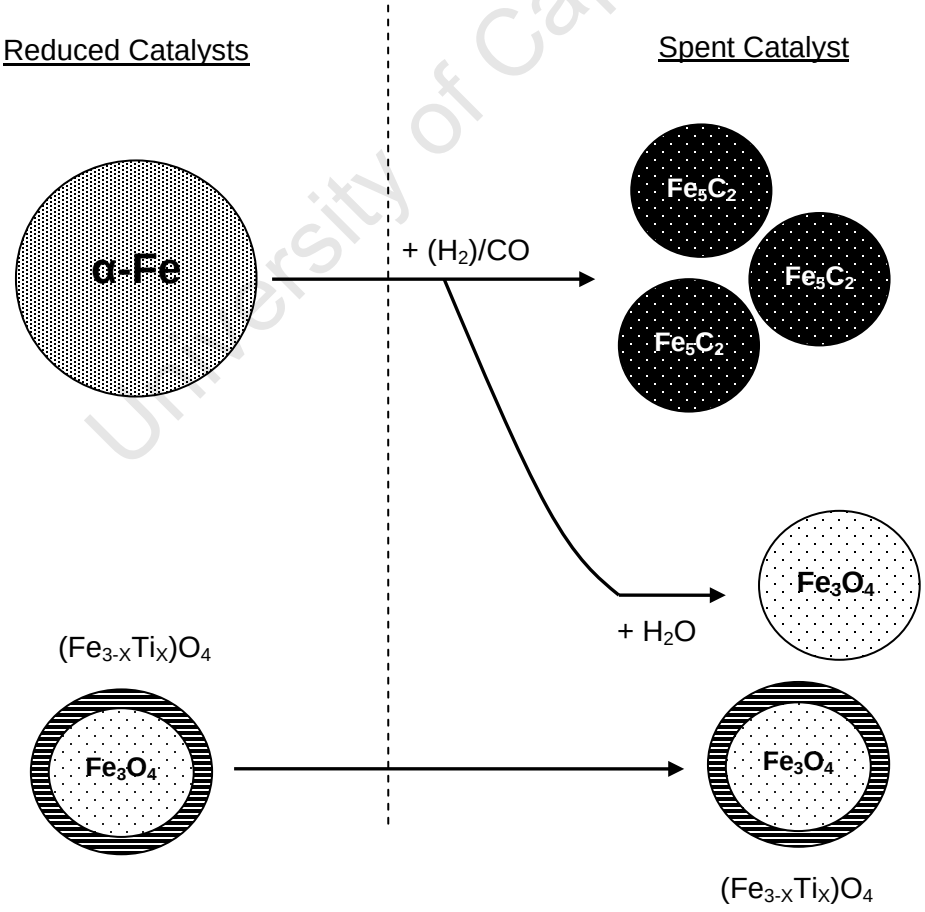


**Scheme 2:** Transformation of α-Fe during the Fischer-Tropsch synthesis at 250 $^0$C

Figure 6.52 shows the specific activity of the catalysts normalized to the $Fe_5C_2$ content found in the spent catalysts after Fischer-Tropsch synthesis at 250 $^0$C. $Fe_5C_2$ found in the TBO modified samples shows a higher integral rate per unit surface area of carbide compared to the unmodified sample (FS-0). The integral rate per unit $Fe_5C_2$ surface area for TBO modified samples is ca. 20 % higher than the unmodified sample, with the specific activity increasing marginally with TBO loading. The size of the $Fe_2C_5$ phase in the spent catalyst was between 11-15 nm. This eliminates the influence of crystallite size on the activity since iron based catalyst consisting of crystallite with diameters that are greater than 7 nm have the same activity per unit area [Mabaso, 2005]. Therefore, the increase in specific activity with TBO loading indicates a promotional effect. The spent catalyst results suggest that the active carbide phase and the titanium in the samples are separated (also see Scheme 2). This implies that the promotional effects observed for TBO modified samples does not result from Ti-ligands on the surface of the active carbide phase but rather occur indirectly through the interaction of the carbide phase with the mixed metal oxide phase present in the TBO modified samples.



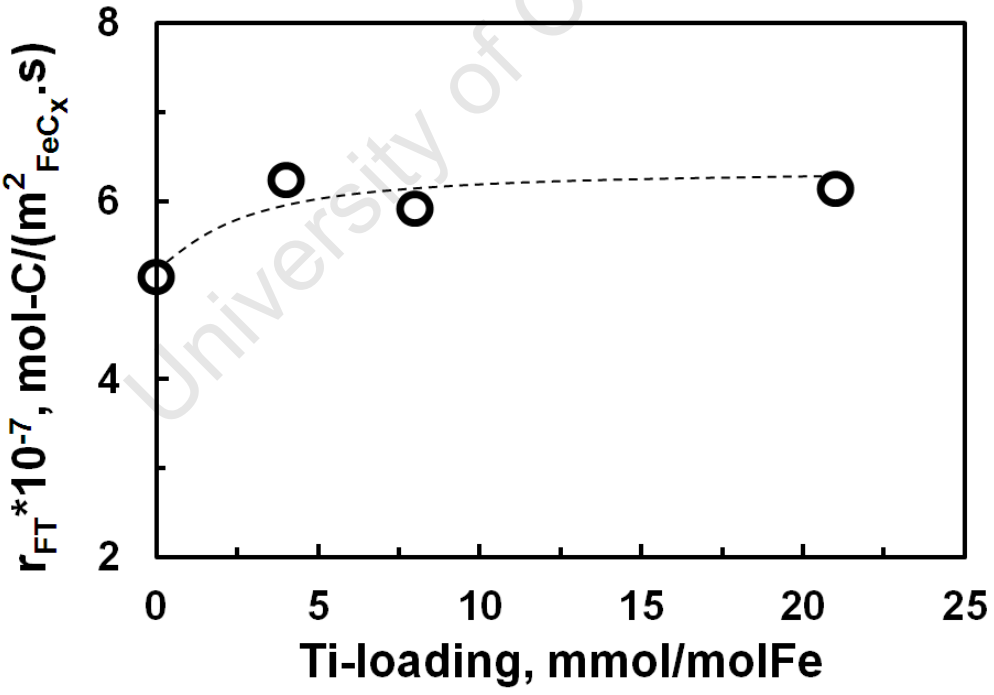


**Figure 6.52**: The rate of Fischer-Tropsch reaction per unit surface area of carbides in the spent catalyst tested at 250 $^0$C after 24 hours times on stream

The activity of noble metals for CO hydrogenation has been generally observed to increase with $TiO_2$ addition [Tauster et al., 1978; Vannice and Sudhakar, 1984; Ishihara et al., 1988]. This is believed to occur because $H_2$ has an enhanced ability to compete with CO for the metal surface on $TiO_2$ supported catalyst [Raupp and Dumesic, 1984; Tauster, 1987; Ishihara et al., 1988; Duvenhage and Coville, 2002]. This is typically accompanied by an increase in methane and the selectivity for lower hydrocarbons ($C_1$-$C_4$). The olefin selectivity is generally shown to decrease. The mechanism for activity enhancement in these catalysts is not well understood. Some researchers [Raupp and Dumesic, 1984] proposed that the metals on the titanium support are more effective as adsorption sites for hydrogen but others proposed the creation of new adsorption sites by the interaction between the metal and the $TiO_2$ support [Tauster, 1987]. Generally, it is believed that new active sites are created at the metal-titania interface due to the reduction of $TiO_2$, and these sites are responsible for the improved activity observed in $TiO_2$ supported catalysts [Burch and Flambard, 1982; Vannice and Sudhakar, 1984; Tauster, 1987].

A similar mechanism is proposed to explain the observed increase in specific activity with increasing TBO loading. The surface of titanomagnetite has been known to have acidic properties [Khaleel, 2009; Neri et al., 2004; Yang et al., 2011]. It has been shown that the acidity of support environment on which the active phase sits impacts on the activity of the catalyst [Niemantsverdriet et al., 1980; Wan et al., 2006]. Therefore, it can be argued that the carbide active sites in direct contact with the mixed oxide phase might possess altered catalytic capabilities. This in line with the results due to increasing mixed oxide surface area (observed with increasing TBO loading, see Table 6.18). During Fischer-Tropsch synthesis, the titanium cations on the surface of titanomagnetite might be partially reduced (to $Ti^{3+}$ state) in a manner similar to which $TiO_2$ is reduced to $TiO_x$ in conversional catalysts (the $TiO_x$ species is believed to be in the $Ti^{3+}$ state [Tauster, 1987; Ishihara et al., 1988]).

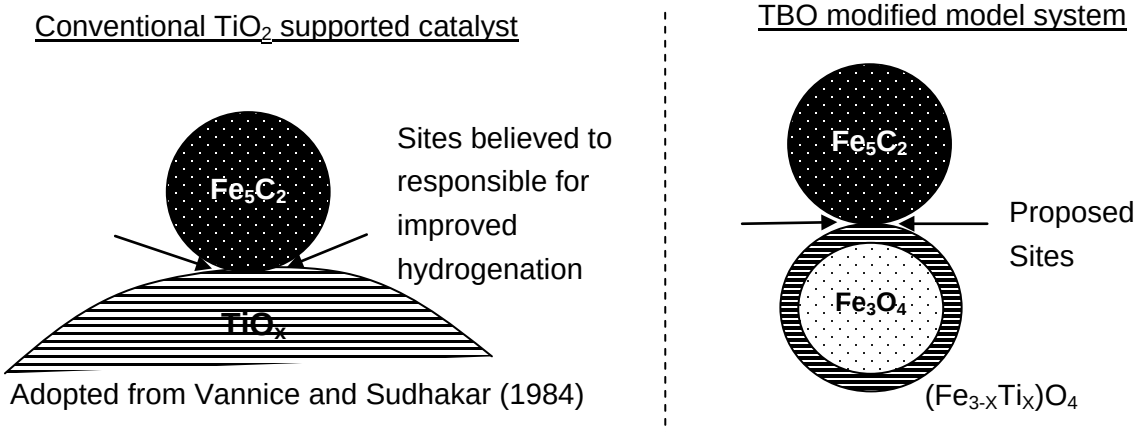


**Scheme 3**: The active sites believed to be responsible for the improved activity

Vannice and Sudhakar (1984) discussed the modification of surface metal atoms via electron transfer with the immediate environment. This would only require direct contact between the active metal and the oxide phase. The interaction of the partially reduced titanomagnetite surface with the Fe atoms on active carbide surface could create active sites similar to those described in literature (Fe-$TiO_x$) between $TiO_x$ species and active metal phase (see Scheme 3). A similar mechanism was proposed by Raupp and Dumesic (1984) to explain the higher activity and methane selectivity that is observed when metals are supported on $TiO_2$. These interface active sites are believed to be more effective for hydrogen adsorption and thus selective to the methanation reaction [Vannice and Sudhakar, 1984; Tauster, 1987; Ishihara et al., 1988].

The presence of these sites may account for the higher methane selectivity that is observed with TBO modified catalysts. Since the titanomagnetite surface area increases with increasing TBO loading, more interface sites could be formed. This would result in an increase in methane selectivity with increasing TBO loading, consistent with the observed results. The conversion of CO in the methanation reaction occurring at these sites would account for the observed increase in specific activity. In a conversional catalyst the surface area of the $TiO_2$ support is much larger than the active phase (10 % metal loading) [Duvenhage and Coville 2005b]. In the prepared samples, the surface area ratio (surface area of oxide phase/ surface area of carbide phase) is between 0.9 – 6.7, increasing with TBO loading. It might be deduced that the concentration of these sites in the TBO modified samples is low. The activity and selectivity of all the other sites on the catalysts surface would not be altered. Therefore, chain growth reaction and olefin formation, occurring at different sites, as expected, show no effects due to TBO modification. However, this explanation does not account for the enhanced double bond isomerisation of α-olefins; the increase in degree of branching and the decrease in oxygenate formation that was observed. The reason for this will be explained in detail at a later stage.



**Activity of the TBO modified samples at 300 $^0$C**

The activity TBO modified samples for a reaction temperature of 300 $^0$C was found to decrease with increasing TBO loading when the integral rate was taken as a function of the surface area of the total carbide content in the spent catalysts. The activity of the unmodified sample was calculated to 15.7 mol-C*$10^{-7}$/($m^2_{FeCx}$.s). With low TBO loading (FT-10) the activity was improved marginally. Following that the activity then decreases significantly with further modification until the lowest activity is reached at the highest TBO loading, FT-21, which was ca. 50 % less active as the unmodified sample (see Figure 6.53).

A decrease in activity is often observed when $TiO_2$ supported catalysts are activated at high temperatures [Tauster et al., 1978]. This effect is ascribed to the blocking of active sites due to the migration of $TiO_x$ species [Tauster, 1987; Vannice and Sudhakar, 1984]. The increase in reaction temperature from 250 $^0$C to 300 $^0$C and the presence of CO might induce similar effects.

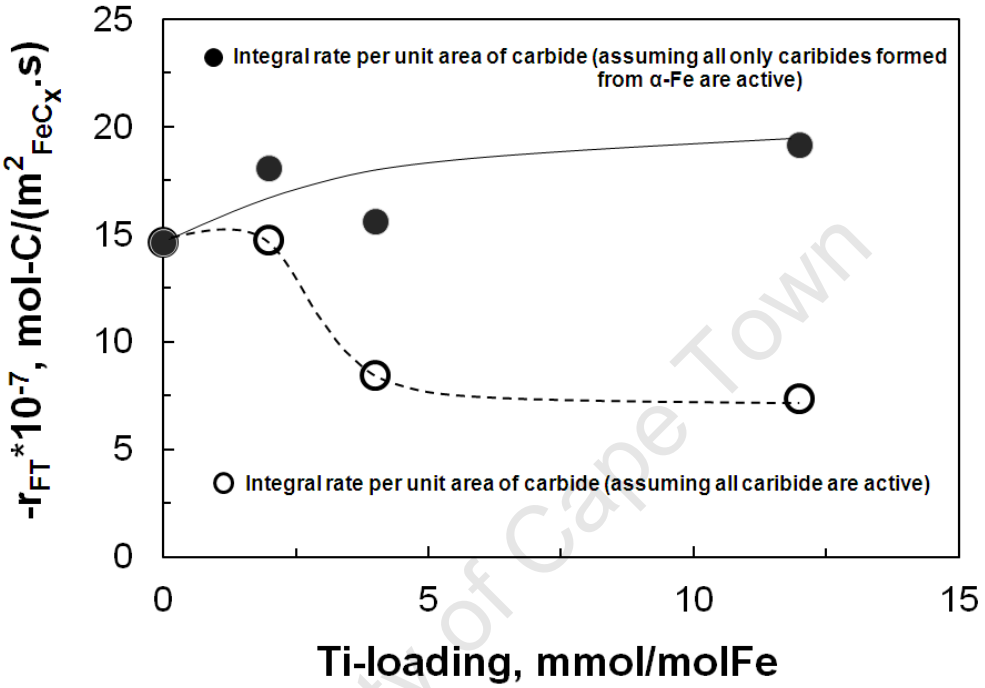


**Figure 6.53**: The rate of Fischer-Tropsch reaction per unit surface area of carbides found in the spent catalyst after 24 hours times on stream

CO is a better reduction agent than $H_2$. At elevated reaction temperatures (300 $^0$C), the CO in the feed synthesis gas may improve the degree of reduction. The mole fraction of Fe in the oxide phase decreases by ca. 12 % across the TBO modified samples. This indicated that some of the titanomagnetite in the reduced sample is reduced to carbide. It seems that the titanomagnetite is transformed into the $Fe_5C_2$ phase (see Scheme 4). As a result, a higher $Fe_5C_2$ content is observed in the TBO modified samples as compared to the unmodified sample (see Table 6.19).

It is thermodynamically less favorable for the Ti atoms to remain within the structure once carbides are formed and is therefore forced out to the surface. This was confirmed by FTIR analysis of the spent catalyst that showed an absorption band at ca. 980 $cm^{-1}$ (see Figure 6.44). This absorption band was assigned to Fe-O-Ti surface interactions. The intensity of the absorption band increased with increasing TBO loading, indicating that more ligands

are pushed out to the surface. This was consistent with the decrease in the oxide content. The Ti-ligands on the $Fe_5C_2$ carbides might effectively block the active sites, providing no improved catalytic capabilities. The reduction of $TiO_2$ resulting in $TiO_x$ has been observed to have the similar effects on noble metal catalysts [Tauster et al., 1978]. The $TiO_x$ species blocks active sites and results on poor activity [Vannice and Sudhakar, 1984; Tauster, 1987]. Therefore, it may be assumed that all the carbide content gained from the oxide phase is inactive due to ligand surface coverage. Then, the integral rate of reaction per unit surface of only the carbide formed from α-Fe carburization increases with increasing TBO loading (see Figure 6.53)

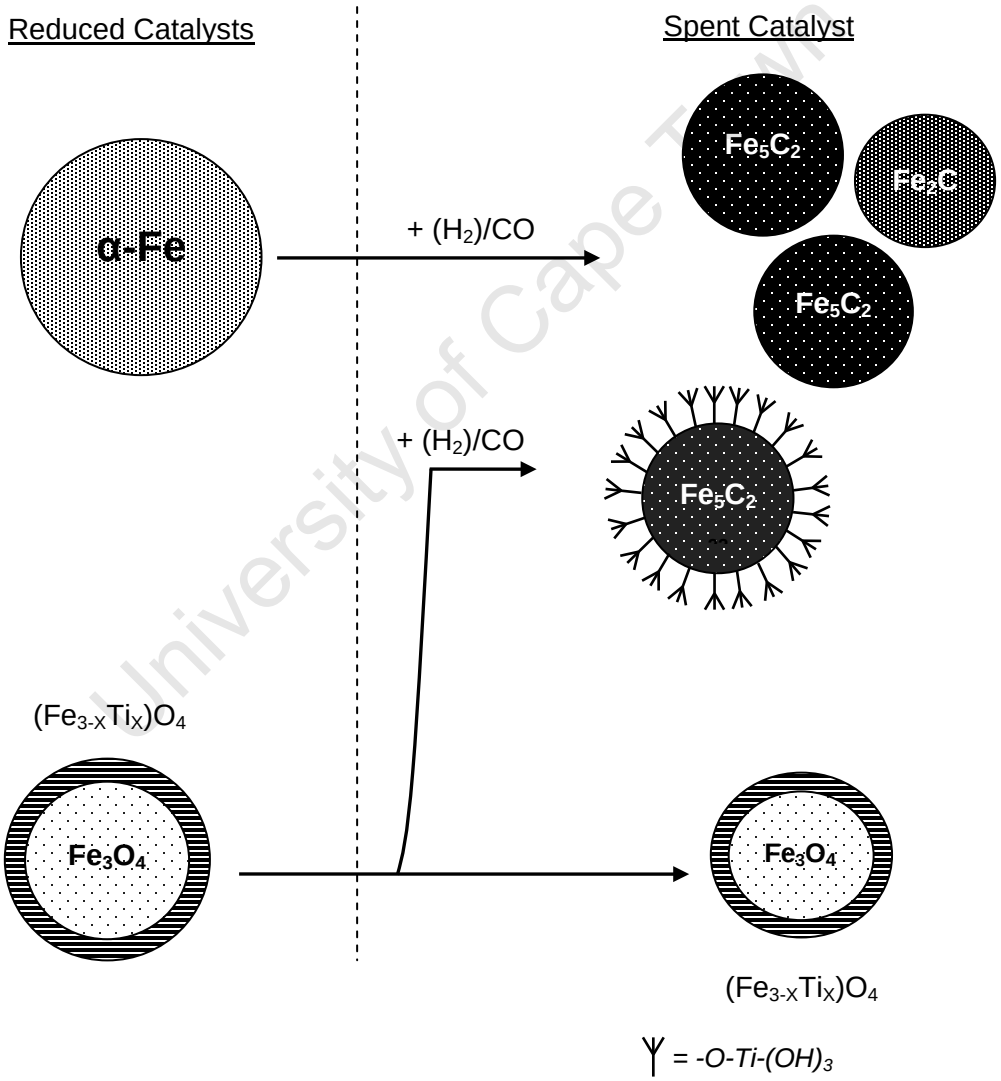


**Scheme 4:** Transformation of α-Fe and titanomagnetite during the Fischer-Tropsch synthesis at 300 $^0$C

Then a promotional effect consistent with the catalysts tested at 250 $^0$C is observed for catalysts tested at 300 $^0$C. The selectivity results also support a promotional effect due to existence of special contact sites with enhanced hydrogenation capabilities. This is shown by an increase in methane selectivity, accompanied by a small a change in the chain growth probability and total olefin selectivity. The selectivity results obtained at a reaction temperature of 300 $^0$C mirror those attained when the samples were tested at 250 $^0$C. This indicates that the process of product formation in the catalysts when tested at both temperatures is similar, which then brings us to the conclusion that promotional effects observed at 250 $^0$C must also occur at 300 $^0$C.

**The isomerization of the α-olefins**

Mixed metal oxides have been widely investigated since they have interesting catalytic properties. The presence of a foreign element in the in the matrix of a pure metal oxide can greatly modify the structural, acid-base and catalytic properties [Neri et al., 2004]. Fe-Ti-O mixed oxides have been shown to have strong Lewis acid sites [Khaleel, 2009; Neri et al., 2004; Yang et al., 2011] due to the presence of unsaturated $Ti^{4+}$ ions on the surface [Neri et al., 2004], see Figure 6.54.

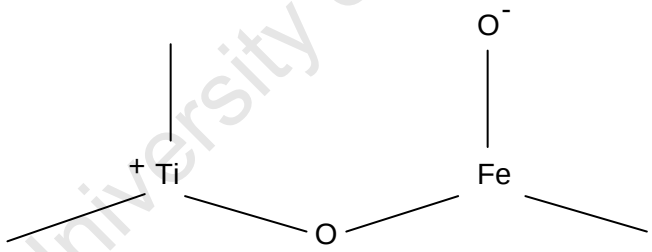


**Figure 6.54**: Schematization of the structure of the Lewis acid active sites on the Fe-Ti-O mixed metal oxide [adopted from Neri et al., 2004]

The synthesis gas ($CO+H_2$) is converted into Fischer-Tropsch products mainly on the carbides surface. If the selectivity of the samples is not affected by TBO modification then the α-olefin selectivity should be approximately 70 % of the linear hydrocarbons produced when the samples are tested at 250 $^0$C (using the selectivity unmodified sample as a baseline). However, α-olefin content was observed to decrease with increasing TBO loading. It can be proposed that following desorption from the Fischer-

Tropsch sites the α-olefins then absorb on the surface acid sites of the mixed oxide phase and undergoes double bond isomerisation.

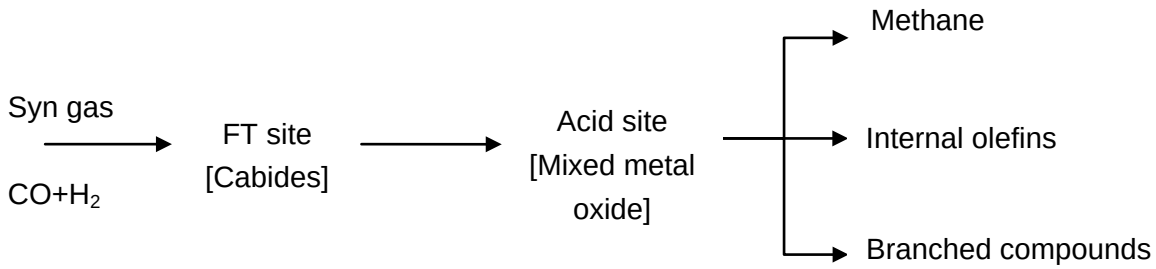


When the samples were tested at 250 $^{0}$C, the changes in the selectivity with increasing TBO loading can be explained by the creation of special contact zones. However, the decrease in the α-olefin content in linear olefins (70-51%) is more consistent with isomerisation on the mixed metal oxide acid sites. With increasing TBO loading the titanomagnetite content in the samples was observed to increase and the average crystallite size decreases (see Table 6.18). Therefore, the number of acid site will increase and thus the degree of isomerisation will increase (as observed). At temperatures as low as 250 $^{0}$C, the formation of branched compounds due to re-absorption of the α-olefins is not expected to be significant. Thus, the increase in methane selectivity is most likely due to the enhanced hydrogenation capability of the catalysts with increasing TBO loading. The slight decrease in the branched compound content in the samples might also be due to the improved hydrogenation capabilities of the catalyst surface or due to the decrease in conversion. Oxygenates can also absorb on the acid sites [Glisenti, 2000]. This might result in the dehydrogenation of oxygenates; resulting in the decrease oxygenates content that was observed.

The isomerisation of the α-olefin is observed for the samples when tested at both operating temperatures. With increasing TBO loading the mixed oxide content was found to increase in both cases. Thus the selectivity data is consistent with an increase in the number of Lewis acid site with increasing TBO modification, i.e. decrease in α-olefin and oxygenate content.

# 7

# Conclusions and recommendations

There are two ways in which metal support interactions are thought to occur, i.e. via chemical bonding (ligand effect) or via intimate contact (contact effect). This study was aimed at investigating metal-support interactions as a ligand effect by modifying the surface of iron oxide crystallites with silicate and titanate groups. The ligands are designed to mimic the interactions found in commercial catalysts. Through the design of the model catalyst, it was possible to isolate the effects of metal support interaction induced by the ligands on Fe-based Fischer-Tropsch catalysts. The use of an inverse approach, i.e. modification of nano-sized iron oxide with surface silicate or titanate groups, allowed for control and manipulation of the degree or extent of metal support interaction generated in a catalyst. This approach eliminates the use of structural promoters to investigate this effect, thereby simplifying the catalysts system and eliminating the effects of varying dispersion. Consequently, it was possible to ensure that the only variable across the synthesized catalyst was the degree of metal support interactions present in the samples. Therefore, the reported differences, in terms of reduction behavior and Fischer-Tropsch activity and selectivity, between the unmodified sample and the samples containing surface ligands can be viewed as mainly the effects of metal-support interaction as a ligand.

**Preparation of the model catalysts**

The first major objective of this study was to design a model type iron based catalysts and with varying degrees of Fe-O-Si and Fe-O-Ti interactions. This was successfully achieved by precipitating the iron catalyst using a microemulsion technique and modifying the surface with either tetra-ethoxy silane (TEOS) or titanium butoxide (TBO) to develop the desired interactions. Varying degrees of interaction (i.e. number of ligands attached) was achieved by varying the amount of the alkoxide compound (TEOS or TBO) added to the precipitated iron oxide catalyst. The presence of Fe-O-Si bonds in the calcined catalysts was evidenced by additional absorption bands between 890-1020 $cm^{-1}$, previously ascribed to $(\equiv FeO)_2$-$Si(OH)_2$ [Yang et al., 2008]. The presence of Fe-O-Si bonds in the calcined catalyst could also be inferred from the high temperature (above 700 $^oC$) peaks in the temperature programmed reduction profile of the TEOS modified samples. The presence of Fe-O-Ti bonds in the calcined samples was indicated by additional absorption bands 1020-1120 $cm^{-1}$, consistent with the frequency assigned to the stretching mode of this interaction.

The dominant phase of the iron oxide in the calcined phase is maghemite, with some larger crystallites present as hematite. The maghemite phase is more stable for smaller crystallites due to surface energy contributions. In the case of TEOS modification, the phase of the iron oxide appears to be a function of the silicon content in the synthesized

catalyst. At low TEOS loadings, the larger crystallites sizes samples have a higher hematite content. With increasing TEOS loading, smaller crystallites were observed which are predominantly maghemite. On the other hand, in the case of TBO modification, all the synthesized samples showed a mixture of both phases. The average crystallite sizes for the TBO modified samples were larger than the average crystallite size of the TEOS samples at similar loading. Furthermore, the crystallite distributions are wider for the TBO modified samples. Thus, the hematite content becomes more dominant in these samples due to larger crystallites sizes.

**Reduction behavior of the modified catalysts**

The Fe-O-Si bonds remain mostly in tact after reduction in hydrogen at 350 $^{o}$C for 16 hrs. The hydrogen activation of the silicon modified samples resulted in the formation of wüstite, whose disproportionation is either kinetically or thermodynamically limited by the modification with surface silicate groups. It is deduced that the FeO-surface is almost fully covered with the silicate surface groups. The average size of the wüstite phase is in agreement with the reduction of maghemite implying an inhibition of the sintering process possibly due to the presence of surface silicate groups. Sintering can take place under the conditions applied for the hydrogen activation, as evidenced by the large increase in the average crystallite size of α-Fe.

Due to the similarity in the $Fe^{2+}$ and $Ti^{4+}$ cations, the reduction of the TBO modified samples results in the incorporation of the Ti atoms into the iron oxide structure, forming Fe-Ti mixed metal oxides. This is evidenced by the decrease in the d-spacing of the (311) plane calculated for the oxide phase present in the TBO modified samples. The presence of mixed metal oxide in the reduced catalyst is also confirmed by the nature of the $H_2$-TPR profiles of the TBO modified samples, which is consistent with profiles previously observed for reduction of titanomagnetite and titanomagnetite [Yang et al., 2011]. At low TBO loading, the lower surface coverage allowed for the reduction of the bulk oxide and titanomagnetite $(Fe_{3-x}Ti_x)O_4$ was formed. At high TBO loadings, due to high Ti-ligand surface coverage, reduction of the bulk oxide was hindered possibly due to the shielding of surface oxygen by the titanate ligands. As a result, the incorporation of the Ti atoms in the iron oxide structure yields the formation of titanomaghemite $(Fe_{3-x}Ti_x)_{1-\delta}O_4$. The low degree of Ti substitution only accounts for the formation of monolayers of the mixed metal oxide surrounding a bulk iron oxide phase. High thermal stability of the mixed metal oxide phase results in a poor reducibility for the TBO modified samples.

**Fischer-Tropsch reaction work**

Exposure of the TEOS modified samples to industrially relevant Fischer-Tropsch conditions results in the formation of $Fe_5C_2$, and for the silicon modified catalysts also $Fe_2C$ (and $Fe_3O_4$ for samples with high silicon content). It is deduced that α-Fe is the origin of $Fe_5C_2$, whereas FeO is transformed into $Fe_2C$, possibly via $Fe_3O_4$. The activity per unit surface area of $Fe_2C$ is ca. 25 % higher than that of $Fe_5C_2$, which might be partially explained in terms of the difference in site density on these carbides. The catalysts with high silicon loading show a further enhancement of the integral rate per unit surface area of $Fe_2C$, which might be ascribed to the presence of surface silicate groups. It is deduced that surface silicate groups results in an increase in the hydrogen availability on the surface by reducing the strength of CO-adsorption [Wan et al., 2006]. An increase in the hydrogen availability on the surface will result in an increase in activity and in methane selectivity, and a decrease in the olefin content of the product and a decrease in the primary rate of formation of branched product compounds relative to the formation of linear product compounds.

The carburization of the α-Fe in the reduced sample of the TBO modified sample resulted in the formation of $Fe_5C_2$ after Fischer-Tropsch synthesis performed at 250 $^0$C. The TBO modified catalysts show a ca. 20 % increase in the integral rate per unit surface area of $Fe_5C_2$. This might be ascribed to the presence of special contact sites occurring at the interface between a partial reduced mixed metal oxide and the carbide surface. These contacts sites are deduced to be selective to the methanation reaction resulting in enhanced integral rate per unit surface area of $Fe_5C_2$ and methane selectivity. The concentration of these sites in the samples is low. Therefore, chain growth and olefin formation, thought to occur at different sites, show no effects due to TBO modification. The formation of branched compounds only shows effects due to varying conversion. The Lewis acid sites present on the surface of the Fe-Ti-O mixed oxides, results in the double bond isomerisation of the α-olefins and a decrease oxygenate content.

An increase in reaction temperature to 300 $^0$C results in the formation of mixed carbide phase; consisting of $Fe_5C_2$ and $Fe_2C$. CO induced reduction of the mixed metal oxide leading to the formation of additional $Fe_5C_2$ was also observed. The carburization of the mixed metal oxides coincided with the appearance of Fe-O-Ti surface species identified using FTIR. The presence of the Ti-ligands on the carbide surface is believed to result in the decrease integral rate per unit surface area of carbide that was observed with increasing TBO loading. This is possibly due to the blocking active sites by these surface ligands. The integral rate per unit surface area of only the carbide formed from

carburization of α-Fe show an increase with increasing TBO loading, consistent with catalysts tested at 250 $^0$C.

**Final remarks**

The presence of the silicate surface ligands at the different stages of the catalysts life (i.e. after calcination, reduction and Fischer-Tropsch synthesis) was confirmed by FTIR. As a result, is it was possible to monitor the changes to the behavior of the active phase brought about by the presence of these interactions. The formation of FeO, which is generally associated with the presence of these (Fe-O-Si) interactions, was confirmed. Through the study of the model catalysts, it is possible to argue that the O-carbides ($Fe_2C$ and $Fe_{2.2}C$), commonly found in the spent of $SiO_2$ catalysts, might be stabilized by the presence of Fe-O-Si. This study also showed that the O-carbides are possibly formed from the FeO phase, which is formed during reduction. The enhanced activity of the $Fe_2C$ phase was shown to result from the presence of Fe-O-Si interaction on the surface of the carbide phase. It might be postulated that the improved activity observed with $SiO_2$ supported catalysts, provided that the metal support interactions present in these catalysts are in ligand form, is due the enhanced hydrogenation capability the O-carbide phase commonly found in the post Fischer-Tropsch analysis of the spent catalysts. Therefore, it can be concluded that the study of metal support interactions as a ligand effect in the TEOS modified samples was successful. For the purposes of future work, it is recommended that in situ Mössbauer analysis be performed on the TEOS modified samples during carburization (to confirm the proposed decrease in carbon diffusion into the α-Fe structure) and during Fischer-Tropsch synthesis (to observed the phase transformations). In situ FTIR might also be used to show the changes in CO adsorption behavior on the modified surface.

Due to the incorporation of the titanium atoms into the iron oxide structure in TBO modified samples, it was not possible to study the effects of Fe-O-Ti interactions as a ligand effect. However, the enhanced activity of the $Fe_5C_2$ phase found in the TBO modified samples showed the 'contact effect', typically associated with $TiO_2$ modified samples. Furthermore, the enhanced methane selectivity, also ascribed to the contact effect, was also observed. In order to study the Fe-O-Ti interaction as a ligand effect, it is recommended that a new catalysts synthesis route should be developed whereby the titanate ligands could be attached to the active phase when it is already in carbide form.

# 8 References

Abrevaya, H. and Targos, W. M.: 1987,
'Microemulsion impregnated catalyst composite and use thereof in a synthesis gas conversion process'. *US Patent (4714692).*

Amelse, J.A., Butt, J.B. and Schwartz, L.H.: 1978,
'Carburization of supported iron synthesis catalysts',
*Journal of Physical Chemistry* **82**, 558.

Anderson, R. B.: 1956,
'Catalysts for the Fischer-Tropsch Synthesis',
**Vol. IV** of *Catalysis*, p. 29. Van Nostrand-Reinhold: New York.

Anderson, R. B.: 1984,
'The Fischer-Tropsch Synthesis',
Academic Press, New York.

Bao, L.-L., Hua, C.-F., Deng, C.-M. and Li, Y.-W.: 2009,
'Structure and stability of the crystal Fe2C and low index surfaces',
*Journal of Fuel Chemistry and Technology* **37**, 104.

Barkhuizen, D., Mabaso, I., E. Viljoen, C. Welker, Claeys, M., van Steen, E. and Fletcher J.C.Q.: 2006, 'Experimental approaches to the preparation of supported metal nanoparticles',
*Pure Applied Chemistry* **78**, 1759.

Barraclough, C.G., Bradley C.D., Lewis J. and Thomas I.M.: 1961,
'The Infrared Spectra of Some metal alkoxides, trialkylsilyloxiedes, and related silanols',
*Journal of the Chemical Society*, 2601.

Bartholomew, C. H.: 1991,
'Recent developments in Fischer-Tropsch catalysis',
In: L. Guczi (ed.): *Trends in CO Activation*, *Study of Surface Science and Catalysis.* **64** (2004), Amsterdam, Chapt. 8, p. 158.

Bartholomew, C. H.: 2001,
'Mechanisms of catalyst deactivation',
*Applied Catalysis A: General* **212**, 17.

Basu, P.K., Basu, S.B., Mitra, S.K., Dasandhi, S.S., Bhattcherjee, S.S and Samuel, P.: 1998,
'The role of silica in the conversion of syngas to middle distillates',
*Studies in Surface Science and Catalysis* **113**, 277.

Belin, T., Guige-Millot, N., Aymes, D. and Niepce, J.C.: 2002,
'Influence of grain size, oxygen stoichiometry, and synthesis conditions of the γ-$Fe_2O_3$ vacancies ordering and lattice parameters',
*Journal of Solid State Chemistry* **163**, 459.

Benvenutti, E.V., Franken, L. and Moro, C.C.: 1999,
'FTIR Study of Hydrogen and Carbon Monoxide Adsorption on Pt/$TiO_2$, Pt/$ZrO_2$, and Pt/$Al_2O_3$'.
*Langmuir* **15**, 8140.

Bergeret, G. and Gallezot, P.: 1997,
'Particle size and dispersion measurements'.
Vol. 2 of *Handbook of heterogeneous catalysis*. VCH, Weinheim, Federal Republic of Germany, Chapt. 3, p. 439.

Bezemer, G.L., Radstake, P.B., Koot, V., van Dillen, A.J., Geus J.W. and de Jong, K.P.: 2006,
'Preparation of Fischer-Tropsch cobalt catalysts supported on carbon nanofibers and silica using homogeneous deposition-precipitation'.
*Journal of catalysis* **237**, 291

Bruce, I.J., Taylor, J., Todd, M., Davies, M.J., Borioni, E., Sangragoroi, C. and Sen, T.: 2004,
'Synthesis, characterization and application of silica-magnetite nanocomposites'.
*Journal of Magnetism and Magnetic Materials* **284**, 145.

Bukur, D. B., Mukesh, D. and Patel, S. A.: 1990,
'Promoter effects on precipitated iron catalysts for Fischer-Tropsch synthesis'.
*Industrial Engineering Chemical Resources* **29**, 194.

Bukur, D. B., Okabe, K., Rosynek, M.P., Li, C., Wang, D., Rao, K.R.P.M., and Huffman, G.P.: 1995a,
'Activation studies with a precipitated iron catalyst for Fischer-Tropsch synthesis: Characterization studies'.
*Journal of Catalysis* **155**, 353.

Bukur, D. B., Nowicki, L., Manne, R.K. and Lang, X.: 1995b,
'Activation studies with a precipitated iron catalyst for Fischer-Tropsch synthesis: Reaction studies'.
*Journal of Catalysis* **155**, 353.

Burch, R., and Flambard, X.: 1982,
'Strong metal-support interactions in nickel titania catalysts: the importance of interfacial phenomena'.
*Journal of Catalysis* **78**, 389.

Broska, I., Harlov, D., Tropper, P. and Siman, P.: 2007,
'Formation of magnetic titanite and titanite-ilmenite phase relations during granite alteration in the Tribeč Mountains, Western Carpathians, Slovakia'.
*Lithos* **95**, 58.

Catlow, C. R. A., Ackermann, L., Bell, R. G., Gay, D. H., Holt, S., Lewis, D. W., Nygren, M. A., Sastre, G., Sayle, D. C., and Sinclair, P. E.: 1997, 'Modelling of structure, sorption, synthesis and reactivity in catalytic systems'.
J. *Mol. Catal. A: Chemical* **115**, 431.

Che M.:1993
'Interfacial Coordination Chemistry: Concepts and Relevance to Catalysis Phenomena'. *Studies in Surface Science and Catalysis* ***75***, 31.

Chen, L., He, B.-Y., He, S., Wang, T.-J. and Jin, Y.: 2011,
'Fe-Ti oxides nano-adsorbent synthesized by co-precipitation for fluoride removal from drinking water and its adsorption mechanism'.
*Power technology* xx, xx (article in press).

Cheng, Z.X., Louis, C., and Che, M.:1991
'Effects of $SiO_2$ content on iron based catalyst for slurry Fischer-Tropsch synthesis'.
*Fuel Processing Technology* **89**, 284.

Cheng, Z.X, Louis, C. and Che, M.: 1991b,
'Nucleation and particle growth in the preparation of silica-supported nickel catalysts by a two step procedure".
*Phys*. **D 20**, 445.

Choi, J.-G., Choi, H.K., Jung, M.-K., Oh, H.-G. and Choi, J..: 1997,
'Characterization of supported cobalt catalysts by TPR and TPD'.
*Journal of Industrial and Engineering Chemistry* **3**, 235.

Chuckin, G.D. and Malevich, V.I.: 1977 ,
'Infrared spectra of silica'.
*Zhurnal Prikladnoi Spektroskopii* **26**, 2.

Claeys, M.: 1997,
'Selektivit¨at, Elementarschritte und Kinetische Modellierung beider Fischer-Tropsch-Synthese'.
Ph.D. thesis, Universit¨at Fridericiana Karlsruhe.

Claeys, M. and van Steen, E.: 2004,
'Basic studies'.
In: A. Steynberg and M. Dry (eds.): *Fischer-Tropsch Technology*, Vol. 152 of *Studies in Surface Science and Catalysis*. Elsevier, Amsterdam, Chapt. 8, p. 601.

Combes, J. M., Manceau, G., Calas, G. and Bottero, J.Y.: 1989,
'Formation of ferric oxides from aqueous solutions: a polyhedral approach by X-ray adsorption spectroscopy: I. hydrolysis and formation of ferric gels'.
Geochimica et Cosmochimica Acta 53, 583.

Darezereshki, E.: 2011,
'One-step synthesis of hematite ($\alpha$-$Fe_2O_3$) nano-particles by direct thermal-decomposition of maghemite'.
*Materials Letters* **65**, 642.

Day, L.K.: 1981,
'Infrared extinction of amorphous iron silicates'.
*The Astrophysical Journal* **246**, 110.

de Andrade Lima Coêlho, R., Yamasaki, H., Perez, E. and de Carvalho Jr, L.B.: 2003,
'The use of Polysilane/polyvinyl alcohol beads as solid phase in IgG anti-toxocara canis detection using a recombinant antigen'.
*Mem. inst*. *Oswaldo Cruz, Rio de Janeiro* **98**, 391.

de Smit, E., Beale, A.M., Nikitenko, S. and Weckhuysen B.M.: 2009,
'Local and long range order in promoted iron-based Fischer-Tropsch catalysts: A combined *in situ* X-ray absorption spectroscopy/ wide angle X-ray scattering study'.
*Journal of Catalysis* **262**, 244.

de Smit, E., Cinquini, F., Beale, A.M., Safonova, O.V., van Beek, W., Sautet, P., and Weckhuysen B.M.: 2010, 'Stability and reaction of $\epsilon$-$\chi$-$\theta$ iron carbide catalyst phases in Fischer-Tropsch synthesis: controlling $\mu_c$'.
*Journal of American Chemical Society* **132**, 14928.

den Breejen, J.P., Sietsma, J.R.A., Fredrich, H., Bitter, H. and de Jong, K.P.: 2010,
'Design of a cobalt catalyst with maximum activity for the fischer-Tropsch synthesis'.
*Journal of Catalysis* **7**, 733.

Diamandescu, L., Feder, M., Tarabasanu-Mihaila, F. and Visiliu, F.: 2007
'Hydrothermal synthesis and structural characterization of $x$$TiO_2$-(1-$x$)α-$Fe_2O_3$ mixed oxide nanoparticles'.
*Applied Catalysis A: General* **325**, 270.

Dlamini, H., Motjope, T., Joorst, G., ter Stege, G. and Mdleleni, M.: 2001
'Change in physico-chemical properties of iron-based Fischer-Tropsch catalyst induced by $SiO_2$ additions'.
*Catalysis Letters* **78**, 201.

Dry, M. E.: 1981,
*Catalysis Science and Technology*, Vol. 1, p. 159. Springer Verlag, New York.

Dry, M. E.: 1990,
'The Fischer-Tropsch process - commercial aspects'.
*Catalysis Today* **6**, 183.

Dry, M. E.: 2004a,
'Chemical concepts used for engineering purposes'. In: A. Steynberg and M. E. Dry (eds.): *Fischer-Tropsch Technology*, *Study of Surface Science and Catalysis.* **152** (2004), Amsterdam, Chapt. 3, p. 196.

Dry, M. E.: 2004b,
'Chemical concepts used for engineering purposes'. In: A. Steynberg and M. E. Dry (eds.): *Fischer-Tropsch Technology*, *Study of Surface Science and Catalysis.* **152** (2004), Amsterdam, Chapt. 7, p. 533.

Duvenhage, D.J and Coville, N.J.: 1997,
'Fe:Co/$TiO_2$ bimetallic catalysts for the Fischer-Tropsch reaction: Part 1. Characterization and reactor studies'.
*Applied Catalysis A: General* **153**, 43.

Duvenhage, D.J and Coville, N.J.: 2002,
'Fe:Co/$TiO_2$ bimetallic catalysts for the Fischer-Tropsch reaction: Part 2. The effects of calcination and reduction temperature'.
*Applied Catalysis A: General* **233**, 63.

Egiebor, N.O. and Cooper, W.C.: 1985,
'Fischer-Tropsch synthesis on a precipitated iron catalyst: Influence of silica support on product selectivities'.
*The Canadian Journal of Chemical Engineering* **63**, 81.

Eilers, J., Posthuma, S. A. and Sie, S. T.: 1990,
'The shell middle distillate synthesis process (SMDS)'.
*Catalysis Letters* **7**, 253.

Eriksson, S., U. Nyl´en, S. Rojas, and M. Boutonnet: 2004,
'Preparation of catalysts from microemulsions and their applications in heterogeneous catalysis'.
*Applied Catalysis A: General* **265**, 207.

Erley, W., McBreen, P. and Ibach, H.: 1983,
'Evidence for CHx surface species after the hydrogenation of CO over an Fe(110) single crystal surface'.
*Journal of Catalysis* **84**, 229.

Ernst, B., Libs, S.. Chaumette, P. and Kiennemann, A.: 1999,
'Preparation and characterization of Fischer-Tropsch active Co/$SiO_2$ catalysts'.
*Applied Catalysis A: General* **186**, 145.

Fischer, F. and H. Tropsch: 1926,
*Brennstoff-Chemie* **7**, 97.

Glisenti, A.: 2000,
'The reactivity of a Fe-Ti-O mixed oxide under different atmospheres: study of the interaction with simple alcohol molecules'.
*Journal of Molecular Catalysis A: Chemicals* **153**, 169.

Gracia, J.M., and Prinsloo, F.F.: 2009,
'Mars-van Krevelen-like mechanism of Co hydrogenation on an iron carbide surface'.
*Catalysis letters* **133**, 257.

Guigue-Millot, N., Champion, Y., Hÿtch, M.J., Bernard, F., Bëgin-Colin, S. and Perriat, P.: 2001,
'Chemical heterogeneities in Nanometric titanomagnetite prepared by soft chemistry and studied ex situ: evidence for Fe-segregation and oxidation kinetics'.
*Journal of Physical Chemistry B* **105**, 7125.

Haller, G.L. and Resasco, D.E.: 1989,
'Metal-support interactions: Group VIII metals and reducible oxides'.
*Advances in Catalysis* **36**, 173.

Hamadanian, M., Reisi-Vanami, A. and Majedi, A.: 2010,
'Sol-gel preparation and characterization of $Co/TiO_2$ nanoparticles: Application to the degradation of methyl orange'.
*Journal of Iranian chemical Society* **7**, 52.

Herranz, T., Rojas, S., Perez-Alonso, J.F., Ojeda, M., Terreros, P., and Fierro, J.L.G.: 2006,
'Carbon oxide hydrogenation over silica-supported iron-based catalysts; Influence of preparation route'.
*Applied Catalysis A: General* **308**, 19.

Hiremath, V.A. and Venkataraman, A.: 2003 ,
'Dielectric, electrical and infrared studies of γ-Fe2O3 prepared by combustion method'.
*Bulletin of Material Science* **26**, 391.

Honda, H., Suzaki, K. and Sugahara, Y.: 2001,
'Control of Hydrolysis and Condensation Reactions of Titanium *tert*-butoxide by Chemical Modification with Catechol'.
*Journal of Sol-Gel Science and Technology* **22**, 133.

Hota, G., S. Jain, and K. C. Khilar: 2004,
'Synthesis of $CdS-Ag_2S$ core-shell composite nanoparticles using AOT-n-heptane-water microemulsions'.
*Colloids and Surfaces A: Physicochemical Engineering Aspects* **232**, 119.

Hou, W., Wu, B., Yang, Y., Hao, Q., Tian, L., Xiang, H. and Li, Y.:2008,
'Effects of $SiO_2$ content on iron based catalyst for slurry Fischer-Tropsch synthesis'.
*Fuel Processing Technology* **89**, 284.

Hou, C.-F., Li, Y.-W., Wang, J. and Jiao, H.: 2009,
'Insight into $CH_4$ formation in iron-catalyzed Fischer-Tropsch synthesis'.
*Journal of American Chemical Society* **131**, 14713.

Huff, Jr., G.A. and Statterfield, C.N.: 1984,
'Instrinsic Kinetics of the Fischer-Tropsch synthesis on a reduced Fused-magnetite catalyst'.
*Industrial and Engineering Chemistry Process Design and Development* **23**,696.

Iglesia, E., Reyes, S. C., Madon, R. J. and Soled, S. L.: 1993,
'Selectivity control and catalyst design in the Fischer-Tropsch synthesis: sites, pellets, and reactors'.
*Advances in Catalysis* **39**, 221.

Iglesia, E.: 1997,
'Design, synthesis, and use of cobalt-based Fischer-Tropsch synthesis catalysts'.
*Applied Catalysis* **161**, 59.

Ishihara, T., K. Eguchi, and H. Arai: 1988,
'Supported Iron-Cobalt-Nickle Ternary Alloy Catalysts for the Hydrogenation of Carbon Monoxide '.
*Applied Catalysis* **40**, 87.

Ishikawa, T., Ueno, T., Yasukawa, A., Kandori, K., Nakayama, T. and Tsubota, T.: 2002,
'Structure of nanosized Fe-Ti mixed oxide particles produced by freezing method'.
*Journal of Materials Chemistry* **12**, 2416.

Jacobs, G., Patterson, P. M., Das, T. K., Luo, M. and Davis, B. H.: 2004,
'Fischer-Tropsch synthesis: effect of water on Co/Al2O3 catalysts and XAFS characterization of reoxidation phenomena'.
*Applied Catalysis A: General* **270**, 65.

Jacobs, G., Ji, Y., Davis, B.H., Cronauer, D., Kropf, A.J. and Marshall, C.L.: 2007,
'Fischer-Tropsch synthesis: Temperature programmed EXAFS/XANES investigation of the influence of support type, cobalt loading, and noble metal promoter addition to the reduction behavior of cobalt oxide particles'.
*Applied Catalysis A: General* **333**, 177.

Jarlbring, M., Gunneriusson, L., Hussmann, B. and Willis, W.: 2005,
'Surface complex characteristics of synthetic maghemite and hematite in aqueous suspensions'.
*Journal of Colloids and Interface Science* **285**, 212.

Jin, X., Talbot, J. and Wang, N.-H.L.: 1994,
'Analysis of steric hinderance effects on adsorption kinetics and equilibria'.
*Materials, interfaces and electrochemical phenomena* **40**, 1685.

Johnston, O. and Joyner, R.: 1993,
'Structure function relationships in heterogeneous catalysis: the embedded surface molecule approach and its application'.
In: L. Guczi, F. Solymosi, and P. Tetenyi (eds.): Proc. "10th Int. Congr. on catalysis", Budapest 1992, Vol. **75A** of *Stud. Surf. Sci. Catal*. p. 165, Elsevier, Amsterdam.

Jothimurugesan J.J., Spiey, S.K., Gangwal, S.K. and Goodwin, J.D.: 1998,
'Effects of silica on iron-based Fischer-Tropsch catalysts'.
*Studies in Surface Science and Catalysis* **119**, 215.

Jozwiak, W.K., Kaczmarek, E., Maniecki, T.P., Ignaczak, W. and Maniukiewicz, W.:2007,
*Applied Catalysis A: General* **326**, 17.

Kaiser, R.: 1969,
'Chromatographie in der Gasphase'.,
*Bibliographisches Institut, Mannheim, band iii*, 2. edition.

Khaleel, A.: 2009,
'Sol-gel synthesis, characterization, and catalytic activity of Fe(III) titanates'.
*Colloids and Surfaces A: Physicochemical and Engineering Aspects* **346**, 130.

Khodakov, A.Y., Chu, W. and Fongarland, P.: 2007,
'Advances in the Development of Novel Cobalt Fischer-Tropsch Catalysis for Synthesis of Long-Chain hydrocarbons and Clean Fuels'.
*Chemical Reviews* **204**, 1692.

Koneracká, M., Závišová, V., Timko, M., Kopčanský, P., Tomašovičová, N. and Csach, K.: 2008,
'Magnetic Properties of Encapsulated Magnetite in PLGA Nanospheres'.
*Acta Physica Polonica A* **113**, 595.

Krishnamoorthy, S., Li, A. and Iglesia, E.: 2002,
'Pathways for CO2 formation and conversion during Fischer-Tropsch synthesis on irn-based catalysis'.
*Catalysis Letters* **80**, 77.

Lamber, R., Jaeger, N. and Schulz-Ekloff, G.: 1990,
*Surface Science* **227,** 268

Lemire, C., Bertarione, S., Scarano D., Chaka A., Shaikhutdinov S. and Freund H. J.: 2005,
'Ferryl (Fe=O) Termination of the Hematite ά-$Fe_2O_3$ (0001) Surface'.
*Physical Review Letters* **94**, 101

Li, S., S. Krishnamoorthy, A. Li, G. D. Meitzner, and E. Iglesia: 2002a,
'Promoted iron-based catalysts for the Fischer-Tropsch synthesis: design, synthesis, site densities and catalytic properties'.
*Journal of Catalysis* **206**, 202.

Li, S., Ding, W. Meitzner, G.D. and Iglesia, E.:2002b,
'Spectroscopic and Transient Kinetic Studies of Site Requirements in Iron-Catalyzed Fischer−Tropsch Synthesis'.
*Journal of Physical Chemistry B* **106**, 85.

Lin, H. Y., Y. W. Chen, and C. Li: 2003,
'The mechanism of reduction of iron oxide by hydrogen'.
*Thermochim. Acta* **400**, 61.

Liu, X. -M., Fu, S. -Y., Xiao, H.-M. and Huang, C.-H.: 2005,
'Preparation and characterization of shuttle-like α-Fe2O3 nanoparticles by supermolecular template'.
*Journal of Solid State Chemistry* **178**, 2798.

López, T., Moreno, J.A., Gómes, R., Bokhimo, X., Wang, J.A., Yee-Madeira, H., Pecchi, G. and Reyes, P.: 2002, 'Characterization of iron-doped titania sol-gel materials'.
*Journal of Materials Chemistry* **12**, 1.

Lox, E. S., Marin, G. B., de Grave, E. and Bussiere, P.: 1988,
'Characterization of a promoted precipitated iron catalyst for Fischer-Tropsch synthesis'.
*Applied Catalysis* **400**, 61.

Mabaso, E.I: 2005,
'Nanosized Iron Crystallites for Fischer-Tropsch Synthesis'.
*Ph.D. thesis, University of Cape Town, chemical engineering.*

Maček, M. and Orel, B.: 1997,
'Electrochemical and structural characterization of dip-coated Fe/Ti oxide films prepared by the sol-gel route'.
*Journal of Sol-Gel Science and technology* **8**, 771.

Maitlis, P. M., R. Quyoum, Long, H. C. and Turner, M. L.: 1999,
'Towards a chemical understanding of the Fischer-Tropsch reaction: alkene formation'. *Applied Catalysis A: General* **186**, 363.

Manceau, A., Ildefonse, P.H., Hazemann, J.L., Flank, A.M. and Gallup, D.: 1995,
'Crystal chemistry of hydrous iron silicate scale deposits at the salton sea geothermal field'. *Clays and Clay minerals* **43**, 304.

Min, B.K., Santra, A.K. and Goodman, D.W.: 2003,
'Understanding silica-supported metal catalysts: Pd/silica as a case study'. *Catalysis Today* **85**, 113.

Morrow, B.A. and McFarlan, A.J.:1992,
'Surface vibration modes of silanol groups on silica'. *Journal of Physical Chemistry* **96**, 1395.

Morsy, S.M.I., Shaban, S.A., Ibrahim, A.M. and Selim, M.M.: 2009,
'Characterization of cobalt oxide nancatalysts prepared by microemulsion with different surfactants, reduction by hydrazine and mechanochemical method'. *Journal of Alloys and Compounds* **486**, 83.

Moulijn, J. A., van Diepen, A. E. and Kapteijn, F.: 2001,
'Catalyst deactivation: is it predictable? What to do?'. *Applied Catalysis A: General* **212**, 3.

Nakamoto, K.: 1962,
'Infrared and Raman spectroscopy of inorganic and coordination compounds'. John Wiley and Sons, Inc.

Navrotsky, A., Mazeina, L. and Majzlan, J.: 2008,
'Size-dirven structural and thermodynamic complexity in iron oxides'. *Science* **319**, 1635.

Neri, G., Rizzo, G., Galvagno, S., Loiacono, G., Donato, A., Musolino, M.G., Pietropaolo, R. and Rombi, E.: 2004, 'Sol-gel synthesis, characterization and catalytic properties of Fe-Ti mixed oxides'. *Applied Catalysis A: General* **274**, 242

Newsome, D. S.: 1980,
'The water-gas shift reaction'. Catalysis Reviews, Science and Engineering **21**, 275.

Niemantsverdriet, J.W., van der Kraan, A.M., van Dijk, W.L. and van der Baan, .H.: 1980,
'Behavior of metallic iron catalysts during Fischer-Tropsch synthesis studies with Mössbauer spectroscopy, X-ray diffraction, carbon content determination and reaction kinetic measurements'. *Journal of Physical chemistry* **84**, 3363.

Niemantsverdriet, J.W. and van der Baan, .H.: 1981,
'On the time-dependent behavior of iron catalysts in Fischer-Tropsch synthesis'. *Journal of Catalysis* **72**, 385.

O'Brien, R.J., Xu, L., Spicer, R.L. and Davis, B.H.: 2006,
'Activation Study of Precipitated Iron Fischer-Tropsch Catalysts'.
*Energy and Fuels* **10**, 921.

Orlović, A. M., Janaćković D.T. and Shala D.U.: 2005,
'Aerogels in Catalysis'.
In: Bevy, L.P. (eds.): 'New Developments in Catalysis Reasearch.' *Nova Science Publishers, Inc.* page 60.

Pal, B., Sharon, M. and Nogami, G.: 1999,
'Preparation and characterization of $TiO_2/Fe_2O_3$ binary mixed oxides and its photocatalytic properties' *Materials Chemistry and Physics* **59**, 254

Petersen, A.M., van der Berg, J-.A., and van Rensburg, W.J.: 2010,
'Role of step sites and surface vacancies in the adsorption and activation of CO on the $\chi$-$Fe_5C_2$ surfaces'. *Journal of Physical Chemistry: C* **144**, 7863.

Pham, H.M. and Datye, A.K.: 2000,
'The synthesis of attrition resistant slurry phase iron Fischer-Tropsch catalyst'.
*Catalysis Today* **58**, 233.

Philipp, W.H.: 1990,
'Polysiloxanes derived from the controlled hydrolysis of tetraethoxysilane as precursors to silica for use in ceramic processing'
*NASA Technical Memorandum* 102489

Pichler, H. and H. Schulz: 1970,
'Neuere Erkenntnnisse auf dem Gebiet der Synthese von Kohlenwasserstoffen aus CO und H2'.
*Chem.-Ing. Techn.* **42**, 1162

Pileni, M. P.: 1993, 'Water in oil colloidal droplets used as microreactors'.
*Adv. Colloid Interface Sci*. **46**, 139.

Puskas, I., Fleisch, T.H., Full, P.R., Kaduk, J.A., Marshall, C.L. and Meyers, B.L.: 2006,
'Novel aspect of the physical chemistry of $Co/SiO_2$ Fischer-Tropsch catalyst preparation: the chemistry of cobalt silicate formation during catalysts preparation or hydrogenation'.
*Applied Catalysis A: General* **311**, 146.

Puskas, I., Fleisch, T.H., Kaduk, J.A., Marshall, C.L., Meyers, B.L., Castagnola, M.J. and Indacochea, J.E.: 2007, 'Novel aspect of the physical chemistry of $Co/SiO_2$ Fischer-Tropsch catalyst preparation: Cobalt oxide-induced silica migration during calcination of cobalt nitrate-impregnated high surface area silica'. *Applied Catalysis A: General* **316**, 197.

Puurunen, R. L.: 2003,
'Grow per cycle in atomic layer deposition: A theoretical model'.
*Chemical vapor Deposition* **9**, 249.

Qing, M., Yang, Y., Wu, B., Xu, J., Zhang, C., Gao, P. and Li, Y.: 2011,
'Modification of Fe-SiO2 interactions with zirconia for iron-based Fischer-Tropsch Catalysts'.
*Journal of Catalysis* **279**, 111.

Ratzinger, G., Länger, U., Neutsch, L., Pittner, F., Wirth, M. and Gabor, F.: 2009,
'Surface modification of PLGA particles: The interplay between stabilizer, ligand size , asnd hydrophobic interaction'.
*Applied Catalysis A: General* **316**, 197.

Riva, R., Miessner, H., Vitali, R. and Del Piero, G.: 2000,
'Metal–support interaction in Co/SiO2 and Co/TiO2'.
*Langmuir* **26**, 1855.

Rao, K.R.P.M., Huggins, F.E., Mahajan, V., Huffman, G.P., Rao, V.U.S., Bhatt, B.L., Bukur, D.B., Davis, B.H. and O'Brien, R.J.: 1995,
*Topics in Catalysis* **2**, 71.

Raupp, G.B. and Dumesic, J.A.: 1984,
'Effects of titania surface species on the chemisorption of CO and $H_2$ on polycrystalline nickle'. *Journal of Physical Chemistry* **88**, 660

Rayner, M.K.: 2011,
'Pretreatment of $TiO_2$-supported Fe, Co and Ru catalysts: An in situ powder diffraction study'
*Ph.D. thesis, University of Witwatersrand, Faculty of Science.*

Roslov, I., Boitsova, T. and Bartak, D.: 2010,
'Precipitation of gold nanoparticles on the quartz surface modified by titanium (IV) butoxide'.
*Journal of Nanoparticle Research* **12**, 1479.

Sadeqzadeh, M., Karaca, H., Safonova, O.V., Fongarland, P., Chambrey, S., Roussel, P., Griboval-Constant, A., Lacroix, M., Curlla-Ferre, D., Luck, F. and Khodakov, Y.: 2011,
'Identification of the active species in the working alumina-supported cobalt catalyst under various conditions of Fischer-Tropsch synthesis'. *Catalysis Today* **164**, 62.

Santos, J., Phillips, J., and Dumesic, J.A.: 1983,
'Metal support interactions between iron and titania for catalysts prepared by thermal decomposition of iron pentacarbonyl and by impegnation '.
*Journal of Catalysis* **81**, 147.

Schulz, H., Rao, B. R. and Elstner, M.: 1970,
'$^{14}$C-Studien zum Reaktionsmechanismus der Fischer-Tropsch-Synthese'.
*Erdöl und Kohle* **22**, 651.

Schulz, H. and Nehren, S.: 1986.
'Die Herstellung von Gas/Dampf – Eichgemischen für die Gaschromatographie'.
*Erdöl und Kohle - Erdgas - Petrochemie* **39**, 93.

Schulz, H., K. Beck, and E. Erich: 1988,
'Mechanism of the Fischer-Tropsch process'.
*Studies in Surface Science and Catalysis* **36**, 457.

Schulz, H., E. Erich, H. Gorre, and E. van Steen: 1990,
'Regularities as a key for discriminating surface reactions and formation of the dynamic system'. *Catalysis Letters* **7**, 157.

Schulz, H., van Steen, E. and Claeys, M.: 1994,
'Selectivity and mechanism of Fischer-Tropsch synthesis with iron and cobalt catalysts'.
*Studies in Surface Science and Catalysis* **81**, 455.

Schulz, H. and Claeys, M.: 1999,
'Reactions of *α*-olefins of different chain length added during Fischer-Tropsch synthesis on a cobalt catalyst in a slurry reactor'.
*Applied Catalysis A: General* **186**, 71.

Schulz, H.: 1999,
'Short history and present trends of Fischer-Tropsch synthesis'.
*Applied Catalysis A: General* **186**, 3.

Schulz, H.: 2003,
'Major and minor reactions in Fischer-Tropsch synthesis on cobalt catalysts'.
*Topics in Catalysis* **26**, 73.

Spieker, W.A. and Regalbuto, J.R.: 2001,
'A fundamental model of platinum impregnation onto alumina'.
*Chemical Engineering Science* **56**, 3491.

Steynberg, A. P.: 2004,
'Introduction to Fischer-Tropsch technology'.
In: A. Steynberg and M. Dry (eds.): Fischer-Tropsch Technology, Vol. 152 Studies in Surface Science and Catalysis. Elsevier Science, Chapt. 1, p. 1.

Steynbeg, A. and Dry, M.E.: 2004,
'Fischer-Tropsch Technology'.
*Elservier, Amsterdam*, 406.

Storch, H. H., Golumbic, N. and Anderson, R. B.: 1951,
'The Fischer-Tropsch andRelated Synthesis'.
John Wiley & Sons, Inc., New York.

Sou, H., Wang, S., Zhang, C., Xu, J., Wu, B., Yang, Y., Xiang, H. and Li, Y-.W: 2012,
'Chemical and Structural effects of silica in Iron-based Fischer-Tropsch synthesis catalyst'.
*Journal of Catalysis* **286**, 111.

Swedlund, P.J., Miskelly, G.M. and McQuillan, J.A.: 2009,
'An attenuated total reflectance IR study of silicic acid adsorbed onto a ferric oxyhydroxide surface'.
*Geochimica et Cosmochimica Acta* **73,** 4199.

Takei, T., Kato, K., Meguro, A. and Chikazawa, M.: 1999,
'Infrared spectra of germinal and novel triple hydroxyl groups on silica surface'.
*Colloids and Surfaces A: Physicochemical and Engineering Aspects* **150**, 77.

Taniguchi, S., Mori, T., Mori, Y., Hattori, T. and Murakami, Y.:1988,
'Another strong metal-support interactions: high intrinsic methanation activity of an alumina-supported platinum catalyst after high temperature reduction without loss of chemisorptions ability'. *Journal of chemical Society, Chemical Communications* **10**, 630.

Tauster, S.J., Fung, S.C. and Garten, R.L.: 1978,
'Strong Metal-Support Interactions. Group 8 Noble Metals Supported in $TiO_2$'.
*Journal of American Chemical Society* **100** (1978), 170.

Tauster, S.J., Fung, S.C., Baker, R.T.K and Horsley, J.A.: 1981,
'Strong Interactions in Metal-Support Catalysts'.
*Science* **211,** 1121.

Tauster, S.J.: 1987
'Strong Metal-Support Interactions'.
*Accounts of Chemical Research* **20**, 11.

Titmuss, A., Wander, A. and King, D.A.:1996,
*Chemical Reviews* **96,** 1291

van Berge, P.J. and. Everson, R.C: 1997,
'Cobalt as an alternative Fischer-Tropsch catalyst to iron for the production of middle distillates'.
*Studies in Surface Science ans Catalysis* **107**, 207.

van der Kraan, A.M., Nonnekens, R.C.H., Stoop, F. and Niemantsverdriet J.W.: 1986,
'Characterization of $FeRu/Ti0_2$ and $Fe/Ti0_2$ catalysts after reduction and fischer-Tropsch synthesis using Mössbauer spectroscopy'.
Applied Catalysis **27**, 285.

van Roosmalen, A.J and Mol, J.C: 1978,
'An Infrared Study of the Silica Gel Surface. 1. Dry Silica Gel'.
*The Journal of Physical Chemistry* **82**, 2748.

van Santen, R.A., Ciobîcă, I.M., van Steen, E. and. Ghouri, M.M.: 2011,
'Chapter 3- Mechanistic issues in Fischer-Tropsch catalysis'.
*Advances in Catalalysis* **54**, 127.

van Steen, E., Sewell, G.S., Makhote, R.A., Micklethwaite, C., Manstein, H., de Lange, M. and O'Connor, C.T.: 1996, 'TPR study on the preparation of impregnated $Co/SiO_2$ catalysts'.
*Journal of Catalysis* **162**, 220.

van Steen, E. and Schulz, H.: 1999,
'Polymerization kinetics of the Fischer–Tropsch CO hydrogenation using iron and cobalt based catalysts'. *Applied Catalysis A: General* **186,** 309.

van Steen, E., M. Claeys, M. E. Dry, J. van de Loosdrecht, E. L. Viljoen, and J. L. Visagie: 2005,
'Stability of nano-crystals: Thermodynamic analysis of oxidation and re-reduction of cobalt in water/hydrogen mixtures'.
*J. Phys. Chem. B* **109**, 3575.

van Steen, E. and Claeys, M.: 2008,
'Fischer-Tropsch catalysts for Biomass-to-Liquids (BTL) process'.
*Chemical Engineering and Technology* **31**, 655.

Vannice, M. A.: 1975,
'The catalytic synthesis of hydrocarbons from carbon monoxide and hydrogen'.
*Journal of Catalysis* **37**, 449.

Vannice, M. A.: 1977,
'The catalytic synthesis of hydrocarbons from $H_2$/CO mixtures over the group VIII metals'.
*Journal of Catalysis* **50**, 228.

Vannice, M. A. and Sudhakar, C.: 1984,
'A model for the metal-support effect enhancing CO hydrogenation rate over Pt-$TiO_2$ catalysts'.
*Journal of Physical Chemistry* **88**, 2429.

Vannice, M.A., Hasselbring, L.C. and Sen, B.: 1985,
'Metal-support effects on hydrogen and carbon monoxide heats of adsorption on titania-supported platinum'.
*Journal of Physical Chemistry* **89**, 2972.

Veintemillas-Verdaguer, S., Morales, M.P. and Serna, C.J.: 1998,
'Continuous production of γ-$Fe_2O_3$ ultrafine powders by laser pyrolysis'.
*Materials Letters* **35**, 227.

Vempati, R.K.., Loeppert, R.H., Sittertz-Bhatkar, H. and Burghardt, R.C.: 1990,
'Infrared vibrations of hematite formed from aqueous- and dry-thermal incubation of Si-containing ferrihydrite'.
*Clays and Clay Minerals* **38**, 294.

Vosloo, A.C.: 2001,
'Fischer-Tropsch: a futuristic view'.
*Fuel Processing Technology*, **77** (2001), 149-155.

Walsh, R.: 1998,
'Fischer-Tropsch Synthesis over SiO2, ZnO and MnO Supported Cobalt Catalyst'.
*Journal of Catalysts* **212**,10.

Walters, D.: 2006,
'Characterization of hydrous hematite pigments',
*Thermochimica Acta* **445**,195,

Wan, H., Wu, B., Zhang, C., Teng, B., Tao, Z., Yang, Y., Zhu, Y., Xiang, H. and Li, Y.:2005,
'Effects of $Al_2O_3$/$SiO_2$ ratio on iron based catalysts for Fischer-Tropsch catalysts'.
*Fuel* **85**, 1371.

Wan, H., Wu, B., Tao, Z., Li, T., An, X., Xiang, H. and Li, Y.: 2006,
'Study of the iron-based Fischer-Tropsch synthesis catalyst incoperated with $SiO_2$'.
*Journal of Molecular Catalyst A: Chemical* **260**, 255.

Wan, H., Wu, B., Zhang, C., Xiang, H., Li, Y., Xu ,B. and Yi, F.: 2007,
'Study on Fe-$Al_2O_3$ interaction over precipitated iron catalyst for Fischer-Tropsch synthesis'.
*Catalysis Communications* **8**, 1538.

Wanke, S. E. and Flynn, P. C.: 1975,
'A model of supported metal catalysts sintering. I. Development of model'.
Catalysis Reviews, Science and Engineering **12**, 93.

Wei, J.H., Leng, C.J., Zhang, X.Z., Li, W.H., Liu, Z.Y. and Shi, J.: 2009,
'Synthesis and magnetorheological effect of $Fe_3O_4$-$TiO_2$ nanocomposites'.
*Journal of Physics: Conference Series* **149**, 012083.

Wise, H. and Oudar, J.: 2001,
'Material concepts in surface reactivity and catalysis'.
Dover Publications inc. Mineola, New York (2001).

Woo, K., Lee, H.J., Ahn, J.-P. and Park, Y.S.: 2003,
'Sol-Gel mediated synthesis of Fe2O3 nanorods'.
`*Advanced materials* **15**, 1761.

Yang, Y., Xiang, H-.W., Tian, L., Wang, H., Zhang, C.-H., Tao, Z.-C., Xu ,Y.-Y., Zong, B. and Li, Y.-W.: 2005, 'Structure and Fischer-Tropsch performance of iron-manganese catalyst incorporated with $SiO_2$'. *Applied Catalysis A: General* **284**, 105.

Yang, Y., Roonasi, P. and Holmgren, A.: 2008,
'Study of sodium silicate in aqueous solution and sorbed by synthetic magnetite using in situ ATR-FTIR spectroscopy'. *Journal of Colloid and Interface Science* **328,** 41.

Yang, S., He, H., Wu, D., Chen, D., Liang, X., Qin, Z., Fan, M., Zhu, J., and Yuan, P.: 2009,
'Decolorization of methylene blue by heterogeneous Fenton reaction using $Fe_{3-X}Ti_XO_4$ ($0 < X < 0.78$) at neutral ph values' *Applied Catalysis B: Environmental* **89**, 527

Yang, S., Gou, Y., Yan, N., Wu, D., He, H., Qu, Z., Yang, C., Zhou, Q. and Jia, J.: 2011,
'Nanosized cation-deficient Fe-Ti Spinel: A novel magnetic sorbent for elemental mercury capture from flue gas'. *Applied Materials and Interfaces* **3**, 209

Zhang, C.H., Wan, H.J., Xiang, H.W., Li, Y.W.: 2006,
'Study on the iron-silica interaction of a co-precipitated Fe/$SiO_2$ Fischer-Tropsch synthesis catalyst'.
*Catalysis Communications* **7**, 733.

# Appendix A: Anderson-Schulz-Flory Polymerization Kinetics

The molar content of Fischer-Tropsch products decreases with increasing carbon number according to the so-called Anderson-Schulz-Flory (ASF) polymerisation kinetics described by the following equation:

$$\lg(x_N) = N\lg(\alpha) + \lg\frac{(1-\alpha)}{\alpha} \qquad \text{(A.1)}$$

where $x_N$ is the mole fraction of products having N carbon atoms and α is the probability of chain growth. Here the probability of chain growth is assumed to be independent of chain length.

The derivation of **Equation A.1** is based on the hydrocarbon synthesis chain growth and desorption scheme shown in **Figure A.1**. The proposed basic model neglects the formation of oxygenates and branched hydrocarbons and making the assumption that only one sort of product $Pr_N$ can desorb per carbon number N, one can propose a simple basic chain growth model of this polymerization (as depicted in **Figure A.1**).

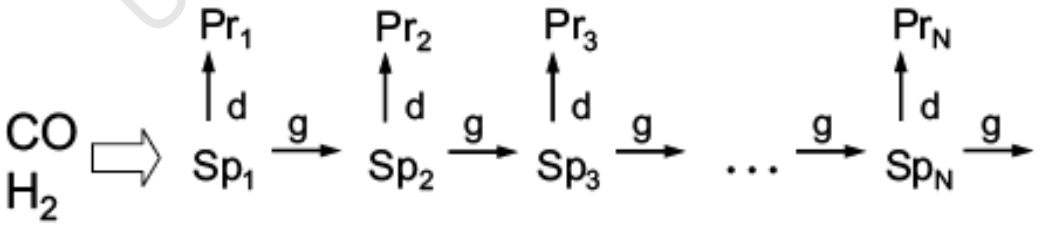


**Figure A.1**: Kinetic scheme of Fischer-Tropsch hydrocarbon chain growth and desorption

A mass balance around a surface species $Sp_N$ at steady state results in:

$$r_{f,SpN} = r_{c,SpN} \qquad \text{(A.2)}$$

Eq. A.2 implies that:

$$r_{g,SpN-1} = r_{d,SpN} + r_{g,SpN} \quad (A.3)$$

Product, $Pr_N$, is formed by the desorption of surface species, $Sp_N$, this results in:

$$r_{f,PrN} = r_{d,SpN} \quad (A.4)$$

Therefore;

$$r_{f.PrN} = \frac{r_{d,SpN}}{r_{d,SpN} + r_{g,SpN}} . \left(r_{d,SpN} + r_{g,SpN}\right) \quad (A.5)$$

Definitions:

$$\text{Desorption probability : } \beta_N = \frac{r_{d,SpN}}{r_{d,SpN} + r_{g,SpN}} \quad (A.6)$$

$$\text{Chain growth probability : } \alpha_N = \frac{r_{g,SpN}}{r_{g,SpN} + r_{d,SpN}} \quad (A.7)$$

From these definitions, it follows that:

$$\beta_N + \alpha_N = 1 \quad (A.8)$$

Substituting Eqs. A.3 and A.6 into Eq. A.5:

$$r_{f.PrN} = \beta_N . \frac{r_{g.SpN-1}}{r_{d,SpN-1} + r_{g,SpN-1}} . \left(r_{d,SpN-1} + r_{g,SpN-1}\right) \quad (A.9)$$

Substituting Eqs. A.3 and A.7 into Eq. A.9:

$$r_{f.PrN} = \alpha_{N-1} . \beta_N . \frac{r_{g.SpN-2}}{r_{d,SpN-2} + r_{g,SpN-2}} . \left(r_{d,SpN-2} + r_{g,SpN-2}\right) \quad (A.10)$$

which leads to:

$$r_{f,PrN} = \beta_N.\alpha_{N-1}.\alpha_{N-2}.....\alpha_2.\alpha_1.r_{f,Sp1} \quad (A.11)$$

Since all product compounds are formed starting from a $C_1$ species, the sum of theformation rates of all products, $Pr_N$ (N = 1, 2, ....., $\infty$), must equal the consumption rate of the species $Sp_1$, the chain starter:

$$r_{f,Sp1} = \sum_{N=1}^{\infty} r_{f,PrN} \quad (A.12)$$

The molar content of a product compound $X_N$ with N carbon atoms in the total organic product spectrum is:

$$X_N = \frac{r_{f,PrN}}{\sum_{n=1}^{\infty} r_{f,PrN}} = \beta_N.\alpha_{N-1}.\alpha_{N-2}.....\alpha_2.\alpha_1. \quad (A.13)$$

If the probability of chain growth α is assumed to be independent of chain length N then Eq. A.15 becomes:

$$X_N = \alpha^{N-1}.\beta = \alpha^{N-1}.(1-\alpha) \quad (A.14)$$

Taking logarithms to both sides of Eq. A.14, we get:

$$\lg(x_N) = N\lg(\alpha) + \lg\frac{(1-\alpha)}{\alpha} \quad (A.15)$$

**Equation A.15** is the Anderson-Schulz-Flory (ASF) equation that describes the product distribution with $p_g$ being the only parameter. A plot of $\lg(x_N)$ against carbon number (N) gives a straight line from which α can be deduced.

The Anderson-Schulz-Flory equation presents straight lines when plotting molar product fractions ($x_N$) logarithmically over the carbon number, with the slope reflecting the chain growth probability. This is merely a theoretical model that was designed to model the distribution of Fischer-Tropsch products. The distributions of the products in real life conditions have been observed to be different from those predicted by the Flory equation [Claeys and van Steen, 2004]. The distribution presented by Figure A.2 corresponds to the ideal case.

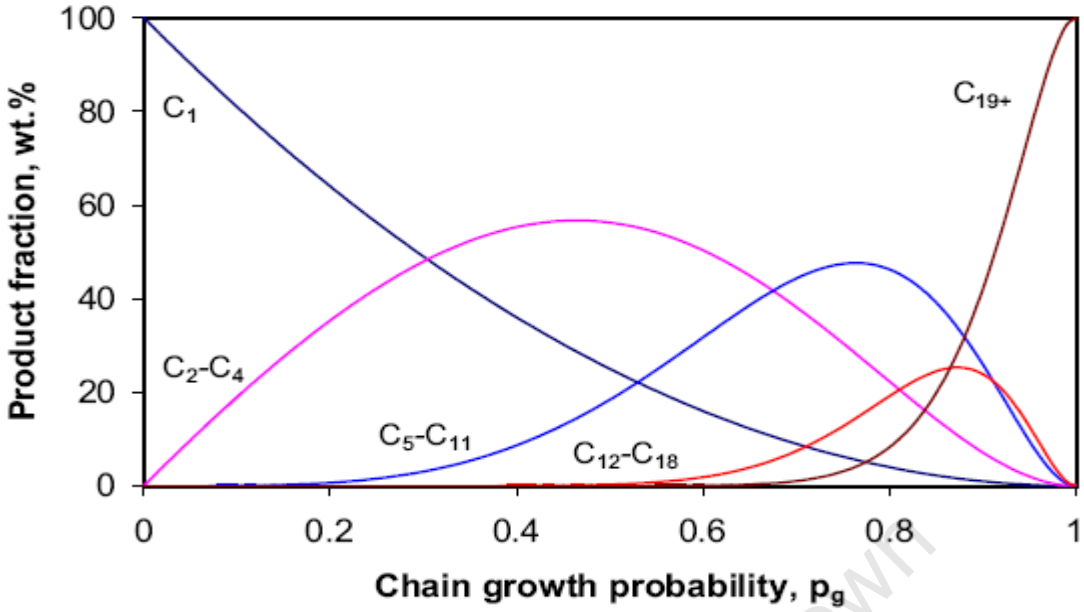


**Figure A.2**: Theoretical product distribution as a function of the chain growth probability assuming ideal kinetics

The figure shows that the product distribution of the Fischer-Tropsch is not selective but it is rather a polymerisation process. The following deviations (from the ideal case) are observed in experimental cases:

- More $CH_4$ than that predicted by the model
- A lower $C_2$ selectivity
- Higher Heavy product selectivity

These deviations can be explained though different models and the Fischer-Tropsch products are also dependent on the metal used. There are other factors such as temperature and pressure (only to mention a few) that contribute to the overall distribution. All these factors have to be considered when predicting the product distribution of the Fischer Tropsch process.

# Appendix B: Additional Experimental information

## B1: Catalyst preparation: Water-in-Oil microemulsion technique

The water-in-oil microemulsion system consists of three components, viz. water, surfactant (Berol 050[1], Akzo Nobel) and n-hexane (HPLC grade, Aldrich Chemical Company). Figure B.1 show the ternary diagram used in this work (as previously by other researchers Abrevaya et al. (1987) and Mabaso (2005)). The shaded portion of the diagram depicts the region stable for water in oil emulsion, within which the system was operated.



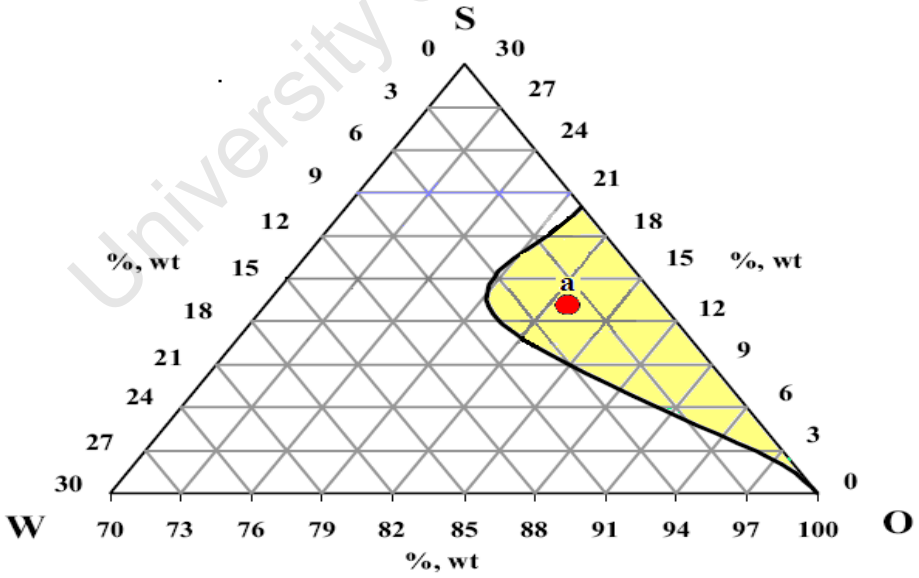


**Figure B.1**: Ternary diagram showing the stable region from which the microemulsion were prepared (**W**: water, **O**: oil, **S**: surfactant)

Specifications and system conditions of experiments conducted for preparation of the specific size of the nanosized crystallites are also shown in Figure B.1. The system shown by point *a* (see Figure B.1) on the ternary diagram represents 12 g of the aqueous phase, 40 g of surfactant phase and 250 g of oil phase. In previous work done by Mabaso (2006) it was shown that the system conditions depicted by point *a* results in a narrow size distribution of nanosized crystallites with an average crystallite diameter of approximately 10 nm.

## B.2 Calcination Set-up

The mass of the recovered sample was measured before it was loaded into the calcination reactor (fixed bed reactor). Glass wool is used to make a bed for the sample at the bottom of the reactor (see **Figure B.2**). The calcination was performed under flowing air. The flow rate of the air into the reactor was controlled using the electronic flow controller and was set at a flow rate of 300 ml/min.$g_{sample}$. A temperature programmer was set to increase the temperature from 25 $^0$C to 350 $^0$C at a heating rate of 10 $^0$C/min. This was done using the temperature control programmer that is connected to the furnace.

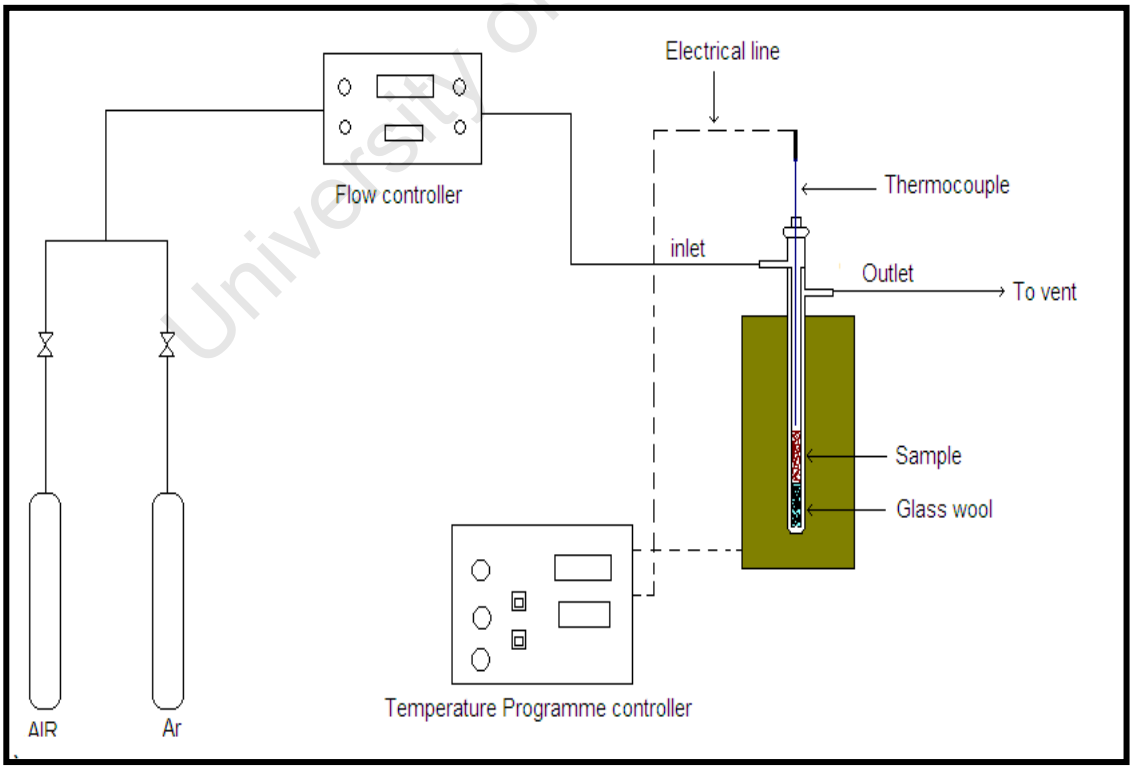


**Figure B.2**: The Calcination rig setup

A thermocouple was inserted into the reactor and was used to monitor the actual temperature of the catalyst. The thermocouple was also used to monitor for temperature overshooting. The temperature was then maintained at 350 $^0$C for 3 hours. After 3 hours the reactor is cooled to room temperature and then calcined samples were removed and recovered.

# B.3 Catalyst Characterization:

## $H_2$-TPR Calibration

40 mg of sliver oxide (AgO) was used as a standard for the analysis. AgO is used as a standard because it's easy to reduce. The standard sample was reduced using 5 % hydrogen in argon at a flow rate of 45 ml/min. The sample was heated from room temperature to 500 $^0$C. The reduction of AgO results in two peaks as shown by Figure B.3.

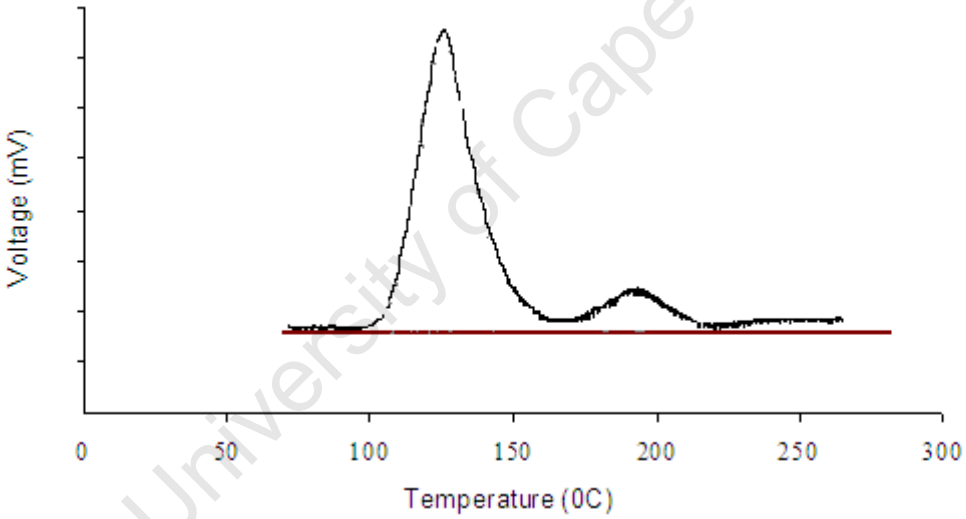


**Figure B.3**: Silver oxide (AgO) Reduction Curve

The graph is then integrated to find the area. The area under the curve represents the amount of hydrogen consumed to reduce the AgO. Using the known mass of silver oxide, the total moles of $H_2$ required for complete reduction can be calculated (see **Equations B.1** and **Equation B.2**). Therefore, the number of $H_2$ moles consumed can be related to the area.

$$2AgO + H_2 \leftrightarrow Ag_2O + H_2O \quad (B.1)$$

$$Ag_2O + H_2 \leftrightarrow 2Ag + H_2O \quad (B.2)$$

# B.4 Fischer-Tropsch synthesis

## B.4.1 Reactor packing (Loading)

A schematic of the reactor is presented in Figure B.4. A frit is placed at the bottom of the reactor and glass wool is added to keep the catalyst bed in place. A thermowell is then inserted in the middle of the reactor and is used to hold the thermocouple the at centre of the reactor during the Fischer-Tropsch synthesis. The thermocouple was used to monitor and control the temperature of the reactor.

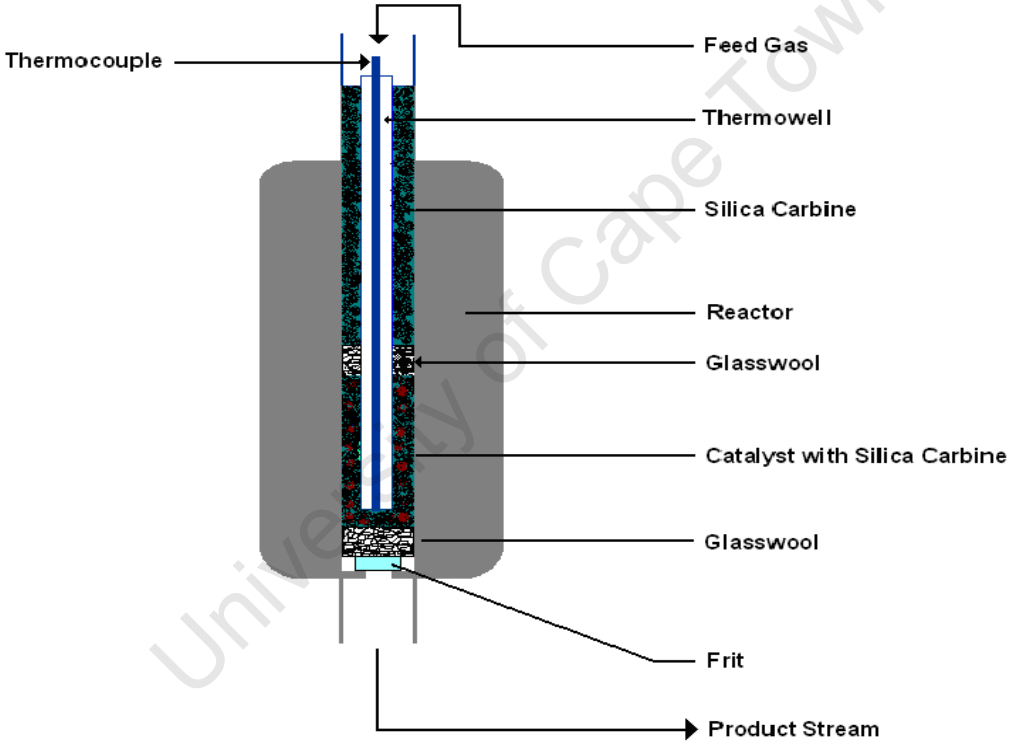




**Figure B.4:** Reactor configuration and catalyst packing

The wetted sample is then added, around the thermowell, into the reactor. Glass wool is then added on top of the catalyst to ensure that the catalyst bed does not move during experiment and during pressuring and depressurising of the system. The reactor is then filled up with silicon carbide (200-250 µm) to the top. The synthesis gas comes in at the top of the reactor and the product stream comes out at the bottom. The reactor system is then connected to the FTS setup and following that the system is pressure tested.

## B.4.2 Pressure test

All connection points were carefully tightened to avoid any gas leaks. Before the process could be started up, it had to pass a pressure test. The pressure test is as follows:

- All exit control valves (CV-6-7) in the system are closed
- The needle valve (NDV-1) is fully open.
- The argon control valve (CV-4) is opened and the system is pressurized to 20 bar.
- The system is left at that constant pressure for one minute.
- The argon flow control valve (CV-4) is then closed and the system is allowed to maintain pressure.
- If there are any leaks in the system then the pressure will drop but if the pressure of the system remains constant for 24 hours then the system has passed the pressure test.

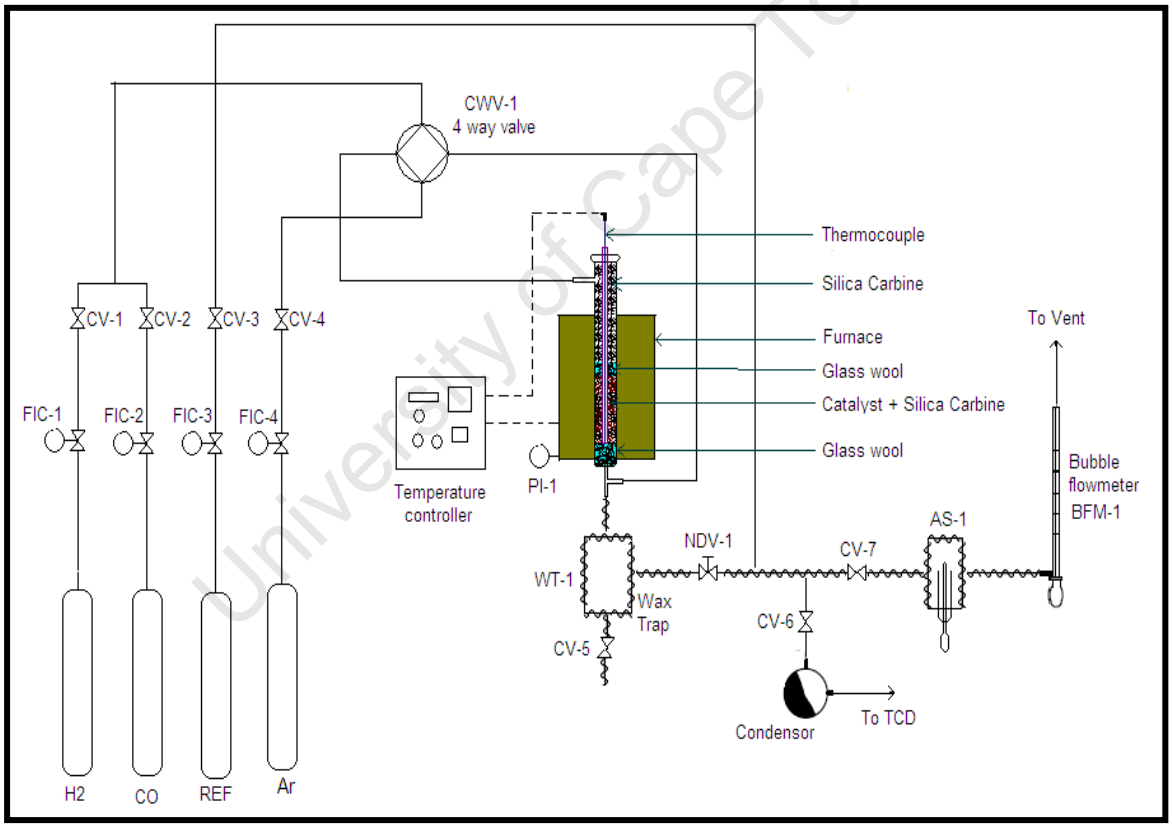


**Figure B.5**: Setup for Fischer-Tropsch synthesis. CV-1-4: flow control valves; FIC-1-4: flow indicator controllers; AS-1: Ampoule Sampler

After the system passed the pressure test, it was depressurized. The Argon control valve (CV-4) is then closed before opening the control valve (CV-7) to the ampoule sampler which will release the gas off to the vent (see Figure B.5). The pressure was then reduced to atmospheric, which is the pressure required for reduction.

### B.4.3 Shutdown procedure

Sampling was done across 24 hours and after the last sample was taken the shut down procedure was commenced. The following steps were followed during shut down of the rig:

Firstly, all the flow controllers (FIC1-3) are reset to zero (see Figure B.5). This will stop the flow of all gases to the rector except argon. The control valves CV-1-3 are then closed. Secondly, the argon flow controller (FIC-4) is closed followed by the control valve (CV-4). Thirdly, the system is then depressurised by opening the needle valve (NDV-1) fully and the gas in the system is then vented off. The programmed running the rector is switched off.

At this point the shut down process is complete. The power switch to the rig is then tripped and the insulation around the reactor is removed to allow the reactor to cool. After the temperature of the system has drop below 100 $^{0}$C the heating element around the reactor is removed to improve cooling. The reactor is then removed from the rig. The catalyst is then removed and labeled as spent and the sample is stored for further analyses.

### B.4.4 Offline FID analysis

A typical FID chromatogram obtained using the ampoule method is shown in **Figure B.6.** All the compounds are labeled according to a sample code; the sample codes are displayed in **Table B.1.**

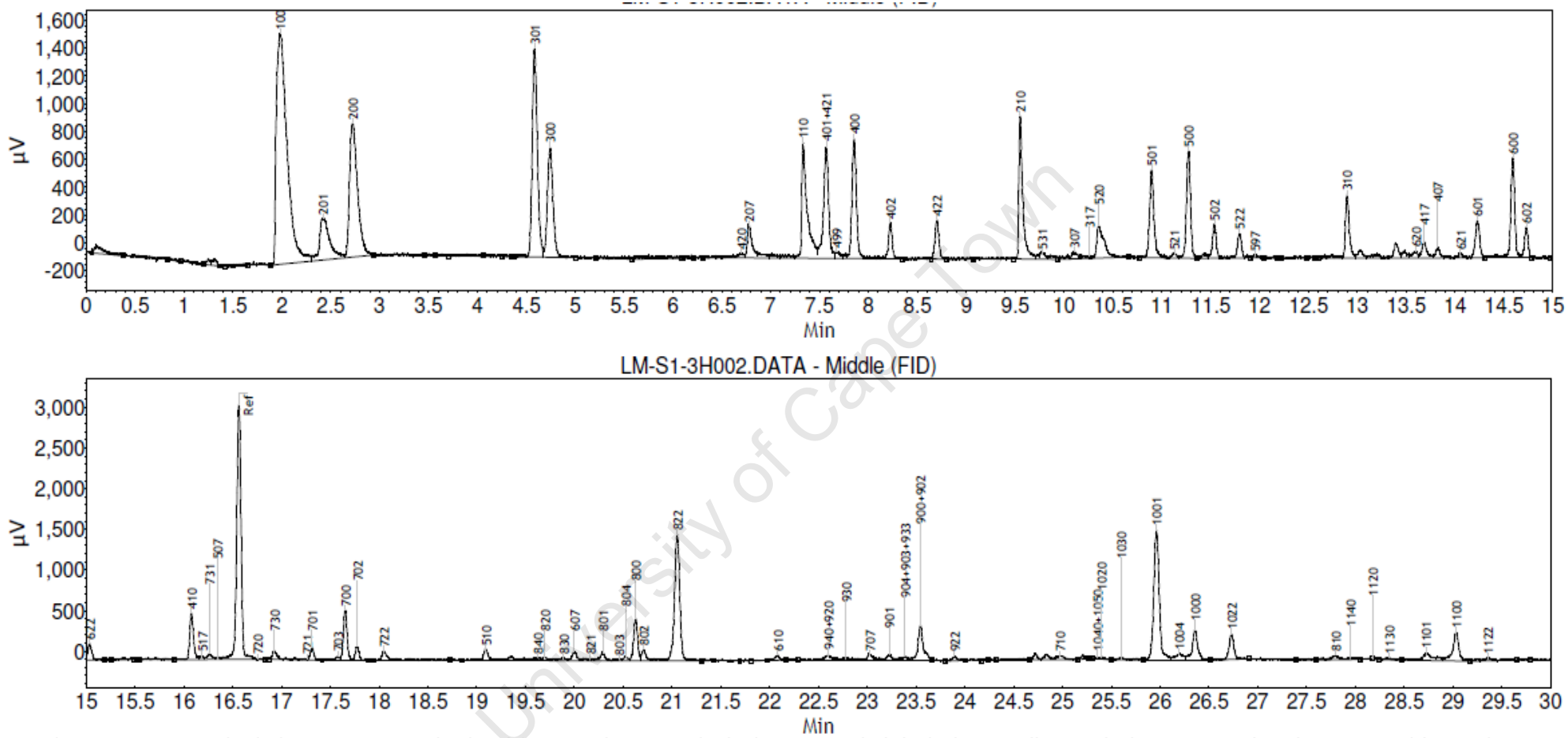


Figure B.6: A typical chromatogram obtained from and FID analysis (compounds labeled according to their compound codes; see Table B.1 )

Table B.1: Compounds analyzed using offlined FID method (sample codes)

| Compound | Code |
|---|---|
| **Methane** | **100** |
| *Methanol* | *110* |
| **Ethane** | **200** |
| Ethene | 201 |
| *Ethanol* | *210* |
| *Ethanal* | *207* |
| **Propane** | **300** |
| Propene | 301 |
| *Propanol -1* | *310* |
| *Propanal* | *307* |
| *Propanol -2* | *315* |
| *Propanone* | *317* |
| **n-Butane** | **400** |
| Butene -1 | 401 |
| trans-Butene-2 | 402 |
| cis-Butene-2 | 422 |
| Butadiene-1,3 | 499 |
| *Butanol -1* | *410* |
| *Butanal* | *407* |
| *Butanol -2* | *415* |
| *Butanone-2* | *417* |
| 2-Methyl-Propane | 420 |
| 2-Methyl-Propene-1 | 421 |
| **n-Pentane** | **500** |
| Pentene-1 | 501 |
| trans-Pentene-2 | 502 |
| cis-Pentene-2 | 522 |
| *Pentanol -1* | *510* |
| *Pentanal* | *507* |
| *Pentanone -2* | *517* |
| 2-Methyl-Butane | 520 |
| 2-Methyl-Butene-1 | 521 |
| 3-Methyl-Butene-1 | 531 |
| 2-Methyl-Butene-2 | 597 |
| **n-Hexane** | **600** |
| Hexene-1 | 601 |
| trans-Hexene-2 | 602 |
| cis-Hexene-2 | 622 |
| trans-Hexen-3 | 603 |
| cis-Hexen-3 | 633 |
| *Hexanol -1* | *610* |
| *Hexanal* | *607* |
| *Hexanone -2* | *617* |
| 2-Methyl-Pentane | 620 |
| 3-Methyl-Pentane | 630 |
| 2-Methyl-Pentene-1 | 621 |
| 3-Methyl-Pentene-1 | 631 |
| 4-Methyl-Pentene-1 | 641 |
| 2-Methyl-Pentene-2 | 697 |
| 3-Methyl-Pentene-2 | 632 |
| 4-Methyl-Pentene-2, cis and trans | 642 |
| 2,3 Di-Methyl-Butane | 623 |
| 2,4 Di-Methyl-Butane | 624 |
| 2,3 Di-Methyl-Butene-1 | 664 |
| Methyl-Cyclopentane/ene | C620 |
| **n-Heptane** | **700** |
| Heptene-1 | 701 |
| trans-Heptene-2 | 702 |
| cis-Heptene-2 | 722 |
| trans-Heptene-3 | 703 |
| cis-Heptene-3 | 733 |
| *Heptanol -1* | *710* |
| *Heptanal* | *707* |
| *Heptanone -2* | *717* |
| 2-Methyl-Hexane | 720 |
| 3-Methyl-Hexane | 730 |
| 2-Meethyl-Hexene-1 | 721 |
| 3-Methyl-Hexene-1 | 731 |
| 4-Methyl-Hexene-1 | 741 |
| 5-Methyl-Hexene-1 | 751 |
| 2-Methyl-Hexene-2 | 797 |
| 3-Methyl-Hexene-2 | 732 |
| 2,3 Di-Methyl-Pentane | 723 |
| 3-Ethyl-Pentane | 780 |
| Methyl-cyclohexane/ene | C720 |
| Toluol | C710 |
| 1,3 Di-Methyl-Cyclopentane | C713 |
| Rest C7 | R7 |
| **n-Octane** | **800** |
| Octene-1 | 801 |
| trans -Octene-2 | 802 |
| cis-Octene-2 | 822 |
| trans-Octene-3 | 803 |
| cis-Octene-3 | 833 |
| trans-Octene-4 | 804 |
| *Octanol-1* | *810* |
| *Octanal* | *807* |
| *Octanone-2* | *817* |
| 2-Methyl-Heptane | 820 |
| 3-Meethyl-Heptane | 830 |
| 4-Methyl-Heptane | 840 |
| 2-Methyl-Heptene-1 | 821 |
| 3-Methyl-Heptene-1 | 831 |
| 4-Methyl-Heptene-1 | 841 |
| 5-Methyl-Heptene-1 | 851 |
| Methyl-C8-Olefin | R81 |
| Rest C8 | R8 |
| **n-Nonane** | **900** |
| Nonene-1 | 901 |
| trans-Nonene-2 | 902 |
| cis-Nonene-2 | 922 |

# Appendix C: CO activation studies of the Fe-O-Si system

## C.1 CO reduction of TEOS modified samples

To investigate the effects of different reducing agents, the samples were also reduced in CO at a flowrate of 400 ml/min/$g_{cat}$. Initially, the reduction was done for 16 hours at 350 $^0$C and the heating heat was maintained at 1 $^0$C/min (see Figure C.1). At temperatures higher than 270 $^0$C the formation of graphite became evident. This was not desirable since graphite has been known to cover the catalyst surface and result in low or even no activity [Bartlomew, 1997]. Therefore, the reduction of the catalyst with CO was maintained at 270 $^0$C and the results are presented in Figure C.2. The XRD analysis of all the CO reduced samples is presented in Figure C.2 and the associated phases, contents and average crystallite size determined using Reitveld refinement is presented in Table C.1.

Figure C.1 shows the XRD analysis of the CO reduction FS-88 catalyst. The conversion of $Fe_2O_3$ to $Fe_3O_4$ is not clearly discernable from the presented data since the maghemite peak ($\gamma$-$Fe_2O_3$) peaks are almost identical to those of the magnetite $Fe_3O_4$. The reduction of the catalyst with CO appears to minimize the formation of FeO as compared with $H_2$ reduction. As shown in Figure X the intensity of the FeO appears to remain low throughout the reduction process as compared to the $H_2$ reduced catalysts. However, at the end of the reduction process $Fe_3O_4$ was still be found in the catalyst as shown in Table C.1.

The carbide formation for catalyst FS-56 begins as early as 180 $^0$C whiles the formation of carbides in the sample FS-88 was delayed to 240 $^0$C. Since the heating rate was the same for both catalysts, this indicates that the carburization process is retarded by increasing TEOS modification.

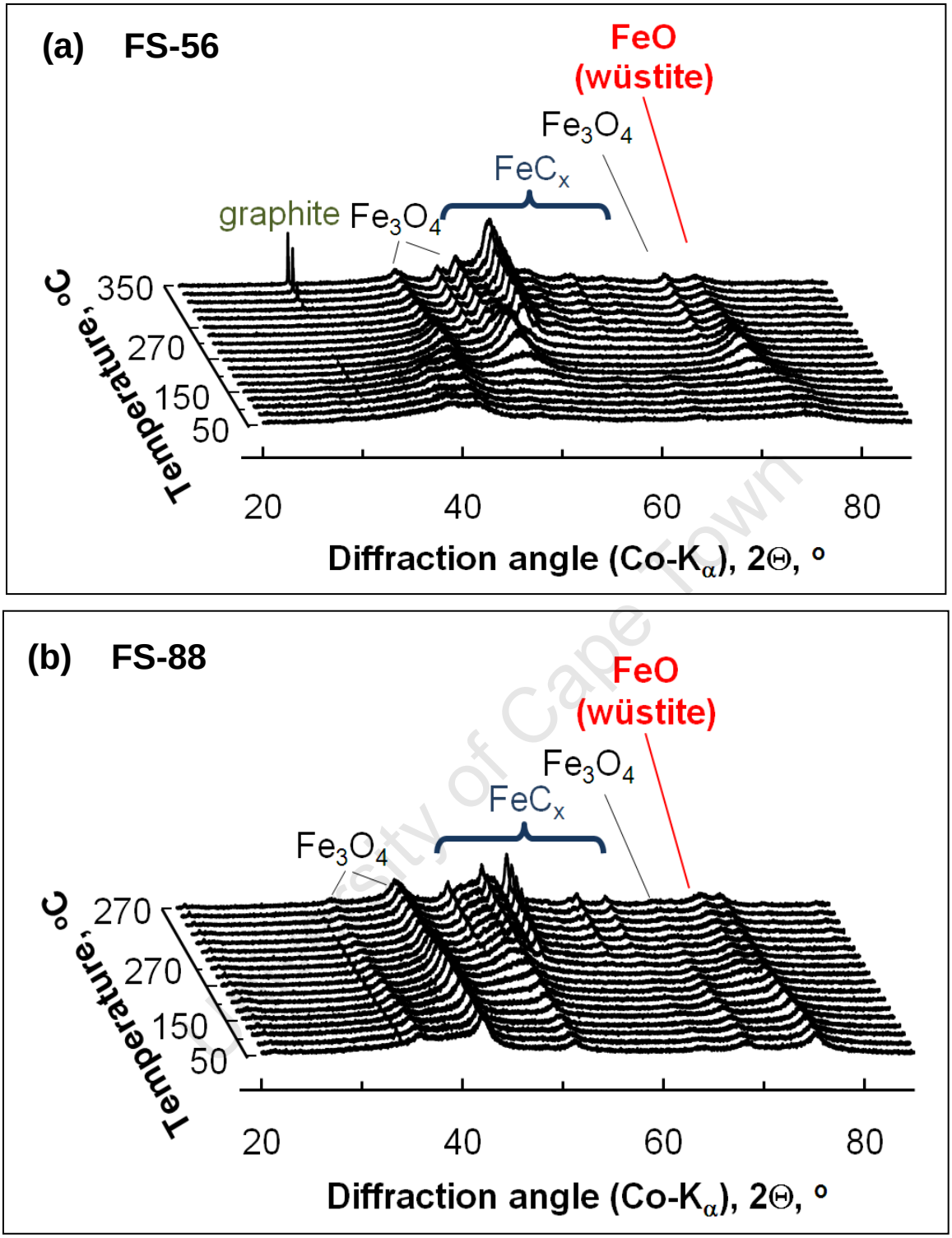


**Figure C.1**: In-situ XRD analysis of the calcined iron oxide nano-crystallites prepared using microemulsion technique and modified with TEOS using instantaneous method.

(a) Reduction analysis of unmodified sample, FS-0

(b) Analysis of sample with highest TEOS loading, FS-88

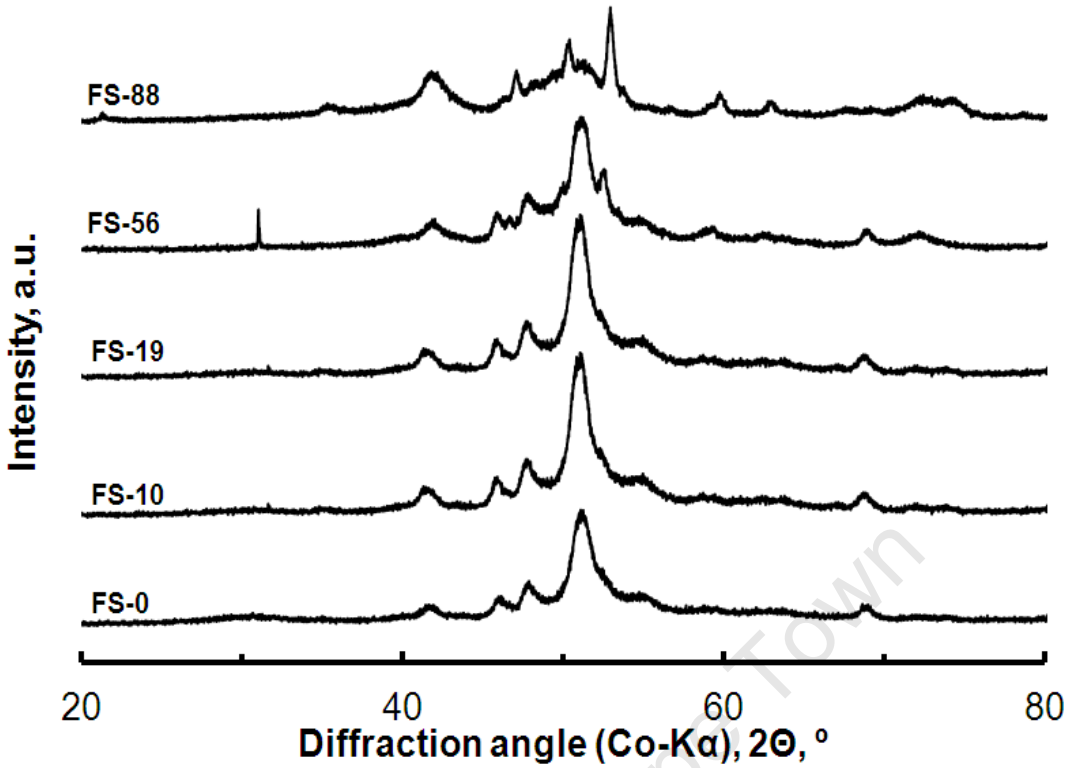


**Figure C.2**: TPR patterns of iron oxide crystallites prepared using micro-emulsion of different Si loadings reduced in CO (40 ml/min NTP) at 270 $^{0}$C for 16 hours

When the catalysts were reduced in CO, their behavior changed. The in situ CO reductions studies indicated, generally, a higher degree of reductions for the modified catalysts. Whiles the unmodified catalyst was fully reduced to carbide, all the modified catalyst showed a lower FeO content (**Table C.1**) as compared to the $H_2$ reduction. The observed decrease in the oxide content for samples FS-19 and FS-56 can be associated with the low FeO content. However, the modification of the catalysts with TEOS appears to stabilize the $Fe_3O_4$ phase when CO is the reducing agent. High content of $Fe_3O_4$ was found at the end of the reduction process.

The two reducing agents, despite the difference in reduction processes, indicated that the existence of the Fe-O-Si interaction on the surface suppresses the reduction of the active metal. This appears to result by the stabilization of an oxide phase (FeO for $H_2$ reduction and $Fe_3O_4$ for CO reduction) making the metal oxide harder to reduce with increasing Si content.

**Table C.1:** Average crystallite sizes (in nm) estimated from Debye-Scherrer equations and the phase quantitative analysis using RIR method.

| Component | FS-0 | FS-10 | FS-19 | FS-56 | FS-88 |
|---|---|---|---|---|---|
| **$Fe_3O_4$**: content (wt %): | — | **9** | **9** | **12** | **32** |
| Size (nm): | — | **8** | **7** | **8** | **7** |
| **FeO**: content (wt %): | — | — | **6** | **10** | **18** |
| Size (nm): | — | — | **7** | **8** | **6** |
| **$Fe_3C$**: content (wt %): | **100** | — | — | — | — |
| Size (nm): | **11.8** | — | — | — | — |
| **$Fe_5C_2$**: content (wt %): | — | **72** | **34** | **39** | **26** |
| Size (nm): | — | **14** | **11** | **12** | **11** |
| **$Fe_2C$**: content (wt %): | — | **19** | **50** | **39** | **24** |
| Size (nm): | — | **24** | **25** | **26** | **26** |

## C.2 Fischer-Tropsch Synthesis of CO activated FS-0 catalysts

To investigate the effects of pretreatment on the catalyst activity, the unmodified catalyst, FS-0, was reduced in 40 ml/min (NTP) $H_2$ at 350 $^0$C for 16 hours. The reduction was done at atmospheric pressure and following that the tested for FT synthesis at the already relayed conditions. Following that, a new batch of the same catalyst was then reduced with 40 ml/min (NTP) of CO at 270 $^0$C for 16 hours at atmospheric pressure and then tested in the same conditions. The results of the FT synthesis are presented in **Figure C.3** which shows CO-conversion of the two catalysts as a function of time on stream. The reduction in CO was done at a lower temperature, 270 $^0$C, because as already shown, CO reduction at higher temperatures results in graphite formation which might result in catalyst bed expansion in the reactor and also cover the catalyst surface. The analysis of the CO reduced catalyst, see Table C.1, also showed that this temperature was adequate to fully reduce the catalyst, FS-0, to carbides.



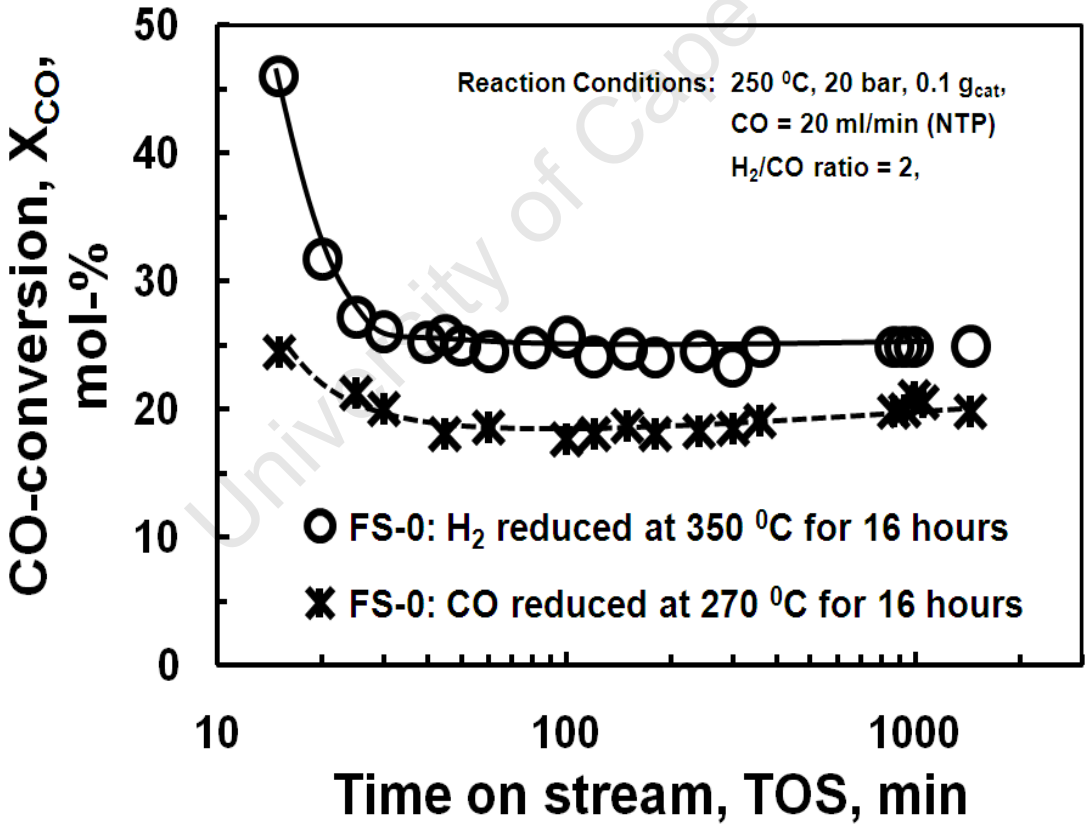


**Figure C.3:** CO-conversion of TEOS modified catalyst in the Fischer-Tropsch synthesis at 250$^0$C, 20 bar, $F_{CO,0}/W$ = 8.2 mmol/(min·g) represented area as a function of Si time on stream.

**Figure C.3** indicates CO-conversion as a function of time of stream of FS-0 catalyst pretreated with both $H_2$ and CO and the results indicate that initial deactivation is affected by pretreatment since the conversion only dropped from an initial CO-conversion of 25% to a conversion of 21% at steady state. This clearly shows that the observed initial loss in activity in the $H_2$ is due to a chemical or physical change in the catalyst.

# Appendix D: Additional Fischer-Tropsch testing results (Fe-O-Si)

## D.1 Oxidation of carbides

The CO reduction study indicated that initially $Fe_3C$ carbide is preferred for the unmodified catalyst, see Appendix 3.

$$Fe_3C + 5H_2O \leftrightarrow Fe_3O_4 + 5H_2 + CO \qquad K_{PI,eq}(250\ ^0C) = 100\ bar \qquad (D.1)$$

$$Fe_3C + 4H_2O + CO_2 \leftrightarrow Fe_3O_4 + 4H_2 + 2CO \qquad K_{PII,eq}(250\ ^0C) = 1.2\ bar \qquad (D.2)$$

Thermodynamically, the oxidation of the of bulk $Fe_3C$ yielding $Fe_3O_4$ is only feasible is the actual Kp values are smaller than the equilibrium constants;

$$\frac{P_{CO}.P_{H_2}^5}{P_{H_2O}^5} < K_{PI,eq}(250\ ^0C) = 100\ bar \qquad (D.3)$$

$$\frac{P_{CO}^2.P_{H_2}^4}{P_{CO_2}P_{H_2O}^4} < K_{PI,eq}(250\ ^0C) = 1.2\ bar \qquad (D.4)$$

The $K_{PI}$ and $K_{PII}$ of the exit stream of all the Fischer-Tropsch tested catalysts were calculated using the exit stream after 24 hours time on stream (see Table D.1). The $Kp_I$ and $Kp_{II}$ values were much larger than the equilibrium values, implying that reoxidation of the $Fe_3C$ carbide to $Fe_3O_4$ is not feasible under these conditions. Note that the same considerations would hold true for other carbides.

**Table D.1:** Actual equilibrium pressure constant, KPI and KPII (calculated using exit partial pressures listed in Table F.2 in Appendix F), after 60 min time on stream in Fischer-Tropsch experiments with Fe/*C* and Fe/*Al*3*O*3 catalysts prepared via precipitation in water-in-oil microemulsions

| **Sample Code:** | **KPI (bar)** | **KPII (bar)** |
|---|---|---|
| **FS-0** | $35x10^{4}$ | $31x10^{5}$ |
| **FS-10** | $87x10^{5}$ | $44x10^{6}$ |
| **FS-19** | $1.5x10^{3}$ | $29x10^{3}$ |
| **FS-38** | $14x10^{3}$ | $20x10^{4}$ |
| **FS-56** | $27x10^{4}$ | $21x10^{5}$ |
| **FS-88** | $31x10^{4}$ | $26x10^{5}$ |